

DEVELOPMENT AND STUDIES ON FIBER GRATING SENSORS

By
JITENDRA KUMAR
PHYS03201204006

Raja Ramanna Centre for Advanced Technology, Indore

*A thesis submitted to the
Board of Studies in Physical Sciences*

*In partial fulfillment of requirements
for the Degree of*

DOCTOR OF PHILOSOPHY

of

HOMI BHABHA NATIONAL INSTITUTE

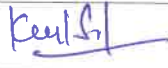
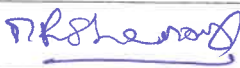
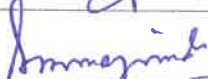
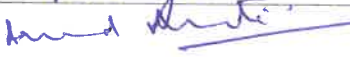
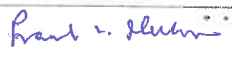


May, 2017

Homi Bhabha National Institute¹

Recommendations of the Viva Voce Committee

As members of the Viva Voce Committee, we certify that we have read the dissertation prepared by Jitendra Kumar entitled "Development and studies on fiber grating sensors" and recommend that it may be accepted as fulfilling the thesis requirement for the award of Degree of Doctor of Philosophy.

Chairman - Prof. K. S. Bindra		Date: 20-06-18
Co-chairman Prof. S. R. Mishra		Date: 20-6-18
Guide / Convener - Prof. O. Prakash		Date: 20-6-18
Examiner - Prof. M. R. Shenoy		Date: 20-6-2018
External Expert Member - Prof. A. K. Ray		Date: 20/06/2018
Member 1- Prof. S. K. Majumder		Date: 20/6/18
Member 2- Prof. A. Moorti		Date: 20/6/2018.
Member 3- Prof. P. K. Mukhopadhyay		Date:
Member 4- Prof. C. Mukherjee		Date: 20/6/18

Final approval and acceptance of this thesis is contingent upon the candidate's submission of the final copies of the thesis to HBNI.

I/We hereby certify that I/we have read this thesis prepared under my/our direction and recommend that it may be accepted as fulfilling the thesis requirement.

Date: 20/06/2018

Place: RRCAT, Indore


Guide

¹ This page is to be included only for final submission after successful completion of viva voce.

STATEMENT BY AUTHOR

This dissertation has been submitted in partial fulfillment of requirements for an advanced degree at Homi Bhabha National Institute (HBNI) and is deposited in the Library to be made available to borrowers under rules of the HBNI.

Brief quotations from this dissertation are allowable without special permission, provided that accurate acknowledgement of source is made. Requests for permission for extended quotation from or reproduction of this manuscript in whole or in part may be granted by the Competent Authority of HBNI when in his or her judgment the proposed use of the material is in the interests of scholarship. In all other instances, however, permission must be obtained from the author.



Jitendra Kumar

DECLARATION

I, hereby declare that the investigation presented in the thesis has been carried out by me. The work is original and has not been submitted earlier as a whole or in part for a degree / diploma at this or any other Institution / University.



Jitendra Kumar

List of Publications arising from the thesis

Journal

1. “Wavelength independent chemical sensing using etched thermally regenerated FBG”, **J. Kumar**, O. Prakash, R. Mahakud, S. K. Agrawal, S. K. Dixit, S. V. Nakhe, J. Canning, *Sensors and Actuators B- Chemical*, **2017**, 244, 54–60.
2. “Studies on the stability of regenerated fiber Bragg gratings at 1100 °C”, **J. Kumar**, O. Prakash, R. Mahakud, S. K. Agrawal, A. Mokhariwale, S. K. Dixit, S. V. Nakhe, *IEEE Xplore -WRAP 2015*, **2017**, 1570213269, 1–4.
3. “Inscription of FBG at multiple wavelengths using single bi-prism and its application in multi-point temperature sensing in high EMI environment”, **J. Kumar**, O. Prakash, S. K. Agrawal, R. Mahakud, A. Mokhariwale, S. K. Dixit, S. V. Nakhe, *Optical Engineering Letters*, **2016**, 55 (9), 0905021–4.
4. “Analysis of experimental results on the adulteration measurement by an Etched Fiber Bragg Grating sensor”, **J. Kumar**, R. Mahakud, U. Kumbhkar, O. Prakash, S. K. Dixit and S. V. Nakhe, *International Journal of light and electron optics-Optik*, **2015**, 24, 5698–5702.
5. “On the role of Ge-doping concentration in the refractive index rollover and thermal annealing characteristics of type IIa fiber Bragg gratings”, **J. Kumar**, O. Prakash, R. Mahakud, S. K. Agrawal, S. K. Dixit, S. V. Nakhe, *Optical Engineering*, **2014**, 53 (11), 1171031–6.

6. “Enhanced temperature (~ 800 °C) stability of type IIa fiber Bragg grating written in Ge doped photosensitive fiber”, O. Prakash, **J. Kumar**, R. Mahakud, S. K. Agrawal, S. K. Dixit, S. V. Nakhe, *IEEE photonics technology letters*, **2014**, *26*, 93–95.
7. “HF based clad etching of Fiber Bragg grating and its utilization in concentration sensing of laser dye in dye-ethanol solution”, **J. Kumar**, R. Mahakud, O. Prakash and S. K. Dixit, *Pramana Journal of Physics*, **2014**, *82*, 265–269.
8. “Development of tilted fiber Bragg gratings using highly coherent 255 nm radiation”, O. Prakash, **J. Kumar**, R. Mahakud, and S. K. Dixit, *Pramana Journal of Physics*, **2014**, *82*, 255–258.
9. “A study on HF based clad etching and chemical sensing characteristics of Fiber Bragg gratings of different reflectivity fabricated under different UV exposure times”, **J. Kumar**, R. Mahakud, O. Prakash, S. K. Dixit, *Optical Engineering*, **2013**, *52* (5), 0544021–6.

Conferences

1. “Development of high temperature (~ 900 °C) distributed fiber Bragg grating sensor”, **J. Kumar**, S. K. Agrawal, O. Prakash, S. K. Dixit and S. V. Nakhe, *DAE-BRNS National Laser Symposium (NLS-26)*, Bhabha Atomic Research Centre (BARC), Mumbai, **Dec. 20-23, 2017**, p. 36.
2. “Studies on the thermal regeneration characteristics of seed FBGs of different reflectivity”, **J. Kumar**, O. Prakash, R. Mahakud, S. K. Agrawal, S. K. Dixit and S.V. Nakhe, *OSA Technical Digest (Optical Society of America) 13th*

International Conference on Fiber Optics and Photonics (Photonics-2016), Indian Institute of Technology (IIT) Kanpur, Dec. 4-8, 2016, p. W3A.21.

3. “Studies on the stability of regenerated fiber Bragg gratings at 1100 °C”, **J. Kumar**, O. Prakash, R. Mahakud, S. K. Agrawal, A. Mokhariwale, S. K. Dixit and S.V. Nakhe, *IEEE Workshop on Recent Advances in Photonics (WRAP-2015), Indian Institute of Science (IISc) Bangalore, Dec. 16-17, 2015*, p. P-37.
4. “Effect of annealing steps on the reflectivity of thermally regenerated fiber Bragg gratings”, O. Prakash, **J. Kumar**, S. K. Agrawal, R. Mahakud, A. Mokhariwale, S. K. Dixit and S.V. Nakhe, *DAE-BRNS National Laser Symposium(NLS-24), RRCAT, Indore, Dec. 2-5, 2015*, p. CP 8.3.
5. “Temperature sustainability of type IIa FBGs written in different Ge doped fiber”, **J. Kumar**, O. Prakash, R. Mahakud, S. K. Agrawal, S. K. Dixit and S.V. Nakhe, *OSA Technical Digest (Optical Society of America) 12th International Conference on Fiber Optics and Photonics (Photonics-2014), Indian Institute of Technology (IIT) Kharagpur, Dec. 13-16, 2014*, p. T2D.4.
6. “On the determination of methanol content in ethyl alcohol using Etched Fiber Bragg Grating (EFBG)”, **J. Kumar**, R. Mahakud, U. Kumbhkar, O. Prakash, S. K. Dixit and S.V. Nakhe, *International Conference on Optics & Optoelectronics-2014 (ICOL-2014) , Instruments Research & Development Establishment (IRDE) Dehradun, Uttarakhand, Mar. 5-8, 2014*, p. 86.
7. “Studies on the thermal regeneration and temperature stability of fiber Bragg gratings written in Ge doped and Ge & B co-doped photosensitive fiber by 255 nm

beam”, **J. Kumar**, R. Mahakud, S. K. Agrawal, A. Mokhariwale, O. Prakash, S. K. Dixit and S.V. Nakhe, *DAE-BRNS National Laser Symposium (NLS-22)* , MIT, Manipal University, Manipal, **Jan. 8-11**.

8. “HF based clad etching of Fiber Bragg grating and its utilization in concentration sensing of laser dye in dye-ethanol solution”, **J. Kumar**, R. Mahakud, O. Prakash, and S. K. Dixit, *DAE-BRNS National Laser Symposium (NLS-21)* , Bhabha Atomic Research Centre (BARC), Mumbai, **Feb. 6-9, 2013**.
9. “Development of tilted fiber Bragg gratings using highly coherent 255 nm radiation”, O. Prakash, **J. Kumar**, R. Mahakud, and S. K. Dixit, *DAE-BRNS National Laser Symposium (NLS-21)* , Bhabha Atomic Research Centre (BARC), Mumbai, **Feb. 6-9, 2013**.



Jitendra Kumar

ACKNOWLEDGEMENTS

It is a matter of great pleasure for me to express my gratitude to all those who have been instrumental in the development of this thesis work, directly or indirectly.

With profound honor and ardent faith, I express my sincere gratitude to Dr. Om Prakash, Head, Fibre Grating Lab for his overall guidance, support and direction in planning and execution of the various experiments and analysis of the results.

I am deeply grateful to Dr. P. A. Naik, Director, RRCAT, for allowing me to carry out the thesis work and his valuable guidance throughout the period.

I am obliged to Dr. S. K Dixit, Head, Fibre Sensors & Optical Spectroscopy Section for constant guidance and critical suggestions during the editing of the draft thesis.

I am indebted to Shri S.V. Nakhe, Head, Laser Group for constant encouragement throughout the work.

I wish to thank the previous doctoral committee members Dr. S. K. Deb, Dr. G. S. Lodha, Dr. S. M. Oak, Dr. H. S. Rawat, Dr. A. Chakrabarti and Dr. S. M. Gupta for their guidance during the yearly review presentations.

My sincere thanks are also due to the present doctoral committee members Dr. K. S. Bindra, Dr. A. K. Ray, Dr. S. R. Mishra, Dr. S. K. Majumder, Dr. A. Moorti, Dr. P. K. Mukhopadhyay and Dr. C. Mukherjee for their valuable suggestions.

I wish to acknowledge the support of colleagues Dr. R. Mahakud, Dr. M. Saxena, Shri U. Kumbhakar, Shri S. K. Agrawal, Smt. A. Mokhariwale, Shri P. Kumar, Shri S. Kumar, Shri V. K. Saini, Shri R. K. Mishra, Shri G. N. Tiwari, Shri S. Singh, Shri J. Kumar, Shri P. Agarwal and Shri G. S. Purbia at different stages of work.

My heartfelt thanks are also due to Shri R. Sridhar, Shri D. P. Yadav and Shri K.V.A. N.P.S. Kumar from Ultra High Vacuum Technology Section for providing the vacuum test setup for the developed FBG sensors.

In the last but not the least, I express my deep appreciation to my family for their whole hearted support during the period of thesis work.

CONTENTS

	Page No.
SYNOPSIS	1
LIST OF FIGURES	9
LIST OF TABLES	16
CHAPTER 1 REVIEW ON FIBER GRATING SENSORS	17
1.0 Introduction	17
1.1 Fiber Optic Sensors (FOSs)	19
1.1.1 Based on sensing location	20
1.1.2 Based on application	21
1.1.3 Based on operating principle	21
1.2 Fiber grating sensors	22
1.3 Fiber Bragg gratings (FBGs).....	24
1.3.1 Photosensitivity and its enhancement.....	24
1.3.2 FBG operating principle and characteristics.....	28
1.3.3 FBG fabrication techniques.....	33
1.3.4 Laser sources for fiber Bragg grating fabrication.....	36
1.3.5 Types of fiber Bragg gratings	38
1.4 Fiber grating sensing principle.....	39
1.5 Current trends on FBG temperature and refractive index sensors.....	41
1.6 The constitution of present thesis.....	43
CHAPTER 2 INSCRIPTION OF TYPE-I, TYPE-IIa AND TILTED FIBER BRAGG GRATINGS	45
2.0 Introduction	45
2.1 Experimental arrangement for inscription of FBG.....	46
2.1.1 Generation and characterization of FBG writing UV beam.....	46

2.1.2	FBG inscription arrangement	49
2.1.3	Online monitoring of FBG characteristics.....	52
2.2	Inscription of type-I FBGs.....	54
2.2.1	Phase-mask approach.....	54
2.2.2	Bi-prism approach.....	57
2.3	Inscription of type-IIa FBGs.....	59
2.4	Inscription of Tilted FBGs (TFBGs)	65
2.5	Inscription of FBGs in hydrogenated fiber	68
2.5.1	Hydrogen loading in optical fibers.....	69
2.5.2	FBGs in hydrogenated fibers	72
2.6	Conclusion.....	74

**CHAPTER 3 THERMAL ANNEALING AND SENSING STUDIES ON
TYPE-I AND TYPE-IIa FBGs** 75

3.0	Introduction	75
3.1	Experimental arrangement for thermal characterization of FBGs.....	76
3.2	Studies on the thermal characterization of type-I FBGs.....	77
3.2.1	Thermal behavior of type-I FBGs with different core doping concentrations.....	77
3.3	Studies on the thermal characterization of type-IIa FBGs.....	83
3.3.1	Studies on the enhanced temperature (~ 800 °C) stability of type-IIa FBG.....	83
3.3.2	Studies on the role of refractive index rollover on the thermal annealing characteristics of type-IIa FBGs.....	87
3.4	Prediction of operating life time of type-I and type-IIa FBG	93
3.5	Application of the developed FBG sensor in temperature monitoring of transformer oil	97
3.6	Conclusion.....	100

CHAPTER 4	STUDIES ON THERMALLY REGENERATED FIBER BRAGG GRATINGS	101
4.0	Introduction	101
4.1	Effect of annealing schedule on the FBG regeneration	102
4.2	Role of core doping concentration on thermal regeneration of FBGs	107
4.3	Role of seed grating reflectivity on thermal regeneration of FBGs	111
4.4	Role of seed grating length on thermal regeneration of FBGs.....	116
4.5	Current status on FBG thermal regeneration vis-à-vis our results.....	119
4.6	Thermal regeneration studies of FBGs in non-hydrogenated fiber.....	121
4.7	Studies on thermal stability of regenerated FBGs.....	123
4.8	Conclusion.....	127
CHAPTER 5	FIBER BRAGG GRATING BASED QUASI DISTRIBUTED TEMPERATURE SENSORS	129
5.0	Introduction	129
5.1	Inscription of multiple fiber Bragg gratings in single fiber	130
5.1.1	By tilting the phase mask (Tilted FBG approach).....	130
5.1.2	By changing the divergence of incident UV beam on bi-prism..	132
5.2	Thermal characterization of the distributed temperature sensor.....	134
5.2.1	Annealing schedule for the thermal stabilization of FBG.....	134
5.2.2	Estimation of temperature response of FBG.....	135
5.3	Utilization of distributed sensor in temperature measurement (up to 500 °C) of electrically pumped pulse gas discharge laser tube.....	138
5.4	Utilization of distributed temperature sensing in Indus-2.....	144
5.4.1	Distributed surface temperature monitoring of an UHV pump...	144
5.4.2	Distributed temperature monitoring of vacuum chamber of dipole magnet.....	148
5.5	Conclusion.....	152

CHAPTER 6	ANALYTICAL AND EXPERIMENTAL STUDIES OF	
	ETCHED FBGs	153
6.0	Introduction	153
6.1	Analysis and simulation on FBG based refractive index sensor (RIS)....	154
6.1.1	Double clad slab waveguide geometry.....	155
6.1.2	Double clad cylindrical waveguide geometry.....	156
6.2	Fabrication of etched FBG based refractive index sensors.....	160
6.2.1	Single step HF-etching of FBG.....	161
6.2.2	Double step HF-etching of FBG.....	164
6.3	Experimental verification of the theoretically calculated effective refractive index at different cladding diameter.....	166
6.4	Etching characteristics of FBGs of different reflectivity	168
6.4.1	Experimental results.....	168
6.4.2	Discussion for the different behavior.....	170
6.5	Etching characteristics of thermally regenerated FBGs.....	172
6.5.1	Inscription and thermal regeneration of the FBG	172
6.5.2	HF based clad etching of fiber gratings.....	175
6.5.3	Discussion about the etching of the FBGs.....	178
6.6	Conclusion.....	179
CHAPTER 7	STUDIES ON THE CHMICAL SENSING	
	CHARACTERISTICS OF ETCHED FBGs	181
7.0	Introduction	181
7.1	Application of HF etched type-I FBGs for chemical sensing.....	182
7.1.1	Concentration sensing of laser dye in dye-ethanol solution.....	182
7.1.2	Determination of methanol content in ethyl alcohol	184
7.2	Studies on the sensing characteristics of FBGs having different reflectivity.....	188
7.2.1	Effect on chemical sensitivity of etched FBGs.....	188

7.2.2 Results and discussion on FBG during chemical sensing.....	190
7.3 Sensing characteristics of thermally regenerated etched FBG.....	192
7.3.1 Chemical sensing using HF etched thermally regenerated FBG	192
7.3.2 Discussion on the wavelength insensitivity of etched FBG.....	195
7.4 Studies on the refractive index sensing using nano-particle coated etched FBG.....	198
7.5 Conclusion.....	201
CHAPTER 8 SUMMARY AND FUTURE SCOPE	203
8.1 Summary of the thesis.....	203
8.2 Future scope of work.....	208
 REFERENCES	 211



Homi Bhabha National Institute

SYNOPSIS OF Ph. D. THESIS

- 1. Name of the Student:** Jitendra Kumar
- 2. Name of the Constituent Institution:** Raja Ramanna Centre for Advanced Technology, Indore
- 3. Enrolment No. :** PHYS03201204006
- 4. Title of the Thesis:** Development and studies on fiber grating sensors
- 5. Board of Studies:** Physical Sciences

SYNOPSIS

The fiber Bragg grating (FBG) sensors are now extensively utilized for measurement of temperature, strain, adulteration, pressure, vibrations etc. The advantages of FBG sensor over competing technologies are high spatial resolution, single point as well as distributed sensing capabilities, high sensitivity, faster response time, accessing the difficult and remote locations and capability to work in harsh environment including high EMI (electromagnetic interference). In addition, the FBG based sensors are light weight, low cost and convenient to handle by standard optical measuring instruments such as optical spectral analyzer and interrogators. A FBG sensor consists of a FBG (for single point sensing) or a sequence of spatially separated FBGs (for distributed sensing) written in the core of a single mode optical fiber as sensing elements. A FBG represents a periodic modulation of the refractive index in a photosensitive

fiber core over a fixed length. This refractive index modulation is imprinted in the photosensitive fiber core by exposing it to the UV interference pattern of submicron period. The pitch, strength of refractive index modulation and grating length decide the spectral and reflection/transmission characteristics of a FBG. Nowadays, there is a general tendency to replace the conventional sensors by fiber sensors, wherever possible. This is prompting an extensive research in the field on fiber sensors particularly based on Bragg gratings written into photosensitive fibers with progressively improved capabilities. The present thesis on “Development and studies on fiber grating sensors” focuses on the development and studies on fiber Bragg grating based temperature and refractive index sensors.

This overall thesis consists of extensive studies on the fabrication of different types of FBGs (Type-I, Type-IIa, Tilted, Regenerated), thermal characterization of FBGs, high temperature sensor development using thermally regenerated gratings, and experiment and analysis of the high sensitivity refractive index (chemical) sensing using different types of FBGs. A specially developed high beam quality UV (255 nm) source, based on second harmonic of high repetition rate copper vapor laser, is used for fiber grating fabrication. The FBGs fabricated by phase mask and bi-prism technique were thoroughly characterized as a part of research work. Thermal response of Type-I and Type-IIa FBGs has been studied in a multi-step annealing process from 30 °C to 800 °C. Role of Ge doping in fiber core on the thermal characteristic of both Type-I and Type-IIa FBG has been studied in detail. Experiment and analysis on the factors affecting thermal stability of FBG based temperature sensors are carried out. The thermal regeneration of the FBGs, in hydrogenated and non-hydrogenated fibers, is carried out for the development of high temperature (~1000 °C) sensors. The thermal regeneration of FBGs with the variation of annealing schedules, fiber doping concentration, grating length and grating

reflectivity is studied. Theoretical analysis on the life time prediction of different FBGs has been carried out.

The multi-point FBG based distributed temperature sensors are fabricated and analyzed. The tuning of Bragg peak wavelength with geometrical divergence of the UV beam is analyzed and experimentally verified. In the thesis, the results are presented for utilization of these distributed FBGs in two experiments for monitoring the spatial temperature distribution from 30 °C to 500 °C. These are, temperature distribution monitoring along the length of a gas discharge laser operating in high voltage and high EMI and multi-point surface temperature monitoring of the ultra-high vacuum chambers used for dipole magnets of Indus-2, a synchrotron radiation facility at RRCAT.

Studies on the refractive index sensing using HF etched Type-I and regenerated FBGs are carried out. The etched FBGs are analyzed for the dependence of effective refractive index on cladding diameter and surrounding refractive index. The change in Bragg wavelength, with surrounding medium refractive index, is estimated. Studies on the applications of etched FBG sensor in adulteration measurement of methanol content in ethanol and laser dye concentration estimation in dye ethanol solution are presented. Studies on the wavelength independent refractive index sensing, using etched thermally regenerated FBG, are carried out.

The overall thesis work is organized into eight chapters as follows,

Chapter 1: Review on fiber grating sensors

The first chapter begins with the types of optical fiber sensors and their classification based on sensing location, operating principle and application. The classification of fiber optic sensor, based on fiber gratings, is discussed. It includes the photosensitivity and its enhancement, fundamentals of fiber gratings, grating types and fabrication techniques. The reflection spectrum

of uniform FBG for different grating parameter such as length and coupling coefficient are presented as calculated using MATLAB software. The laser sources for writing FBGs are discussed. The importance of FBG inscription using high repetition rate, low peak power, highly coherent 255 nm radiation generated from second harmonic conversion of copper vapour laser (CVL) is also discussed. A literature survey about the application of FBG in temperature and refractive index sensing is presented. The review ends with the presentation of current status of this rapidly evolving field.

Chapter 2: Inscription of Type-I, Type-IIa and Tilted fiber Bragg gratings

This chapter presents the detailed experimental results on fiber Bragg grating fabrication using 255 nm UV beam. Both germanium and germanium–boron co-doped photosensitive fibers are employed in the FBG fabrication. Experimental investigation on FBG fabrication, by phase mask and bi-prism technique, has been carried out. In phase mask technique, refractive index modulation is induced in the photosensitive fiber core by exposure of UV interference pattern, formed by the overlap of the +1 and -1 order beam of the phase mask. A 24° apex angle bi-prism is employed to write FBGs in communications band (~1550 nm) by 255 nm UV radiation. Different types such as Type-I, Type-IIa and Tilted FBGs have been fabricated. FBGs are inscribed in hydrogenated fiber for the development of high temperature sensors (~1000 °C). Typically Type-I FBGs of reflectivity 99.9% (~30 dB) are fabricated within 70 seconds in Ge and Ge-B co-doped fibers with refractive index modulation of about 3.0×10^{-4} . The Type-IIa FBG of reflectivity about 90 % (~ 10 dB) with refractive index modulation of 1.2×10^{-4} was observed in about 30 minutes. Overall, the FBGs of different Bragg wavelengths, reflectivity and bandwidth (up to 1 nm) have been inscribed. These fabricated FBGs are subsequently utilized in development of various sensors as outlined from Chapter 3 to Chapter 7.

Chapter 3: Thermal annealing and sensing studies on Type-I and Type-IIa FBGs

The temperature sensitivity and thermal stability are the two important parameters for FBGs to be used as sensors in high temperature applications. This chapter presents the studies on the Bragg wavelength shift with change in temperature and the thermal sustainability of FBG reflection in the temperature range 30 °C to 800 °C. Thermal response of Type-I and Type-IIa FBGs has been studied in a multi-step annealing process from 30 °C to 800 °C. Role of fiber core Ge doping on the thermal characteristics of both Type-I and Type-IIa FBG has been carried out. The average temperature sensitivity ($\sim 13.9 \text{ pm}/^\circ\text{C}$) is almost same for both the Type-I and Type-IIa FBGs. The reflectivity of Type-I FBG decreased substantially after 500 °C. In contrast for Type-IIa grating, the reflectivity is almost constant upto 900 °C. Analytical study on the temperature rise during FBG fabrication and its role in temperature sustainability of the FBG has been presented. The studies on the prediction of decay time of Type-I and Type-IIa FBG, using power law approach, are also performed. Type-IIa FBG provided higher thermal stability in comparison with Type-I FBG. The chapter ends with the application of FBG sensor in monitoring of transformer oil temperature varying from 30 °C to 110 °C with the accuracy of ± 1 °C, in high voltage and high EMI environment.

Chapter 4: Studies on thermally regenerated fiber Bragg gratings

For the development of FBG based high temperature sensor (~ 1000 °C), the studies on the thermal regeneration of FBG in hydrogenated and non-hydrogenated fibers is carried out. Studies on the factors affecting the regeneration such as fiber doping concentration, annealing schedules, seed FBG reflectivity and grating length are performed. The optimization of these factors led to regenerate the one of the highest reflectivity of regenerated FBG ($\sim 88\%$) in hydrogen loaded telecommunication fiber (SMF-28). The reflectivity of the thermally

regenerated FBG increased non-linearly with increase in the seed FBG reflectivity. The refractive index modulation of regenerated FBG decreases with increase in length of seed FBG having almost similar reflectivity. Study on the residual reflectivity of the thermally regenerated grating at 1100 °C and its relation with change in dc refractive index is established. The residual reflectivity of the FBG, after ~10 hours dwell time at 1100 °C, was about 40 % for the FBG written in H₂ loaded SMF-28 fiber. The decay characteristics of FBG at 1000 °C are analyzed in terms of normalized integrated coupling coefficient. A single point temperature sensor upto 1000 °C with accuracy of ± 1 °C is developed using thermally regenerated FBG.

Chapter 5: Fiber Bragg grating based quasi distributed temperature sensors

FBG based quasi distributed temperature sensor has been developed and implemented. The number of sense points in a single fiber is decided by the bandwidth of broadband ASE source and the temperature measurement range. The studies on the multiple FBGs fabrication on a single fiber using phase mask and bi-prism technique are carried out. Theoretical studies on the Bragg wavelength shift with divergence of the UV beam and its experimental verification are done to write multiple FBGs in a single fiber. Experimentally, the Bragg wavelength tuning of ~26 nm and ~40 nm is achieved using phase mask and bi-prism approach, respectively. A six point FBGs based distributed temperature sensor is developed and utilized for monitoring the temperature (upto ~ 500 °C) of gas laser discharge tube in high voltage and high EMI environment. The FBG based distributed temperature sensor is also developed for monitoring the temperature distribution of surface of the exit port of a dipole magnet (DP-12) vacuum chamber of synchrotron radiation source Indus-2. The temperature of the exit port of DP-12 varied from 40 °C to 100 °C as monitored by a distributed sensor comprising of ten FBGs.

Chapter 6: Analytical and experimental studies of etched FBGs

Analytical and experimental studies on the etching characteristics of FBGs are carried out. The experimental results are analyzed based on double clad approximation theory for cylindrical/rectangular waveguide geometry. A graphical method is used to find out the dependence of effective refractive index of the double clad fiber on cladding diameter and surrounding refractive index. The effective refractive index is almost unaffected by the surrounding medium refractive index for cladding diameter reduction from 125 μm to 30 μm . Below 30 μm clad diameter, the effective refractive index increased with increase in surrounding medium refractive index. An experimental study on etching characteristics of fiber Bragg gratings, of different reflectivity fabricated under different UV exposure time, is also carried out. The etching rates were $\sim 2.03 \mu\text{m}/\text{min}$ and $\sim 1.69 \mu\text{m}/\text{min}$ for low reflectivity FBG $R \sim 11\%$ and high reflectivity FBG $R \sim 93\%$, respectively. The differing behavior of FBGs is linked to the different degree of densification in fused silica fiber under different UV flux exposures. Studies on HF etching of thermally regenerated FBGs have been also carried out. The regenerated grating shows no shift in Bragg wavelength during HF etching, which is contrary to HF etched Type-I FBG characteristics.

Chapter 7: Studies on the chemical sensing characteristics of etched FBGs

Applications of the etched FBG based refractive index sensor in adulteration measurement of methanol content in ethanol and concentration sensing of laser dye in dye ethanol solution is carried out. The minimum 1% concentration of methanol in ethanol was measured corresponding to change in refractive index of 2×10^{-4} . The sensitivity of the developed sensor in terms of refractive index unit (RIU) was $\sim 30 \text{ nm}/\text{RIU}$. An experimental study on the chemical sensing characteristics of etched fiber Bragg gratings of different

reflectivity fabricated under different UV (255 nm) exposure times is also done. It has been demonstrated that same refractive index sensitivity could be achieved under smaller etching time (larger residual clad diameter) for FBG with lower reflectivity. The etched thermally regenerated fiber grating was applied for chemical sensing and the concept of amplitude only detection is demonstrated by reducing the wavelength sensitivity. It has been demonstrated that the high refractive index sensitivity with good mechanical strength could be achieved by coating the etched FBG with silver nanoparticles.

Chapter 8: Summary and future scope

This chapter is a summary of the experimental and analytical investigations on FBG based temperature and refractive index sensors as carried out during the course of thesis work. The scope for future extension of the work such as further research into Regenerated and Tilted FBGs, distributed high temperature and high sensitivity refractive index sensing are outlined.

LIST OF FIGURES

1.1	Transmission loss spectrum of a 15 mm thick preform before and after being irradiated by UV radiation (Ref. 16)	25
1.2:	Schematic of a fiber Bragg grating structure	28
1.3:	(a) Calculated reflection spectra of uniform Bragg grating as a function of wavelength with different grating length (b) Calculated reflection spectra of 10 mm long uniform Bragg grating as a function of wavelength with different refractive index modulation	31
1.4:	FBG reflectivity with (a) grating length and (b) refractive index modulation	32
1.5:	FBG inscription using interferometric fabrication technique	34
1.6:	Setup for point-by-point grating fabrication	34
1.7:	Schematic of the phase mask based FBG fabrication	35
1.8:	Copper vapour laser (CVL) and its second harmonic generation	37
2.1:	(a) Schematic and (b) actual set up of SH generation and FBG writing	47
2.2:	(a) UV beam near field spot along with its intensity profile and (b) UV interferogram with its intensity variation along line	48
2.3:	Photograph of the phase-mask and bi-prism used for FBG inscription	51
2.4:	Mechanical mounting, fiber positioning setup and its graphical user interface	52
2.5:	A fiber optic circulator	53
2.6:	Experimental arrangement for FBG inscription using a phase mask	54
2.7:	OSA traces showing evolution of FBG-A3 with increased UV fluence	55
2.8:	Refractive index modulation with UV fluence for FBG-A1, A2 and A3	57
2.9:	Actual experimental set up of FBG inscription using bi-prism	58

2.10:	FBG written in PS-270 fiber with bi-prism based inscription technique	58
2.11:	OSA traces showing Type-IIa FBG evolution at different fluence for FBG-B1	59
2.12:	Variation of grating reflectivity with inscription time	61
2.13:	Variation of (a) Δn_{ac} and (b) Δn_{dc} with UV fluence during FBG inscription	62
2.14:	Experimental set-up for writing Tilted fiber Bragg grating	65
2.15:	Transmission spectra for grating tilt angle (a) 0^0 and (b) 3^0	66
2.16:	Fig. 2.16: Variation in (a) Bragg wavelength and reflectivity and (b) refractive index modulation and coupling coefficient with tilt angle	68
2.17:	(a) Schematic and (b) actual hydrogen loading set up for optical fibers	69
2.18:	(a) Diffusivity and (b) saturation concentration of hydrogen in silica	71
2.19:	Evolution of FBG spectra with UV exposure for FBG-C1	72
2.20:	Refractive index modulation for FBGs written in hydrogenated fibers	73
3.1:	(a) Schematic and (b) experimental set up for thermal characterization of FBGs	76
3.2:	Variation in FBG reflectivity with time at temperature (A) $30\text{ }^{\circ}\text{C}$ to $600\text{ }^{\circ}\text{C}$ (B) at $600\text{ }^{\circ}\text{C}$ (C) at $700\text{ }^{\circ}\text{C}$ and (D) at $800\text{ }^{\circ}\text{C}$	78
3.3:	Bragg wavelength shift with time at various temperatures for all FBGs	80
3.4:	Variation of NICC (η) with time at $600\text{ }^{\circ}\text{C}$ for all FBGs	81
3.5:	Variation in the Bragg wavelength (solid symbols) and reflectivity (open symbols) with time at $700\text{ }^{\circ}\text{C}$	82
3.6:	Variation of Type-I and Type-IIa FBG reflectivity with time for temperature (A) $30\text{ }^{\circ}\text{C}$ to $600\text{ }^{\circ}\text{C}$ (B) at $600\text{ }^{\circ}\text{C}$ (C) at $700\text{ }^{\circ}\text{C}$ and (D) at $800\text{ }^{\circ}\text{C}$	83
3.7:	Average UV power (solid sphere) and fringes intensity variation (inset)	86
3.8:	Normalized reflectivity of FBGs with time at $600\text{ }^{\circ}\text{C}$, $700\text{ }^{\circ}\text{C}$ and $800\text{ }^{\circ}\text{C}$	87

3.9:	Bragg wavelength shift with time at temperature 600 °C, 700 °C and 800 °C	89
3.10:	Estimated temperature rise per pulse with Ge doping in fibers	91
3.11:	Estimated average temperature rise and Bragg wavelength shift with Ge doping	91
3.12:	Typical change in normalized reflectivity and Bragg wavelength with temperature for annealed FBG-B2 and B3	92
3.13:	Developed FBG sensor for temperature measurement up to 500 °C	92
3.14:	Developed FBG sensor for temperature measurement up to 800 °C	92
3.15:	NICC for Type-I and Type-IIa FBGs at temperature 600 °C, 700 °C and 800 °C	94
3.16:	(a) Power law factor and (b) power law decay coefficient with temperature for Type-I and Type-IIa FBGs	95
3.17:	The calculated thermal decay of Type-I and Type-IIa FBGs	96
3.18:	Test set up used for calibration of FBG based temperature sensor for temperature monitoring of transformer oil	97
3.19:	Characterization curve of the FBG used for the oil temperature measurement	98
3.20:	Actual experimental set up for deployment of FBG sensor	99
3.21:	Temperature display captured from the computer screen	99
4.1:	(a) Transmission spectra of the FBG and (b) reflectivity and Δn_{ac} of FBG written in H ₂ loaded SMF-28 fiber	103
4.2:	Reflectivity/transmission dip at different time and temperature of a step annealed FBG	104
4.3:	(a) OSA traces showing growth of RFBG with time at 900 °C and (b) RFBG spectra obtained with step annealing process	105
4.4:	(a) Reflectivity and transmission dip at different time and temperature of ramp	

annealed FBG and (b) RFBG spectra obtained with ramp annealing process	106
4.5: Thermal annealing studies of FBGs (transmission dip) up to temperature of 900 °C	110
4.6: Thermal annealing studies of FBGs (reflectivity) up to temperature of 900 °C	110
4.7: Variation in FBG reflectivity and refractive index modulation with UV fluence	112
4.8: (a) FBG transmission dip with time at different temperature (600 °C to 900 °C) and (b) FBG reflectivity with time at 1000 °C	113
4.9: Variation of transmission dip of RFBG with seed FBG	114
4.10: Variation of NICC (η) with time at 1000 °C for all FBGs	115
4.11: Predicted decay time at 1000 °C for all RFBGs	115
4.12: Change in FBG reflectivity with time at different temperature	117
4.13: Variation of Δn_{ac} of regenerated FBG with Δn_{ac} of seed FBG	118
4.14: Variation of Δn_{ac} of regenerated and seed FBG with in seed FBG length	118
4.15: Thermal regeneration studies in non-hydrogenated fiber	121
4.16: Transmission spectra at different temperature and time for RFBG	123
4.17: Thermal annealing studies up to temperature of 1100 °C	123
4.18: Thermal response of post annealed RFBG	124
4.19: Residual reflectivity and change in Bragg wavelength from pre to post annealed and from decayed to regenerated FBG	125
4.20: OSA traces showing Bragg wavelength shift with applied temperature for post annealed FBG-C1	126
4.21: Thermal response of post annealed RFBG	127
5.1: Calculated Bragg wavelength shift with phase mask tilt angle for (a) different effective	

refractive index and (b) different phase mask periods	132
5.2: Bragg wavelength tuning by splicing two fibers and writing Tilted FBGs	132
5.3: Translation of lens position and its effect on divergence	133
5.4: Change in Bragg wavelength as a function of lens translation	134
5.5: Variation of normalized integrated coupling coefficient with time at 600 °C	135
5.6: (a) Bragg wavelength and (b) average temperature sensitivity with temperature	136
5.7: Simulated Bragg wavelength shift vs temperature change	137
5.8: Predicted temperature with FBG-4 vs Thermocouple temperature	137
5.9: Waveform of voltage and current pulses across the laser head for 40 W copper bromide (CuBr) laser	139
5.10: Variation of refractive index modulation with cumulative fluence	140
5.11: (a) Schematic of temperature monitoring system and (b) actual implementation of multiple FBGs at different locations along the CuBr laser tube	142
5.12: Interrogator results showing Bragg wavelength shift with temperature for all the FBGs	143
5.13: Temperature profile along the laser tube with applied electrical power	144
5.14: (a) schematic and (b) actual implementation of distributed FBG temperature sensor to UHV set up	146
5.15: Screen shot of the measured wavelength shift and corresponding temperature along the arm of the UHV pump	147
5.16: Measured temperature of the UHV set up using FBG-UH7 and the thermocouple-4 with respect to time (~28 hours)	147
5.17: Temperature profile along the length of the UHV pump	148

5.18:	Schematic of the distributed temperature monitoring	149
5.19:	Experimental arrangement of the distributed temperature monitoring	150
5.20:	Expanded view of the experimental arrangement	150
5.21:	Indus-2 beam current on 06/12/2016	151
5.22:	Temperature of the exit port of DP-12 on 06/12/2016	151
6.1:	Schematic of the refractive index profile for double clad fiber	155
6.2:	Estimation of effective refractive index	156
6.3:	Variation of δ_1 and δ_2 with n_{eff} for different surrounding refractive index ($n_{sur} = 1.0, 1.2, 1.3, 1.42$) at fixed clad diameter of $10 \mu\text{m}$	159
6.4:	Theoretical variation of effective refractive index (n_{eff}) of an EFBG with surrounding medium refractive index based on the algorithm defined in the text	159
6.5:	(a) Schematic and (b) experimental set up for FBG clad etching/ refractive index sensing	160
6.6:	Microscopic view of FBG cladding (a) before etching (b) after etching	162
6.7:	OSA traces of Bragg wavelength shift with etching time ($t_1 < t_2 < t_3 < t_4 < t_5$)	162
6.8:	Change in Bragg wavelength and clad diameter as a function of etching time	163
6.9:	OSA traces showing Bragg wavelength shift with etching time (t_1 to t_5)	164
6.10:	Shift in Bragg wavelength with etching time observed during experiment	165
6.11:	Microscopic images of the optical fiber before and after HF etching	165
6.12:	Effective refractive index of an EFBG with different cladding diameter - calculated and experimental data	167
6.13:	Bragg wavelength shift with etching time	169

6.14:	Cladding diameter as a function of etching time	169
6.15:	Typical OSA transmission spectra of (a) Type-I seed FBG and (b) RFBG	172
6.16:	Annealing schedule and regeneration of grating	173
6.17:	Bragg wavelength shift during HF etching	176
6.18:	FBG reflection power shift during HF etching	176
6.19:	Microscopic images of the etched FBGs and their intensity profile	177
7.1:	OSA traces showing change in Bragg wavelength for different dye concentration (C_1 – Air, C_2 – 0.0 mM, C_3 – 0.5 mM, C_4 – 1.0 mM, C_5 – 1.5 mM)	183
7.2:	Change in Bragg wavelength as a function of dye concentration	183
7.3:	Estimated refractive index of the ethanol-methanol solution at different percentage of methanol concentration in ethanol (Eq. 7.1)	184
7.4:	OSA traces for different methanol content in ethanol for (A) 100%, (B) 50%, (C) 33% and (D) 0% methanol content in ethanol	186
7.5:	Bragg wavelength shift and sensitivity of EFBG for different methanol content in alcohol (a) For 0% to 10% (b) For 0% to 100%	187
7.6:	OSA traces showing refractive index sensing with (a) non-etched FBG-F1 (b) non-etched FBG-F2 (c) 38 min etched FBG-F1 and (d) 42 min etched FBG-F2	189
7.7:	Bragg wavelength shift as a function of etching time	189
7.8:	Refractive index sensitivity as a function of etching time	190
7.9:	Refractive index sensitivity as a function of cladding diameter of FBG	190
7.10:	Typical OSA traces for FBG-A, B and C for different surrounding media	193
7.11:	Bragg wavelength shift and reflection power change for different surrounding media	

for FBG-A, B, C and D	194
7.12: Schematic of HF etching and Ag nano-particle coating on FBG	199
7.13: Reflection spectra of FBG before and after HF etching	199
7.14: Reflection spectra of FBG before and after Ag nano-particle coating	200
7.15: Response of nano-particle coated etched FBG for different chemicals	200

LIST OF TABLES

2.1: The parameters of the CVL and its second harmonic UV beam	49
2.2: Parameters of different optical fibers used in FBG inscription	50
2.3: Transmission dip with UV fluence of FBGs written in different fibers	60
2.4: Bragg wavelength and transmission dip for different tilt angles	66
3.1: Normalized reflectivity of FBGs with time at 600 °C, 700 °C and 800 °C	88
4.1: Transmission dip during the whole annealing process	108
4.2: Transmission dip during the whole annealing process	112
4.3: Parameters of seed FBGs of different length	116
4.4: Variation of transmission dip during the whole annealing process	117
4.5: Parameters of regenerated FBGs of different length	118
4.6: Results on high reflectivity RFBG reported in different types of fibers and strength of seed Type-I FBG	120
4.7: Observed thermal regeneration for hydrogenated and non-hydrogenated fiber	122
7.1: Estimated refractive index of the solution and Bragg wavelength shift	185

Chapter 1

Review on fiber grating sensors

1.0 Introduction

Fiber optic sensor (FOS) has been one of the most widely utilized technological developments achieved by optoelectronics and fiber optic communication industries [1-10]. A fiber optic sensor works on the principle of modulating/perturbing one or more properties of a propagating light wave such as intensity, phase, polarization, and wavelength, in response to the environmental parameter being measured [1-10]. The most common optical sensing methods are (a) Raman and Brillouin scattered radiation from the fiber [11-12] (b) Surface plasmon resonance (SPR) from metal coated fibers, [13-14] (c) Transmission/reflection resonances from Fabry-Perot fiber structure [15] and (d) Transmission/reflection resonances from in-built fiber grating such as fiber Bragg grating (FBG) and long period fiber grating (LPFG) [16-17].

The ability to measure temperature and strain, at hundreds of points along a single fiber, is particularly interesting for the monitoring of large structures such as bridges, pipelines, flow lines, oil wells, dams and dikes. Sensing systems based on Brillouin and Raman scattering have been used, for example, to measure temperature of cables and pavement in bridges, detect pipeline leakages, prevent failure of pipelines installed in landslide areas, optimize oil production from wells and detect hot-spots in high-power cables. The maximum temperature measured with Raman and Brillouin scattering based sensor is ~ 200 °C with accuracy of 1 °C. However the minimum spatial resolution, achieved by this type of sensor, is limited to 1 meter. Also in Raman scattering based distributed temperature sensor, the Raman back scattered signal is very low. Therefore, high peak power laser pulse and long measurement time are needed to ensure good temporal and spatial resolutions [18].

The SPR technique, using metal coated fiber, has been used for temperature and chemical sensing. The temperature sensing upto 300 °C is reported using such sensor [19]. The SPR probe can be miniaturized for detecting samples which are available in minute quantity and costly. However, this sensor works in only transmission mode and also quite complex for distributed sensing applications.

Fiber-optic Fabry–Perot interferometric (FFPI) sensors have attractive characteristics such as high sensitivity, linear response, small size, and small temperature cross-sensitivity. Also, the phase of the interference signal is linearly proportional to the optical length, defined as the product of the micro-cavity length and the refractive index of the filling medium. Therefore, FFPI sensors have been widely used for measurement of a variety of parameters such as refractive index (RI), temperature, strain, etc [20-21]. However when the RI of the measuring medium is close to that of optical fiber, the reflected light from the surface is very weak according to Fresnel law. In this case, the FFPI sensor shows very poor optical performance, and the accuracy and resolution of the RI measurement become deteriorative accordingly [22].

In-built fiber grating based sensors such as long period fiber grating (LPFG) and fiber Bragg grating (FBG) have their own advantages and disadvantages for sensing applications. LPFG has higher temperature and refractive index sensitivity as compared to FBG. However the spectral response of LPFG can be measured only in transmission mode and often with poor resolution due to broad (typically tens of nm) transmission loss type resonances. To reduce the bandwidth of LPFG, the device length has to be increased substantially. This leads to difficulty in using LPFG as point or localised sensor [23]. Fiber Bragg grating based sensors offer advantages such as point sensor, high spatial resolution (typically few mm), single as well as distributed sensing capabilities, reflection mode operation and the wavelength coded operation

not significantly affected by the source intensity fluctuations or insertion losses. Since last two decades, the FBG sensors have gained tremendous importance for temperature, strain, refractive index and radiation measurements. The FBG based sensors are now being extensively used in aerospace, civil engineering, gas and petroleum, healthcare and nuclear industries. There is a general tendency to replace the conventional sensor by fiber sensors, wherever possible, due to their light weight, EMI immunity, low cost, high sensitivity and faster response time. This is prompting an extensive research in the field of fiber sensors particularly based on grating written into photosensitive/non-photosensitive fibers with progressively improved capabilities.

The present thesis is focused on the research work related to the development of temperature and refractive index sensors using different types of fiber Bragg gratings (FBGs). The Type-I, Type-IIa, regenerated and etched FBG, employed for sensing, are developed and characterized as a part of research work. The thesis is divided into eight chapters wherein the present Chapter 1 is an exhaustive and updated review on the fiber grating sensors including basic physics, sensors development and their deployment. The chapter begins with tracing the evolution of the fiber optic sensor field. Discussion about the fiber grating sensor, the fundamentals of fiber grating, types and fabrication techniques of fiber grating is presented. The laser sources for writing fiber gratings are discussed. The applications of FBGs in research, technology and industrial areas are presented. The review ends with the current status of this rapidly evolving field on fiber Bragg grating sensors.

1.1 Fiber Optic Sensors (FOSs)

In 1967, the first fiber optic “Fotonic” sensor was suggested to measure the position and spacing in the machine tool industry [24]. Since then, the Fiber optic sensors (FOSs) have been used in a wide variety of applications such as for measurement of temperature [25], strain [26],

pressure [27-28], rotation [29], velocity [30], acceleration [31], magnetic field [32], vibration [33], chemical and biological species [34-39], pH level [40], blood oxygen [41], acoustic waves [42], pollutants [43], natural structures for prediction of earthquakes [44] and many other physical and chemical parameters [45-58]. There have been excellent reviews, books and articles on fiber optic sensors [1–10]. Fiber optic sensors offer the possibility of measurement in harsh environments where conventional electrical and electronic sensors have difficulties. Their demand from industry is increasing because of the advantages of small size, high multiplexing capability, immunity to EMI, high temperature operation, improved measurement accuracy and reliability. Nowadays a variety of commercial discrete sensors based on Fabry–Perot (FP) cavities and fiber Bragg gratings (FBGs), as well as distributed sensors based on Raman and Brillouin scattering methods, are commercially available along with pertinent interrogation instruments. In fiber optic sensing, the optical radiation characteristics changes due to change in external parameter such as temperature, stress, strain, rotation or electric currents. Fiber optic sensors can be classified under following three categories.

1.1.1 Based on sensing location

Based on the sensing location, a fiber optic sensor can be classified as extrinsic or intrinsic sensor. In an extrinsic sensor, light has to leave the fiber and reach the sensing region outside and then comes back to the fiber. In this case, the fiber just acts as a means of getting the light to the sensing location. For an intrinsic sensor, one or more of the physical properties of the propagating light in the fiber such as its phase, polarization, amplitude or wavelength and spectrum undergo a change. Perturbations act on the fiber and the fiber in turn changes some characteristic of the light inside the fiber [1-10].

1.1.2 Based on application

Based on the application, a fiber optic sensor can be classified as (a) Physical sensor: used to measure physical properties such as temperature, strain/stress, pressure etc. (b) Chemical sensor: used for pH measurement, refractive index sensing, gas analysis, spectroscopic studies, etc. and (c) Bio-medical sensor: used in bio-medical applications such as measurement of blood flow, glucose content, temperature of the tissues, etc..

1.1.3 Based on operating principle

Based on the operating principle or modulation/demodulation process, a fiber optic sensor can be classified as intensity, phase, frequency, or polarization sensor [1-10]. All these parameters may be subjected to change due to external perturbations. Thus, by detecting these parameters and their changes, the external perturbations can be sensed. Correspondingly, FOSs can be further grouped into the following four broad categories.

(a) Intensity modulated fiber optic sensors – Intensity modulated fiber optic sensors rely on signal undergoing some losses. These are made by using an apparatus to convert what is being measured into a force that bends the fiber and causes attenuation of signal. Other ways to attenuate the signal is through absorption or scattering from a target such as Raman and Brillouin scattering. The intensity modulated sensor requires more light and therefore usually uses multimode large core fibers [59-62]. Simplicity of implementation, low cost, possibility of being multiplexed, and ability to perform as real distributed sensors, are some of the basic advantages of these sensors. Intensity modulated fiber optic sensors have a series of limitations imposed by variable losses in the system that are not related to the environmental effect to be measured. Potential error sources include variable losses due to connectors and splices, micro bending loss, macro bending loss, mechanical creep and misalignment of light sources and detectors.

(b) Phase modulated fiber optic sensors - In the phase modulated sensors, an interferometer (such as Mach-Zehnder interferometer) is used to sense the output signal by comparing the phase of the received signal with a reference signal. These are used to measure pressure, rotation and magnetic field, etc. These sensors usually give accurate results, but are expensive to manufacture [63-65]. The other problems associated with these sensors are multi-sensing, signal division, sensitivity stabilization and tuning control.

(c) Polarization modulated fiber optic sensors – In polarization-modulated fiber optic sensors, the polarization state of light propagating in the fiber is changed due to an external perturbation such as electric field, magnetic field, etc. By detecting the change in the output polarization state of the light propagating in the fiber, the external perturbation can be sensed. One example of polarization modulated sensor is an optical current sensor based on magneto-optic (Faraday) effect [66]. Generally, these types of sensors are used in a variety of measurements, communication and signal processing applications. However, the unintentional polarization alteration by other processes such as bending, stretching, and twisting causes error in the results.

(d) Wavelength modulated fiber optic sensors - In the wavelength modulated sensors, the spectrum of the transmitted, reflected or emitted light is changed. Such sensors include blackbody radiation, fluorescence, phosphorescence and fiber grating sensors [67-68]. Wavelength modulated sensors experience a shift in wavelength depending upon displacement, temperature or the presence of chemical species. Fiber gratings are an excellent sensing element due to their high sensitivity, multiplexing capability and reasonable fabrication cost.

1.2 Fiber grating sensor

The wavelength modulated fiber optic sensors are very sensitive and not strongly affected by light loss in connections or source intensity fluctuations. Among the wavelength modulated

fiber optic sensors, the most promising developments are those based on fiber gratings. A fiber grating is a phase grating, consisting of periodic modulation of refractive index in a small segment in the fiber core [16]. The fiber gratings can be divided into different types based on their light coupling mechanism.

(A) Short period gratings/Fiber Bragg gratings - For fiber Bragg gratings (FBGs), the grating period (uniform) is typically 0.22-0.54 μm . Under phase matching conditions, a fiber Bragg grating couples the forward propagating core mode to the backward propagating core mode. Depending on parameters such as grating length and magnitude of induced refractive index change, the Bragg grating can perform as narrowband transmission or reflection filter [16].

(B) Long period fiber gratings - A long period fiber grating (LPFG) can couple the forward propagating core mode to one or a few of the forward propagating cladding modes. Due to the long period (100-500 μm) of the grating, these can be successfully manufactured using amplitude mask or point-by-point writing with either UV exposure or heat [17].

(C) Tilted fiber gratings - A Tilted fiber grating can couple the forward propagating core mode to the backward propagating core mode and the forward propagating core mode to the backward propagating cladding modes [69]. The Bragg wavelength tuning with the tilt angle is discussed in **Chapter 2** and its utilization for multipoint temperature sensing is discussed in **Chapter 5**.

(D) Chirped fiber gratings - A chirped fiber grating, with unequal periods, has a wider reflection spectrum and each wavelength component is reflected at different positions along the grating length. This results in a delay time difference for different reflected wavelengths. Chirped fiber gratings are used as dispersion compensators in communication networks and for intra-grating sensing.

Among all these fiber gratings, fiber Bragg gratings (FBGs) are the most widely used as sensor heads. FBG sensors have a number of distinguishing advantages such as,

(i) FBG sensors can give an absolute measurement which is insensitive to fluctuations in the intensity of the light source, as the information is usually obtained by detecting the wavelength shift.

(ii) FBGs can be directly written into the fiber without changing the fiber diameter, making them compatible with a wide range of situations where small diameter probes are essential, such as in advanced composite materials or the human body.

(iii) FBGs can be mass produced at low cost, making them potentially competitive with conventional electrical sensors [70].

(iv) FBGs can be multiplexed using wavelength-division multiplexing (WDM), time-division-multiplexing (TDM), and their combinations [71-72] making quasi distributed sensing feasible in practice.

1.3 Fiber Bragg Gratings (FBGs)

1.3.1 Photosensitivity and its enhancement

The ability to permanent change in the refractive index of the fiber core with radiation is referred as photosensitivity [73-75]. Several models have been proposed for these photo induced refractive index changes such as colour-center model [76], compaction model [77] and stress relief model [78].

(a) Colour-center model - During the high-temperature gas-phase oxidation process of the modified chemical vapor deposition technique (MCVD), GeO_2 dissociates to GeO due to its higher stability at elevated temperatures manifesting in the form of oxygen vacancy Ge-Si and Ge-Ge bonds [76]. These defects, normally caused during the fiber drawing process, are called color centers due to their strong absorption. The Ge-Si wrong bond has an absorption band at ~

244 nm (5.1 eV). The refractive index change induced by 244 nm (5.1 eV) photons, below the band gap energy (~8.5 eV) of Ge-doped silica glass implied that the point defects in the ideal tetrahedral network of glass are responsible for FBG inscription. This absorption has been shown to bleach when exposed to UV radiation as shown in Fig. 1.1. 255 nm radiation which is generated from second harmonic of copper vapour laser (CVL-UV) is close to the peak absorption wavelength 244 nm. So for 255 nm laser beam also the same model can be used for the explanation of photosensitivity.

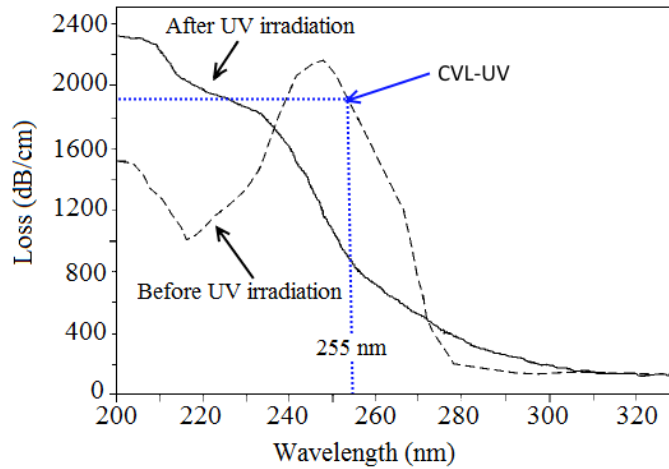


Fig. 1.1: Transmission loss spectrum of a 15 mm thick preform before and after being irradiated by UV radiation (Ref. 16)

The bleaching of this absorption band with 255 nm, results in the evolution of new absorption bands due to creation of new defects [79-81]. With the 255 nm UV exposure the wrong bonds breaks in the glass and creates GeE' centers. These centers liberated the free electron which is free to move throughout glass matrix. These free electrons re-attach to either Ge (1) or Ge (2). The color center model is based on the change in absorption spectrum of the fiber core subject to UV illumination, particularly bleaching of 255 nm absorption band. The absorption changes in the short wavelength (UV) region lead to change in refractive index in the long wavelength (IR) region through the Kramers-Kronig relation [76] given by

$$\Delta n_{eff}(\lambda) = \frac{1}{2\pi^2} \int_0^\infty \frac{\Delta\alpha_{eff}(\lambda')}{1-(\lambda/\lambda')^2} d\lambda' \quad (1.1)$$

where Δn_{eff} is the effective refractive index change at wavelength λ' due to a change in absorption coefficient $\Delta\alpha_{eff}$ at wavelength λ . The color center model is the most widely accepted model for the formation mechanism of Bragg gratings. However, it is not clear whether this model alone can always account for all the observed index changes.

(b) Densification model – This model is based on UV laser irradiation induced density changes in germanosilicate glass. This results into variations of stress and refractive index of the glasses [77]. Fiori *et al.* reported compaction in fused silica slab waveguides that leads to positive refractive index changes on UV illumination [82]. This model is applied for the explanation of chemical sensing behavior of FBGs of different reflectivity in **Chapter 7**.

(c) Stress-relief model – This model [83-84] is based on the hypothesis that the refractive-index change arises from the alleviation of thermo-elastic stresses in the core of the fiber built-in during drawing of fiber. The fiber-optic core in a germanosilicate fiber is under tension due to the difference in the thermal expansion of the core and the cladding material. Tension reduces the refractive index through the stress-optic effect. Therefore, it is expected that stress relief will lead to the increase in refractive index. It is believed that stress relief is one of the reasons of Type-IIa FBG formation which is discussed in **Chapters 3, 4 and 7**.

There are various **photosensitization techniques** used in optical fibers for inscribing strong FBGs such as, addition of boron in optical fiber during fiber drawing [85], FBG inscription with vacuum UV radiation [86-87], and hydrogenation & flame brushing [88] of optical fiber before FBG inscription.

(a) Raising of Ge content in the fiber core - raising of germanium dopant levels increased the number of germanium oxygen deficiency centers and results into higher photosensitivity.

(b) Boron co-doping in the germanosilicate fiber during fiber drawing - if the Ge dopant levels are too high, the refractive index can become higher than desired value and also the optical loss can be increased significantly. Moreover the mechanical strength of the fiber also decreases. To avoid the undesirable effects of excessive Ge doping levels, additional co-dopants such as boron can be used. The addition of boron into the silica lowers the refractive index, thus compensating for some of the refractive index increase due to Ge inclusion, and is also found to enhance the photosensitivity [85].

(c) Grating inscription using vacuum UV radiation - It has been demonstrated that gratings can be inscribed in telecommunication fibers using the ArF excimer vacuum UV radiation at 193 nm by a two-photon mechanism [86-87]. An advantage of using shorter-wavelength light in inscribing Bragg gratings is the possibility of higher spatial resolution in diffraction-limited techniques, such as the point-by-point writing.

(d) Hydrogenation & hydrogen flame brushing of optical fiber before FBG inscription - Hydrogenation of optical fibers is a simple technique for achieving very high UV photosensitivity in germanosilicate optical fibers [88]. The hydrogen molecules react in the glass at normal Si – O – Ge sites, forming OH species and UV bleachable GODCs, which are responsible for the enhanced photosensitivity. In hydrogen flame brushing technique the region of the optical fiber to be photosensitized is brushed repeatedly by a flame fueled with hydrogen and a small amount of oxygen. In this process the hydrogen diffuses into the core of the fiber very quickly and reacts with the germanosilicate glass to produce germanium oxygen deficiency centers.

1.3.2 FBG operating principle and characteristics

A fiber Bragg grating consists of periodic modulation of the refractive index in the core of single-mode optical fiber. Schematic and operation of basic FBG are illustrated in figure 1.2.

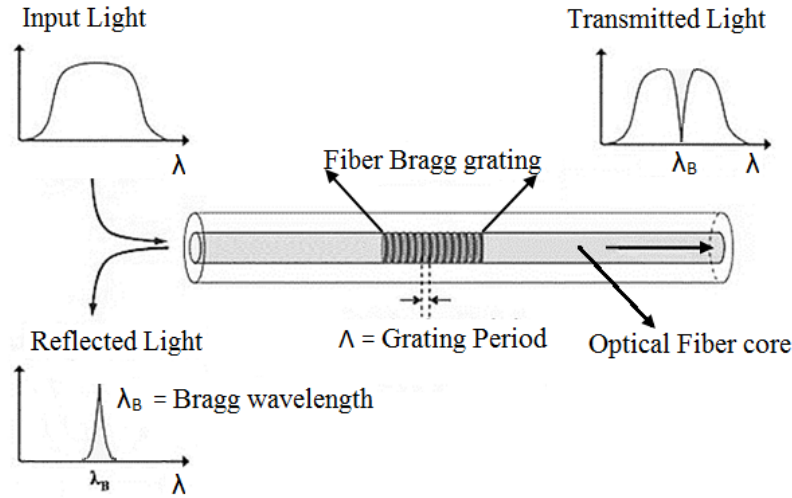


Fig. 1.2: Schematic of a fiber Bragg grating structure

When light from a broadband source is launched from one side of the fiber, only a particular wavelength which satisfies Bragg condition will be reflected while the remainder is transmitted without any loss. Periodic refractive index variations reflect the incoming wavefront and constructively form a back reflected power peaked at a centre wavelength defined by the grating characteristics. The Bragg grating resonance condition is the requirement to satisfy both energy and momentum conservation. The energy conservation ($\hbar\omega_i = \hbar\omega_f$) requires that the frequency of the reflected radiation should be the same as that of the incident radiation. The momentum conservation requires that the sum of incident wave vector (\vec{k}_i) and the grating wave vector (\vec{K}) should be equal to the wave vector of the scattered radiation (\vec{k}_f). This can be expressed as,

$$\vec{k}_i + \vec{K} = \vec{k}_f \quad (1.2)$$

where the grating wave vector \vec{K} , has a direction normal to the grating plane with a magnitude $2\pi/\Lambda$, with Λ being the grating spacing [89]. The diffracted wave vector is equal in magnitude

and opposite in direction with regard to the incident wave vector and hence the momentum conservation condition can be represented as [90]

$$2 \left(\frac{2 \pi n_{eff}}{\lambda_B} \right) = \frac{2 \pi}{\Lambda}$$

This simplifies to the first order Bragg condition

$$\lambda_B = 2 n_{eff} \Lambda \quad (1.3)$$

where λ_B is the Bragg wavelength and n_{eff} is effective refractive index of the fiber core. If the Bragg condition is not satisfied, the reflected light from each subsequent plane in the grating becomes out of phase progressively and gradually cancel out. Hence, light that is not coincident with the Bragg wavelength will simply get transmitted and experience very little reflection. The grating filter characteristics have been modeled by several approaches [91-95]. Coupled-mode theory is often the foundation for many of these computations. In its simplest form, this analysis leads to a single differential equation for a modified local reflectivity, which is easily integrated by standard numerical methods. The simplest uniform fiber Bragg grating structure in an optical fiber is an axial (z) and periodic change of the refractive index of the core, with a refractive index modulation given by [96],

$$n(z) = n_0 + \Delta n \cos \frac{2 \pi z}{\Lambda} \quad (1.4)$$

where Δn is the amplitude of the induced refractive index modulation (typically 10^{-5} - 10^{-2}), n_0 is the average refractive index, z is the distance along the fiber's longitudinal axis, and Λ is the geometrical grating period. From the coupled mode theory, the reflectivity of a grating with constant modulation amplitude and period is given by the following expression [89]

$$R(L, \lambda) = \frac{\kappa^2 \sinh^2(L\sqrt{\kappa^2 - \Delta\beta^2})}{\Delta\beta^2 \sinh^2(L\sqrt{\kappa^2 - \Delta\beta^2}) + (\kappa^2 - \Delta\beta^2) \cosh^2(L\sqrt{\kappa^2 - \Delta\beta^2})} \quad (1.5)$$

where $R(L,\lambda)$ is the reflectivity, which is a function of the grating length L , and wavelength λ . κ is the coupling coefficient, $\Delta\beta$ is the detuning wave vector,

$$\Delta\beta = \beta - \frac{\pi}{\Lambda} = \frac{2\pi n_0}{\lambda} - \frac{\pi}{\Lambda} \quad (1.6)$$

The coupling coefficient, κ , for the sinusoidal variation of index modulation along the fiber axis is given by [97]

$$\kappa = \frac{\pi \Delta n \eta}{\lambda} \quad (1.7)$$

Where $\eta=1-(1/V^2)$. This η is a function of the fiber parameter V that represents the fraction of the integrated fundamental-mode intensity contained in the core. The reflectivity increases as the induced index of refraction change increases. Similarly, as the length of the grating increases so does the resultant reflectivity. Using Eq. (1.5), the reflectivity of the FBG is calculated using MATLAB for different grating parameter such as length and refractive index modulation, used in the experiment of present thesis work. The parameters used for these calculations are grating length ($L= 0.2$ cm, 0.5 cm and 1.0 cm), refractive index modulation ($\Delta n = 1 \times 10^{-4}$, 2×10^{-4} and 5×10^{-4}), average refractive index ($n_0 = 1.46$), wavelength ($\lambda = 1550$ nm) and geometrical grating period ($\Lambda=1060$ nm). These parameters were chosen so that their values lie nearby the actual values as discussed in Chapter 2 and 5. For hydrogen loaded SMF-28 fiber the refractive index modulation is $\sim 3 \times 10^{-4}$ and for normal SMF-28 fiber the refractive index modulation will be $\sim 2 \times 10^{-5}$. In our actual set up the grating length varied from 0.7 cm to 1.0 cm. Figure 1.3 (a) shows that the reflectivity increases as the grating length increases. The side lobes of the resonance are due to multiple reflections to and from opposite ends of the grating region.

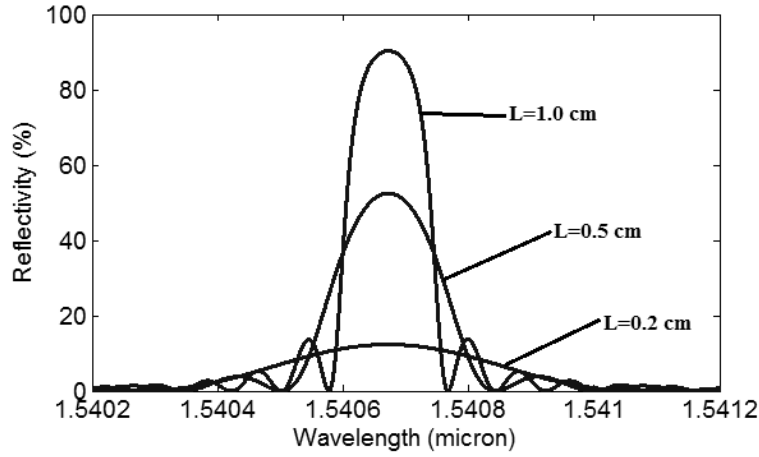


Fig. 1.3 (a): Calculated reflection spectra of uniform Bragg grating as a function of wavelength with different grating length

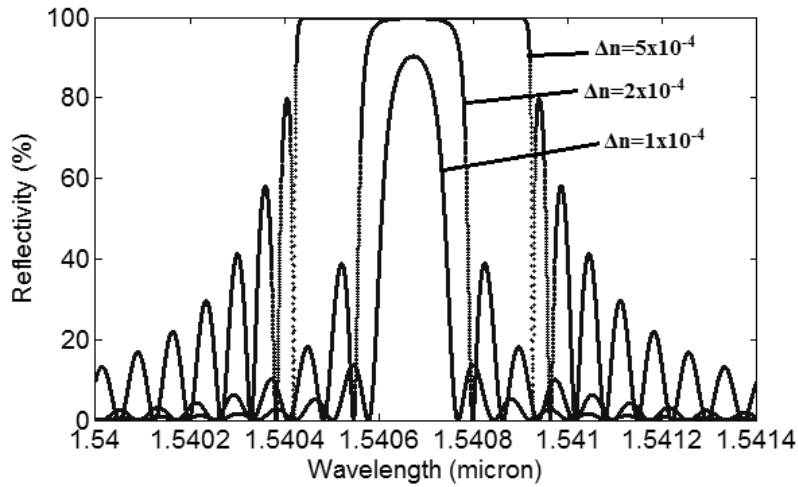


Fig. 1.3 (b): Calculated reflection spectra of 10 mm long uniform Bragg grating as a function of wavelength with different refractive index modulation

The reflection spectrum of a 10 mm uniform grating with different refractive index modulation is simulated using MATLAB and shown in figure 1.3 (b). The reflectivity is calculated for three different values of refractive index modulation 1×10^{-4} , 2×10^{-4} and 5×10^{-4} . It is evident from the graph that reflectivity and its FWHM increases with increase in coupling coefficient. At the Bragg grating centre wavelength, there is no wave-vector detuning and $\Delta\beta = 0$, therefore, the expression for the reflectivity becomes

$$R = \tanh^2(\kappa L) = \tanh^2\left(\frac{\pi \Delta n \eta L}{\lambda}\right) \quad (1.8)$$

Fiber Bragg grating reflectivity increases with increase in grating length (L) and refractive index modulation (Δn) as shown in figure 1.4 (a). It is clear from the graph that higher reflectivity gratings can be written with better coupling even when the grating length is very low. Similar results, showing reflectivity for different coupling (refractive index modulation) and length, are re-plotted in figure 1.4 (b).

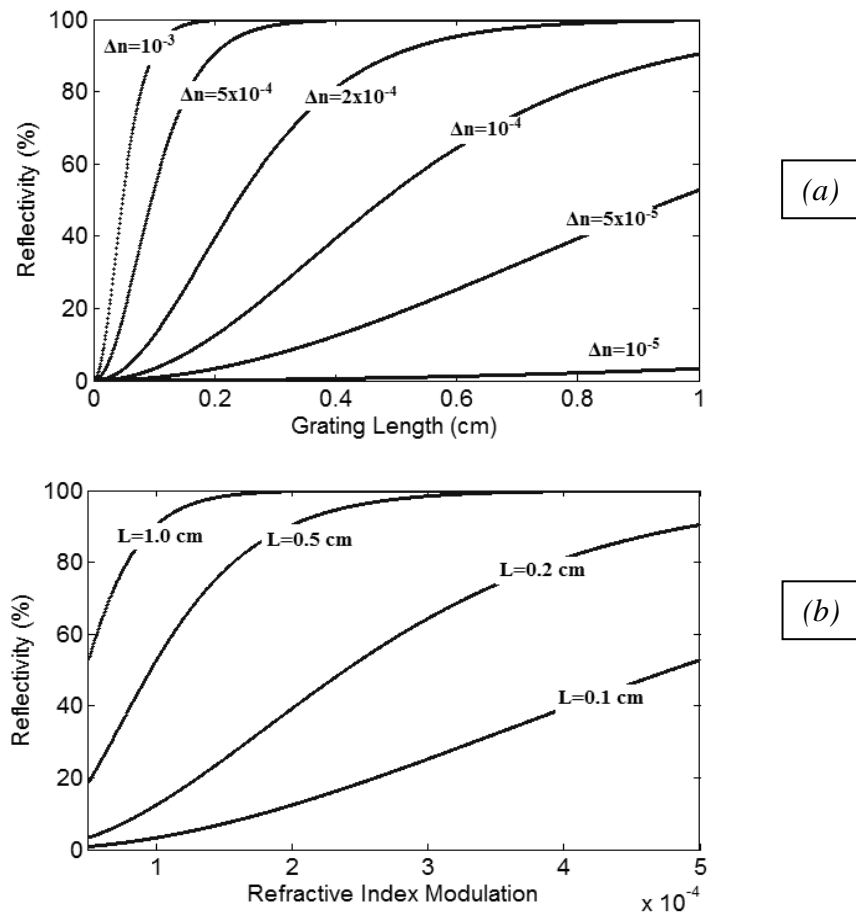


Fig. 1.4: FBG reflectivity with (a) grating length and (b) refractive index modulation

The bandwidth of the grating is defined as the width between the first zeros on either side of the maximum reflection. A general expression for the approximate full width at half-maximum bandwidth of a grating is given by [98-99]

$$\Delta\lambda = \lambda_B \alpha \sqrt{\left(\frac{\Delta n}{2n_0}\right)^2 + \left(\frac{\Lambda}{L}\right)^2} \quad (1.9)$$

The parameter $\alpha \sim 1$ for strong gratings whereas $\alpha \sim 0.5$ for weak gratings. Typical values of $\Delta\lambda$ are in range of 0.2 to 0.3 nm at $\lambda \sim 1550$ nm.

1.3.3 FBG fabrication techniques

The FBG fabrication requires, the exposing the core of a photosensitive fiber with a suitable UV fringe pattern. There are various techniques to create such sub-micron spaced fringe patterns such as Interferometric technique [97-101], Point-by-Point Inscription method [102-103] and Phase Mask technique [104-119]. These techniques differ in the principle of writing and consequently, in the equipment used in the grating writing process.

The interferometric fabrication technique was first demonstrated by Meltz *et al.* in 1989 [97], in which a single laser beam is split into two components, which are subsequently recombined at the fiber to produce an interference pattern. Bragg gratings can be written by splitting the amplitude or wave-front [97-101] of the incident UV laser beam. In an amplitude splitting interferometer, the UV writing laser light is split into two equal intensity beams and are later recombined after traversing through two different optical paths of almost same path length. This forms an interference pattern at the core of a photosensitive fiber. Cylindrical lenses are used to focus the fringe pattern at the fiber core. The advantage of the amplitude splitting interferometric fabrication technique is the ability to inscribe Bragg gratings at any wavelength by changing the intersecting angle between the UV beams. The wave-front-splitting interferometers like prism interferometer and Lloyd interferometers are also used for writing FBGs where incident wave-front is divided and superposed to produce interference fringes as shown in figure 1.5. A key advantage of the bi-prism based wave-front-splitting interferometers

is that it reduces the sensitivity to mechanical vibrations due to single optical component used. The FBG fabrication with interferometric technique is discussed more in **Chapters 2 and 5**.

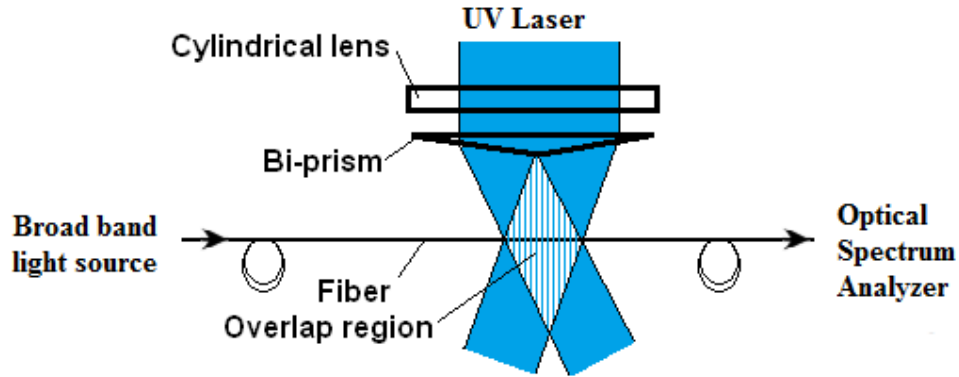


Fig. 1.5: FBG inscription using interferometric fabrication technique

The point-by-point FBG fabrication technique was first demonstrated by Malo *et al.* in 1993 [102]. This technique uses a pulse UV laser or femtosecond laser [103] to inscribe individual grating planes, one step at a time, along the core of the fiber. In this technique, the light passes through the core of the fiber containing a slit and thus the refractive index of the corresponding core section increases locally as shown in figure 1.6.

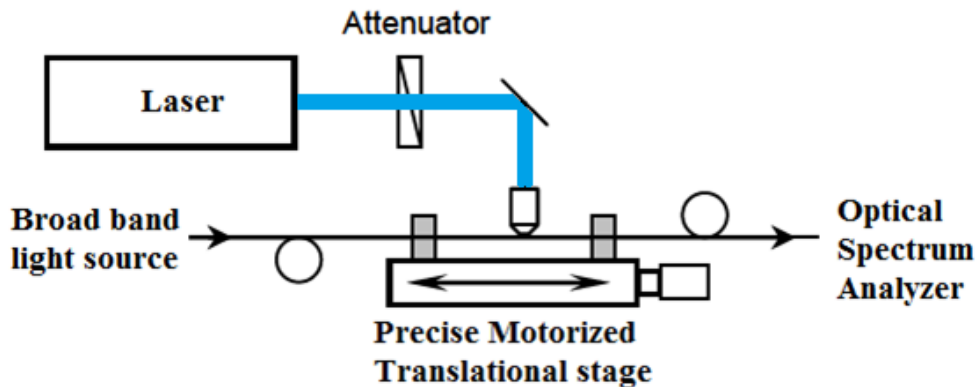


Fig. 1.6: Setup for point-by-point grating fabrication

The fiber is then translated through a distance corresponding to the grating pitch in parallel direction to the fiber axis and the process is repeated to form the grating structure in the fiber core. For the point-by-point fabrication process, a precise submicron translational system is

needed. This procedure is repeated until the desired grating length/reflectivity is obtained. Since the grating structure is built up a point at a time, variations in grating length, grating pitch and spectral response can be easily incorporated. Disadvantages of this technique are long process time and errors in the grating spacing which limits the gratings to a very short length.

The phase mask method is the most widely used and effective method for inscribing FBGs in photosensitive fibers [67, 104-120]. This technique makes use of phase mask as a key component of the interferometer to generate the interference pattern as shown in figure 1.7.

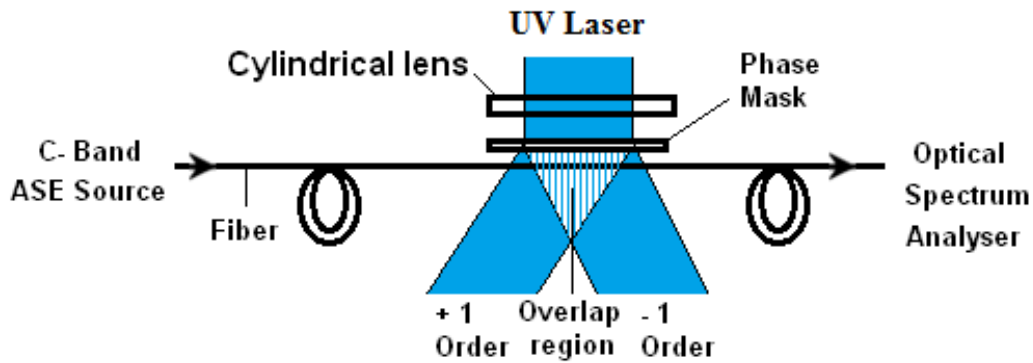


Fig. 1.7: Schematic of the phase mask based FBG fabrication

Phase mask is a diffractive optical element which spatially modulates the intensity of the incident UV beam by interference of different orders. The phase mask grating has a one-dimension surface-relief structure fabricated in a high-quality fused silica flat transparent to the UV writing beam [119, 121-122]. The profile of the periodic gratings is chosen such that when an UV beam is incident on the phase mask, the zero-order diffracted beam is suppressed to less than a few percent of the transmitted power. In addition, the diffracted +1 and -1 order are maximized. The intensity of this orders contain typically more than 35% of incident power. A near-field fringe pattern is produced by the interference of the plus and minus first-order diffracted beams. The fringe period is one-half that of the mask period and is independent of the incident wavelength. The interference pattern photo imprints a refractive index modulation in the core of

a photosensitive optical fiber placed in contact with or in close proximity immediately behind the phase mask. The phase mask based fabrication technique is utilized for inscription of uniform and Tilted FBGs as discussed in **Chapter 2 and 5**.

1.3.4 Laser sources for fiber Bragg grating fabrication

Since the wavelength, repetition rate, peak power/average power and beam coherence of writing beam determines the speed of writing and fiber Bragg grating characteristics. There are several UV laser sources that may be used for inducing refractive index change and for fabricating gratings in optical fibers [73-75]. The most commonly used sources are Excimer lasers [KrF (248nm), ArF (193nm)] which has low repetition rate (< 1 kHz) and low coherence [123-124]. The femtosecond UV radiation at 264 and 267 nm has been also used for FBGs writing [125-126]. The primary advantage with these sources is the high average and peak power available in the UV region. Due to high pulse energy of excimer laser source, single pulse FBG writing in fiber draw tower has also been possible [127]. However, the high pulse energy led to weakening of the silica fiber after FBG inscription. Low spatial- temporal coherence put limit on the fringe contrast and length of the grating and affects fabrication efficiency in interferometric technique of FBG writing. For 193 nm beam, the transportation of the UV beam through the air, phase mask and fiber cladding is not an easy task. The CW highly coherent UV source such as Argon ion laser (257, 244nm; intra cavity frequency doubled in KFD/BBO) [73, 128], 262 nm QS frequency quadrupled Nd³⁺:YLF laser [109], line narrowed frequency doubled dye laser [129], Argon ion laser (302 nm) [73] and Krypton ion laser (323.5 nm, frequency doubled in BBO) have been also utilized for writing the FBGs [73]. These lasers have been successful for inducing large index changes though having the disadvantage of lower peak power densities.

Recently, the inscription of FBG has been also demonstrated using high repetition rate, low peak power, highly coherent 255 nm radiation generated from the second harmonic frequency conversion of copper vapour laser (CVL) [108, 130-132]. 255 nm UV is high repetition rate (5.5 kHz) source retaining some of the advantages of CW 244 nm such as high fringe contrast and has low peak power compared to the most commonly used excimer laser (248 nm or 193 nm). For FBGs writing with the pulsed UV laser, the core of fiber cools down quickly ($\sim 3 \times 10^{-4}$ second) due to heat transfer to cladding and reaches the temperature just slightly higher than the room temperature after the irradiation of single UV pulses [133]. However for UV irradiation with high repetition rate (~ 5.5 kHz, pulse interval time $\sim 180 \mu\text{s}$) may lead to thermal heating due to cumulative UV absorption. Hence, the combined effect of high UV fringe contrast, in-situ heating due to high repetition rate UV absorption may lead to a grating with different characteristics. Figure 1.8 shows the experimental set up of CVL and its second harmonic generation which is used for inscription of FBGs as discussed in Chapter 2.

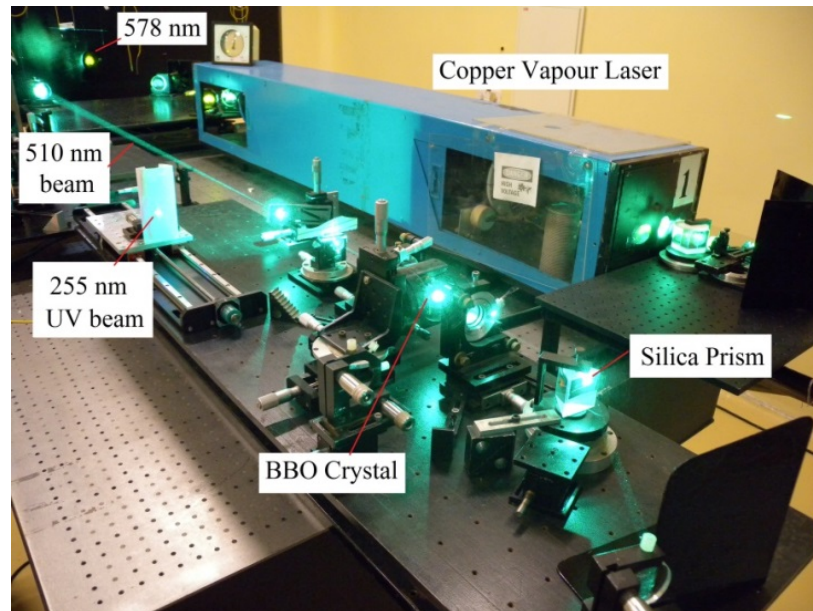


Fig. 1.8: Copper vapour laser (CVL) and its second harmonic generation

1.3.5 Types of Fiber Bragg gratings

Several different types of fiber Bragg gratings have been reported in the literature. The following section briefly describes different types of FBGs depending upon their growth characteristics during manufacturing.

(A) Type-0 FBGs – Type-0 gratings or Hill gratings, are the self-organized gratings, discovered by Hill *et al.*, formed by launching visible light (~ 488 nm) in the fiber from which partial reflection at the cleaved fiber end-face creates the periodic interference pattern [134-135]. These gratings have limited use, as the writing wavelength is also the Bragg wavelength of the grating and the generated refractive index modulation ($\sim 10^{-6}$) is very small.

(B) Type-I FBGs – Type-I gratings refer to the most common gratings characterized by a monotonous growth of refractive index modulation with light exposure. It is commonly observed in most photosensitive fibers under either continuous wave (CW) or pulsed UV irradiation. High refractive index modulation ($\sim 2 \times 10^{-4}$) is possible in Type-I FBG. Type-I FBGs can be erased at relatively low temperatures (~ 200 °C) [16].

(C) Type-II FBGs – Type-II gratings are high power single-pulse ($>0.5\text{J}/\text{cm}^2$) "damage" gratings characterized by large losses on the short wavelength side of the Bragg wavelength [127]. The refractive index modulation for Type-II FBGs is as high as 0.006, which is comparable to the core-cladding index difference of 0.02. The damage is often localized at the core-cladding interface. Type-II gratings can withstand temperature upto 1000 °C. At 800 °C over a period of 24 hours, no degradation in grating reflectivity was observed [16].

(D) Type-IIa FBGs – Type-IIa gratings are characterized by the fact that the reflection initially grows as for Type-I gratings then decreases followed by a subsequent increase again. Also referred as negative index gratings, these gratings probably contain two

components; one positive index grating (Type-I) and one negative index grating [136]. The refractive index modulation for Type-IIa FBG ($\sim 1 \times 10^{-4}$) is lower than that of Type-I FBG. Type-IIa FBGs can withstand temperature upto 850 °C.

1.4 Fiber grating sensing principle

The basic operating principle of commonly used FBG based sensor system is to monitor the shift in wavelength of the returned Bragg signal with the changes in the measurand. The Bragg wavelength, or resonance condition of a grating, is given by the Eq. (1.3). Perturbation of the grating results in a shift in the Bragg wavelength of the device which can be detected in either the reflected or transmitted spectrum, as shown in figure 1.1. Fiber gratings can be utilized for sensing of different parameters such as temperature, strain, pressure, humidity, refractive index, bio-chemical species, rotation, displacement etc. The focus of the present thesis is to develop temperature and refractive index sensors using different types of fiber Bragg gratings. Therefore, the following discussion is mainly related to the application of FBGs in temperature and refractive index sensors.

Temperature sensing: A variation in temperature applied to a grating, results in a change in its refractive index and period, hence shifting its Bragg wavelength. The Bragg wavelength shift can occur due to thermal expansion of the fiber and the refractive index change with temperature, which is attributed to the thermo-optic effect [16, 73-74, 99]. These lead to a fractional change in the Bragg wavelength, which is given by

$$\lambda_B = \frac{d\lambda_B}{dT} \Delta T = \lambda_B \left(\frac{1}{n_{eff}} \frac{dn_{eff}}{dT} + \frac{1}{\Lambda} \frac{d\Lambda}{dT} \right) \Delta T = \lambda_B (\xi + \alpha) \Delta T \quad (1.10)$$

where α is the thermal expansion coefficient of the fiber ($0.55 \times 10^{-6} / ^\circ\text{C}$ for fused silica). The quantity ξ represents the thermo-optic coefficient, which is about $8.3 \times 10^{-6} / ^\circ\text{C}$ for Ge-doped silica-core fiber and ΔT is the applied temperature change. From Eq. (1.10) the typical

temperature sensitivity ($\Delta\lambda_B/\Delta T$) of the FBG will be $\sim 13.6 \text{ pm}/^\circ\text{C}$ for a FBG of central Bragg wavelength at 1550 nm. It is also possible to further improve the thermal sensitivities of FBGs. One method involves gluing the FBG containing fiber to a metallic substrate that has a large thermal expansion coefficient, e.g. aluminum, zinc etc. [137]. This technique resulted in the increase of an overall temperature sensitivity to $\sim 38 \text{ pm}/^\circ\text{C}$. Higher temperature sensitivity was also observed for a polymer over layer coated FBG [138]. Using Nylon, which has large thermal expansion coefficients, as driving elements for the inscribed structure, the thermal sensitivity can be enhanced to $\sim 150 \text{ pm}/^\circ\text{C}$. There is also interest in producing extremely high and low temperature (cryogenic) sensor [139] based on FBG to use in extreme environments. In **Chapter 3 and 4**, the results on the FBG based temperature sensor development will be presented.

Refractive index sensing: A standard fiber Bragg grating consists of refractive index modulation in the core of an optical fiber that acts to couple the fundamental forward to backward propagating core mode. Since the light coupling takes place between well-bound core modes that are screened from the influence of the surrounding-medium refractive index (SRI) by a thick cladding layer, normal FBGs are intrinsically insensitive to SRI. However, if cladding diameter is reduced partially or totally along the grating region, the effective refractive index is significantly affected by the surrounding medium [140-144]. As a direct consequence, strong changes in the spectral response of the FBG occur in an etched optical fiber. This effect can be useful in chemical as well as in bio sensing applications [144-148]. The properties of the sensor are determined by Bragg wavelength λ_B or rather by its shift $\Delta\lambda_B$ as a function of refractive index of analyte, n_A . The wavelength shift $\Delta\lambda_B$ is linearly related to changes Δn_{eff} of the effective index n_{eff} of the guided core mode as given by [149]

$$\frac{\Delta n_{eff}}{n_{eff}} = \frac{\Delta \lambda_B}{\lambda_B} \quad (1.11)$$

The relations $\Delta \lambda_B (n_A)$ and $\Delta n_{eff} (n_A)$ are the sensor characteristics of the refractometer. Usage of chemically etched fiber Bragg grating as refractive index sensor is discussed in detail in **Chapter 6 and 7** of this thesis.

1.5 Current trends on FBG temperature and refractive index sensors

During the last two decades, the applications of FBGs for sensing have increased tremendously. The FBGs have been used in medical field for 3D shape sensing using spun multicore fiber [150]. The high dose gamma γ -radiation levels of 10^4 – 10^5 Gy has been also measured using FBGs [151]. The fiber Bragg grating has been also written directly in the core of Yb^{3+} doped silica laser fiber to work as a mirror for operation of 100 W CW fiber laser [152]. FBGs have been made sensitive to surrounding refractive index medium by etching the clad region around the FBGs by HF acid [153]. HF etched FBG has been used for sensing the different gases by coating the FBG with a gas absorbing medium [154]. The quasi distributed sensors find many applications in civil structure health monitoring, automotive and aerospace [155-156]. The wavelength division multiplexing (WDM) interrogation method allows for multiplexing single element FBG sensors in arrays within a single fiber to form 1-D multipoint quasi-distributed sensing systems.

High temperature sustainable FBGs are critical in the application of high power fiber laser [157], fiber optical flow sensor for high temperature environment [158] and high temperature pressure sensing etc. [159]. The temperature sensing in harsh environment such as oil and gas industries, power stations, aircraft engines and furnaces requires FBG temperature operation from 400 °C to above 1000 °C [157-160]. The temperature sustainability of typical Type-I FBGs is limited to 300-500 °C [161]. Several types of FBGs have been developed for

high temperature sensor operations, such as Type-IIa FBG [162], Sapphire fiber Bragg grating inscribed by femtosecond laser [163], FBG inscribed in nitrogen doped silica fiber [164], chemical composition [165] and regenerative gratings [166-168]. Type-II FBGs are created using high intensity UV pulses near damage threshold of the fiber core and can withstand temperature upto 1000 °C. However the Type-II FBGs suffer from the high insertion loss and poor spectral profile [160]. Type-IIa FBGs can withstand temperature upto 850 °C [162]. These Type-IIa FBGs are inscribed in H₂ free fiber either due to overexposure of UV pulses [169-176] or thermal regeneration [177-178]. The regenerative gratings possesses features of good spectral shape of a Type-I grating with a Type-II like temperature stability. Regenerative gratings are obtained by the thermal annealing of Type-I seed gratings written by UV pulses in H₂ loaded photosensitive fibers [167]. These gratings are shown to work upto 1295 °C [178]. New glass composition based photosensitive fibers have been used to produce thermally regenerated FBG that can sustain temperature upto 1400 °C [179]. FBG written in sapphire fiber can withstand temperature upto 1700 °C [180].

There are various types of fiber optic sensors for refractive index measurements [1-10]. The first all fiber refractometer was developed using a single biconical filter fabricated in multi-mode fiber [181]. The first demonstration of an FBG as a refractometer was done in 1998 which was based on the application of chemical etching to the fiber region where the grating was located [140]. Several reports have been published on fiber sensors for refractive index measurement [181-192]. For long period fiber grating (LPFG) based refractive index sensor, the refractive index sensitivity varied from 90 to 600 nm/RIU [193-194]. Higher refractive index sensitivity of 1500 nm/RIU was observed for PCF based sensor [195-197]. It has been shown that the clad diameter and position of microstructure, controlled the refractive index

sensitivity of a thinned and microstructured fiber Bragg grating [198-203]. Very high sensitivity of about 7120 nm/RIU was observed with surface plasmon resonance (SPR) based refractive index sensor [204]. The Tilted FBGs (TFBGs) offered refractive index sensitivity of 11.2 nm/RIU [205-206]. Tilted FBG offers the refractive index sensing without HF etching of the fiber [205-206]. Although the refractive index sensitivity of an etched FBG based refractive index sensor is low but advantages such as reflection mode operation and high multiplexing capability ensures its competitiveness and usefulness. It has been shown that the clad diameter of etched FBGs controlled the refractive index sensitivity [207]. The etched FBGs (EFBGs) have also applied for the measurement of surface adsorption phenomena of charged polymers and DNA [208-210]. Simultaneous measurement of refractive index, strain and temperature has been also demonstrated using EFBGs [211]. It has been shown using numerical model that the EFBGs can offer competitive performance to currently dominant optical techniques for refractive index sensing such as SPR when the fiber is etched down to 2 microns or below [212].

1.6 The constitution of present thesis

The theme of the present thesis is to study the temperature and refractive index sensing characteristics of different types of FBGs written by high repetition rate UV source. The detailed study on the inscription of different types of FBGs is discussed in the **Chapter 2**. The **Chapter 3** deals with the studies and development of temperature sensor upto 500 °C and its application in monitoring the temperature of transformer oil in high voltage (HV) and high EMI environment. The phenomena of thermal regeneration with UV over exposure and thermal annealing in view to develop high temperature sensors are studied in **Chapter 4**. The effect of Ge-doping on the thermal characteristics of Type-IIa grating written with UV exposure is also studied in detail. The studies and development of multi-point temperature sensors are discussed in **Chapter 5**. The

developed multipoint temperature sensor has been implemented for the measurement of quasi distributed temperature sensor in high voltage and high EMI radiation such as CuBr laser tube and ultrahigh vacuum test setup of Indus-2 beam line. The theoretical and experimental studies on the etching characteristics of different types of FBGs are discussed in **Chapter 6**. The application of the etched FBG based refractive index sensor and the studies on the refractive sensing characteristics of thermally regenerated FBG are presented in **Chapter 7**. The conclusion and future scope of expansion of the work are discussed in **Chapter 8**.

Chapter 2

Inscription of Type-I, Type-IIa and Tilted fiber Bragg gratings

2.0 Introduction

A fiber Bragg grating is a submicron periodic perturbation of the refractive index in the fiber core, created by the exposure to a spatially patterned UV radiation [73-75]. This submicron period in the fiber core is created either by a phase mask or a two beam interferometer. The contrast of UV fringes is crucial for achieving high FBG reflectivity or high refractive index modulation. Incidentally, the contrast of UV fringes is controlled by the coherence characteristics of the UV beam. Also the high spatial coherence relaxes the placement distance of optical fiber from the phase mask. Hence for a given fluence, a highly coherent UV beam leads to high modulation of interference fringes for perpetrating large refractive index modulations [132], a safer placement of fiber from phase mask [132] and an affordability to tilt the fiber for fabrication of Tilted gratings [69]. A prism based interferometer, suitable to write FBGs at different wavelength, demands stable UV beams of high spatial and temporal coherence [132, 213]. For Type-IIa FBG writing where long UV exposure time is needed, the positional stability of UV fringes is also very crucial. The most commonly source for inscription of FBGs are the excimer lasers [KrF (248nm), ArF (193nm)] which has low repetition rate (< 1 kHz) and poor coherence [123-124]. The CW frequency doubled Argon ion laser of high spatial and temporal coherence source has been used for FBGs writing. However, low average power of CW radiation leads to long exposure times (~ 1 hr), thus requiring careful elimination of ambient vibration, thermal cycling and air current disturbances. Furthermore, the long-time exposure of the fiber can cause it to become heated itself; this changes its dimensions and can alter grating characteristics. A high repetition rate, moderate peak power, highly coherent UV ($\lambda = 255$ nm)

radiation from second harmonic of copper vapour laser (CVL, $\lambda = 510$ nm) has been demonstrated for efficient FBGs writing. This chapter presents the studies on fabrication of different types of fiber FBGs such as Type-I, Type-IIa and Tilted FBG using 255 nm UV source.

2.1 Experimental arrangement for inscription of FBG

The FBG inscription set-up consisted of UV laser beam, photosensitive optical fiber, phase mask/interferometer set up to create interference pattern, optical spectrum analyzer, broadband ASE light source, CCD camera arrangement for alignment of fiber, mechanical mounting of the optical fiber, fiber optic circulator and fusion splicer. All the requirements for efficient FBG writing and recording are described in detail as follows.

2.1.1 Generation and characterization of FBG writing UV laser beam

The high repetition rate (~ 5.5 kHz) and highly coherence UV laser beam ($\lambda = 255$ nm) is generated from the second harmonic (SH) conversion of copper vapour laser (CVL) beam fitted with generalized diffraction filtered resonator (GDFR) [132, 214]. The combined experimental setup for the SH generation of CVL and FBG writing are shown in figure 2.1(a-b). The beam quality of SH beam such as spatial coherence and beam pointing stability is controlled by these parameters of fundamental CVL beam which in turn depends on optical resonator configuration of CVL [215-218]. The resonator parameters employed for CVL are: GDFR (Magnification = 107, $F_1 = -20$ cm, $F_2 = \infty$, $L = 230$ cm, diameter of hard aperture A_1 at plane mirror $M_2 = 0.6$ mm). The output is taken out through reflection of a scrapper mirror SC. The CVL wavelength 510 nm component, separated from 578 nm by a dichroic mirror DC, is used for converting into second harmonic in β -BBO (Beta Barium Borate) crystal (Type-I, cut angle 50° for $\lambda = 510$ nm). For this purpose, the $\lambda = 510$ nm output radiation was compressed from 28 mm to 2.8 mm using telescopic combination of spherical lenses ($L_1 = 100$ cm and $L_2 = 10$ cm). An aperture A_2 was

placed at the common focal plane to remove amplified spontaneous emission (ASE). The divergence of ASE is significantly higher than laser beam. The focal spot of the ASE component at focal plane of lens will be higher than that of laser beam. So using an aperture at focal plane will block the high divergence ASE part and will allow the low divergence laser beam to pass. The compressed green beam is finally focused on a BBO crystal by a cylindrical lens, L_3 , of focal length 6.0 cm. The fundamental and the SH beam are re-collimated and separated by another cylindrical lens, L_4 and a fused silica prism, P, respectively.

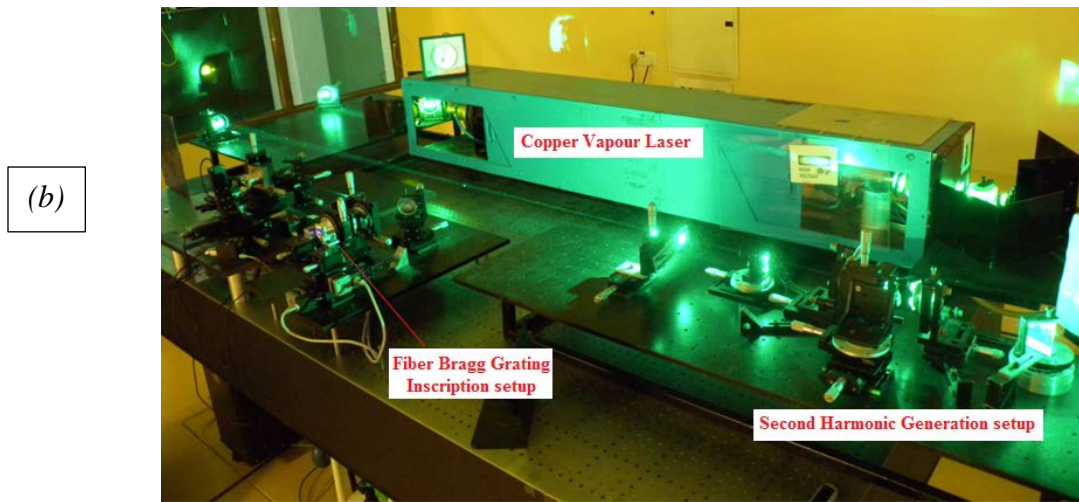
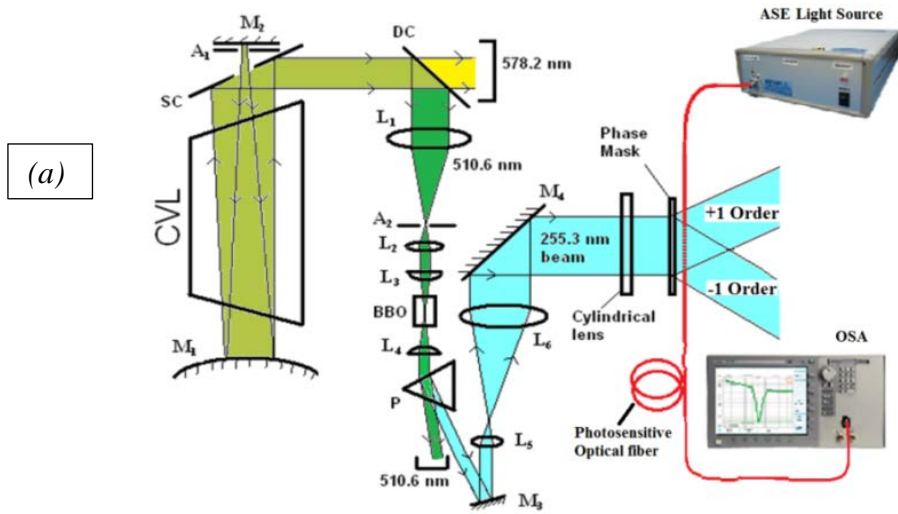


Fig. 2.1: (a) Schematic and (b) actual set up of SH generation and FBG writing

The UV beams obtained is then magnified to about four times (11.2 mm) with the telescopic combination of UV grade fused silica spherical lenses L_5 and L_6 . Mirrors M_3 and M_4 are used for folding the UV beam. The CVL average power was measured just at the entrance of BBO crystal while the UV power was measured at the exit point of prism P (Figure 2.1a). The maximum average UV power obtained was 600 mW at the fundamental CVL power of 2.1 W with a conversion efficiency of 30 %. Due to specialized resonator scheme of CVL oscillator, a very high beam quality 255 nm is generated. The main beam parameters of the CVL and its second harmonic are summarized in table 2.1. Figure 2.2 (a) show the UV beam near field spot with its intensity variation along a line. It is apparent from the figure that the near field intensity distribution is nearly super Gaussian.

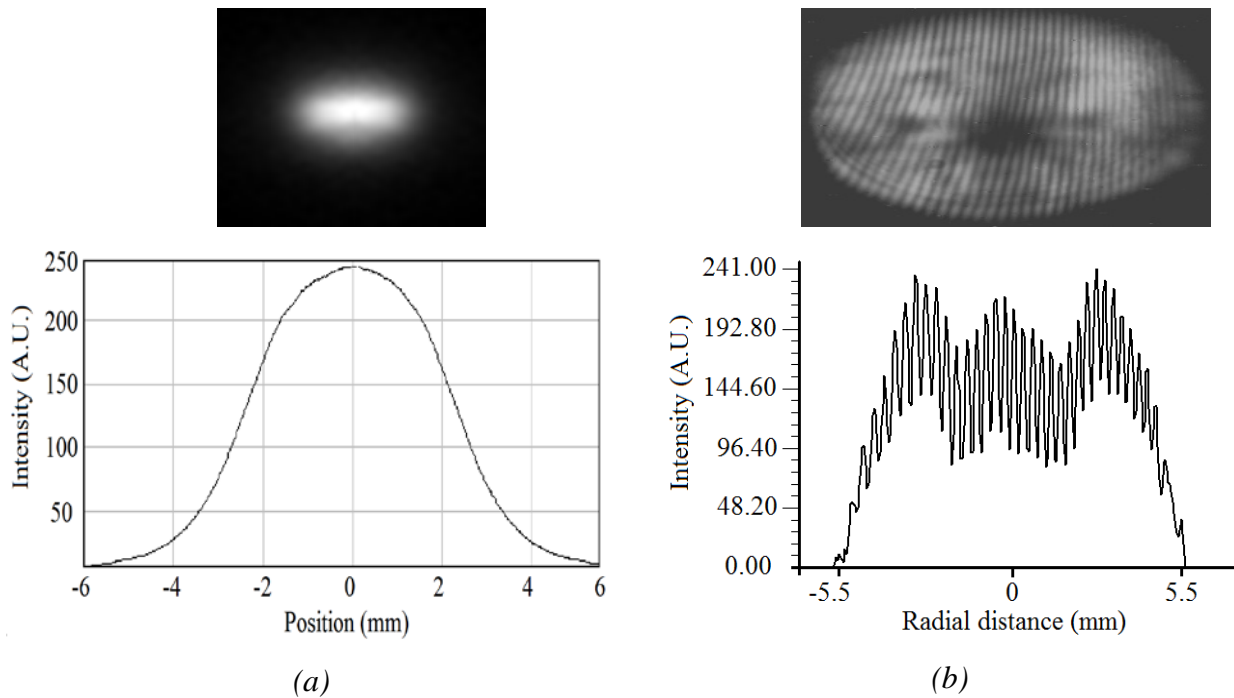


Fig. 2.2: (a) UV beam near field spot along with its intensity profile and (b) UV interferogram with its intensity variation along line [219]

Since the spatial coherence plays an important role in deciding the contrast of interference fringe responsible for refractive index modulation, an in-house developed cylindrical lens based

reversal shear interferometer was used to measure spatial coherence of both UV and fundamental visible radiations [219]. Figure 2.2 (b) shows the recorded typical reversal shear interferogram and the line intensity variation for $\lambda=255$ nm beam. As apparent from the figure, the fringes across the whole beam cross section are observed. Therefore, the phase correlation exists across the whole cross section of the beam confirming high spatial coherence. The coherence length of the UV beam is around 20 mm. The UV beam characteristics and average power level are good enough to write high reflectivity FBGs.

Table 2.1 The parameters of the CVL and its second harmonic UV beam

	Copper Vapour Laser	UV Beam
Wavelength (λ)	510.6 nm	255.3 nm
Average Power	2.1 W	600 mW
Peak Power	25 kW	1.8 kW
Repetition Rate	5.5 kHz	5.5 kHz
Pulse Width	40 ns	30 ns
Line-width (typical)	6 GHz	12 GHz
Divergence (in terms of DL-diffraction limit)	1.2 DL	1.2 DL
Pulse Energy	1 mJ	54 μ J
Power Stability	$\pm 3\%$	$\pm 3\%$
Pointing stability	~ 8 μ rad	~ 8 μ rad
Coherence width	0.9 of beam diameter	0.9 of beam diameter
Coherence length (typical)	~ 40 mm	~ 20 mm

2.1.2 FBG inscription arrangement

Optical fiber - FBGs are written in different types of fibers with and without hydrogen loading as listed in table 2.2. The typical fiber parameters such as doping concentration, cut-off wavelength ($\lambda_{cut-off}$), numerical aperture (NA), mode field diameter (MFD), cladding diameter

and coating diameter for different fibers are also listed in the table. The fibers used for FBG inscription are single mode fiber.

Table 2.2: Parameters of different optical fibers used in FBG inscription

Fiber	SM-1500	NM-113	CMS-1550-R1	SMF-28	BF-SMF-02	PS-270	PS-1250
Make	Fibercore Ltd. UK	CGCRIK olkata	Stocker Yale	Corning	Birla Furukawa	CGCRI Kolkata	Fibercore Ltd. UK
Doping mol%	Ge ~ 18	Ge ~ 10	Ge ~ 6	Ge ~ 3	Ge ~ 3	Ge ~ 8 B~ 6	Ge – B (Doping not known)
$\lambda_{cut-off}$	1350 – 1520 nm	≤ 1260 nm	1250 ± 50 nm	≤ 1260 nm	≤ 1260 nm	-	1100-1260 nm
NA	0.29-0.31	0.12	0.13	0.14	-	-	0.13
MFD	4.0 - 4.5 μm	6.2 μm	8.6 ± 0.8 μm	10.4 ± 0.5 μm	9.2 - 10.4 μm	-	8.8-10.6 μm
Clad diameter	125 ± 1 μm	~ 125 μm	125 ± 1 μm	125 ± 0.7 μm	125 ± 0.7 μm	~ 125 μm	125 ± 1 μm
Coating diameter	245 ± 7 μm	~ 250 μm	245 ± 7 μm	242 ± 5 μm	235 – 245 μm	~ 250 μm	245 ± 7 μm
Coating type	Dual Acrylate	Acrylate	Dual Acrylate	Acrylate	Acrylate	Acrylate	Dual Acrylate

Phase mask and Bi-prism based FBG inscription set up- The FBG writing in C-band (1525 nm -1565 nm) has been carried out by a standard phase mask (manufactured by Ibsen, zero order suppressed at 255 nm) of pitch 1060 nm with the period accuracy and uniformity better than 0.01 nm. The diffraction efficiency of different orders of the phase mask, illuminated by a UV beam of wavelength 255 nm, was measured by placing an optical detector behind the phase mask. The measured phase mask diffraction efficiency in zero and ± 1 orders with respect to total incident

power in all the orders were approximately 0.5 % and 35.0 % respectively. The fringe pattern is created due to interference of ± 1 order. The interference pattern can be also created by the interferometer such as bi-prism. The fused silica bi-prism used in C-band at 1550 nm FBG writing was of 24° apex angle. This was necessary for fringe formation with $0.5 \mu\text{m}$ separation for C-band operation. Figure 2.3 shows the photograph of the phase-mask (period~1060 nm) and bi-prism (apex angle~ 24°) used for FBG inscription for the present thesis work.

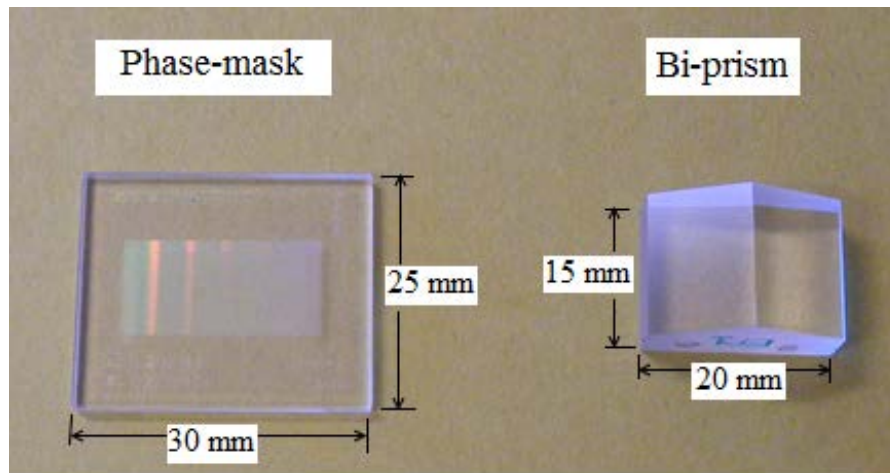


Fig. 2.3: Photograph of the phase-mask and bi-prism used for FBG inscription

Mechanical mounting and Camera arrangement – Since the exact location of fiber behind the phase mask is very important for the efficient inscription of FBGs, a computer controlled fiber holding and movement set-up is developed as shown in figure 2.4. The fiber is supported, over the entire length of the grating to be fabricated, in a long V-groove kept firm by magnetic clamp. The phase mask/bi-prism was placed on the rotational mount having resolution of 10 arcmin. The fiber holding translation stage based mounts, could be moved precisely in both X and Y directions. The least count of the movement in X and Y direction was $2 \mu\text{m}$. The maximum ranges that could be moved, in both directions were 25 mm each. The cylindrical lens was mounted on three axis translation stage for alignment of focal spot along the fiber. A CCD

camera based fiber positioning system and graphical user interface set-up for monitoring the precise movement of optical fiber is developed as shown in figure 2.4.

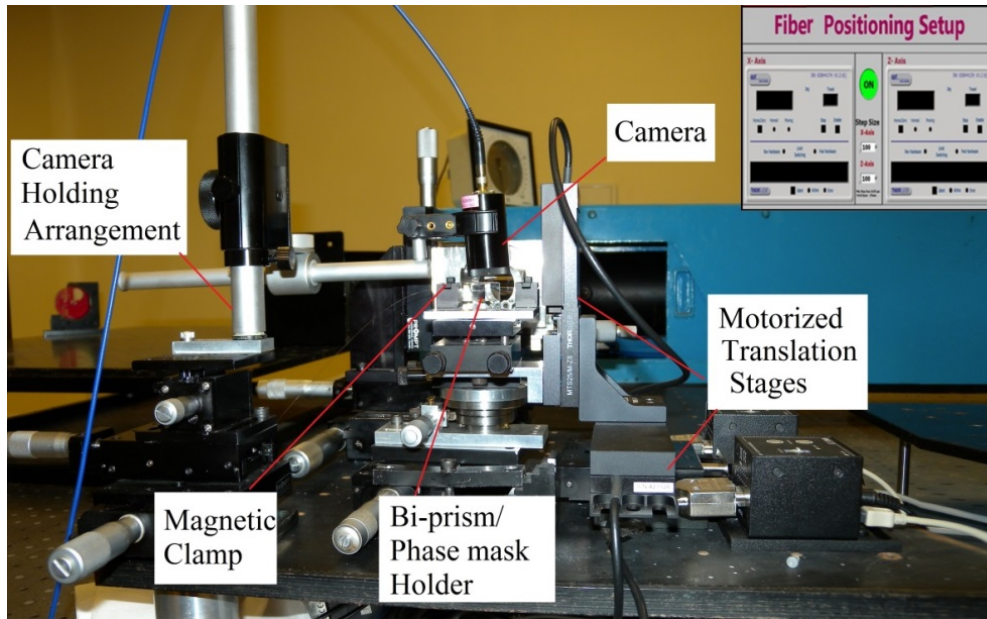


Fig. 2.4: Mechanical mounting, fiber positioning setup and its graphical user interface

2.1.3 Online monitoring of FBG characteristics

The online FBG monitoring set-up consisted of optical spectrum analyzer, broadband ASE source and fiber optic circulator.

Optical spectrum analyzer (OSA) – The online growth of FBG is monitored by optical spectrum analyzers (OSA) manufactured from Agilent and JDSU. The specification of optical spectrum analyzer (Agilent 86142B) are wavelength range - 600 nm to 1700 nm , resolution – 0.06, 0.1, 0.2, 0.5, 1, 2, 5, 10 nm, amplitude sensitivity : -90 dBm (1250-1610 nm wavelength range) and -75 dBm (900-1250 nm wavelength range), applied input fiber: single mode (9/125 μm) and maximum measurement power: +15 dBm. The wavelength measurement accuracy of OSA is ± 10 pm. The specification of optical spectrum analyzer (JDSU- OSA-500) are wavelength range -1250 nm to 1650 nm, wavelength accuracy ± 10 pm, wavelength readout

resolution 1 pm, resolution bandwidth (FWHM) 35 pm, power measurement ranges -70 to +20 dBm, absolute accuracy ± 0.5 dB, linearity ± 0.1 dB, total safe power +23 dBm, power readout resolution 0.01 dB, scanning time (C-band) < 1 s and applied input fiber single mode (9/125 μm). The shape of the intensity vs. wavelength diagram is displayed on the OSA monitor. Here it may be noted that dB is used when expressing the ratio between two power values and dBm is used when expressing an absolute value of power.

ASE light source – A C-band amplified spontaneous emission (ASE) light source with gain flattening filter (Opto-Link Corporation Ltd.) was used for FBG interrogation. The wavelength range of this light source, based on erbium doped fiber, was 1525 nm to 1565 nm with spectrum flatness < 2 dB at output power ~ 17 dBm. The power stability of the output was ± 0.005 dB (5 mins) and ± 0.02 dB (8 hrs).

Fiber optic circulator – In the experiment, three port optical circulators (Opto-Link Corporation) operating in the wavelength range 1520-1625 were used. Light entering in port 1 is emitted from port 2. If some of the emitted light is reflected back to the circulator, it does not come out of port 1 but instead exit from port 3. It is shown by a schematic of fiber optic circulator in figure 2.5.

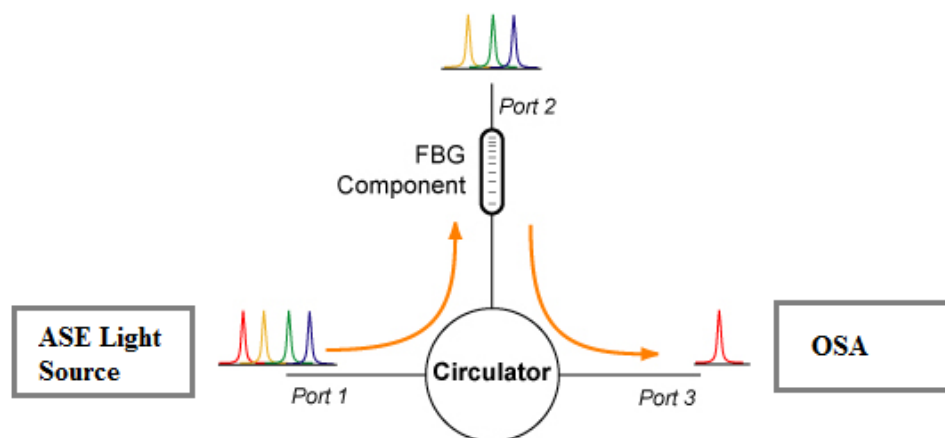


Fig. 2.5: A fiber optic circulator

2.2 Inscription of Type-I FBGs

2.2.1 Phase-mask approach

The experimental set-up for FBG writing is shown in figure 2.1 and 2.6. The average UV power of about 300 mW at 255 nm wavelength beam is utilized for FBG writing. The focused UV beam on the fiber was having dimensions about 10 mm x 250 μm . The fiber is mounted about 0.5 mm behind the phase mask (grating period 1060 nm). The fiber was kept slightly before the focal plane of the lens to prevent the damage of the fiber. The interference pattern formed between the +1 and -1 diffraction order of phase mask produces the fringes of about 530 nm spacing on the fiber. The online growth of the FBGs is monitored using a broadband ASE source, 3 dB coupler and optical spectrum analyzer as shown in the figure 2.1.

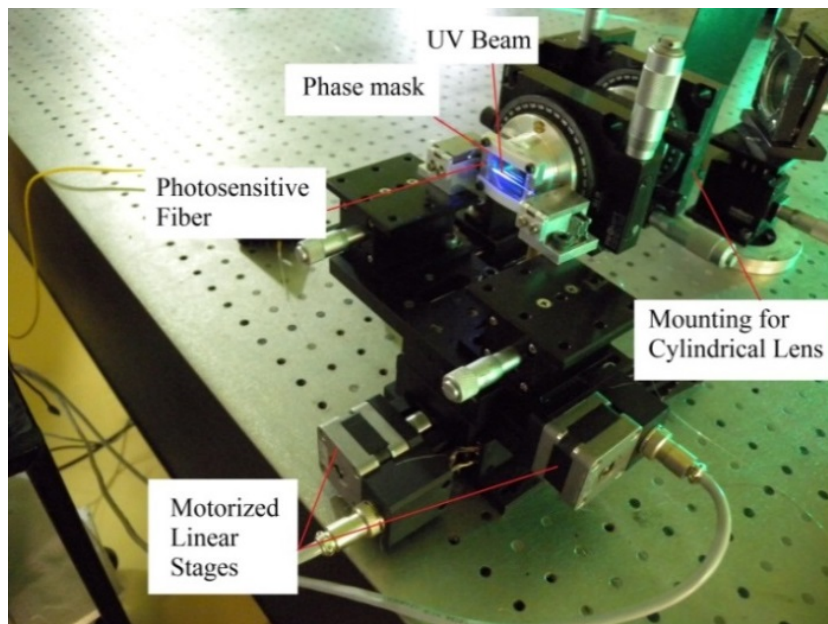


Fig. 2.6: Experimental arrangement for FBG inscription using a phase mask

The FBGs of the same length (~10 mm) are written in non-hydrogenated PS-270 (doping: typical B ~ 6 mol %, Ge ~ 8 mol %), NM-113 (doping: typical Ge ~ 10 mol %,) and SM-1500 fused silica fiber (doping: typical Ge ~ 18 mol %), with same UV exposure time and cumulative flux

(CF). Henceforth for discussion, we will refer the FBGs written in fibers PS-270, NM-113 and SM-1500 as FBG-A1, FBG-A2 and FBG-A3 respectively. The cumulative fluence (CF) of the UV beam is calculated as

$$CF = \frac{E t f}{A} \quad (2.1)$$

where E is UV pulse energy (0.055 mJ), t is the exposure time in second, f is repetition rate (5.5 kHz) and A is the cross section area of the UV beam falling on the fiber ($250 \times 10^{-4} \text{ cm}^2$). Figure 2.7 shows the typical evolution of FBGs transmission spectra with cumulative UV fluence for FBG-A3.

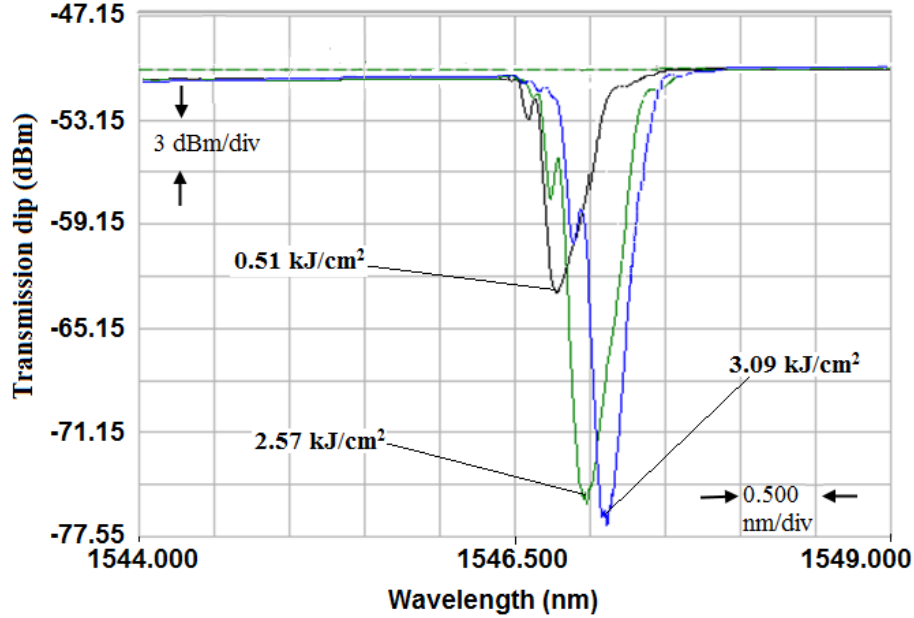


Fig. 2.7: OSA traces showing evolution of FBG-A3 with increased UV fluence

It is observed that the Bragg peak wavelength is red shifted with increased reflectivity as the cumulative UV fluence is increased. The maximum reflectivity of 99.7 % (~ 26 dB), 96.9 % (~ 15.2 dB) and 99.6 % (~ 24.7 dB) are observed at the same cumulative fluence of 3.09 kJ/cm² for FBG-A1, FBG-A2 and FBG-A3 respectively. The reflectivity of the fiber Bragg grating is calculated from the observed transmission dip (T_d), given as

$$R = 1 - 10^{-T_d/10} \quad (2.2)$$

From the evolution of transmission spectra, the variation of refractive index modulation Δn_{ac} (solid symbols) and average refractive index, Δn_{dc} (open symbols) with the cumulative fluence are estimated and shown in figure 2.8. The refractive index modulation is estimated from the reflectivity of the FBG, grating length L and Bragg wavelength λ_B , using the relation [73-75]

$$\Delta n_{ac} = \frac{\lambda_B}{\pi \eta L} \tanh^{-1}(\sqrt{R}) \quad (2.3)$$

The average refractive index is estimated from the Bragg wavelength shift $\Delta \lambda_B$ during writing FBG [73-75],

$$\Delta n_{dc} = \frac{\Delta \lambda_B n_{eff}}{\eta \lambda_B} \quad (2.4)$$

where η is mode overlap integral which can be estimated from the expression [126, 220],

$$\eta = \frac{\pi^2 a^2 K^2}{\lambda_B^2 + \pi^2 a^2 K^2} \quad (2.5)$$

where K is the numerical aperture (NA) of the fiber. For typical fibers used, the parameter η is about 0.85. This value has been taken for calculation in the experimental studies. From figure 2.8, it is observed that the refractive index modulation (Δn_{ac}) increases with the fluence and reaches the maximum value of 2.6×10^{-4} , 1.7×10^{-4} and 2.5×10^{-4} at 3.09 kJ/cm^2 for FBG-A1, FBG-A2 and FBG-A3, respectively. The average refractive index (Δn_{dc}) also increases with fluence for all the fibers. For accumulated fluence of 3.09 kJ/cm^2 , the average refractive index change reaches to value of 3.87×10^{-4} , 3.45×10^{-4} and 3.25×10^{-4} for FBG-A1, FBG-A2 and FBG-A3, respectively. Hence at same fluence level, the value of refractive index modulation and average refractive index change of Ge-B co-doped fiber (FBG-A1) is higher than only Ge doped fiber

(FBG-A2 and FBG-A3). It is attributed to higher photosensitivity of Ge and B co-doped fiber as compared to only Ge doped.

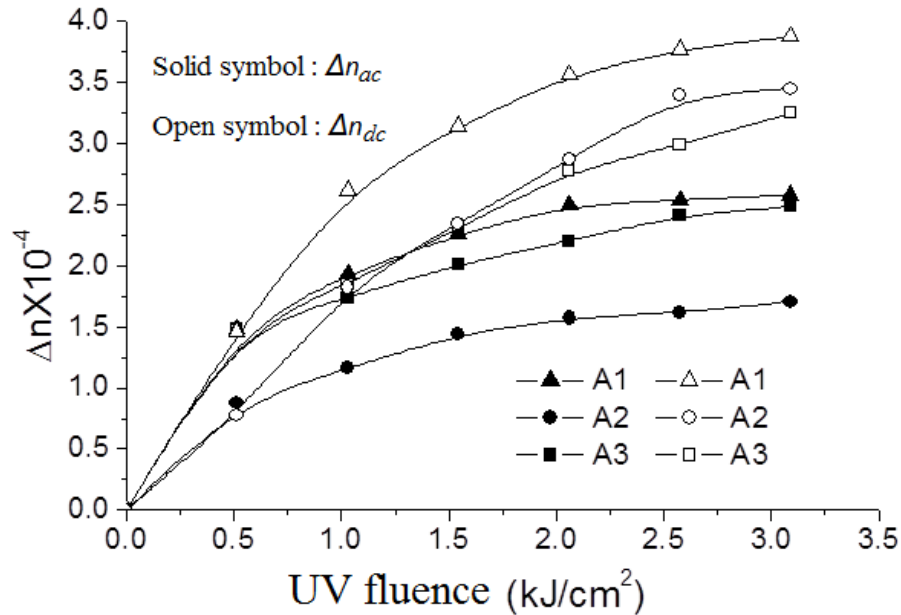


Fig. 2.8: Refractive index modulation with UV fluence for FBG-A1, A2 and A3

2.2.2 Bi-prism approach

For bi-prism based FBG fabrication, the writing set up and procedure are same as described in figure 2.1 for phase mask technique, except that the phase mask was replaced by a bi-prism. The actual set up of FBG writing using bi-prism is shown in figure 2.9. About 8 mm diameter UV beam of average power 300 mW was allowed to fall on the bi-prism of apex angle 24° . In a bi-prism, the divided wave-front is combined to form an interference pattern over the rhombohedron shaped volume, one edge of which is the apex edge of the prism (figure 1.5). The fiber was placed at the maximum overlap region and slightly before the focal plane of the lens to avoid the fiber damage. The UV beam interference pattern was line focused on the fiber by a cylindrical lens of focal length of 7.5 cm. The fiber was placed at a distance of about 5 mm from the apex of bi-prism. Typical transmission spectra of FBG written PS-270 fiber using bi-prism

based inscription technique is shown in figure 2.10. The maximum reflectivity of about 90 % ($T_d=10$ dB) was observed for an FBG written in PS-270 fiber. This writing technique has been used for fabrication of multiple FBGs in a single fiber for the development of distributed temperature sensor. This aspect is discussed in detail in **Chapter 5**.

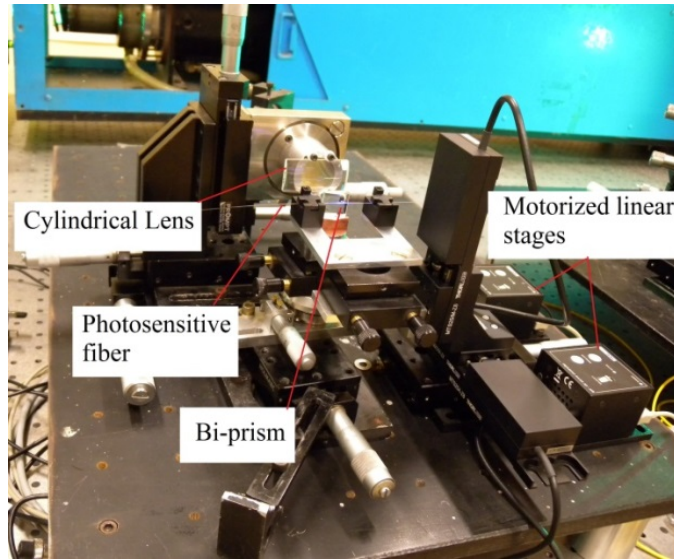


Fig. 2.9: Actual experimental set up of FBG inscription using bi-prism

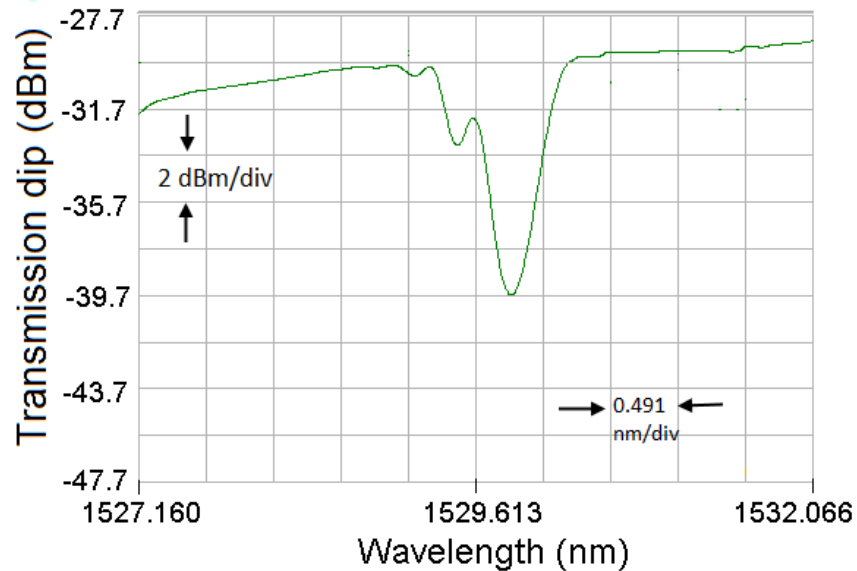


Fig. 2.10: FBG written in PS-270 fiber with bi-prism based inscription technique

2.3 Inscription of Type-IIa FBGs

Type-IIa or negative refractive index grating evolves from the Type-I grating with continued UV exposure after achieving the maximum refractive index modulation [221-223]. After attaining the maximum value, the refractive index modulation starts to decrease (full or partial erasure of Type-I grating) and also the wavelength shifts back to shorter wavelength (blue shifted) or remains constant [106]. With further continued UV fringes exposure, the refractive index modulation increases again. Hence the refractive index rollover is observed during the Type-IIa grating formation.

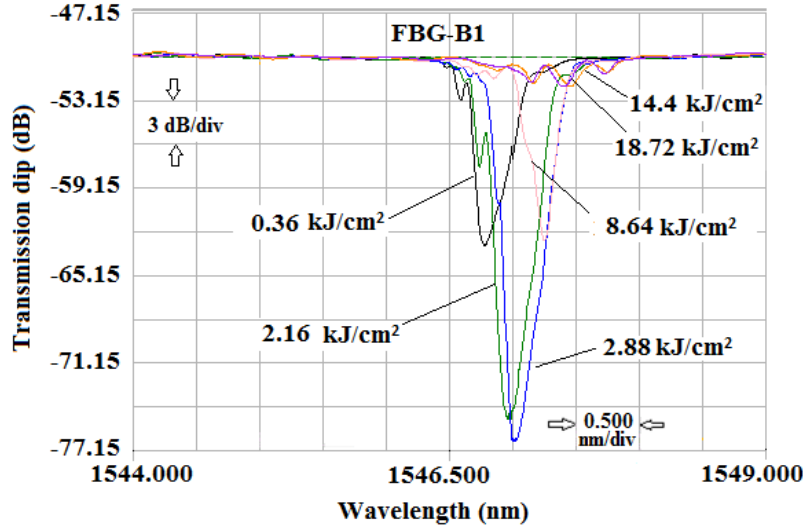


Fig. 2.11: OSA traces showing Type-IIa FBG evolution at different fluence for FBG-B1

The whole process of Type-I grating formation, its erasure and then formation of Type-IIa grating takes about 45 minutes. Hence for writing of Type-IIa grating, a very stable UV fringe pattern for long exposure (~30 to 45 minute) is needed. The beam parameters and the set up used for inscription of Type-IIa FBG was same as discussed in for inscription of Type-I FBG. About 300 mW average power UV beam of diameter 10 mm was used to write the Type-IIa FBG in non-hydrogenated photosensitive germanium doped SM-1500 (doping: typical Ge ~ 18 mol %), NM-113 (doping: typical Ge ~ 10 mol %) and CMS-1550-R1 (doping: typical Ge ~ 6 mol %)

fused silica fibers. These fibers containing Type-IIa grating are designated as FBG-B1, FBG-B2 and FBG-B3 respectively for further discussion in the text. The single pulse energy density of 255 nm beam was $\sim 2.18 \text{ mJ/cm}^2$. Figure 2.11 shows the typical evolution of transmission dip (T_d) with the cumulative UV fluence for FBG-B1.

Table 2.3: Transmission dip with UV fluence for FBGs written in different fibers

Fluence (kJ/cm ²)	FBG-B1		FBG-B2		FBG-B3	
	λ_B (nm)	T_d (dB)	λ_B (nm)	T_d (dB)	λ_B (nm)	T_d (dB)
0.00	1546.665	0.00	1536.426	0.00	1535.200	0.00
1.44	1546.930	21.30	1536.700	13.60	1535.660	4.50
2.88	1546.985	27.00	1536.865	16.37	1535.900	9.00
3.96	1547.065	25.90	1536.965	17.90	1536.030	11.50
5.76	1547.150	24.30	1537.060	20.02	1536.200	15.00
8.64	1547.245	12.38	1537.115	19.08	1536.430	17.00
10.80	1547.330	5.80	1537.170	18.20	1536.510	19.00
14.40	1547.450	1.90	1537.220	14.80	1536.690	22.00
15.82	1547.470	1.20	1537.425	11.10	1536.720	23.00
21.6	1547.560	3.20	1537.565	1.50	1536.780	24.00
24.48	1547.465	5.56	1537.735	0.20	1536.810	24.00
31.68	1547.138	8.70	1537.935	2.05	1537.040	24.00
37.44	1546.795	9.00	1537.835	2.35	1537.220	23.00
57.60	-	-	-	-	1537.920	10.00
63.36	-	-	-	-	1536.970	15.00

It is observed that for FBG-B1 the maximum T_d of about 27 dB ($R\sim 99.80\%$) is obtained at the fluence of 2.88 kJ/cm^2 in UV exposure time $t_{exp}\sim 4$ minutes. When the fluence is further increased, the grating T_d reduces about 1.2 dB ($R\sim 24.14\%$) at 15.82 kJ/cm^2 ($t_{exp}\sim 22$ minutes) and then increased upto 8.7 dB ($R\sim 86.51\%$) at the fluence of 31.68 kJ/cm^2 ($t_{exp}\sim 44$ minutes). Further

UV exposure of ~10 minutes led to a marginal increase in the transmission dip from 8.7 dB ($R \sim 86.51\%$) to 9.0 dB ($R \sim 87.41\%$). The UV fringe exposure was stopped at this stage since the reflectivity was almost unaltered by further exposure. The central wavelength of FBG-B1 starts to increase from 1546.665 nm and reaches to 1547.560 nm at 21.6 kJ/cm^2 . After this point the Bragg wavelength started to blue shift and reaches 1546.795 nm at 37.44 kJ/cm^2 .

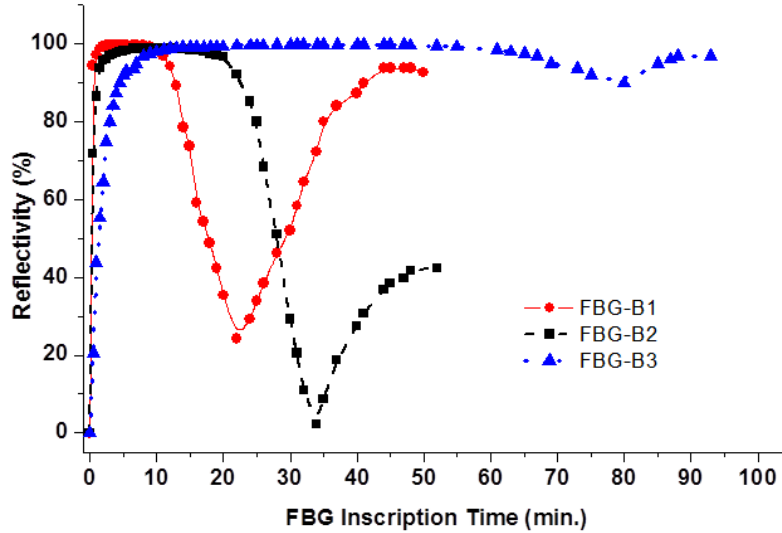


Fig. 2.12: Variation of grating reflectivity with inscription time

The similar trend of evolution of T_d was noticed for FBG-B2 and FBG-B3 as listed in table 2.3. FBG-B2 attains the maximum $T_d \sim 20 \text{ dB}$ ($R \sim 99\%$) at a cumulative fluence of 5.76 kJ/cm^2 in $t_{exp} \sim 8$ minute. When the fluence is increased further, the T_d reduces about 0.2 dB ($R \sim 4.5\%$) at 24.48 kJ/cm^2 ($t_{exp} \sim 34$ minutes) and then increased upto 2.05 dB ($R \sim 37.63\%$) at 31.68 kJ/cm^2 ($t_{exp} \sim 44$ minutes). Further UV exposure of ~10 minutes led to a marginal increase in the transmission dip from 2.05 dB ($R \sim 37.63\%$) to 2.35 dB ($R \sim 41.79\%$). For FBG-B3, the $T_d \sim 24 \text{ dB}$ ($R \sim 99.60\%$) was observed at the cumulative fluence of 21.6 kJ/cm^2 . The T_d reduces to 10 dB ($R \sim 90\%$) at fluence of 57.6 kJ/cm^2 . The T_d again increased and ultimately reached to 15 dB ($R \sim 96.84\%$) at the fluence of 63.36 kJ/cm^2 . The transmission dip, T_d , of the FBG-B1 to FBG-B3

at various cumulated fluence (CF) values is listed in table 2.3. Figure 2.12 shows the change in FBG reflectivity with inscription time. From the evolution of transmission spectra, the refractive index modulation (Δn_{ac}) and average refractive index (Δn_{dc}) are estimated and shown in figure 2.13 (a) and (b) for FBG-B1, FBG-B2 and FBG-B3, respectively.

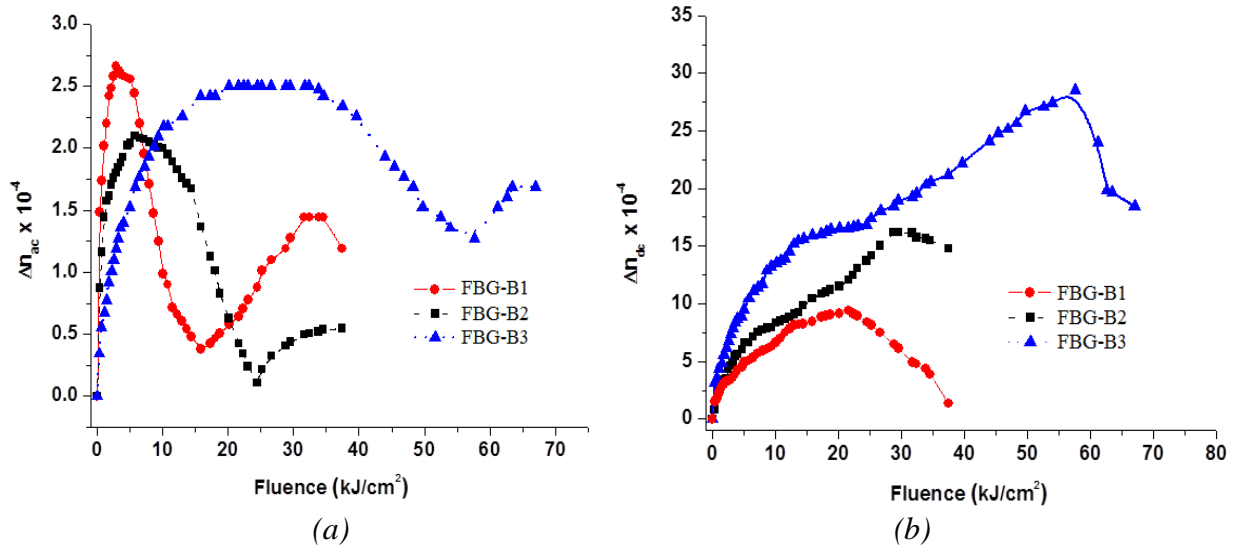


Fig. 2.13: Variation of (a) Δn_{ac} and (b) Δn_{dc} with UV fluence during FBG inscription

From figure 2.13 (a) it is noticed that for FBG-B1 the refractive index modulation (Δn_{ac}) increases with the fluence and reached to maximum value of 2.66×10^{-4} at the cumulative fluence of $2.88 \text{ kJ}/\text{cm}^2$. As the fluence increased further, Δn_{ac} reduced to 0.38×10^{-4} at the fluence of $15.84 \text{ kJ}/\text{cm}^2$. Thereafter Δn_{ac} again increases and ultimately reaches to 1.19×10^{-4} at the fluence of $37.4 \text{ kJ}/\text{cm}^2$. Similar trend of change in Δn_{ac} was observed for FBG-B2 and FBG-B3. Maximum Δn_{ac} of 2.1×10^{-4} and 2.5×10^{-4} was observed at the cumulative fluence of $5.76 \text{ kJ}/\text{cm}^2$ and $21.6 \text{ kJ}/\text{cm}^2$ for FBG-B2 and B3 respectively. At the cumulative fluence of $24.48 \text{ kJ}/\text{cm}^2$ and $57.6 \text{ kJ}/\text{cm}^2$ the Δn_{ac} reaches to a minimum value of 0.11×10^{-4} and 1.27×10^{-4} for FBG-B2 and B3 respectively. After this point the Δn_{ac} starts to increase with the fluence and reaches to a value of 0.55×10^{-4} and 1.69×10^{-4} at the $37.44 \text{ kJ}/\text{cm}^2$ and $66.96 \text{ kJ}/\text{cm}^2$ fluence for FBG-B2 and B3 respectively. From figure 2.13 (a), it is clear that the value of rollover fluence for writing Type-

IIa FBG increases as the Ge concentration in the photosensitive fiber decreases. In other words Type-IIa FBG can be inscribed at lower fluence in high Ge doped fibers. It is also noticed that the Bragg wavelength shift is higher for low Ge doping. This could be due to fact that the absorption coefficient for UV light in the core of fiber increases linearly with increase in Ge doping concentration [220-224]. This in turn leads to faster grating growth for FBG-B1 as compared to FBG-B2 and FBG-B3. Also the time required to reach the maximum will also be lower for fiber having higher Ge-doping as observed experimentally. Figure 2.13 (b) shows the variation of average refractive index (Δn_{dc}) with the fluence for FBG-B1, FBG-B2 and FBG-B3 respectively. For FBG-B1, Δn_{dc} initially increases to 9.38×10^{-4} at the fluence of 21.6 kJ/cm^2 and then reduces to 1.36×10^{-4} at the fluence of 37.4 kJ/cm^2 . The value of maximum Δn_{dc} change was 16.18×10^{-4} and 28.51×10^{-4} at fluence of 28.8 kJ/cm^2 and 57.6 kJ/cm^2 for FBG-B2 and FBG-B3 respectively. The maximum value of Δn_{dc} was higher for fiber having low Ge doping. It is also observed that the width of the transmission dip of FBG-B1 is lower as compared to FBG-B2 and FBG-B3. The width of the transmission curve (FWHM) is around 0.2 nm, 0.35 nm and 0.5 nm for FBG-B1, FBG-B2 and FBG-B3 respectively. From the behavior of Δn_{ac} and Δn_{dc} curve, these inscribed FBGs are Type-IIa gratings. The role of refractive index rollover fluence on the thermal stability of the Type-IIa FBG is discussed in **Chapter 3**.

The refractive index growth with UV exposure is a cumulative effect of change in absorption spectrum, induced stress and photo elastic effects [224]. The UV-induced index change, during the formation of the Type-I grating, is contributed by two factors. These are the positive contribution from the compaction of the irradiated fiber core network and the negative contribution from the axial stress change via the photo-elastic effect. The variation of Δn_{ac} and Δn_{dc} with UV fluence during Type-IIa FBG inscription may be explained as follows [220-225].

During the initial growth of the Type-I FBG, the change in Δn_{ac} and Δn_{dc} is mainly controlled by the UV-induced compaction of the core network. The compaction may be related with the transformation of the high-order ring network structure into a low-order ring structure through the annihilation of ODCs [222]. At further higher fluences, the Δn_{ac} saturates and decreases but Δn_{dc} increases with UV fluence. Since the irradiation UV fringe pattern along the fiber is generally assumed to be sinusoidal, the largest value of Δn_{ac} could be achieved first at the central region of each irradiated section where the maximum degree of compaction is reached. As the irradiation is further continued, the region with maximum degree of compaction is widened until it covers the whole irradiated section of the grating. As a consequence, the increase of Δn_{dc} remains after the maximum value of Δn_{ac} has been achieved. The decrease in Δn_{ac} appears, indicating that the volume dilation of the core network may begin in the region with highest degree of compaction. The volume dilation seems to begin when a depletion of ODCs and a high tensile stress develop in the core as a result of the UV-induced compaction [223]. The Type-I grating is completely erased when the compaction-related index changes are compensated by the dilation-related index changes. With further continued UV exposure, the Δn_{ac} again increases but Δn_{dc} decreases. This may be due to overall positive index changes caused by a reduction of the axial stress in the fiber core compared to negative index changes via volume dilation caused by depletion of ODCs. The dilation and the compaction could occur simultaneously in the fiber core. The central region of the irradiated section is dilated whereas the regions near its edges are compacted [224]. After the tensile stress in the fiber core attains its limit and the maximum degree of compaction is achieved at the edges of the irradiated section, only the volume dilation remains. As the volume dilation develops towards the edges of the irradiated section, the value of Δn_{dc} decreases or remains constant.

2.4 Inscription of Tilted FBGs (TFBGs)

In a normal FBG, the grating planes are normal to fiber axis [226-228]. However, the Bragg resonant wavelength of a FBG can be tuned in a limited range by tilting the fiber in the fringe plane. The induced index planes in the core of the fiber will be tilted. The tilt angle can be introduced by rotating the phase mask and cylindrical lens in the vertical plane by same angle so that the line focus remains on the fiber (Figure 2.14).

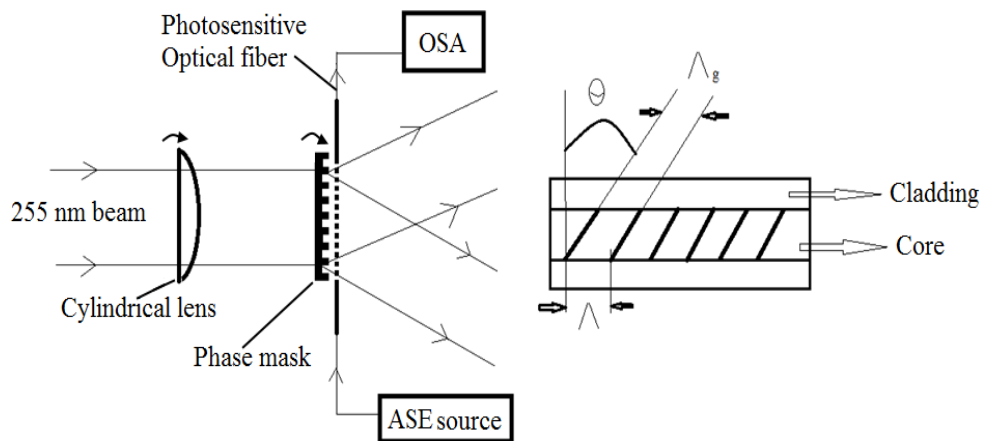


Fig. 2.14: Experimental set-up for writing Tilted fiber Bragg grating

In this case, the FBG length remains constant with change in tilt angle. Maximum tilt angle that could be applied in the writing system is about 10° . Tilted fiber Bragg gratings have been developed using highly coherent 255 nm radiation [229]. This technique has been used for writing the multiple grating in a single fiber for distributed temperature sensor as discussed in **Chapter 5**. The transmission and reflection spectra of the Tilted fiber Bragg gratings (TFBG) are studied for the tilt angles of 0° (normal FBG), 1° , 3° and 4° between the fiber axis and the interference fringe plane. It is observed that as the angle of fiber axis and phase mask increased, the main Bragg peak shifted towards the higher wavelength and transmission dip also decreased. The transmission dip of the cladding mode first increased and then decreased after reaching a maximum with the increase in the tilt angle. At tilt angle of 0° the Bragg peak wavelength and

transmission dip are 1534.41 nm and 10 dB respectively with no cladding modes. For 1° tilt angle, central Bragg wavelength is shifted to 1534.74 nm with reflectivity 8 dB. The cladding modes start appearing at the lower wavelength. At further higher tilt angle of 3° , the transmission dip of the Bragg peak (1536.77 nm) reduces to 4.5 dB. With increased cladding mode transmission dip 1.5 dB. At further higher angle of 4° , transmission dip reduces for both i.e. cladding mode and core mode to 0.5 dB and 1.5 dB, respectively. Again the Bragg peak is shifted towards the longer wavelength of 1538.46 nm. The Transmission spectra for different tilt angles are shown in figure 2.15 (a and b) and corresponding values of Bragg wavelength and transmission dip are listed in table 2.4.

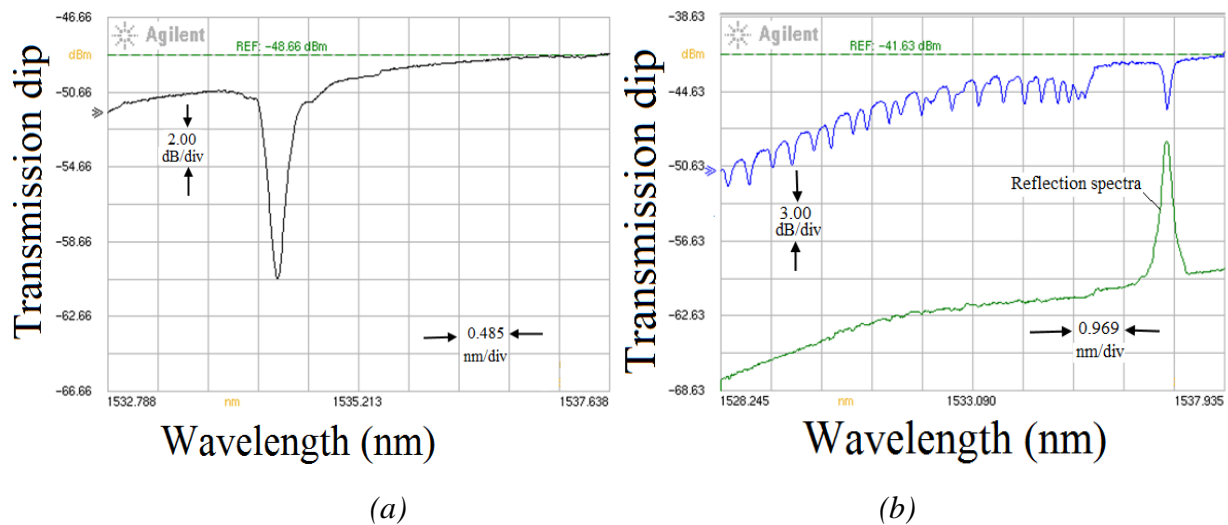


Fig. 2.15: Transmission spectra for grating tilt angle (a) 0° and (b) 3°

Table 2.4: Bragg wavelength and transmission dip for different tilt angles

Tilt angle	Bragg wavelength (nm)	Bragg peak transmission dip	Cladding modes transmission dip
0°	1534.41	10 dB	0.0 dB
1°	1534.74	8.0 dB	0.5 dB
3°	1536.77	4.5 dB	1.5 dB
4°	1538.46	1.5 dB	0.5 dB

The resonance condition satisfying the Bragg condition can be written as

$$\lambda_B = (n_{eff,co} + n_{eff,co}) \Lambda \quad (2.6)$$

where $n_{eff,co}$ is the refractive index of the fiber core, Λ corresponds to the normal grating period and $\Lambda_g = \Lambda / \cos \theta$ corresponds to the grating period along the axis of the fiber (figure 2.14). For the Tilted grating, the resonance condition can be written as (taking grating period along the fiber axis into account)

$$\lambda_B = (n_{eff,co} + n_{eff,co}) \frac{\Lambda}{\cos \theta} \quad (2.7)$$

where θ is the angle between grating fringe and the fiber cross-section. Due to presence of tilt angle, the part of forward propagating mode will be coupled into counter propagating cladding modes and the resonance wavelength of the cladding mode is given by

$$\lambda_{cl,i} = (n_{eff,co} + n_{eff,cl,i}) \frac{\Lambda}{\cos \theta} \quad (2.8)$$

where $n_{eff,cl,i}$ is the effective refractive index of i^{th} cladding mode. From eq. (2.7), it is clear that as the angle between the grating fringe and fiber cross section increases, the value of grating period increases and thus the central Bragg peak shifts towards the longer wavelength. For grating period of 530 nm and the refractive index ($n_{eff,co}$) of effective core mode of 1.446, the theoretically calculated central Bragg peak wavelength were 1534.61 nm, 1534.87 nm, 1536.74 nm and 1538.36 nm for the tilt angle of 0° , 1° , 3° and 4° respectively. Theoretical calculated peak Bragg wavelength are in good agreement with the experimentally observed value. As the tilt angle increases, the losses of the core mode increase and thus the transmission dip of the central Bragg peak reduces. The coupling coefficient for the Bragg peak is calculated using relation given by [65]

$$\kappa = \frac{\pi \Delta n_{ac} \eta}{\lambda_B} = \frac{\tanh^{-1}(\sqrt{R})}{L} \quad (2.9)$$

where Δn_{ac} is estimated from the reflectivity of the main mode of FBG. The coupling coefficient of tilt gratings decreased from 1 for $\theta = 0^\circ$ (uniform FBG) to 0.33 for $\theta = 4^\circ$. It is evident from figure 2.16 (a and b) that as the tilt angle increases, the Bragg wavelength increases but the grating reflectivity, refractive index modulation and coupling coefficient decreases. The grating reflectivity in main mode decreased with increase in tilt angle, due to decrease in backward coupling coefficient [230].

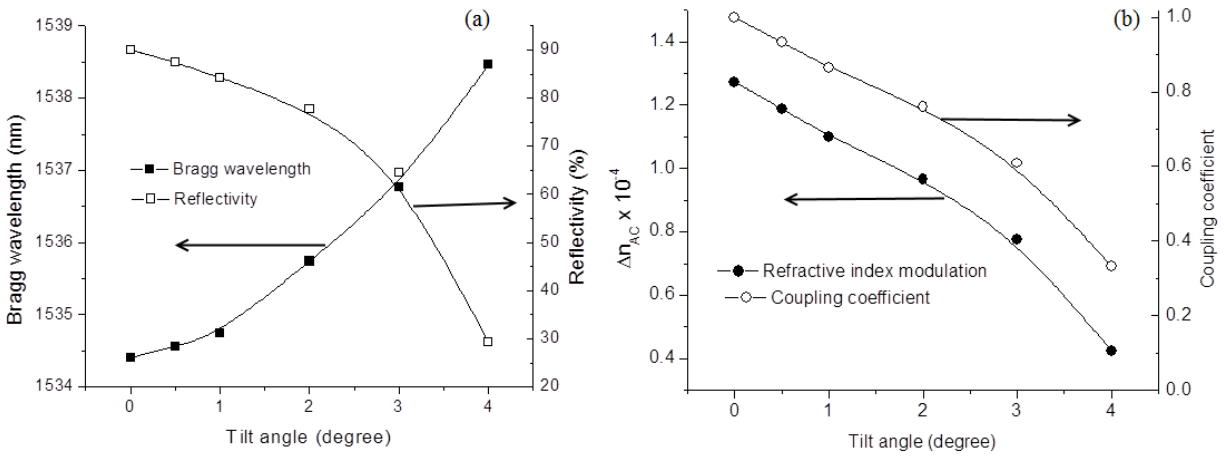


Fig. 2.16: Variation in (a) Bragg wavelength and reflectivity and (b) refractive index modulation and coupling coefficient with tilt angle

2.5 Inscription of FBGs in hydrogenated fiber

Although, the fiber Bragg gratings are often referred to as permanent refractive index structures, however they decay substantially at higher temperature. Usually, the Type-I FBGs written in standard photosensitive fiber, decay substantially for the operating temperature higher than 500°C [231-232]. Recently reported results on regenerated grating technique is a promising way to extend the working temperature range of the Type-I gratings [166-167, 233-235]. The regenerated fiber Bragg gratings (RFBGs) can be obtained through high temperature annealing treatment of Type-I seed FBGs written in hydrogenated fiber [233-234]. So for the observation of thermal regeneration and development of high temperature sensor, the FBGs were written in

different hydrogenated fused silica fibers. The FBGs written in hydrogenated fibers differ from other types of FBGs because their refractive index structure is attributed to the change in the hydroxyl groups and germanium oxygen deficient centers.

2.5.1 Hydrogen loading in optical fibers

The fibers used for FBGs inscription were hydrogen loaded using an in-house developed set up as shown in figure 2.17 (a and b).

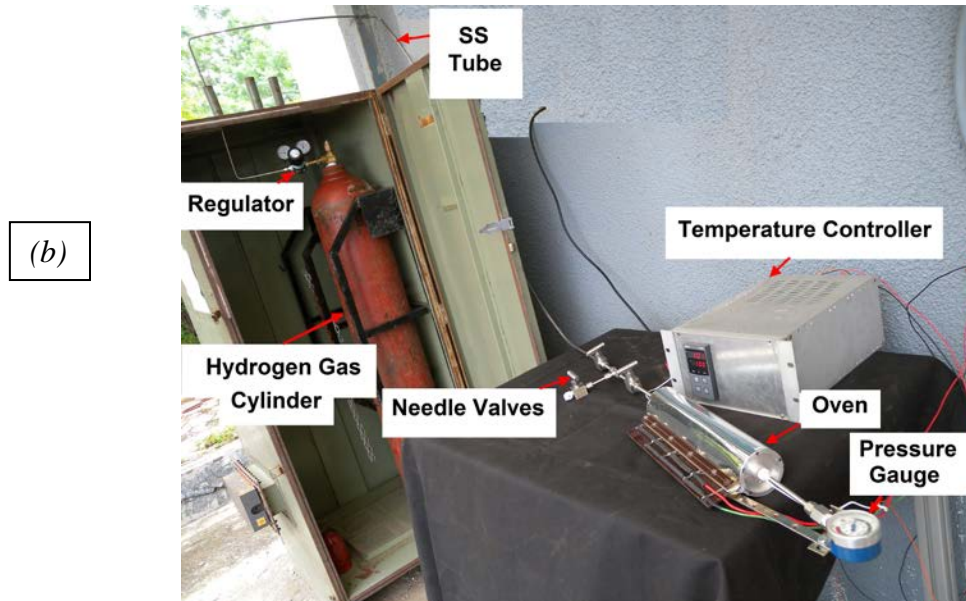
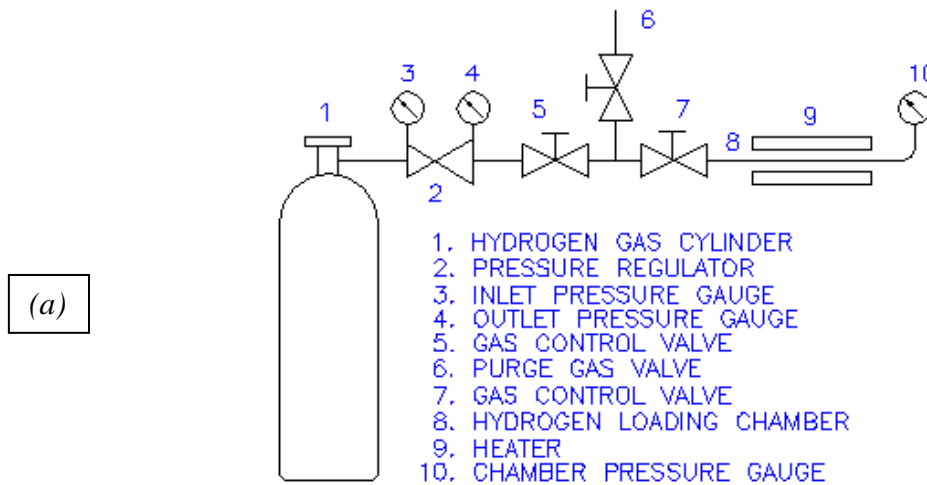


Fig. 2.17: (a) Schematic and (b) actual hydrogen loading set up for optical fibers

The hydrogen loading chamber is made with stainless steel tube of 6.35 mm outer diameter, 4 mm inner diameter, 600 mm length and needle valves (Swagelok). The volume of the system is about 10 ml. The system consisted of three needle valve (Swagelok) connected in T-configuration as shown in figure 2.17 (a). One of the needle valve is connected to the hydrogen cylinder through a gas regulator to fill the hydrogen in the chamber. Two other needle valves are used for loading the hydrogen at high pressure (~ 100 bars) and releasing the hydrogen after loading respectively. The one end of chamber is connected with pressure gauge for monitoring the on-line pressure of the system. All joints of the system are checked by hydrogen leak detector (TIFF 8800A) having capability of minimum detectable concentration 500 ppm. Temperature of the SS tube containing hydrogen is controlled using a home-made PID controller based oven which can be operated up to maximum 300 °C. A thermocouple transducer connected to the temperature controller is used to measure the temperature. At a time multiple optical fiber pieces of length about 50 cm could be placed in the chamber. The concentration of hydrogen molecules and the rate at which these molecules diffuse into the core of the optical fiber depend on the temperature and pressure at which the fiber is soaked. The in-diffusion rate of the Hydrogen gas in silica as calculated from the diffusion equation is given by [236-238]

$$D (cm^2 s^{-1}) = 2.83 \times 10^{-4} \cdot p \cdot e^{\left[\frac{-40.19 \text{ kJ mol}^{-1}}{RT} \right]} \quad (2.10)$$

where p is the pressure of the hydrogen in atmospheres, T is the temperature in Kelvin, R is the gas constant (8.31451 J K⁻¹ mol⁻¹). The variation in diffusion rate of hydrogen in silica with pressure and temperature is shown in figure 2.18 (a). It is clear that the diffusion rate of hydrogen increase with pressure and temperature. The concentration of hydrogen molecules in the optical fiber core at saturation K_{sat} , is given by

$$K_{sat}(ppm) = 3.3481 \cdot p \cdot e^{\left[\frac{8.67 \text{ kJ mol}^{-1}}{RT} \right]} \quad (2.11)$$

1 ppm is equivalent to 10^{-6} moles hydrogen per mole SiO_2 . The variation of saturation concentration with pressure (p) and temperature (T) is shown in figure 2.18 (b).

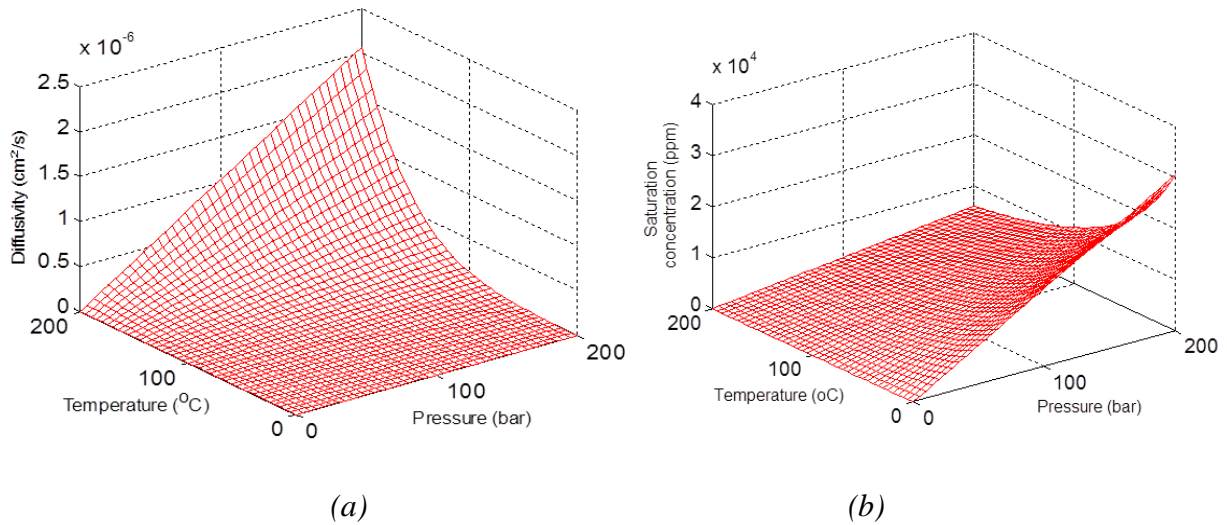


Fig. 2.18: (a) Diffusivity and (b) saturation concentration of hydrogen in silica

The saturated hydrogen concentration increases linearly with pressure and decreases as the temperature increases. Figure 2.18 (a) and (b) give the optimum pressure and temperature for hydrogenating optical fibers. Higher temperatures mean that it is possible to hydrogenate the fiber relatively quickly, but only at the expense of the final concentration of hydrogen in the core of the optical fiber. The concentration of hydrogen molecules and the diffusion rate into the core of the optical fiber depend on the pressure and temperature of the hydrogen gas. The effective loading conditions for inscription of gratings are estimated from figure 2.18. In our case we have chosen the pressure ~ 100 bar at temperature ~ 100 °C for ~ 150 hours to have optimum saturation concentration and diffusivity of H_2 in silica fiber. At these loading conditions the H_2 saturated concentration was 5.5×10^3 ppm and the diffusivity was 6.7×10^{-8} cm^2/s . The FBGs are inscribed within 30 minutes after removing the fibers from H_2 loading set-up.

2.5.2 FBGs in hydrogenated fibers

About 300 mW average power UV beam is used to write the FBG in fused silica fibers having different doping concentration of Ge and Ge-B. Phase mask based FBG writing method is used for grating fabrication. Four FBGs of the same length (~10 mm) and almost similar reflectivity $R \sim 99.9\%$ are written in hydrogen loaded SMF-28, NM-113, SM-1500 and PS-270 fused silica fiber, with same UV exposure time and cumulative flux. Henceforth for discussion, we will refer the FBGs written in these fibers SMF-28, NM-113, SM-1500 and PS-270 as FBG-C1, FBG-C2, FBG-C3 and FBG-C4 respectively. Typical evolution of FBG spectra with UV fringe exposure time is shown in figure 2.19.

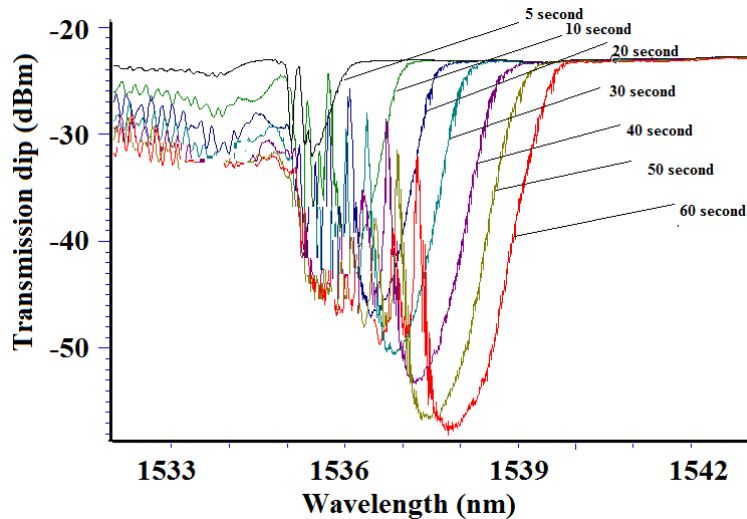


Fig. 2.19: Evolution of FBG spectra with UV exposure for FBG-C1

During inscription of FBGs, it is observed that the Bragg peak wavelength is red shifted as the cumulative fluence is increased. The maximum reflectivity of 99.98 % (~ 36.42 dB), 99.97 % (~ 35 dB), 99.95% (~ 32.87 dB) and 99.98% (~37.42 dB) are observed at the cumulative fluence of 0.84 kJ/cm^2 within 70 seconds for FBG-C1, FBG-C2, FBG-C3 and FBG-C4 respectively. Figure 2.20 shows the refractive index modulation of FBGs written in different fibers with the cumulative UV fluence (CF). The refractive index modulation is

estimated from the transmission spectra at various fluence levels. From figure 2.20, it is observed that the refractive index modulation (Δn_{ac}) increases with the fluence and reaches the maximum value of 2.9×10^{-4} , 2.8×10^{-4} , 2.7×10^{-4} and 3.0×10^{-4} at 0.84 kJ/cm^2 , for FBG-C1, FBG-C2, FBG-C3 and FBG-C4 respectively. The FBG recording results have been repeated several times to avoid any influence from the external parameters such as fiber positioning, laser power or beam quality. For precise placement of optical fiber in front of phase-mask, a CCD camera based fiber positioning system and graphical user interface set-up is also used in each case. The wavelength and reflectivity repeatability in each case was within experimental error.

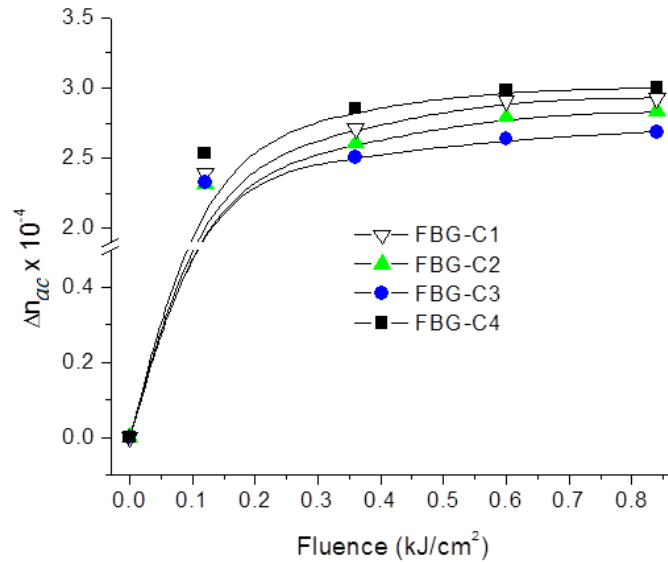


Fig. 2.20: Refractive index modulation for FBGs written in hydrogenated fibers

It is noticed that for same fluence level, the value of Δn_{ac} of Ge-B co-doped fiber (FBG-C4) is slightly higher than the only Ge doped fiber (FBG-C1, FBG-C2 and FBG-C3). This may be due to higher photosensitivity of hydrogen loaded Ge-B co-doped fiber as compared to hydrogen loaded only Ge doped fiber. It is also observed that for hydrogen loaded fibers, the Δn_{ac} decreases with increase in Ge doping concentration. The Δn_{ac} is higher for FBG-C1 as

compared to FBG-C2 and FBG-C3. The thermal annealing characteristics of these FBGs are presented in **Chapter 4** in view of high temperature sensor development.

2.6 Conclusion

In conclusion, the detailed experimental results on fiber grating fabrication using 255 nm beam obtained from the second harmonic of copper vapour laser (CVL) are presented. Both, the germanium and germanium–boron co-doped photosensitive fibers are employed in the FBG fabrication. Experimental investigation on FBG fabrication by phase mask and bi-prism technique, using 255 nm UV beam has been carried out. Different types of FBG such as Type-I, Type-IIa and Tilted FBGs have been fabricated. The fabrication of Tilted gratings, with grating planes at angles 0° to 4° to the fiber axis, is studied. Overall, the FBGs with different parameters Bragg wavelengths, reflectivity and different bandwidth have been written and studied in different fiber types. The FBGs are also inscribed in hydrogenated fiber. For this purpose, the study about the optimum condition of pressure and temperature for hydrogen loading is carried out in detail. The FBGs written in pristine and hydrogen loaded fiber will be used for the development of temperature sensors as discussed in **Chapter 3 to 5**.

Chapter 3

Thermal annealing and sensing studies on Type-I and Type-IIa FBGs

3.0 Introduction

Optical fiber Bragg gratings (FBGs) are widely used in temperature sensing. For this application, the thermal decay of FBGs puts a limit on the maximum operating temperature. It has been observed that Type-I FBGs decay substantially for operating temperature higher than 500 °C [231-232]. The second harmonic of CVL (255 nm) is high repetition rate (5.5 kHz) source retaining some of the advantages of both the CW and pulsed UV laser system. In particular, 255 nm CVL based UV source has high spatial coherence characteristics of 244 nm Ar⁺ source and good peak power characteristics of Excimer (248 nm) laser. In fact lower peak power of 255 nm vs 248 nm source provide better control on FBG characteristics. Also high repetition rate (~5.5 kHz) UV irradiation may lead to in-situ thermal annealing of FBG being fabricated due to cumulative UV absorption. Hence, the combined effect of high UV fringe contrast and in-situ heating due to high repetition rate UV absorption may lead to a grating with different characteristics. The studies on the thermal behavior of the Type-I and Type-IIa FBG inscribed using 255 nm radiation is the focus of the present chapter.

In the present chapter the thermal characteristics of Type-I and Type-IIa FBGs are discussed as part of research work. The effect of core doping concentration on the thermal stability and sustainability is highlighted. After the thermal characterization, the study on the decay characteristics of the different FBGs is presented. The last section of the chapter presents the implementation of the single point temperature sensor for monitoring of transformer oil temperature in high voltage and high EMI environment.

3.1 Experimental arrangement for thermal characterization of FBGs

The schematic and actual experimental set up for the thermal characterization of FBG is shown in figure 3.1 (a and b). The FBG interrogation system consists of broadband ASE source connected through one of the ports of three ports circulator. The other two ports of circulator are connected through to the one end of FBG and other to the OSA in order to record the FBG reflection spectra.

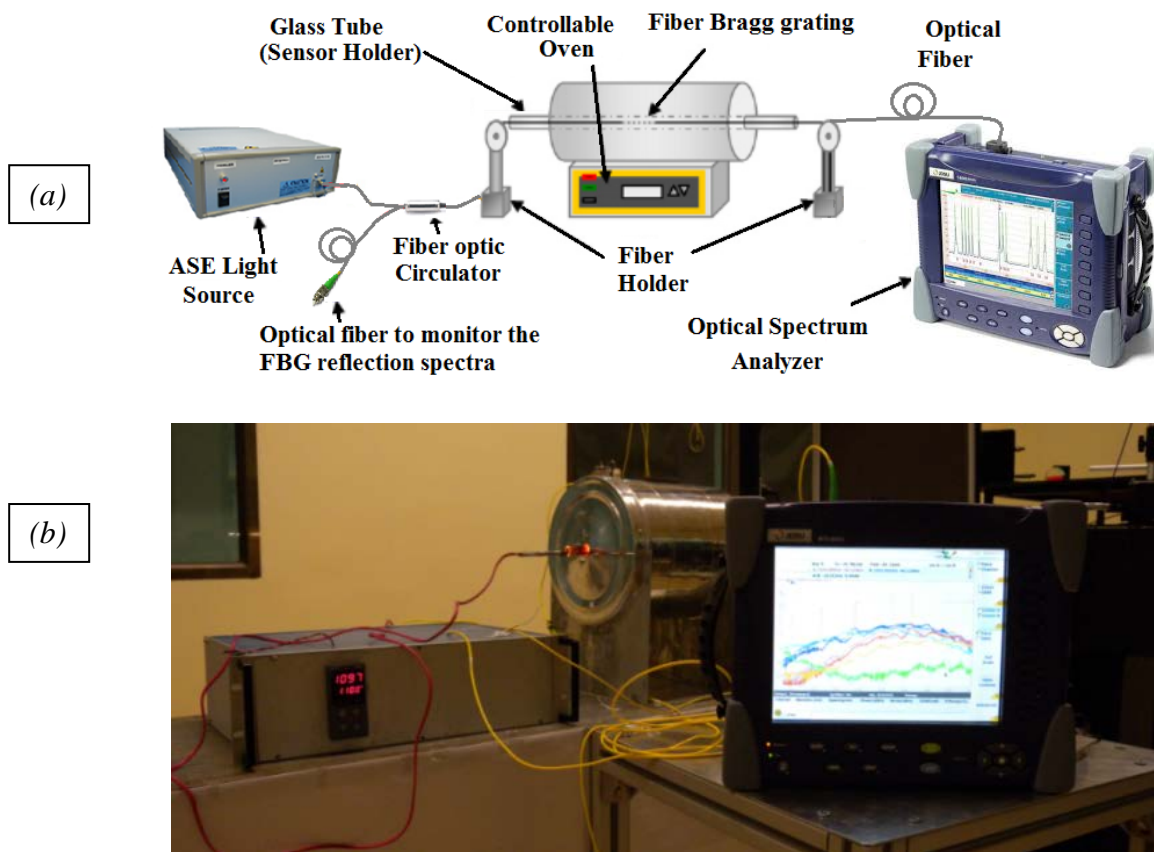


Fig. 3.1: (a) Schematic and (b) experimental set up for thermal characterization of FBGs

The center wavelength is recorded from peak detection. The temperature response of the FBG is recorded by heating it in an in-house built programmable PID controller based oven. A thermocouple transducer connected to a temperature controller is used to measure the temperature. The minimum resolution of the thermocouple was 0.5 °C. For protection and use of

a FBG as temperature sensor, the fiber incorporating FBG is kept inside the SS or ceramic tube. The wavelength shift for the developed temperature sensor of FBG is measured using a fiber interrogator (JPFBG-3000). The wavelength range of the measurement by interrogator was 1525-1565nm with repeatability ± 5 pm and resolution of 1pm.

3.2 Studies on the thermal characterization of Type-I FBGs

The FBG reflectivity depends directly on the refractive index modulation induced in the fiber core by the UV beam. A slow decay of this modulation is expected from relaxation of some unstable defects due to heating of FBGs. The thermal deactivation of these defects is the most important source of grating degradation [176, 231, 239-242]. As the FBG temperature is elevated, the decay of refractive index modulation is higher leading to reduced FBG reflectivity [176, 231]. For uses in different applications, gratings have often been pre-annealed to wipe out the unstable portion of the refractive-index change within a short period of time.

3.2.1 Thermal behavior of Type-I FBGs with different core doping concentrations

Three FBGs of the same length (~10 mm) are written in non-hydrogenated PS-270, NM-113 and SM-1500 fused silica fiber with same UV exposure time and cumulative flux [176]. These FBGs are referred as FBG-A1, FBG-A2 and FBG-A3 in **Chapter 2** for fibers PS-270, NM-113 and SM-1500, respectively. The maximum reflectivity of 99.7 % (~ 26 dB), 96.9 % (~ 15.2 dB) and 99.6 % (~ 24.7 dB) are observed at the cumulative fluence of 3.09 kJ/cm² for FBG-A1, FBG-A2 and FBG-A3 respectively as discussed in **Chapter 2**. A variation in temperature applied to a grating, results in a change in its Bragg wavelength and reflectivity. Variation in the reflectivity with time at various temperatures for FBG-A1, FBG-A2 and FBG-A3 are shown in figure 3.2 (a-d). In the first step, as the temperature is increased from room temperature

(30 °C) to 600 °C within 60 minutes, the reflectivity for FBG-A1, FBG-A2 and FBG-A3 decreased only marginally by 5%, 3 % and 3% respectively (fig. 3.2 a). Now the FBGs were kept at this temperature (600 °C) for about four hours. At the end of this period the reflectivity for FBG-A1, FBG-A2 and FBG-A3 was 84%, 93% and 92% respectively (fig. 3.2 b).

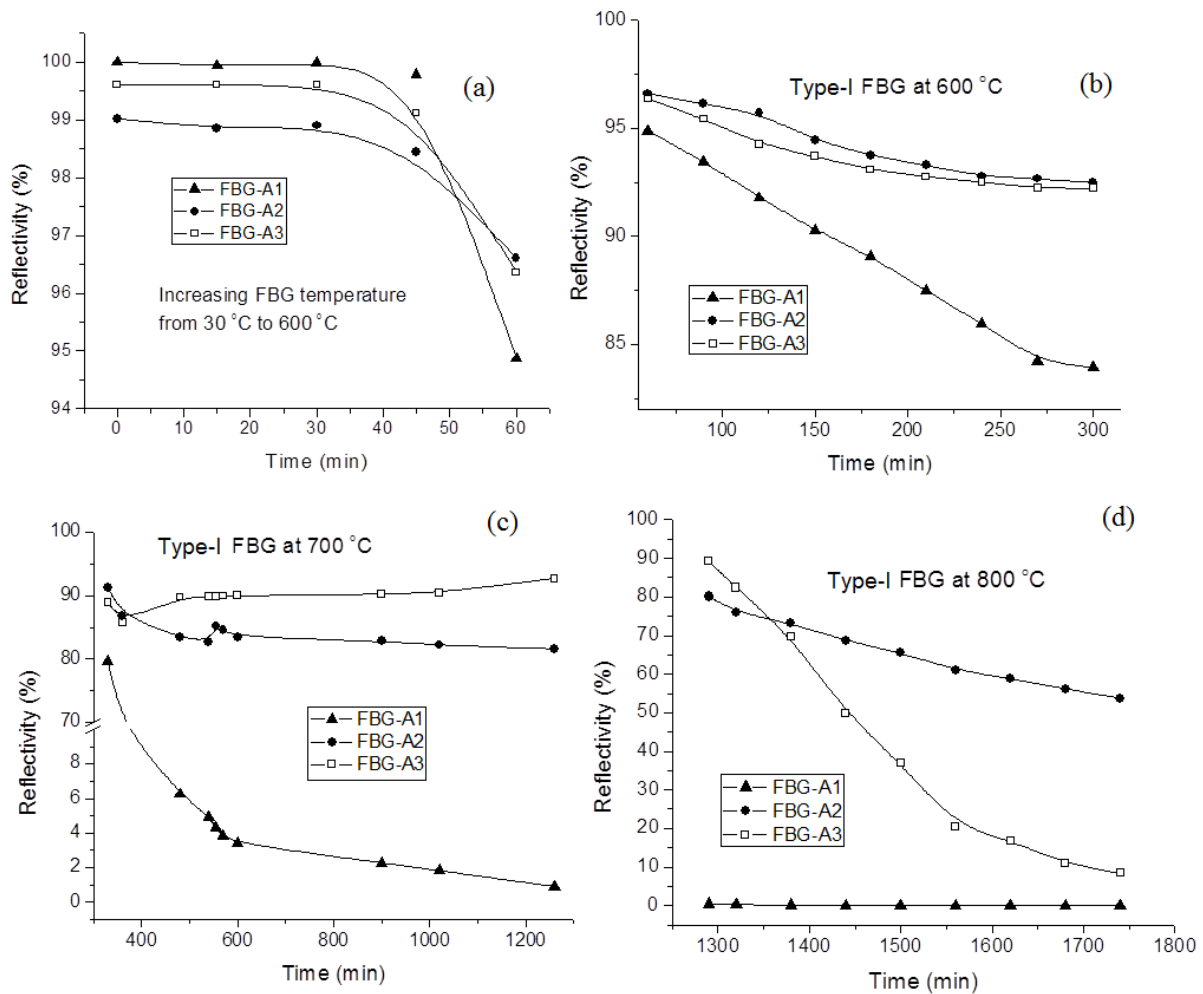


Fig. 3.2: Variation in FBG reflectivity with time at temperature (a) 30 °C to 600 °C (b) at 600 °C (c) at 700 °C and (d) at 800 °C

In the second step, the temperature of the FBGs is further increased from 600 °C to 700 °C and kept constant for about 19 hours (fig. 3.2 c). For FBG A1 the final reflectivity after 19 hours dwell time at 700 °C was ~ 0.9 %. For FBG-A2, the reflectivity initially reduced from 92.2% to 83.55% within 210 minutes and then increased to 86.05%. After 19 hours dwell time at

700 °C, the FBG-A2 reflectivity was about 82%. In case of FBG-A3, the final reflectivity after this step was ~96%. So the FBG-A2 and FBG- A3 show a sign of regeneration at temperature 700 °C. This thermal regeneration of gratings was different and also observed at different time. For FBG-A2, the thermal regeneration was observed after 210 minutes while for FBG-A3 after 30 minutes at 700 °C. It is worth mentioning that for non-hydrogenated Ge doped fiber, thermal regeneration was stronger for grating having higher Ge concentration which is contrary to observed results with hydrogen loaded fiber [240]. This is possibly due to fact that the amount of induced stress in core, between UV exposed and unexposed region, is higher for seed FBGs having larger refractive index modulation. Also the strength of thermal regeneration increases almost linearly with refractive index modulation of seed FBGs. Since for FBG-A3, the refractive index modulation ($\sim 2.5 \times 10^{-4}$) is higher as compared to FBG-A2 ($\sim 1.7 \times 10^{-4}$), the strength of thermal regeneration for FBG-A3 is higher as compared to FBG-A2. However for FBG-A1, there was no such thermal regeneration observed at 700 °C. The reflectivity of FBG decreased from 80 % to 0.9 % for FBG-A1.

In third step, the temperature of the oven is increased to 800 °C and kept constant for about 9 hour (fig. 3.2 d). The reflectivity of gratings after 9 hour becomes 54%, 10% (of the initial reflectivity at room temperature) for the FBGs written in FBG-A2 and A3 respectively. The FBG-A1 almost disappeared as the temperature reached to 800 °C. Finally gratings were cooled down to room temperature. The Bragg wavelength shift with time at various temperatures for FBG-A1, FBG- A2 and FBG-A3 is shown in figure 3.3. It is noticed that for each constant temperature, the Bragg wavelength was red shifted for FBG-A1 (B-Ge codoped). While for FBG-A2 and A3, it were blue shifted at each temperature.

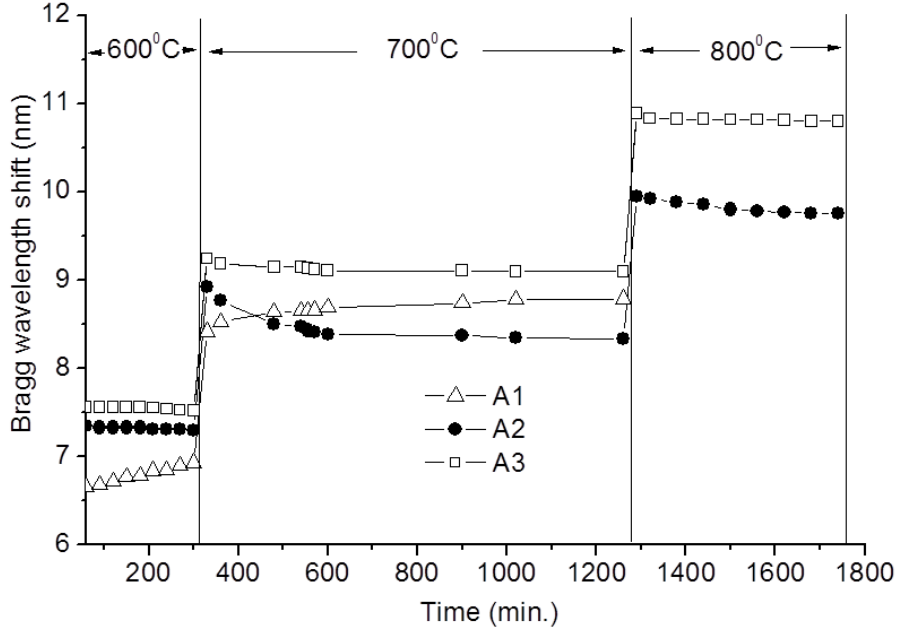


Fig. 3.3: Bragg wavelength shift with time at various temperatures for all FBGs

The observed thermal degradation of the FBG with time at a fixed temperature of 600 °C can be analyzed by calculating normalized integrated coupling coefficient (NICC) η . If Δn_T and Δn_0 are the changes in refractive index modulation at temperature T and room temperature respectively, then the NICC can be calculated as [177]

$$\eta = \frac{\Delta n_T}{\Delta n_0} = \frac{\tanh^{-1} \sqrt{R_T}}{\tanh^{-1} \sqrt{R_0}} \quad (3.1)$$

where R_T and R_0 are the reflectivity of the FBG at any temperature T and room temperature respectively. By use of the experimental data obtained (figure 3.2), the thermal decay characteristics are simulated using the power-law model proposed by Erdogan [231], expressed as,

$$\eta = \frac{1}{1 + A_p \left(\frac{t}{t_1} \right)^\alpha} \quad (3.2)$$

where t is decay time in minute, A_p is the power-law factor and α is the power-law decay coefficient. A_p and α both are dimensionless in this form, but they are temperature dependent.

Time t_I is taken as 1 minute to keep the dimensions consistent in the formula. Normalized integrated coupling coefficient (NICC) calculated from both the Eq. (3.1) and (3.2) is plotted as a function of time at 600 °C for all the fibers (figure 3.4). The power law factor and decay coefficients are estimated by fitting the power law to the experimental data. The values of A_p and α are 0.026 and 0.50 for FBG-A1, 0.029 and 0.32 for FBG-A2 and 0.031 and 0.33 for FBG-A3 respectively. Hence the model fits reasonably well to the experimental data. For FBG-A1 written in Ge-B co-doped fiber, the decay of the reflectivity was faster than FBG written in only Ge doped. So the addition of boron made the fiber less thermally stable under typical operating conditions. In order to understand high temperature stability of FBGs written in Ge doped fused silica fiber as compared to Ge-B co-doped fused silica fibers, the wavelength shift with time is also recorded.

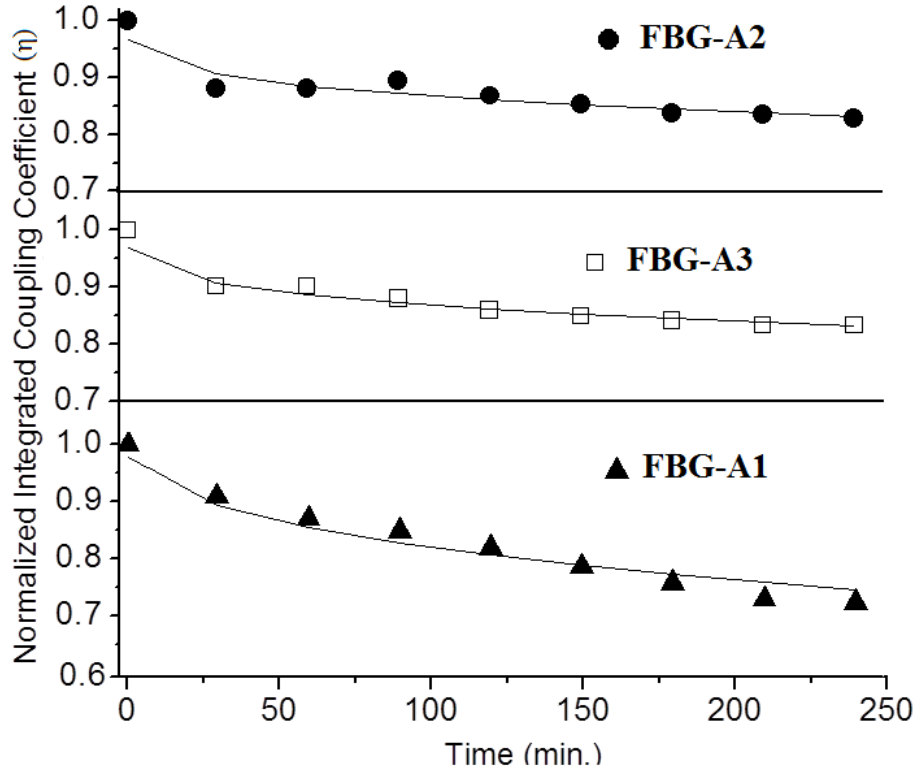


Fig. 3.4: Variation of NICC (η) with time at 600 °C for all FBGs

Figure 3.5 shows the Bragg wavelength shift and reflectivity with time for all three FBGs at 700 °C. The Bragg wavelength was blue shifted for FBG-A2 (-0.60 nm) and FBG-A3 (-0.15 nm), whereas it was red shifted (+0.37 nm) for FBG-A1. The blue shift of Bragg wavelength peak suggests that Type-I FBG is converting into a FBG having properties similar to Type-IIa gratings, since Type-IIa grating sustained the higher operating temperature as compared to Type-I gratings [162]. This thermal regeneration of FBG may be due to stress relaxation of the fiber core between high exposed and less exposed region by the UV interferogram or due to crystallization of fused silica fiber [177]. However for B-Ge doped fused silica fiber, the softening temperature of glass lowered due to doping of Boron. This may lead to no thermal regeneration and FBG decayed at lower temperature as compared to only Ge doped fibers. The Bragg wavelength shift and reflectivity with temperature are also recorded for thermally annealed FBG-A2 and FBG-A3. The average wavelength shift is around ~ 13.9 pm/ °C for both FBGs. The reflectivity of FBG-A2 and FBG-A3 remains constant at $\sim 45\%$ and $\sim 10\%$, respectively up to 800 °C and decreases slightly up to maximum studied temperature of 900 °C.

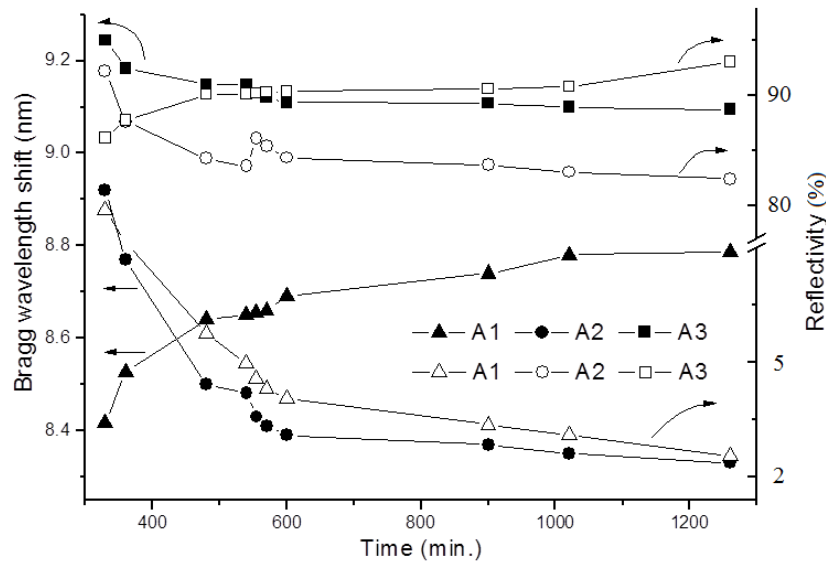


Fig. 3.5: Variation in the Bragg wavelength (solid symbols) and reflectivity (open symbols) with time at 700 °C

3.3 Studies on the thermal characterization of Type-IIa FBGs

3.3.1 Studies on the enhanced temperature (~ 800 °C) stability of Type-IIa FBG

The temperature stability of Type-IIa FBGs is studied by recording the transmission dips of the FBGs at various temperatures. Two FBGs i. e. Type-I ($R \sim 99\%$, FBG-A2) and Type-IIa ($R \sim 42\%$, FBG-B2) are inscribed separately at the cumulative fluence of 5.76 kJ/cm^2 and 37.4 kJ/cm^2 as discussed in **Chapter 2**. Figure 3.6 (a-d) shows the variation in reflectivity of Type-I (solid circle) and Type-IIa (open circle) FBGs with time at various temperatures.

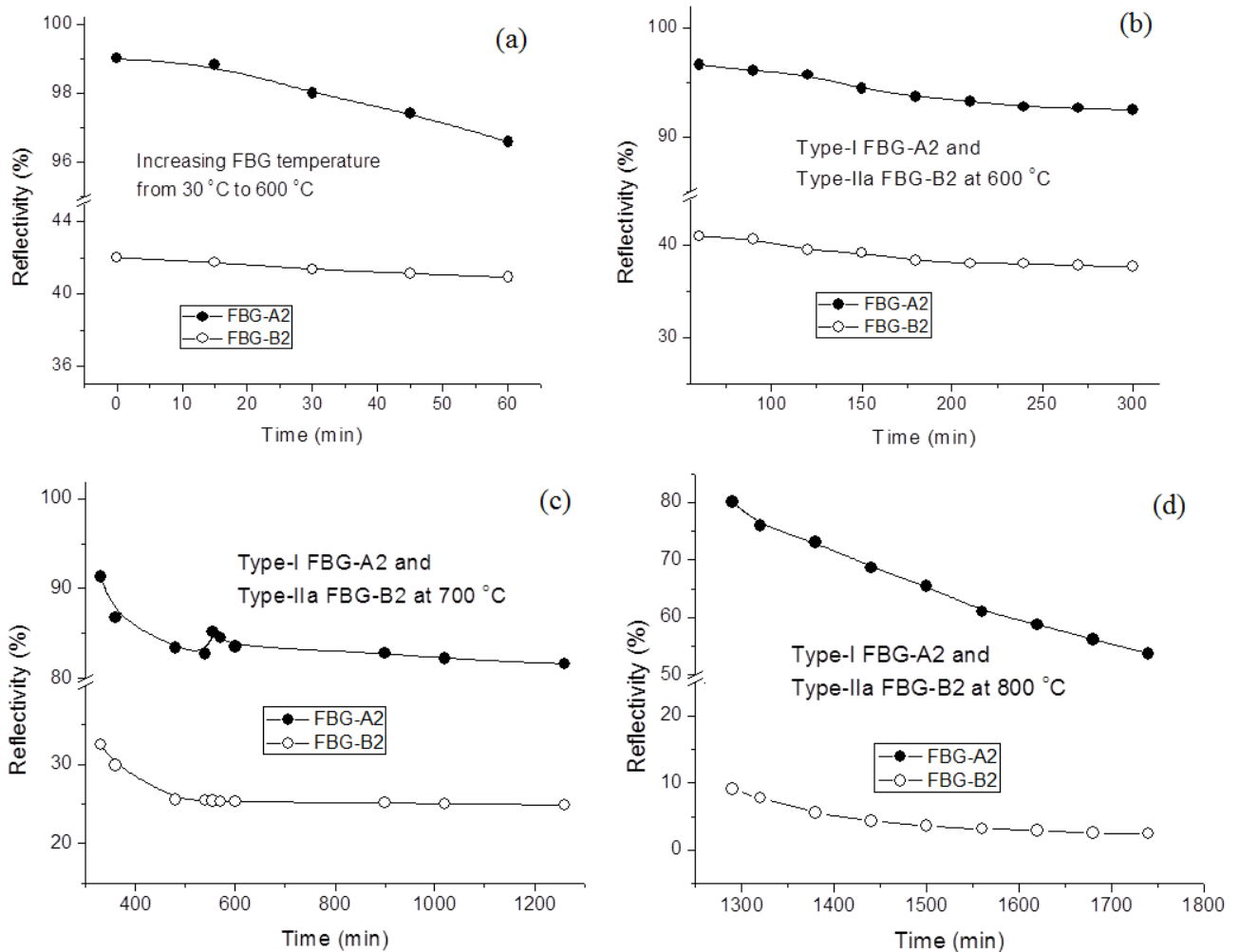


Fig. 3.6: Variation of Type-I and Type-IIa FBG reflectivity with time for temperature (a)

30 °C to 600 °C (b) at 600 °C (c) at 700 °C and (d) at 800 °C

The temperature is varied in steps. In the first step the temperature is increased from room temperature ($\sim 30^\circ\text{C}$) to 600°C in 50 minutes and kept at 600°C for four hours. From figure 3.6 (a and b), it is observed that the reflectivity of both the FBGs was reduced marginally at 600°C . The reflectivity of Type-I and Type-IIa FBGs, after 4 hours dwell time at 600°C , was $\sim 92\%$ and $\sim 35\%$ respectively. In second step, the temperature is raised further to 700°C and kept constant for about 19 hours (fig. 3.6 c). For Type-I grating, reflectivity initially reduced from 92 % to 83 % within 130 minutes (at 400 minutes in the graph) followed by a marginal increase due to the thermal regeneration of the grating. However no such thermal regeneration is noticed for Type-IIa grating. After 19 hours, the reflectivity of Type-I grating reduced to 81 %. In contrast for Type-IIa FBG, the reflectivity reduced from 35 % to 24 % after 19 hours. Higher stability of Type-I grating as compared to Type-IIa at 700°C is due to thermal regeneration of Type-I grating. As per our past experience regarding thermal characterization of FBG, if the FBG is quite stable at a certain temperature then we can try for next higher temperature ($\Delta T \sim 100$ to 150°C). So the temperature of the FBG was raised to 800°C . In third step, the temperature of oven is increased to 800°C and kept constant for 9 hours (fig. 3.6 d). The reflectivity of Type-I grating reduced from 80 % to 50 % after 9 hours. However for Type-IIa grating, the reflectivity reduced from 11 % to 2.5 %. Thus the rate of fall of reflectivity for Type-IIa grating of 1.28 %/hr is about three times lower than the value of 3.34 %/hr for Type-I. Now, both the FBGs are cooled down to room temperature.

In the next step, the Bragg wavelength shift and reflectivity of these FBGs are recorded with rise in temperature upto 900°C . The temperature of the FBGs is raised from room temperature (30°C) to 900°C in ~ 1 hour. The average wavelength shift ($\sim 13.9 \text{ pm}/^\circ\text{C}$) is almost same for both the gratings. The reflectivity of Type-I FBG remains constant ($\sim 45\%$) upto 800°C

and then decreases slightly after 800 °C. In contrast for Type-IIa grating, the reflectivity is almost constant (~2.5%) upto 900 °C. It is worth mentioning here that there is only one published study on the temperature stability of Type-IIa grating (upto 800 °C) produced by continuous exposure of UV radiation [152]. The unstable resonator based writing ArF (193 nm) laser was of <5% pulse to pulse fluctuation, low repetition rate (30 Hz) and high pulse energy (133 mJ/cm²) density [152]. At 800 °C, the Type-IIa decayed completely in 2.9 hrs. In the present study, the FBG stability at 800 °C for over 9 hrs needs explanation. The present data may be explained as follows based on current understanding.

It is well understood that the enhanced thermal stability of Type-IIa (Type-In) FBG whether formed by thermal regeneration or by continued UV writing involves the process of axial stress relief [221-223]. Also stronger the seed grating (Type-I, formed by depletion of oxygen deficiency defect centers), larger will be stress between core and cladding. Correspondingly larger will be the stress relaxation by proper annealing or UV fringes exposure, leading to enhanced FBG temperature stability. Now, under repetitive pulsed UV laser writing (as in present study), the strength of seed grating is linked to pulse to pulse stability in divergence, pointing angle and amplitude, thereby contrast stability of UV fringes. In the present set up, this is ascertained by special resonator scheme in copper vapour laser which is based on spatial filtering on intra-cavity diffracted radiation in every round trip [132, 213-214]. This ensures that diffraction limited beam divergence is constant throughout the pulse as well as pulse to pulse characteristics is maintained. The SH UV (255 nm) beam followed the same excellent characteristics of fundamental CVL beam. Figure 3.7 shows the variation of average power of UV with time for about 30 minutes. The variation in average UV power was within 4 %. The graph in inset shows the typical intensity fluctuations of 255 nm UV interference pattern with

time generated by a bi-prism of angle 2° . These data was recorded by placing UV enlarge pattern on a BK-7 fluorescent glass plate (thickness $\sim 400 \mu\text{m}$). The visible fluorescence was recorded in time using a special scheme [213]. Typical fluctuation in the peak intensity of 5-peaks out of 8-peaks is shown in the scan, for the time duration of 300 second. The separation between the two peaks of UV fringes formed by 2° bi- prism is about $8 \mu\text{m}$. It is noted that the peak position of the interference pattern is very stable. This stable UV pattern imprints a very clean grating in fiber core with high axial stress. This implication is also evident from the fact that for Type-IIa grating onset was observed at higher cumulative UV fluence of 24.45 kJ/cm^2 in the present study as compared to 7.39 kJ/cm^2 in Ref. [162]. This explains the higher thermal stability of Type-IIa FBG written with 255 nm source. Also exposing fiber to second harmonic of CVL beams, both the in-situ UV and thermal sensitization due to partially coherent UV radiation and cumulative UV absorption, respectively, may also be operative. These factors are also known to improve the FBG thermal stability [220].

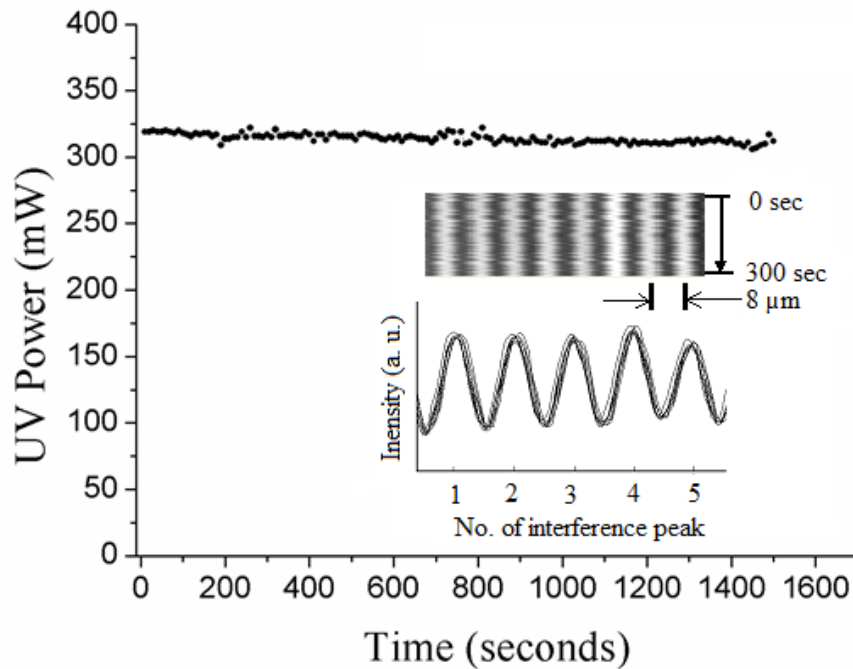


Fig. 3.7: Average UV power (solid sphere) and fringes intensity variation (inset)

3.3.2 Studies on the role of refractive index rollover on the thermal annealing characteristics of Type-IIa FBGs

To study the role of refractive index rollover on the thermal annealing characteristics of Type-IIa gratings FBG-B1, FBG-B2 and FBG-B3 are employed in the study (Chapter 2). The rollover in refractive index modulation (Δn_{ac}) was observed at cumulative fluence of 15.84 kJ/cm², 24.48 kJ/cm² and 57.6 kJ/cm² for FBG-B1, FBG-B2 and FBG-B3 respectively (Figure 2.13 a). From figure 2.13 (a), it is clear that the value of rollover fluence for writing Type-IIa FBG increases as the Ge concentration in the photosensitive fiber decreases. The thermal stability of these Type-IIa FBGs are studied upto ~ 800 °C. The initial reflectivity of the FBG-B1, FBG-B2 and FBG-B3 at room temperature was 93.5%, 65.2% and 98.4% respectively. Figure 3.8 and table 3.1 shows the variation in the normalized reflectivity with time at various temperatures for FBG-B1, FBG-B2 and FBG-B3, respectively. In the first step, as the temperature is increased from room temperature 30 °C to 600 °C, the normalized reflectivity for FBG-B1, FBG-B2 and FBG-B3 decreased about 10%, 3% and 2% respectively.

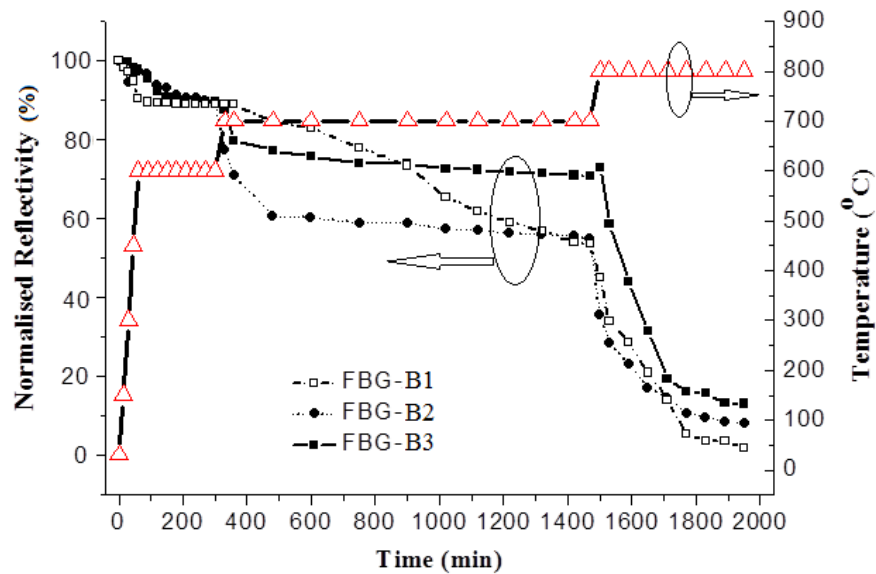


Fig. 3.8: Normalized reflectivity of FBGs with time at 600 °C, 700 °C and 800 °C

Table 3.1: Normalized reflectivity of FBGs with time at 600 °C, 700 °C and 800 °C

Time (min)	Temperature (°C)	Normalized Reflectivity (%)		
		FBG-B1	FBG-B2	FBG-B3
0	30	100	100	100
60	600	90.59	97.38	97.99
Isothermal Heating at 600 °C for 4 hours				
300	600	89.03	89.57	89.73
Isothermal Heating at 700 °C for ~ 19 hours				
330	700	89.02	77.41	87.56
1470	700	53.57	55.00	70.88
Isothermal Heating at 800 °C for ~ 9 hours				
1500	800	45.10	35.65	72.94
1950	800	1.85	8.13	13.12

During 4 hours dwell time at 600 °C, the reflectivity of FBG-B1, FBG-B2 and FBG-B3 was reduced by 11%, 10% and 10% (of the normalized reflectivity at 30 °C) respectively. In the second step, the temperature of the gratings is further increased from 600 °C to 700 °C and kept constant for about 19 hours. After this time the normalized reflectivity becomes 53%, 55% and 71% for FBG-B1, FBG-B2 and FBG-B3 respectively. In third step, the temperature of the oven is increased to 800 °C and kept constant for about 9 hour. The reflectivity of the gratings after 9 hour becomes 2%, 8% and 13% for FBG-B1, FBG-B2 and FBG-B3 respectively. During the annealing process the shift in Bragg wavelength with time at various temperatures are also recorded and shown in figure 3.9, for FBG-B1, FBG-B2 and FBG-B3 respectively. At 600 °C, the Bragg wavelength shift was blue shifted for FBG-B2 (-0.23 nm) and FBG-B3 (-0.34 nm), whereas it was red shifted (+0.59 nm) for FBG-B1. At 700 °C the Bragg wavelength shift was blue shifted for FBG-B2 (-0.38 nm) and FBG-B3 (-0.71 nm), whereas it was red shifted (+0.26

nm) for FBGs written in FBG-B1. At 800 °C the Bragg wavelength shift was +0.66 nm and -0.12 nm for FBG-B1 and FBG-B2 respectively. But for FBG-B3 this shift was initially towards blue (-0.15 nm) and then towards red (+0.40 nm).

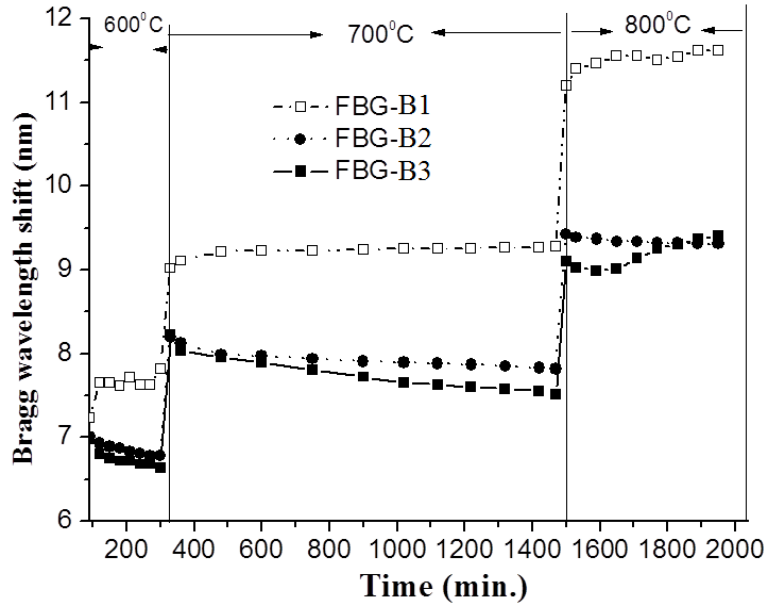


Fig. 3.9: Bragg wavelength shift with time at temperature 600 °C, 700 °C and 800 °C

Higher temperature sustainability of FBG-B3 as compared to FBG-B1 and FBG-B2 needs to be explained. Since for writing Type-IIa gratings with low single pulse energy density requires continued UV fringe exposure for longer time, a very stringent control of the pulse to pulse intensity variation of writing UV beam is needed. It is shown that the intensity and peak position of the interference pattern generated from 255 nm beam is very stable [213]. This stable UV pattern imprints a very clean grating in fiber core with high stress. For the FBGs written at high cumulative flux the high axial stress will be generated between core and clad. Higher the rollover cumulative fluence (as in case of FBG-B3) larger will be the stress between core and cladding. Correspondingly larger will be the stress relaxation by continued UV fringes exposure or by heating. It has been shown that the absorption of UV radiation increases with increase in Ge-doping concentration [220]. The average absorbed energy per pulse is given as

$$\Delta E_{abs} = (1 - e^{-\alpha d}) \Delta E \left(\frac{A_{core}}{A_{beam}} \right) \quad (3.3)$$

where α is the absorption coefficient for UV light in the core of the fiber, d is the diameter of the core, ΔE is the pulse energy (~ 0.056 mJ), A_{core} is the cross section area of the UV beam falling at the core (10 mm x 10 μ m) and A_{beam} is the full cross section area of UV beam (10 mm x 250 μ m). Although the absorption coefficient for 255 nm for different Ge doping concentration is not available in the literature, the absorption coefficients are taken for present calculation for 248 nm. The absorption coefficient roughly depends linearly on the doping concentration of Ge [220]. The estimated value of absorption coefficients are approximately 2100 (dB/cm), 3500 (dB/cm) and 6500 (dB/cm) for Ge doping of 5 mol%, 10 mol % and 18 mol% respectively [224]. Using these values in Eq. (3.3), the average absorbed pulse energy comes out 1.18×10^{-3} mJ, 0.744×10^{-3} mJ and 0.482×10^{-3} mJ for FBG-B1, FBG-B2 and FBG-B3 respectively. This average absorbed energy per pulse will be higher for FBG written in high Ge doped fiber. The rise in temperature due to single pulse of FBG writing UV beam can be estimated from absorbed energy as

$$\Delta T = \frac{\Delta E_{abs}}{\rho V c} \quad (3.4)$$

where ΔE_{abs} is the pulse energy absorbed by the FBG, ρ is the density, V is the FBG volume (78.5×10^{-14} m³) and c is specific heat (0.74×10^3 J/Kg K). The value of density for the core of the fiber will be 2.27 g/cm³, 2.344 g/cm³ and around 2.488 g/cm³ for 5 mol%, 10 mol% and 18 mol% doping concentration of Ge in silica [220]. Estimated temperature rise per pulse from Eq.(3.4) will be around 0.82 °C, 0.55 °C and 0.37 °C for FBG-B1, FBG-B2 and FBG-B3 respectively as shown in figure 3.10. Although the absorbed energy per pulse is higher for FBG-B1 but the time of UV exposure is higher for FBG-B3. This leads to higher average temperature

rise for FBG-B3 as compared to FBG-B1. This conclusion is drawn from the experimental observation on Bragg wavelength shift between UV exposure on and off at final fluence. Figure 3.11 shows the shift in Bragg wavelength and the estimated average temperature rise after removing the UV exposure for fiber of different Ge-doping concentration. This temperature rise (ΔT) is estimated from the relation,

$$\Delta T = \frac{\Delta\lambda}{\alpha_{ts}} \quad (3.5)$$

Where $\Delta\lambda$ is the Bragg wavelength shift and α_{ts} is the average temperature sensitivity of the FBG. The temperature rise was about 4.28 °C, 47.62 °C and 89.52 °C for FBG-B1, FBG-B2 and FBG-B3 respectively. It is clear that the in-situ temperature rise was higher for FBG-B3. Correspondingly larger will be the stress relaxation for FBG-B3 leading to enhanced FBG temperature stability.

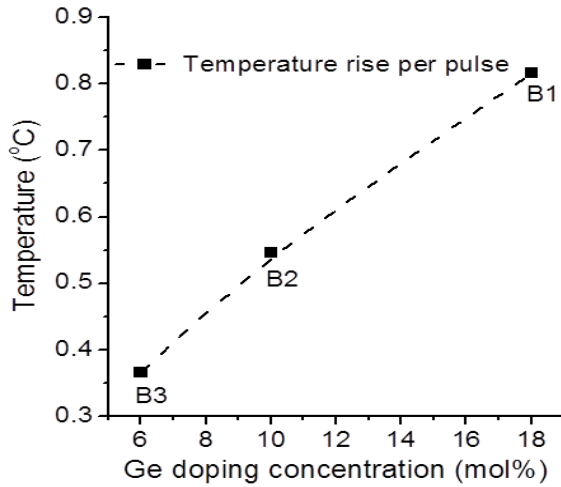


Fig. 3.10: Estimated temperature rise per pulse with Ge doping in fibers

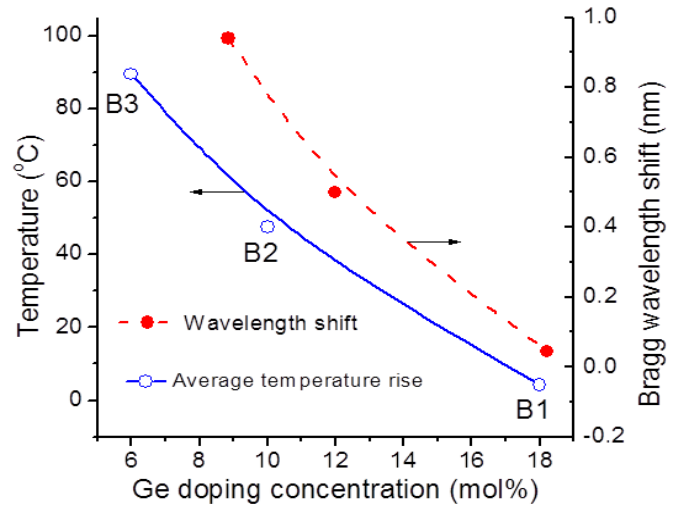


Fig. 3.11: Estimated average temperature rise and Bragg wavelength shift with Ge doping

Figure 3.12 shows the typical change in normalized reflectivity and Bragg wavelength with temperature for these thermally annealed FBG-B2 and FBG-B3. The Bragg wavelength changes from 1534.933 nm to 1547.634 nm for FBG-B2 and 1535.02 nm to 1547.247 nm for

FBG-B3 as the temperature of the oven is changed from room temperature (30 °C) to 900 °C. The average wavelength shift is around ~13.9 pm/ °C for both FBGs. The reflectivity of both FBGs remains constant up to 800 °C and decreases slightly up to maximum studied temperature of 900 °C.

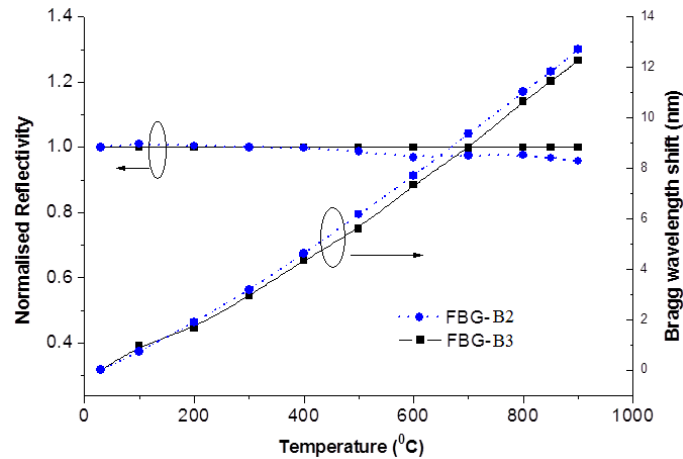


Fig. 3.12: Typical change in normalized reflectivity and Bragg wavelength with temperature for annealed FBG-B2 and B3

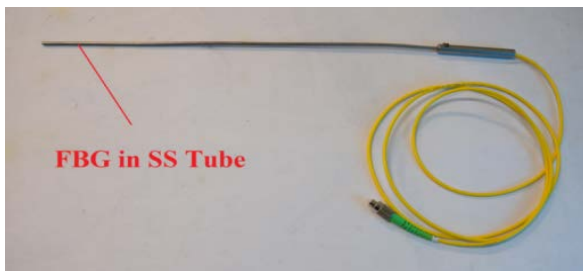


Fig. 3.13: Developed FBG sensor for temperature measurement up to 500 °C

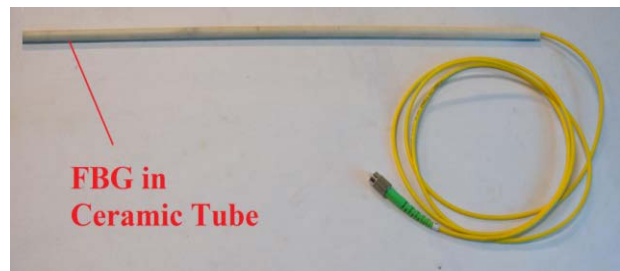


Fig. 3.14: Developed FBG sensor for temperature measurement up to 800 °C

These Type-IIa FBGs will be extremely useful for the development of repeated use high-temperature resistance fiber Bragg grating temperature sensor. The single point FBG temperature sensors are developed by encapsulating the FBGs in SS and ceramic tubes. Figure 3.13 and 3.14 shows the developed temperature sensors for monitoring temperature upto 500 °C and 800 °C. The systematic calibration of the developed temperature sensors is carried out using

a standard compact split tube furnace (OTF-1200X-S25-UL-220V) from MTI Corporation. The maximum heating temperature the heater can sustain is 1200 °C (for 1 hour). The temperature accuracy of the heater is +/- 1°C and the temperature uniformity is +/-1°C within 50 mm of the heater length. The developed FBG sensors were placed inside the heater for their calibration. The Bragg wavelength of the FBG sensor with temperature was recorded using OSA (JDSU- OSA-500). The specification of OSA are wavelength range 1250 nm to 1650 nm, wavelength accuracy ± 10 pm with wavelength readout resolution 1 pm. The possible error sources in the measurement are the spectral profile of the FBGs and the applied strain or bending during placing the FBG inside heater. To minimize the inaccuracy in the temperature measurement, the bandwidth of the FBGs is tailored during the inscription process and all FBGs are placed freely in the oven without any strain.

3.4 Prediction of operating life time of Type-I and Type-IIa FBG

For reliable operation of FBGs as temperature sensors, the study on the long term thermal stability of UV exposed Type-I and Type-IIa FBG is very important. Thus the study on the decay in the reflectivity of the gratings with time at different temperatures is carried out and modelled according to a power-law approach. For this study, a series of nearly identical Type-I and Type-IIa FBGs of reflectivity ~97% and ~90%, respectively, and of the length of 10 mm, are fabricated in the same fiber (SM-1500). The thermal sustainability of both of these types of FBGs is studied with time by placing the gratings carefully (so that there would be no strain effect on the gratings) inside a well-calibrated tubular oven. The temperature is increased step-wise from room temperature to 600 °C, 700 °C and then up to 800 °C. The temperature was kept fixed for 4 hour at each stage before moving up to the next higher temperature. The normalized integrated coupling coefficient (η) is calculated from Eq. (3.1) by using FBG reflectivity values

at each temperature. Figure 3.15 shows the variation in NICC with time for Type-I and Type-IIa FBGs at temperature 600 °C, 700 °C and 800 °C. It is apparent from figure 3.15 that initially the gratings decay very rapidly, followed by a substantial decrease in the rate of decay at longer times. This behavior is indicative of a “power-law” dependence on time. By use of the experimental data obtained, the thermal decay characteristics are simulated using the power-law model as discussed in Eq. (3.2). Figure 3.15 shows the thermal decay characteristics along with the power law model fitted graph (solid symbols for Type-I FBGs and hollow symbols for Type-IIa FBGs). For the decay of each type of FBGs, the set of values of A_p and α used are calculated separately from the experimental points for each temperature, according to Eq. (3.2). Following that, A_p and α are plotted against temperature to evaluate the temperature dependence of these parameters as shown in figure 3.16 (a and b).

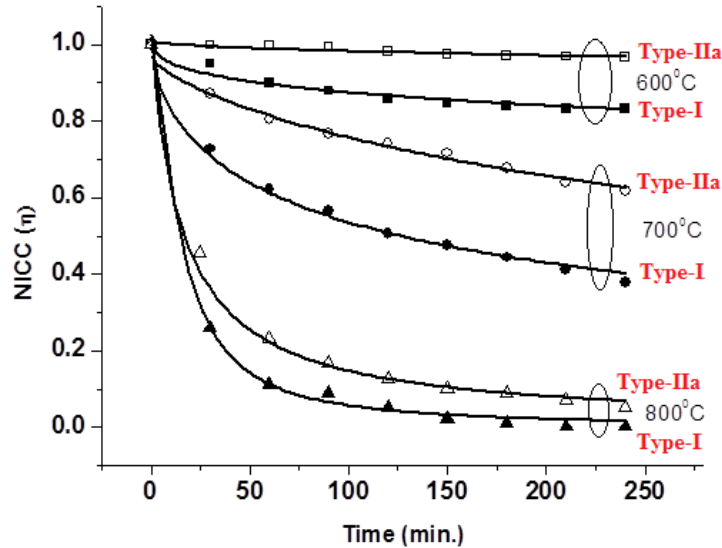


Fig. 3.15: NICC for Type-I and Type-IIa FBGs at temperature 600 °C, 700 °C and 800 °C

The value of the decay factor, A_p , is evaluated by exponential growth fit to data, the nature of which can be written as,

$$A_p = A_0 e^{(\alpha_0 T)} \quad (3.6)$$

The value of A_0 and a_0 was 0.00162 min^{-1} & 0.00168 min^{-1} and $0.00356/\text{K}$ & $0.00338/\text{K}$ for Type-I FBG and Type-IIa FBG respectively. The variation of Power law decay coefficient (α) with temperature was assumed to be linear [231] passing through zero on the temperature axis and thus the temperature dependence of this parameter can be expressed as

$$\alpha = \frac{T}{T_0} \quad (3.7)$$

where the temperature is measured in Kelvin. A fit to Eq. (3.7) through the temperature data points yields $T_0 = 2493 \text{ K}$ and 2863K for Type-I and Type-IIa FBG respectively.

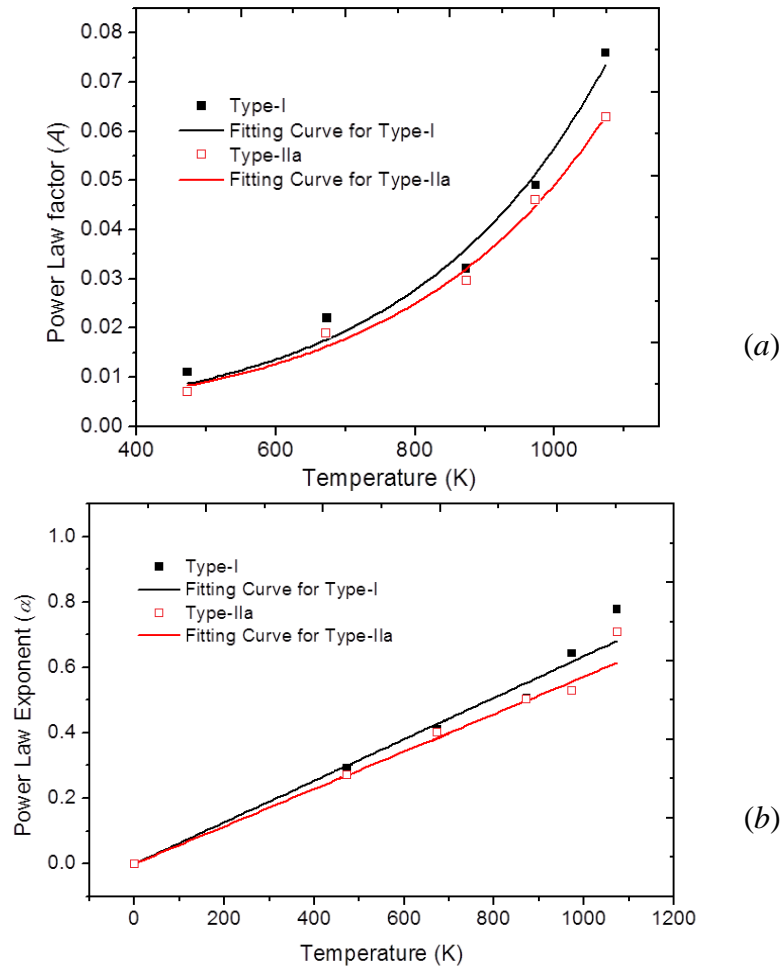


Fig. 3.16: (a) Power law factor and (b) power law decay coefficient with temperature for Type-I and Type-IIa FBGs

Eq. (3.2) can be re-written in the following form,

$$t = \left(\frac{1-\eta}{A_p \eta} \right)^\alpha \quad (3.8)$$

For the remaining NICC value of $\eta \sim 0.1$,

$$t = \left(\frac{9}{A_p} \right)^\alpha$$

For some quantitative predictions of the decay of gratings written in the fiber used here, Figure 3.17 shows the calculated decay of Type-I and Type-IIa FBG with change in temperature.

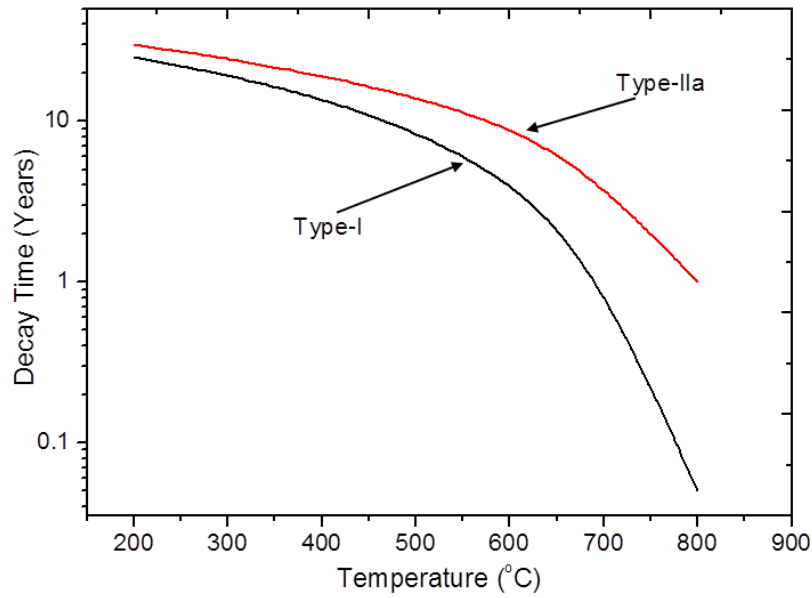


Fig. 3.17: The calculated thermal decay of Type-I and Type-IIa FBGs

For this calculation A_p and α are calculated from Eq. (3.6) and Eq. (3.7) respectively. Note the plotted decay time ranges from about nine hours to 15 years. It is clear from the figure that at any temperature the decay time of Type-IIa FBG will be higher than the decay time of Type-I FBG.

3.5 Application of the developed FBG sensor in temperature monitoring of transformer oil

The developed FBG sensor based on Type-I FBG (**Chapter 2**) is used for online temperature monitoring of oil immersed ferrite core used in high voltage (~25 kV) pulse power supply. Temperature monitoring of oil immersed components in high voltage power supplies, with conventional sensors is practically very difficult task due to limited access, high electromagnetic interference and presence of high voltage. In the present work, details of the FBG sensor its calibration methodology and deployment of the sensor in the high voltage pulse power supply are carried out. Optical signal interrogator is used for temperature monitoring.

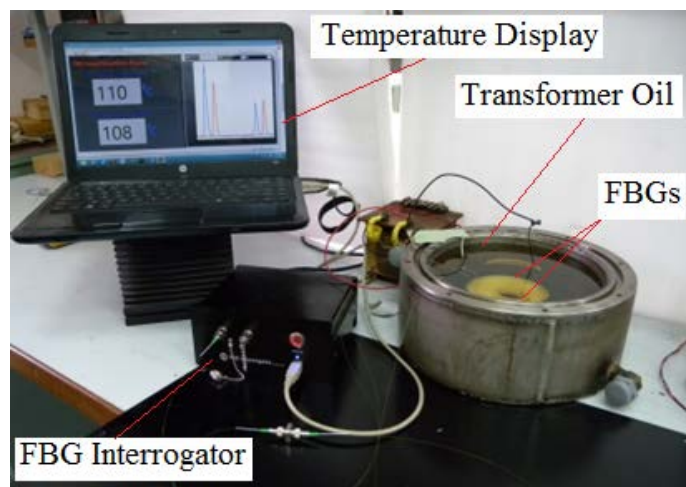


Fig. 3.18: Test set up used for calibration of FBG based temperature sensor for temperature monitoring of transformer oil

As shown in figure 3.18 the FBG under test is placed in oil bath. One end of the FBG is connected to interrogator which provides the reflected wavelength spectrum received from the FBG corresponding to its current temperature. Wavelength corresponding to peak power in reflection spectrum represents the central Bragg wavelength of FBG. Systematic calibration of the FBG temperature sensor is carried out using a thermocouple. The temperature of the oil was varied over a temperature range from 25 °C to 100 °C in steps of 5 °C.

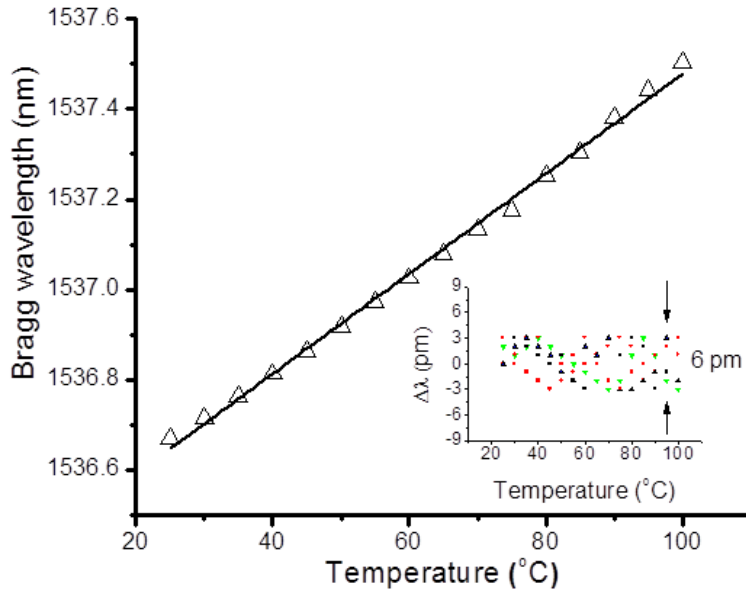


Fig. 3.19: Characterization curve of the FBG used for the oil temperature measurement

Figure 3.19 shows the shift in Bragg wavelength with change in temperature. The average temperature sensitivity of the FBG sensor was about 11.09 pm/°C for the temperature range of 25°C to 100°C. The experiment was repeated for five times. The variation in the wavelength at a particular temperature is plotted in the inset of figure 3.19. It is clear from the figure that the error in the measurement is ~ 6 pm i. e. ± 0.5 °C. The two calibrated FBG sensors (Bragg wavelengths 1536.423 nm and 1544.845 nm at room temperature ~ 30 °C) were deployed for online temperature monitoring of ferrite core immersed in transformer oil in high voltage laser power supply (figure 3.20). As the electrical input power to ferrite core is increased its temperature increases. Under steady state full power operation at input electrical power level of 6.3 kW the FBG Bragg wavelength shifted to 1537.315 nm and 1545.737 nm at two locations on ferrite core. The corresponding temperature at these locations was 110.4 °C and 108.6 °C.

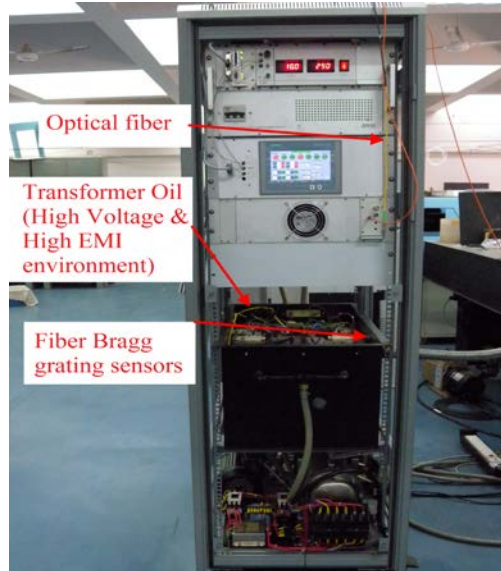


Fig. 3.20: Actual experimental set up for deployment of FBG sensor

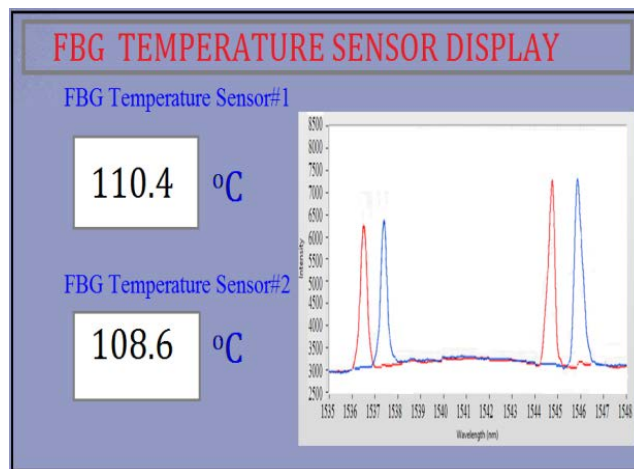


Fig. 3.21: Temperature display captured from the computer screen

The measured temperature of the ferrite core was ~ 50 °C higher than the ambient temperature of the transformer oil (~ 58 °C). Figure 3.21 shows the FBG interrogator traced recorded for the wavelength shift with temperature and the calculated temperature. The FBG sensor proved to be an optimum and effective way to measure temperature in high voltage oil immersed power system, providing accurate and online, fast response.

3.6 Conclusion

This chapter presents the studies on the Bragg wavelength shift with change in temperature and thermal sustainability of FBG reflection in the temperature range 30 °C to 800 °C. Thermal response of Type-I and Type-IIa FBGs has been studied in a multi-step annealing process from 600 °C to 800 °C. Role of fiber core Ge doping on the thermal characteristic of both Type-I and Type-IIa FBG has been carried out. Studies on the role of refractive index rollover fluence on the thermal stability of Type-IIa FBG are discussed. It is demonstrated that Type-IIa FBG can be inscribed at lower fluence in high Ge doped fibers. The refractive index rollover was observed at lower fluence ($\sim 15.84 \text{ kJ/cm}^2$) for high Ge-doped fiber ($\sim 18 \text{ mol } \%$) as compared to higher fluence ($\sim 57.6 \text{ kJ/cm}^2$) for low Ge doped fiber ($\sim 6 \text{ mol } \%$). Analytical studies on the temperature rise during FBG fabrication and its role in temperature sustainability of the FBG has been done. Theoretical analysis on the life time prediction of different FBGs using Erdogan power law approach has been performed. At the end of the chapter an application of the FBG sensor in temperature monitoring of oil immersed components in high voltage power supplies is discussed.

Chapter 4

Studies on thermally regenerated fiber Bragg gratings

4.0 Introduction

The research on the reliable fiber-based temperature sensors capable of operating continuously up to 1000 °C or more is currently a topic that has attracted considerable interest by the sensor community [20, 163, 243-248]. To operate at such high temperatures, FBGs can be inscribed in standard optical fibers with a femtosecond laser [249]. During the fs-laser interaction with the glass fiber, the energy absorption takes place through nonlinear phenomena such as multiphoton, tunneling and avalanche ionization. As long as the absorbed energy is high enough, the catastrophic material damage occurs, which leads to the formation of voidlike structures [171]. Such intensive index modulation of the fiber material ($\sim 10^{-3}$) in fs-laser inscribed FBGs provides high temperature stability. However, the fs written FBGs suffer high insertion loss and complex spectral profile. The other option is to regenerate the FBG by means of a thermal annealing process [166-167, 177-179, 250]. In this case a seed FBG written in H₂ loaded photosensitive fiber is annealed at high temperatures (~ 800 °C to 900 °C). During the annealing process the original FBG is completely or partially erased and a new refractive index modulation is created leading to regenerated FBG. The initial Type-I grating is formed from a UV-induced periodic modulation of OH and local structure that gives rise to periodic variation in the stress at the interface between core and cladding. OH formation in glass is known to exert a dilatatory hydrostatic internal pressure within glass. Therefore in the regions where OH is formed we can expect stress relief in typical fibers where there is tensile stress on the core from the cladding. Consequently, heating to very high temperatures leads to a periodic variation in pressure and therefore stress that is sufficient to seed crystallization in a periodic fashion

probably at the interface. Since the regenerated FBGs are obtained at high temperature (~900 °C) and high internal pressures (~250 MPa) they can withstand temperatures as high as 1295 °C [167, 179, 250]. The high temperature sustainability of the RFBGs obtained from different Ge and Ge-B doped fiber is an important aspect for development of high temperature sensors. In the present chapter, the effect of different parameters on the characteristics of RFBG such as annealing schedule, hydrogenation, doping concentration of fiber core and seed FBG refractive index modulation are presented. The optimization of regenerated FBG reflectivity and its high temperature sustainability is also discussed.

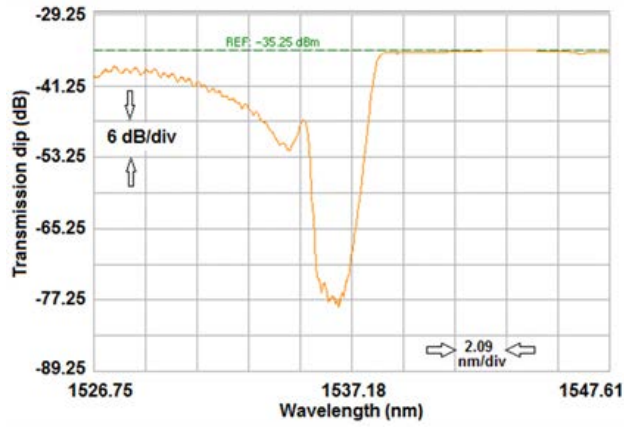
4.1 Effect of annealing schedule on the FBG regeneration

In the thermal regeneration process of FBG, the glass structural transformation arising from stress relaxation between fiber core and clad, at high temperature, leads to formation of crystalline polymorph of silica [240, 250]. This stress relaxation depends on the annealing temperature and duration in a multi-step process [240]. The influence of annealing profiles on the reflectivity of regenerated FBG of two Type-I seed FBGs having same reflectivity, are studied. The seed Type-I FBG has been inscribed in hydrogen loaded SMF-28 fiber using high quality UV beam at 255 nm (5.5 kHz) as described in **Chapter 2**. Both the Type-I FBGs of almost similar reflectivity have been inscribed by keeping the same UV exposure time (60 seconds). The transmission spectrum of one of the final FBG is shown in figure 4.1 (a). Reflectivity of the FBG at different UV fluence is estimated from the transmission dip. The reflectivity of a uniform FBG at resonance wavelength (λ) is given as [73]

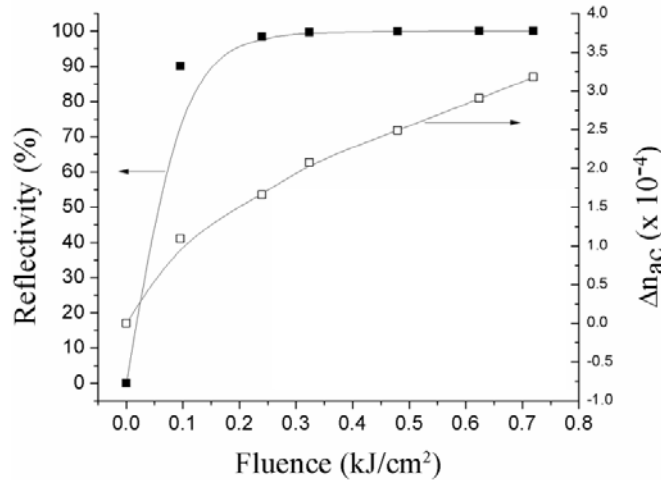
$$R = \tanh^2 \left(\frac{\pi \eta_{mop} \Delta n_{ac} L}{\lambda} \right) \quad (4.1)$$

where Δn_{ac} is refractive index modulation, L is length of the FBG, and η_{mop} is the mode overlap parameter (fraction of the fiber mode power contained in the core). For SMF-28 fiber, the value

of η_{mop} is estimated to be 0.85 using Eq.(2.5). From Eq. (4.1), Δn_{ac} is estimated at cumulative UV fluence for L=10 mm and shown in figure 4.1 (b). The maximum Δn_{ac} of 3.2×10^{-4} is achieved within 60 second of UV exposure. The maximum transmission dip of the 1st gratings and 2nd grating is ~40 dB (reflectivity ~ 99.99 %) and ~42 dB (reflectivity ~ 99.993 %), respectively. Two annealing schedules are followed in the present work. In the first schedule (step annealing schedule), the temperature of 900 °C is raised in four steps with different dwell times as shown in figure 4.2.



(a)



(b)

Fig. 4.1: (a) Transmission spectra of the FBG and (b) reflectivity and Δn_{ac} of FBG written in H_2 loaded SMF-28 fiber

Step I: The temperature is increased from room temperature (30 °C) to 600 °C in ~30 minutes and dwell for 240 minutes (~4 hours).

Step II: The temperature is further raised to 700 °C and dwell for 1020 minutes (~17 hours). In figure 4.2, the x-axis break is applied to show the thermal regeneration clearly. The dwell time at 700 °C kept long enough to see if any regeneration occurs as observed in case of hydrogen loaded high photosensitive fibers [177, 251]. However, no regeneration was observed in the present study.

Step III: The temperature is further increased to 800 °C and dwell for 180 minutes (~3 hours).

Step IV: Finally, the temperature is raised to 900 °C and dwell for ~130 minutes (~2.2 hours).

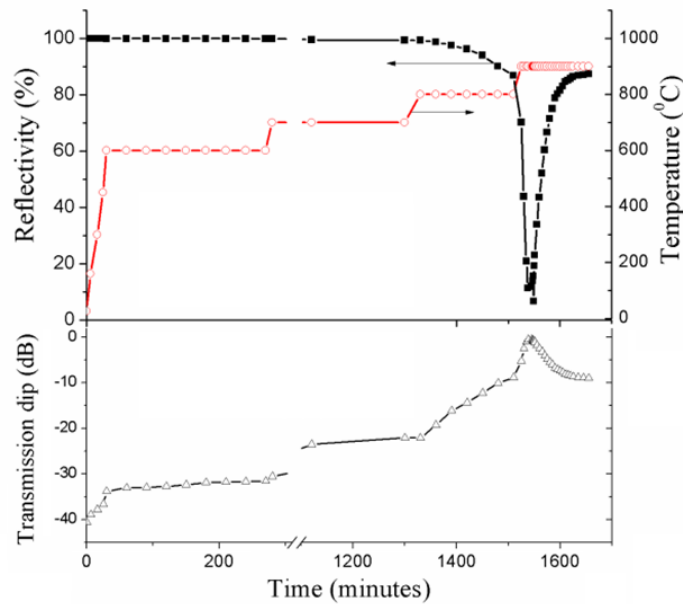
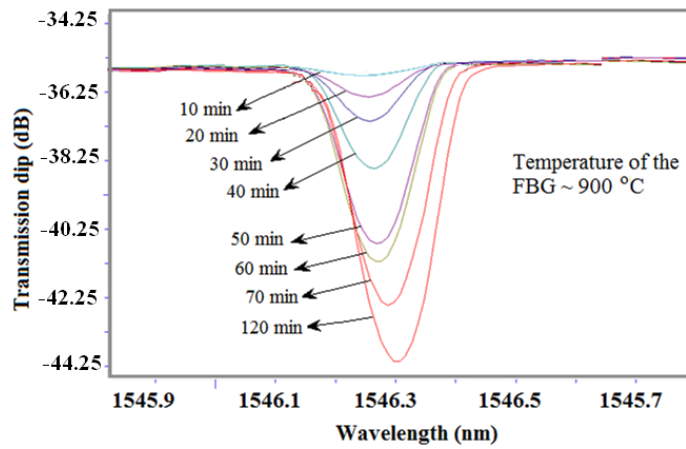


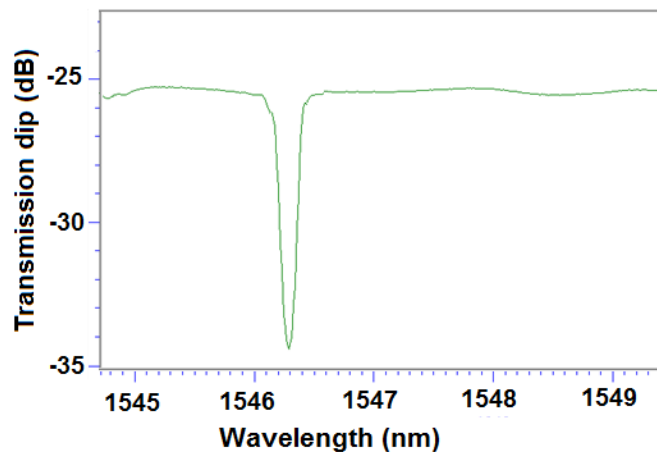
Fig. 4.2: Reflectivity and transmission dip at different time and temperature of a step annealed
FBG

From figure 4.2, it is clear that the transmission dip reduced from ~40.5 dB to ~33.7 dB as temperature increased from 30 °C to 600 °C. However, the reflectivity reduced marginally from ~99.99 % to ~99.95 %. At 600 °C, the reflectivity reduced from 99.95 % (~33.7 dB) to 99.93 % (~31.6 dB) in 240 minutes. As the temperature further increased to 700 °C, the reflectivity

reduced from 99.93 % (~31.6 dB) to 99.3 % (~22.1 dB) in 1020 minutes. At 800 °C, the grating reflectivity reduced from 99.3 % (~22.1 dB) to 86.8 % (~8.8 dB) in 180 minutes. At 900 °C, the grating erased almost completely within 25 minutes and then regeneration started. The maximum reflectivity of regenerated grating ~ 88 % (~ 8.9 dB) is observed in about 130 minutes. Thereafter, the FBG reflectivity remains unchanged. After achieving the maximum regeneration, the FBG was cooled down to the room temperature. Figure 4.3 (a) shows the growth of regenerated FBG with time at 900 °C. The transmission spectrum of final regenerated grating is shown in the inset of figure 4.3 (b).



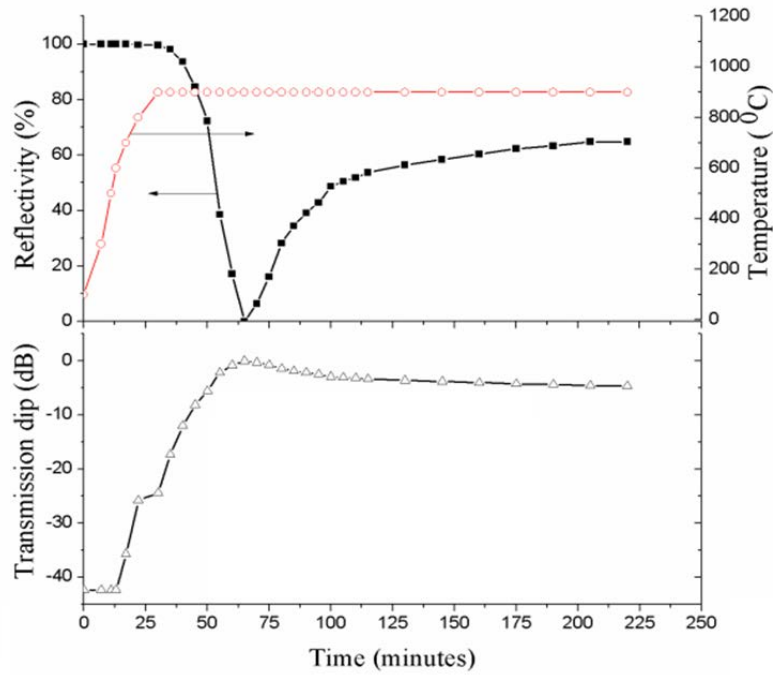
(a)



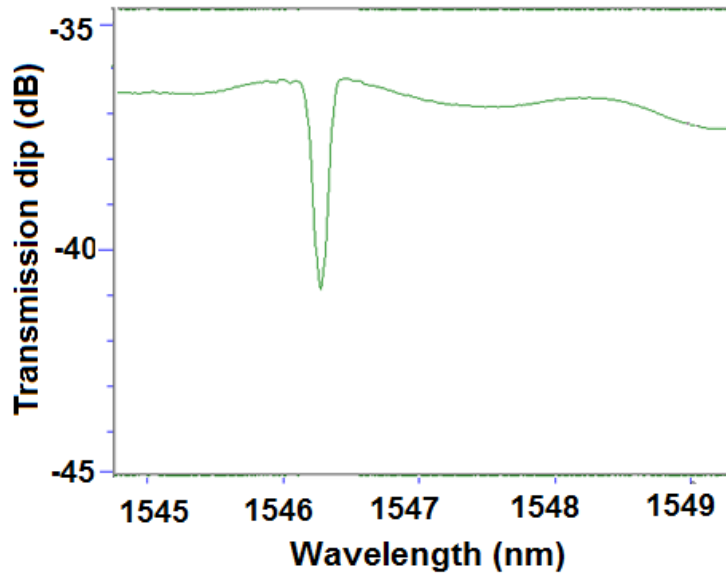
(b)

Fig. 4.3: (a) OSA traces showing growth of RFBG with time at 900 °C and (b) RFBG spectra obtained with step annealing process

In the second schedule (Ramp annealing schedule), FBG is ramp heated directly from room temperature (30 °C) to 900 °C in 30 minutes and then dwell for 180 minutes as shown in figure 4.4 (a).



(a)



(b)

Fig. 4.4: (a) Reflectivity and transmission dip at different time and temperature of ramp annealed FBG and (b) RFBG spectra obtained with ramp annealing process

The FBG reflectivity reduced from 99.993 % (~ 42 dB) to 99.63 % (~24.4 dB) as the temperature increased from room temperature (30 °C) to 900 °C. The FBG erased almost completely in 35 minutes. After seed FBG erasure, the regenerated FBG appeared. The maximum reflectivity of regenerated FBG was about 64.8 % (~4.6 dB). Transmission spectrum of final regenerated FBG is shown in figure 4.4 (b). The strength of step annealed regenerated FBG (~ 88 %) was much higher than the ramp heated regenerated FBG (~ 65 %) although the reflectivity and length of Type-I seed FBGs used in both annealing schedules are same. This higher strength of step annealed regenerated FBG may be attributed to larger stress relief and better transformation of vitreous silica under slow and prolong heating [240]. The observed reflectivity in both annealing schedules (88 % for step annealing and 64.8 % for ramp annealing) is considerably higher than the reported maximum reflectivity of regenerated FBG in H₂ loaded SMF-28 fiber of 35 % obtained in the Type-I seed FBG of reflectivity ~47.5 dB [240].

4.2 Role of core doping concentration on thermal regeneration of FBGs

The thermal regeneration characteristics of four gratings FBG-C1, FBG-C2, FBG-C3 and FBG-C4 (as discussed in **Chapter 2**), with same grating length (~10 mm) and reflectivity (~99.95%) but different core doping concentration, is studied in a multi-step annealing process. The temperature of 900 °C is raised in four steps with different dwell times as discussed earlier in this chapter (figure 4.2). The transmission dip during the whole annealing process is monitored and given in Table 4.1. Figure 4.5 shows the variation in transmission dip/loss of the FBGs with time for the temperature variation from 30°C to 900 °C.

Step I: As the temperature is increased from 30 °C to 600 °C, the transmission dip reduced from 36.42 to 26.84 dB, 35 to 27.42 dB, 32.87 to 30.62 dB and 37.42 to 23.18 dB for FBG-C1, FBG-C2, FBG-C3 and FBG-C4 respectively. At 600 °C, the transmission dip reduced from

26.84 to 23.63 dB, 27.42 to 22.76 dB and 23.18 to 8.18 for FBG-C1, FBG-C2 and FBG-C4 respectively in 240 minutes. But for FBG-C3, the transmission dip first decreased from 30.62 to 25.05 dB within 150 minutes at 600 °C and then started to grow and reaches to 26.17 dB in 90 minutes. During this time the net increase in the transmission loss of 1.12 dB is observed in FBG-C3 at temperature of 600 °C (circle A in figure 4.5).

Table 4.1: Transmission dip during the whole annealing process

T (°C)	Time (min.)	FBG Transmission dip (dB)			
		FBG-C1	FBG-C2	FBG-C3	FBG-C4
30		36.42	35.06	32.87	37.42
30 – 600	30	26.84	27.42	30.62	23.18
600	240	23.63	22.76	25.05(150 min) 26.17 (90 min)	8.18
600 – 700	10	22.63	22.42	25.7	6.17
700	1020	19.58 (90 min) 21.15 (60 min) 17.65 (870 min)	22.42 (start) 22.92 (90 min) 12.65 (930 min)	1.10 (620 min) 7.30 (400 min)	0.04 (60 min) 1.80 (960 min)
700 – 800	20	17.50	12.65	7.89	1.90
800	180	7.99	1.48	9.31	1.96
900	130	0.24 (30 min) 9.03 (100 min)	0.24 (30 min) 5.49 (100 min)	5.50	1.90
30		7.06	5.49	5.50	1.90
1000	240	3.51	3.31	3.87	1.12
1100	240	2.45	3.01	0.64	0.15

Step II: As the temperature of the oven is further raised to 700 °C, the transmission dip for all FBGs reduces. It decreased to 22.63 dB, 22.42 dB, 25.7 dB and 6.17 dB for FBG-C1, FBG-C2, FBG-C3 and FBG-C4 respectively. For FBG-C1 at 700 °C, the transmission loss first reduces from 22.63 dB to 19.58 dB in ~90 minutes, then increases to 21.15 dB in next 60 minutes. Thereafter it decreases again and reaches to 17.65 dB in next 870 minutes. Similarly for FBG-C2, the transmission dip starts to increase from 22.42 to 22.92 dB in about 90 minutes thereafter it decreases and reaches to 12.65 dB in ~930 minutes. So the thermal regeneration is observed in FBG-C1 and FBG-C2 at 700 °C (circle A in figure 4.5). The strength of this regeneration was 1.57 dB and 0.50 dB for FBG-C1 and FBG-C2 respectively. However for FBG-C3 at 700 °C, the transmission dip reduced from 25.17 dB to 1.1 dB in 620 minutes. Thereafter the Bragg peak starts to increase (circle C in figure 4.5) and reaches 7.3 dB in next 400 minutes at 700 °C. For FBG-C4 the transmission dip reduced from 6.17 dB to 0.04 dB in ~60 minutes and thereafter increases to 1.8 dB in next 960 minutes at 700 °C (as shown by circle D in figure 4.5).

Step III: The temperature of oven is raised further to 800 °C. For FBG-C1 and FBG-C2, the grating transmission dip reduced from 17.65 to 7.99 dB and 12.65 to 1.48 dB respectively in 180 minutes. In case of FBG-C3 and FBG-C4 the transmission dip increases from 7.89 to 9.31 dB and 1.90 to 1.96 dB at 800 °C. Therefore for FBG-C3 and FBG-C4, the thermal regeneration is observed at 800 °C although the seed grating did not decay completely.

Step IV: The temperature of the oven is further raised to 900 °C. FBG-C1 and FBG-C2 erased almost completely within 30 minutes and then a new grating started to grow. The transmission dip of regenerated grating increased to 9.03 dB and 5.49 dB for FBG-C1 and FBG-C2 within 130 minutes and became almost constant (marked by circle B in figure 4.5). For FBG-C3 and

FBG-C4, no such increase in transmission dip was observed at 900 °C. After 130 minutes at 900 °C, the transmission dip reduced to 5.5 dB for FBG-C3. However for FBG-C4, the transmission dip remains almost constant at 1.9 dB. The temperature of oven reduced to room temperature at 30 °C. The reflectivity is calculated from the transmission dip using Eq.(2.2).

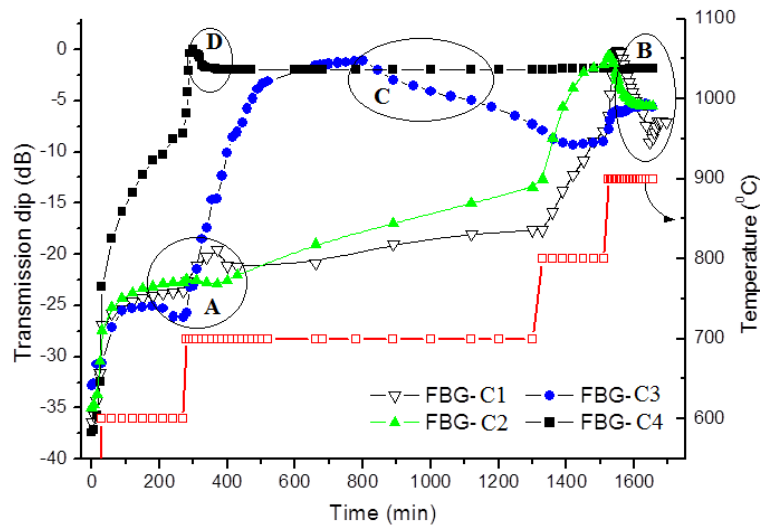


Fig. 4.5: Thermal annealing studies of FBGs (transmission dip) up to temperature of 900 °C

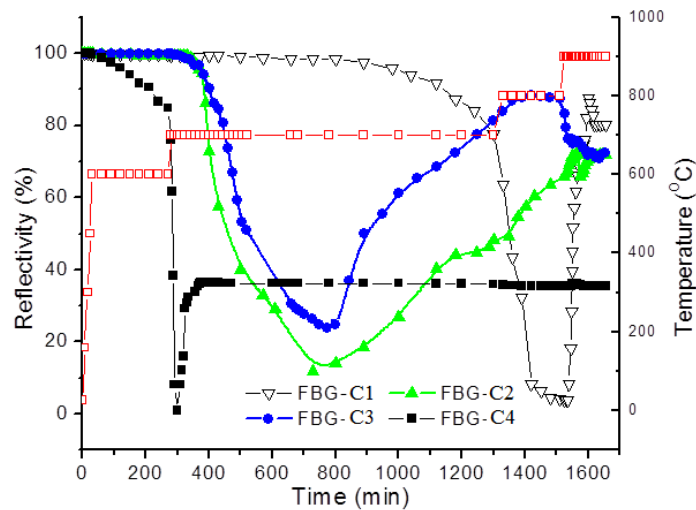


Fig. 4.6: Thermal annealing studies of FBGs (reflectivity) up to temperature of 900 °C

Figure 4.6 shows the change in the reflectivity for all the FBGs with applied step annealing profile. In this figure only second regeneration is clearly visible as the value of first thermal regeneration is very low in terms of reflectivity. The FBG reflectivity after this part of

annealing was 80.14%, 71.75%, 72.39% and 35.43% for FBG-C1, FBG-C2, FBG-C3 and FBG-C4 respectively. Bragg wavelength is also recorded for all the FBGs during entire annealing process. The final thermal regeneration was blue shifted for FBG-C1, C2 and C3 whereas it was red shifted for FBG-C4. At the time of final thermal regeneration, the Bragg wavelength shifted from 1546.048 nm to 1545.928 nm, 1547.886 nm to 1547.681 nm, 1556.671 nm to 1556.621 nm and 1543.463 nm to 1543.513 nm for FBG-C1, FBG-C2, FBG-C3 and FBG-C4 respectively. The final thermal regeneration temperature was at 900 °C for FBG-C1 and C2 and 700 °C for FBG-C3 and C4. From figure 4.5, it is clear that the regeneration temperature for FBGs depend on the Ge doping in the core of fiber. For FBG written in high Ge doped fiber the first regeneration of the grating started at lower temperature (600 °C) and second regeneration was observed at 700 and 800 °C. For FBG written in low Ge doped fibers (FBG-C1 and C2) the first regeneration started at 700 °C and second regeneration observed at 900 °C.

4.3 Role of seed grating reflectivity on thermal regeneration of FBGs

To study the effect of seed FBGs strength on the thermal regeneration characteristics, four FBGs of the same length ($L \sim 10$ mm) and different transmission dip $T_d = 3.5$ dB ($R = 55.31\%$), 7.2 dB ($R = 80.94\%$), 24.02 dB ($R = 99.61\%$) and 32.87 dB ($R = 99.95\%$) are written in the same fiber (hydrogen loaded SM-1500) by controlling the UV exposure time. Henceforth for discussion, we will refer these FBGs as FBG-R1, FBG-R2, FBG-R3 and FBG-R4 respectively. Figure 4.7 shows the variation in reflectivity and refractive index modulation (Δn_{ac}) with UV fluence during FBG inscription. The refractive index modulation (Δn_{ac}) is estimated from the percentage reflectivity, Bragg wavelength, grating length, overlap factor and effective refractive index using Eq. (2.3). Figure 4.7 shows that the Δn_{ac} increases with the fluence and reached to a

maximum value of 2.69×10^{-4} at the cumulative fluence of 0.84 kJ/cm^2 . Temperature stability of these FBGs is studied in a multi-step process from 30°C to 900°C as discussed previously. The variation in transmission dips with time at various temperatures for FBG-R1, FBG-R2, FBG-R3 and FBG-R4 is shown in figure 4.8 (a). The final transmission dip at a particular temperature for all FBGs is also listed in table 4.2.

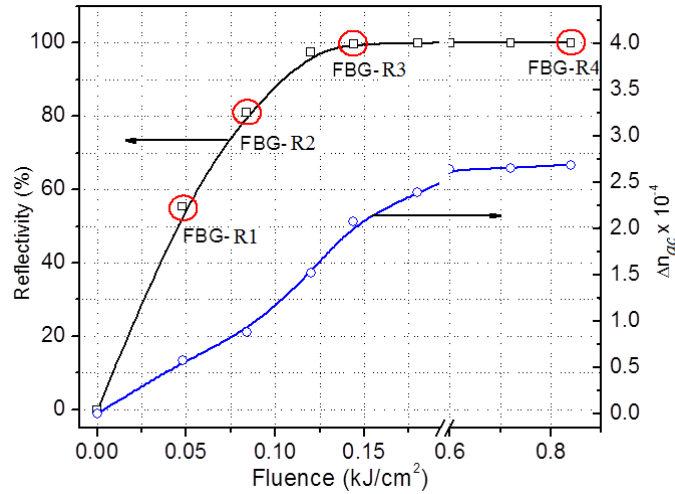
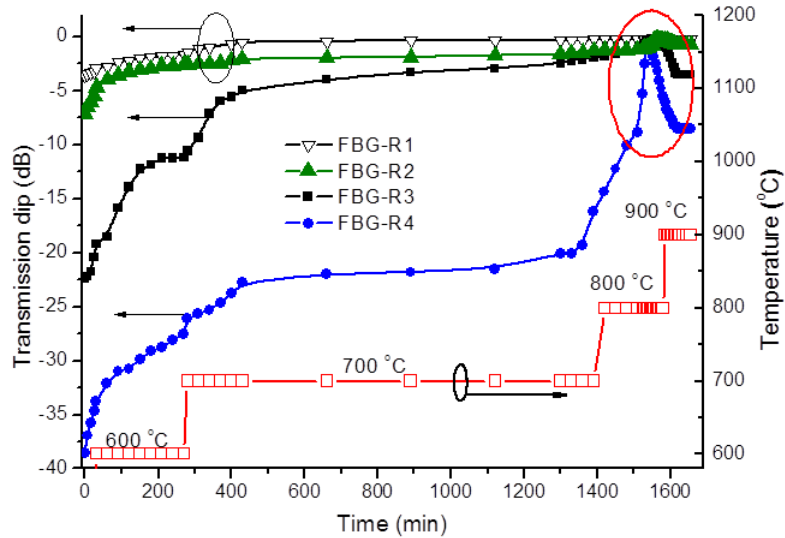


Fig. 4.7: Variation in FBG reflectivity and refractive index modulation with UV fluence

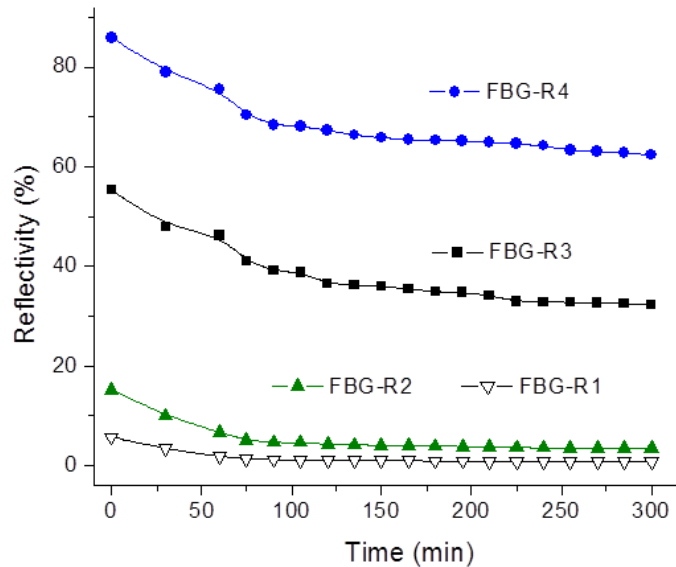
Table 4.2: Transmission dip during the whole annealing process

T ($^\circ\text{C}$)	Dwell Time (min.)	FBG Transmission dip (dB)			
		FBG-R1	FBG-R2	FBG-R3	FBG-R4
30		3.52	7.12	22.42	34.56
600	0	2.81	3.95	18.51	32.07
	240	1.63	2.58	11.20	27.56
700	0	1.43	2.54	10.59	26.06
	1020	0.17	0.21	0.25	0.52
800	0	0.16	0.23	0.29	1.14
	180	0.21	0.29	0.79	5.46
900	0	0.22	0.32	0.89	6.03
	110	0.26	0.72	3.52	8.50

It is clear that the thermal regeneration is observed in all FBGs in the temperature range of 800 – 900 °C. Strength of the thermal regeneration was $T_d \sim 0.10$ dB ($R \sim 2.28$ %), $T_d \sim 0.51$ dB ($R \sim 11.08$ %), $T_d \sim 3.30$ dB ($R \sim 53.22$ %) and $T_d \sim 8.50$ dB ($R \sim 85.87$ %) for FBG-R1, FBG-R2, FBG-R3 and FBG-R4 respectively. Thus, for same grating length and applied annealing schedule, the reflectivity of RFBGs depends on the reflectivity of seed FBGs.



(a)



(b)

Fig. 4.8: (a) FBG transmission dip with time at different temperature (600 °C to 900 °C) and (b) FBG reflectivity with time at 1000 °C

Figure 4.9 shows the variation in transmission dip of the RFBG with that of seed FBG. Exponential growing fit is applied to the experimental data points.

$$T_{RFBG} = 28.11 \times 10^{-2} \exp[0.1038 T_{SFBG}] \quad (4.2)$$

where T_{RFBG} and T_{SFBG} are the transmission dip of the RFBG and seed FBG respectively.

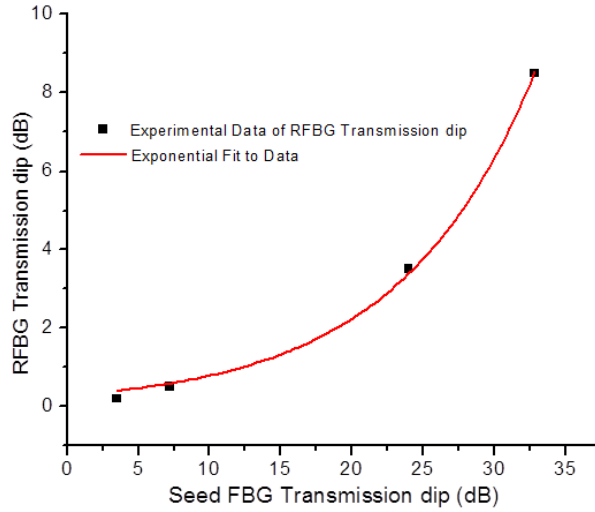


Fig. 4.9: Variation of transmission dip of RFBG with seed FBG

The RFBG reflectivity increased non-linearly with the seed FBG strength. This may be due to higher stress relaxation during annealing process for the seed FBG of high reflectivity (FBG-R4). Since the developed stress in the FBG will be higher for high reflectivity seed FBGs. For actual operation in high temperature sensors, the studies on the life time prediction for all FBGs were also carried out by raising the temperature of all RFBGs to 1000 °C and dwelling for ~4 hours as shown in figure 4.8 (b). As the temperature of RFBG is raised to 1000 °C (in ~ 60 minutes), the reflectivity of the RFBG (as estimated from the transmission dip, T_d) were $R \sim 1.83 \%$, $R \sim 6.67 \%$, $R \sim 46.29 \%$ and $R \sim 75.45 \%$ for FBG-R1, FBG-R2, FBG-R3 and FBG-R4, respectively. After dwelling of about 4 hours at 1000 °C, the RFBG reflectivity reduces to $R \sim 0.62 \%$, 3.51% , 31.52% and 62.23% for FBG-R1, FBG-R2, FBG-R3 and FBG-R4 respectively. The observed thermal degradation of the FBG with time at a fix temperature can be analyzed by calculating

normalized integrated coupling coefficient (NICC) η as discussed in Eq. (3.1) and (3.2). NICC calculated from both the equations is plotted as a function of time at 1000 °C for all the RFBGs and shown in figure 4.10. The power law factor and decay coefficients are estimated by fitting the power law (Eq. 3.2) to the experimental data. The values of A_p and α are 0.052 & 0.4, 0.05 & 0.38, 0.04 & 0.36 and 0.037 & 0.35 for FBG-R1, R2, R3 and R4 respectively. From Eq. (3.1) and (3.2), the reflectivity of the FBG at any temperature T after time t can be written as,

$$R_{t,T} = \tanh^2 \left[\frac{\tanh^{-1} \sqrt{R_{0,T_0}}}{1 + A_p t^\alpha} \right] \quad (4.3)$$

Reflectivity decay at any temperature is shown in figure 4.11. It is clear from the figure that at 1000 °C, the residual reflectivity of FBG-R4 is higher than the reflectivity of others FBGs.

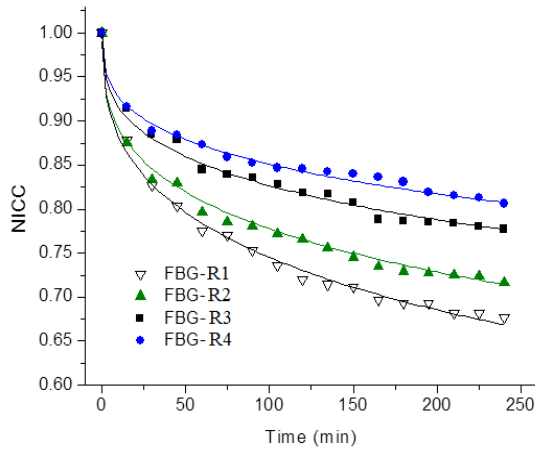


Fig. 4.10: Variation of NICC (η) with time at 1000 °C for all FBGs

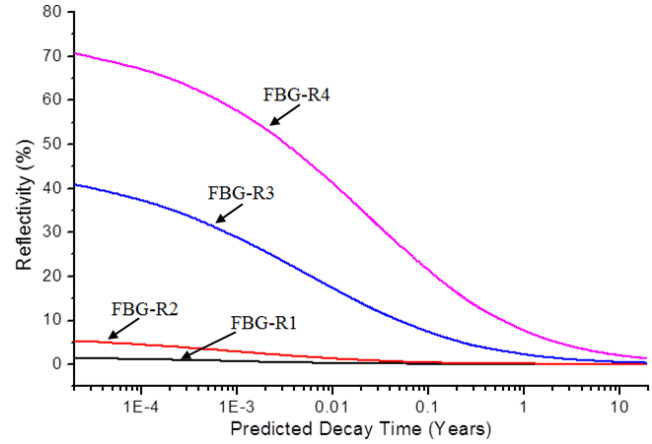


Fig. 4.11: Predicted decay time at 1000 °C for all RFBGs

Using Eq. (3.8), for the remaining NICC value of $\eta \sim 0.1$, the predicted life time of the FBGs at 1000 °C were $t \sim 0.75, 1.64, 6.50$ and 12.4 year for FBG-R1, FBG-R2, FBG-R3 and FBG-R4 respectively. The structural transformation in case of FBG-R4 will be higher due to higher stress relaxation which will lead to higher life time of the FBG. These studies will be useful for the development of high temperature sensors.

4.4 Role of seed grating length on thermal regeneration of FBGs

Three FBGs of almost same reflectivity ($R \sim 99.9\%$) and different length ($L = 4$ mm, 7 mm and 15 mm) are inscribed in similar fiber (hydrogen loaded Birla-Furukawa) by controlling the UV exposure time. Henceforth for discussion we will refer these FBGs as FBG-L1, FBG-L2 and FBG-L3 respectively. The transmission dip of the FBG-L1, FBG-L2 and FBG-L3 was 33.06 dB, 32.05 dB and 32.67 dB respectively. The UV exposure time to achieve almost same reflectivity was 120 s, 60 s and 45 s for FBG-L1, FBG-L2 and FBG-L3 respectively.

Table 4.3: Parameters of seed FBGs of different length

FBG	FBG-L1	FBG-L2	FBG-L3
Inscription time	120 s	60 s	45 s
UV Fluence (kJ/cm^2)	1.44	0.72	0.54
FBG Length	4 mm	7 mm	15 mm
Transmission Dip (T_d)	33.06 dB	32.05 dB	32.67 dB
Reflectivity (R)	99.95%	99.94%	99.95%
Bragg wavelength (nm)	1537.277	1535.414	1534.67
Refractive index Modulation (Δn_{ac})	6.48×10^{-4}	3.60×10^{-4}	1.71×10^{-4}

Table 4.3 lists the values of maximum refractive index modulation for all FBGs. Depending upon the Bragg wavelength, grating length and reflectivity, the refractive index modulation for seed gratings FBG-L1, FBG-L2 and FBG-L3 is 6.48×10^{-4} , 3.60×10^{-4} and 1.71×10^{-4} respectively. As discussed earlier, four steps thermal annealing schedule from 30°C to 900 °C is applied for thermal characterization and regeneration of the FBG. The variation in FBG reflectivity with time at various temperatures for FBG-L1, FBG-L2 and FBG-L3 is shown in figure 4.12. It is clear from figure 4.12 that the thermal regeneration is observed in all FBGs in the temperature range of 800-900 °C. Strength of the thermal regeneration is $T_d \sim 0.81$ dB ($R \sim 17.01\%$), $T_d \sim 1.24$ dB ($R \sim 24.84\%$) and $T_d \sim 1.59$ dB ($R \sim 30.66\%$) for FBG-L1, FBG-L2 and

FBG-L3 respectively. The final transmission loss (reflectivity) at a particular temperature for all FBGs is listed in Table 4.4. The value of refractive index modulation (Δn_{ac}) of regenerated FBG-L1, L2 and L3 is 0.63×10^{-4} , 0.45×10^{-4} and 0.24×10^{-4} respectively.

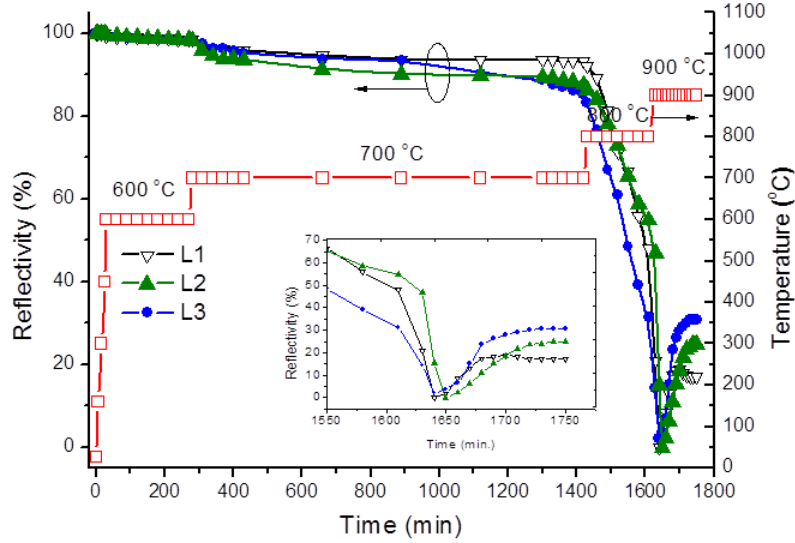


Fig. 4.12: Change in FBG reflectivity with time at different temperature

Table 4.4: Variation of transmission dip during the whole annealing process

T (°C)	Dwell Time (min.)	FBG Transmission dip (dB)		
		FBG-L1	FBG-L2	FBG-L3
30		33.06 dB (99.95%)	32.05 dB (99.94%)	32.67 dB (99.95%)
600	0	22.15 dB (99.39%)	23.44 dB (99.55%)	22.99 dB (99.51%)
	240	18.18 dB (99.48%)	18.11 dB (99.45%)	18.23 dB (98.50%)
700	0	17.81 dB (98.34%)	17.37 dB (98.17%)	18.06 dB (98.44%)
	1140	11.62 dB (93.11%)	9.07 dB (87.61%)	8.28 dB (85.14%)
800	0	11.01 dB (92.06%)	8.61 dB (86.20%)	7.82 dB (83.37%)
	180	2.84 dB (48.01%)	3.45 dB (54.81%)	1.63 dB (31.29%)
900	0	1.02 dB (20.93%)	2.75 dB (46.91%)	0.67 dB (14.31%)
		0.00 dB	0.00 dB	0.00 dB
	110	0.81 dB (17.01%)	1.24 dB (24.84%)	1.59 dB (30.66%)

Table 4.5: Parameters of regenerated FBGs of different length

Regenerated FBG	FBG-L1	FBG-L2	FBG-L3
FBG Length	4 mm	7 mm	15 mm
Transmission Dip (T_d)	0.81 dB	1.24 dB	1.59 dB
Reflectivity (R)	17.01%	24.84%	30.66%
Refractive index Modulation (Δn_{ac})	0.63×10^{-4}	0.45×10^{-4}	0.24×10^{-4}

Thus, for same grating strength and applied annealing schedule, the refractive index modulation of RFBGs depends on the refractive index modulation of seed FBG (figure 4.13). Figure 4.14 and table 4.5 shows the variation in Δn_{ac} for seed and regenerated FBG with seed FBG length. It is clear that for same reflectivity FBGs, Δn_{ac} decreases with increase in grating length for seed as well as regenerated FBG.

$$\Delta n_{ac} \propto 1/L$$

Δn_{ac} for RFBG scales up with the Δn_{ac} of seed FBG which may be due to higher stress relaxation during annealing process. Since the developed stress in FBG is higher for higher RI modulation FBG.

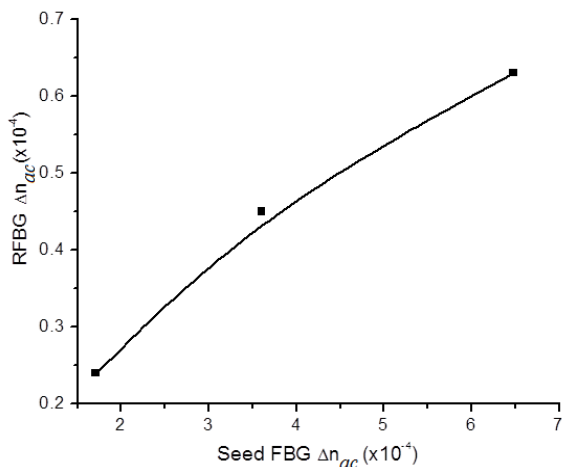


Fig. 4.13: Variation of Δn_{ac} of regenerated FBG with Δn_{ac} of seed FBG

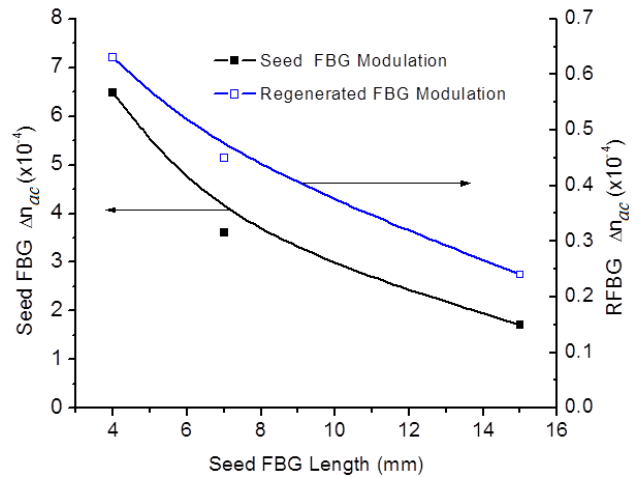


Fig. 4.14: Variation of Δn_{ac} of regenerated and seed FBG with in seed FBG length

4.5 Current status on FBG thermal regeneration vis-à-vis our results

Table 4.6 summarizes the prominent high reflectivity results on regenerated fiber Bragg gratings (RFBGs) as reported in literature including our results. It is very clear from table that our observed reflectivity of ~ 88 % of RFBG in SMF-28 fiber is one of the highest reported values in the field including both SMF-28 fiber as well as other high photosensitive fibers. Usually the reported RFBGs reflectivity is in the range of 2 % to 60 % for grating length of 3-10 mm. In one special case with 120 dB seed grating written with CW Ar⁺ source of 50 mm length, the RFBG reflectivity is ~99.999 %. The observed higher reflectivity of our RFBG may be explained as follows. It is well understood that the thermal regeneration involves the process of axial stress relief [221-225]. For strong seed grating (Type-I, formed by depletion of ODCs), the stress between high and low UV intensity exposed region at the core and cladding interface, will be high. This stress pattern will depend on the contrast of the UV beam interference fringes. Higher the UV fringe contrast, higher will be the stress. High beam quality 255 nm beam is generated using specialized resonator scheme to copper vapour laser (CVL) [132]. This high quality UV beam produces a very stable interference pattern. It imprints a very clean seed grating in fiber core with high differential stress between high intensity and low intensity exposed region. This results into high stress in seed grating. Also, it was demonstrated that the properties introduced by the seed grating are retained within nm resolution during the thermal annealing process [240, 250]. Also exposing fiber to high repetition rate (5.5 kHz) UV beam, both the in-situ UV and thermal sensitization due to partially coherent UV radiation and cumulative UV absorption, respectively, may also be operative.

Table 4.6: Results on high reflectivity RFBG reported in different types of fibers and strength of seed Type-I FBG

Reference	Type of fiber and writing source	loading	Seed FBG reflectivity/trans. dip	Seed FBG length	RFBG Reflectivity
L. Polz <i>et al.</i> 2014. Ref [251]	High photosensitive GF1B fiber, SMF-28, 248 nm	With H ₂ Without H ₂ With H ₂	R~ 70 % R~ 65 % Not known	3 mm	R ~ 2.3 % No-RFBG R ~ 2.3 %
K. Cook <i>et al.</i> 2012. Ref [235]	B-Ge doped fiber [B-20 mol.%, Ge-11 mol. %], 193 nm	Without H ₂ Without He With He (post-load) With H ₂ (pre-load)	T _d ~50 dB T _d ~50 dB T _d ~50 dB T _d ~120 dB	10 mm	No-RFBG No-RFBG R~ 2 % R~ 30 %
E. Lindner <i>et al.</i> 2011. Ref [177]	High photosensitive fiber [Ge~18 mol. %], 248 nm	Without H ₂	T _d ~ 21 dB	5 mm	R~ 60 %
S. Bandyopa dhyay <i>et al.</i> 2011. Ref [240]	SMF-28 [Ge~3 mol. %], NM-113 [Ge~10mol. %], UVS-EPS[Ge~20mol.%], NM-41 [Ge~10 mol. %], 248 nm	With H ₂ With H ₂ With H ₂ With H ₂	T _d ~47.4 dB T _d ~47.5 dB T _d ~ 21 dB T _d ~ 21 dB	5 mm	R~ 35 % R~ 21 % R~ 18 % R~ 15 %
J. Canning <i>et al.</i> 2009 ref [250]	High photosensitive fiber [Ge~33 mol. %, B~10 mol. %], CW 244 nm	With H ₂	T _d >120 dB	50 mm	R~99.999 %
Our results	SMF-28 [Ge~3 mol. %], 255 nm	With H ₂	T _d ~42 dB	10 mm	R~ 88 %

4.6 Thermal regeneration studies of FBG in non-hydrogenated fiber

The thermal annealing and regeneration characteristics of FBG written in non-hydrogen loaded photosensitive fibers FBG-A1, FBG-A2 and FBG-A3 have been studied and presented in previous **Chapter 3**. The initial reflectivity of FBG-A1, FBG-A2 and FBG-A3 are 99.7 % (~ 26 dB), 99.6 % (~ 24.7 dB) and 96.9 % (~ 15.2 dB), respectively. For the sake of comparison, the variation of transmission dip with time at different temperature for FBG-A1 (solid rectangle), FBG-A2 (solid triangle) and FBG-A3 (solid circle) are shown in figure 4.15. The strength of the FBG written in non-hydrogen loaded SMF-28 fiber was very weak (~ 0.3 dB) so the thermal annealing characteristics for this grating could not be performed.

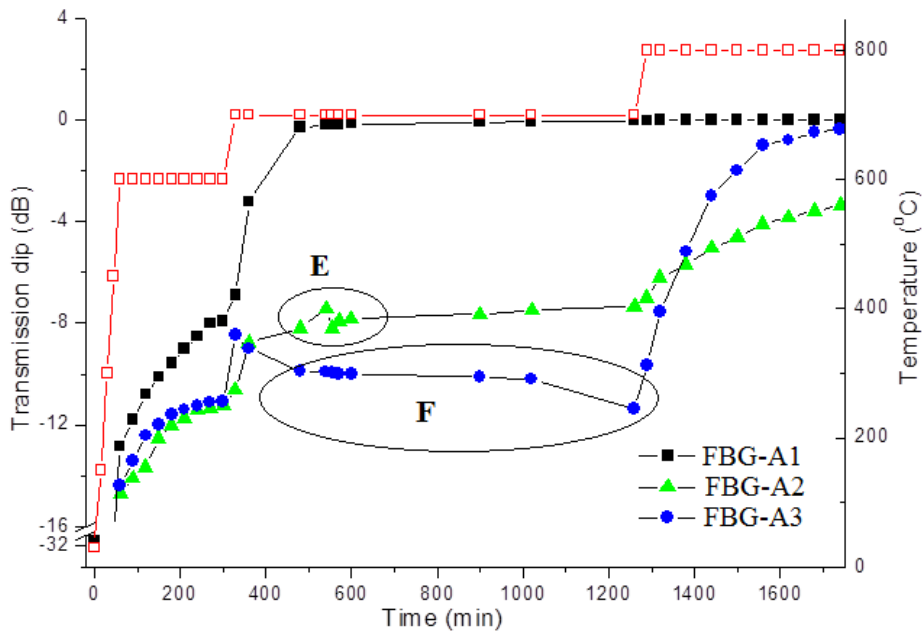


Fig. 4.15: Thermal regeneration studies in non-hydrogenated fiber

For FBG-A2 written in non-hydrogenated fiber, the thermal regeneration was observed at 700 °C. There was an increase in transmission loss from 7.43 to 8.19 dB (marked circle E in figure 4.15). However for FBG-A3, the increase in transmission loss was from 8.47 to 11.37 dB (marked circle F in figure 4.15). So FBG-A2 and A3 show a sign of regeneration at

temperature 700 °C. However for FBG-A1 written in B-Ge co-doped fiber, there was no such thermal regeneration observed at 700 °C. It is worth mentioning that for non-hydrogen loaded Ge doped fiber, thermal regeneration was stronger for grating having higher Ge concentration whereas with hydrogen loaded fiber, it is higher for lower Ge-doping [240]. The maximum regeneration observed for non-hydrogenated fiber was 2.9 dB (FBG-A3) whereas for hydrogenated fiber the maximum regeneration was 8.8 dB (FBG-C1). Therefore, the hydrogen played an important role in deciding the thermal regeneration strength. In case of FBG written in non-hydrogenated Ge-B doped fiber (FBG-A1) no thermal regeneration was observed whereas for hydrogenated fiber, the regeneration (FBG-C4) occurred at 700 °C. Thus it is clear that the temperature sustainability of regenerated grating obtained from seed grating written in hydrogen loaded fiber is enhanced as compared to seed grating written in non-hydrogenated Ge doped fiber. The observed thermal regeneration for both hydrogenated and non-hydrogenated fiber is given in table 4.7.

Table 4.7: Observed thermal regeneration for hydrogenated and non-hydrogenated fiber

Fiber	Core doping	Thermal Regeneration of FBG (dB)	
		First	Second
FBG-C1(H ₂)	Ge (3%)	1.57 (at 700 °C)	8.8 (at 900 °C)
FBG-A2	Ge (10%)	0.10 (at 700 °C)	-
FBG-C2 (H ₂)	Ge (10%)	0.50 (at 700 °C)	5.25 (at 900 °C)
FBG-A3	Ge (18%)	2.90 (at 700 °C)	-
FBG-C3 (H ₂)	Ge (18%)	1.12 (at 600 °C)	8.21 (at 700-800 °C)
FBG-A1	Ge (8%) B (6%)	-	-
FBG-C4 (H ₂)	Ge (8%) B (6%)	1.80 (at 700 °C)	-

4.7 Studies on thermal stability of regenerated FBGs

The long term temperature stability studies of RFBG at 1100 °C has not been paid due attention in the reported literature. The temperature of the heat oven is increased from room temperature (30 °C) to 1000 °C in 60 minutes and dwell for 240 minutes. Figure 4.16 shows the transmission spectra of FBG-C1 at different temperature. Figure 4.17 shows the variation of transmission dip of regenerated grating with time at different temperature.

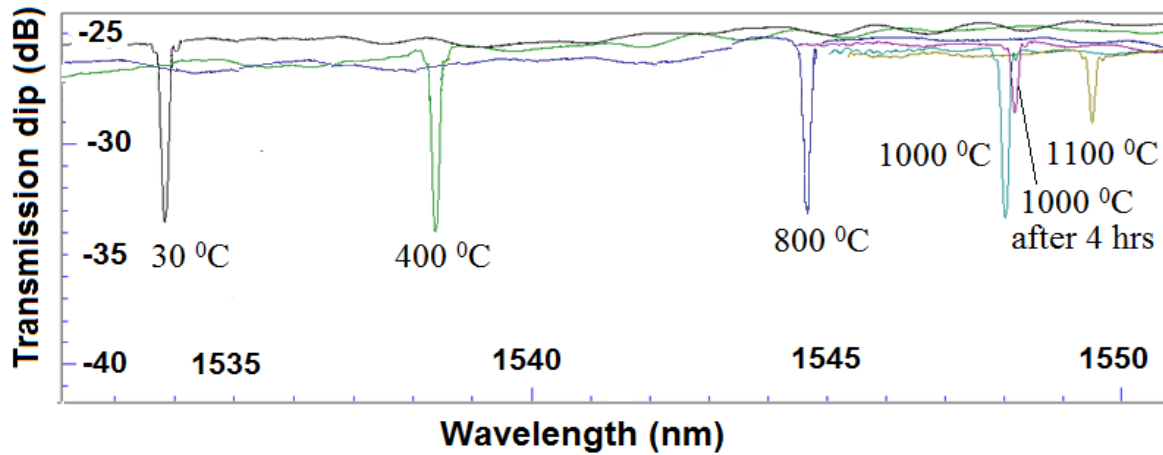


Fig. 4.16: Transmission spectra at different temperature and time for RFBG

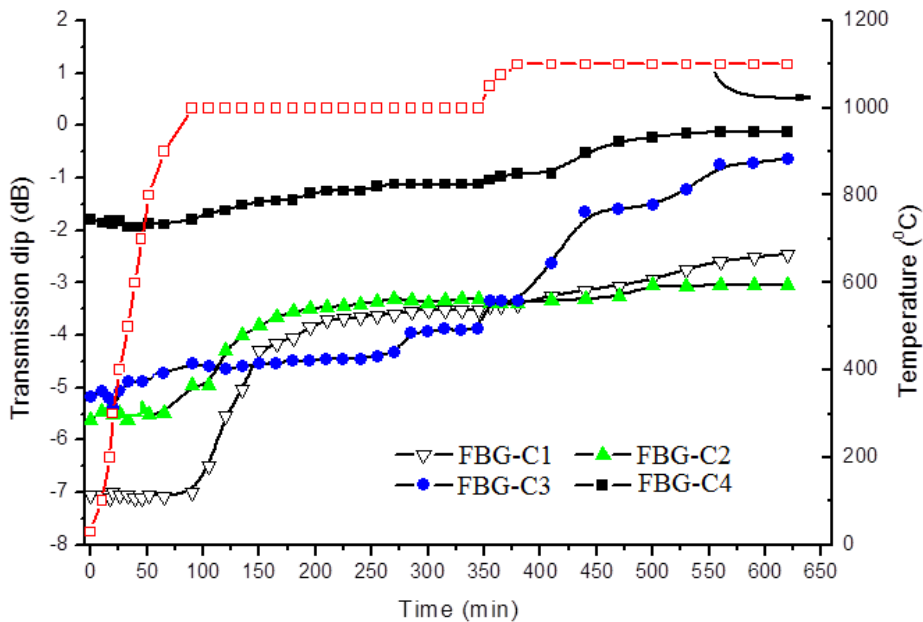


Fig. 4.17: Thermal annealing studies up to temperature of 1100 °C

The transmission dip after 240 minutes at 1000 °C was 3.51 dB (55.43 %), 3.31 dB (53.33 %), 3.87 dB (58.98 %) and 1.12 dB (22.73 %) for FBG-C1, FBG-C2, FBG-C3 and FBG-C4, respectively. Then, the temperature is further raised to 1100 °C and dwell for 240 minutes (~ 4 hours). After 4 hours annealing at 1100 °C, the transmission dip was 2.45 dB (43.11 %), 3.01 dB (50.22 %), 0.64 dB (13.7 %) and 0.15 dB (3.39 %) for FBG-C1, FBG-C2, FBG-C3 and FBG-C4 respectively. The thermal stability of all the post annealed and thermally regenerated gratings was recorded at a temperature of 1100 °C for longer times (~10 hours) as shown in figure 4.18.

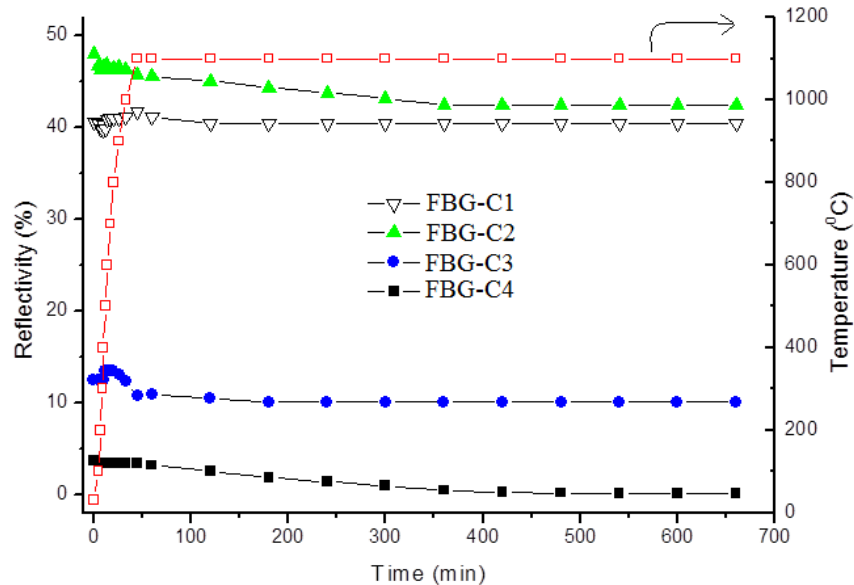


Fig. 4.18: Thermal response of post annealed RFBG

It is clear from the figure 4.18 that the FBG written in Ge-B doped fiber (FBG-C4) decayed at 1100 °C but the reflectivity of the FBG written in Ge doped fiber initially decreased and became almost constant at this temperature. The final constant reflectivity (residual reflectivity) of the gratings was 40.43 %, 42.56 %, 10.05 % and 0.11 % for FBG-C1, FBG-C2, FBG-C3 and FBG-C4 respectively. The Bragg wavelength of the pre annealed FBG and post annealed FBG at room temperature (30 °C) was also recorded. The FBG wavelength shifted

from 1536.220 nm to 1533.522 nm, 1538.231 nm to 1535.266 nm, 1548.144 to 1546.101 nm and 1536.263 nm to 1534.915 nm for FBG-C1, FBG-C2, FBG-C3 and FBG-C4 respectively from pre to post annealed FBG at room temperature. Figure 4.19 shows the residual reflectivity and shift in wavelength from pre to post annealing for all the FBGs.

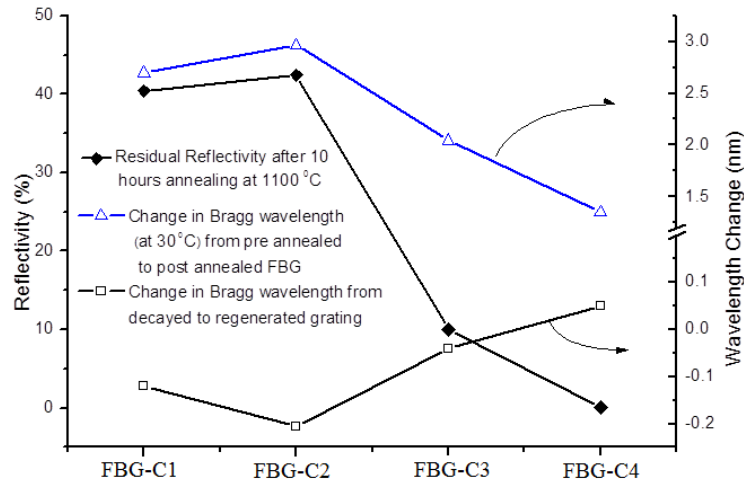


Fig. 4.19: Residual reflectivity and change in Bragg wavelength from pre to post annealed and from decayed to regenerated FBG

It is clear from the figure 4.19 that the trends of both the plots are almost same. For FBG-C1 and FBG-C2 the wavelength shift and the residual reflectivity both are higher and for FBG-C3 and FBG-C4 the wavelength shift and the residual reflectivity both are lower. It gives indication that for FBG-C1 and FBG-C2 the structural modification is higher as compared to FBG-C3 and C4. The structural transformation can be confirmed from the change in Bragg wavelength at thermal regeneration temperature. The Bragg wavelength shift ($\Delta\lambda_B$) between the thermally regenerated grating and the original decayed grating is -120 pm, -200 pm, -50 pm and +50 pm for FBG-C1, FBG-C2, FBG-C3 and FBG-C4 respectively as shown in figure 4.19. So according to Eq. (2.4), the change in dc refractive index will also be higher for FBG-C2 as compared to other FBGs. Higher change in dc index for FBG-C2 gives an indication of

higher structural modification. The higher structural modification may be responsible for higher residual reflectivity of the grating in case of FBG-C1 and FBG-C2. It is also clear from the figure 4.19 that there is certain Ge concentration for which the residual reflectivity is higher (FBG-C2). Although the residual reflectivity decreases with increase in Ge concentration but at minimum value of Ge doping (~3 mol %) the residual reflectivity is not the maximum. So in addition to hydrogen, Ge also plays important role in thermal regeneration and hence the thermal stability of the grating. Boron is detrimental for grating sustainability at higher temperature due to fact that B_2O_3 reduce stresses in germanosilicate fiber at elevated temperature. The single point FBG temperature sensors (1000 °C) are developed by encapsulating the FBGs in ceramic tubes. Figure 4.20 shows the typical OSA traces with applied temperature (upto 1100 °C) for post annealed FBG-C1. The reflectivity of the FBG is almost same for all temperature starting from room temperature to 1100 °C. Temperature of the FBG was estimated from the Bragg wavelength shift using Eq. (5.8) which will be discussed in next chapter of the thesis (**Chapter 5**).

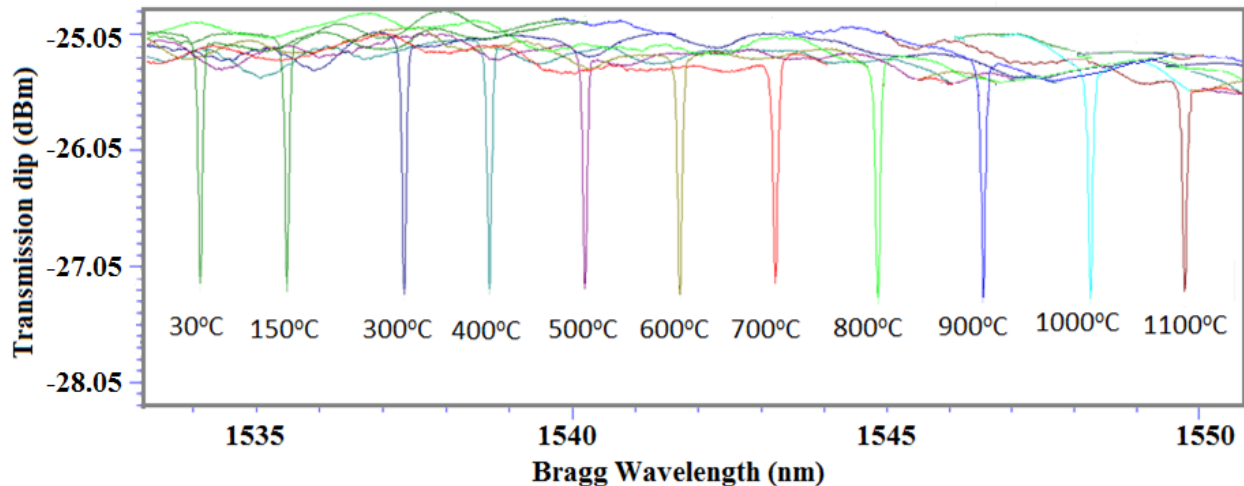


Fig. 4.20: OSA traces showing Bragg wavelength shift with applied temperature for post annealed FBG-C1

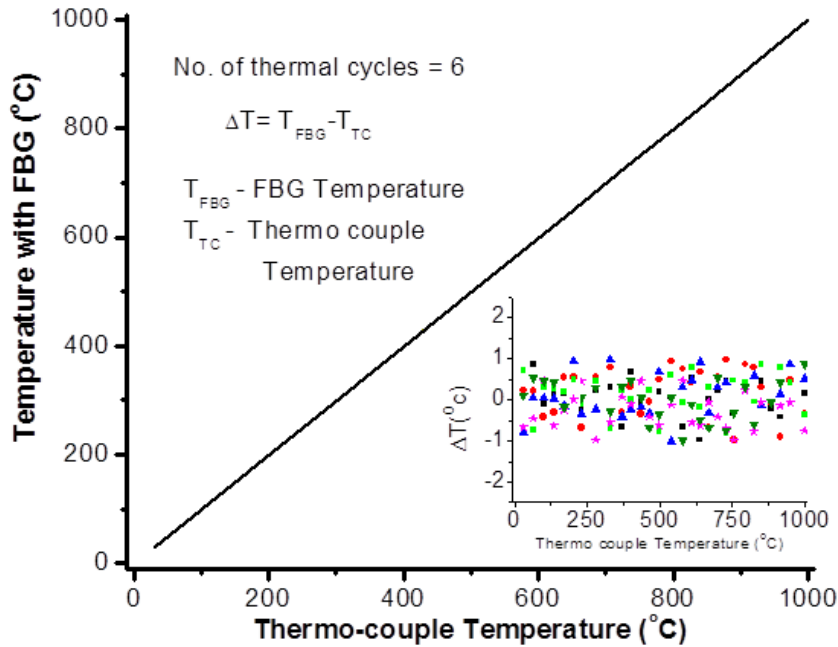


Fig. 4.21: Thermal response of post annealed RFBG

Figure 4.21 shows the temperature measured using FBG as a function of thermocouple temperature. Six cycles of thermal annealing (temperature upto 1000 °C) were applied to experimentally find out the accuracy of the FBG temperature (T_{FBG}) measurement. The variation of FBG temperature ($\Delta T = T_{FBG} - T_{TC}$) at particular thermocouple temperature (T_{TC}) is shown in the inset of figure 4.21. For all the cycles, the value of ΔT at particular thermocouple temperature (T_{TC}) was within ± 1 °C.

4.8 Conclusion

In conclusion, the studies on the thermal regeneration of fiber Bragg grating is carried out. The role of various factors like hydrogenation, fiber core doping, thermal annealing schedule, seed FBG reflectivity and length are discussed. The reflectivity and the predicted life time of regenerated FBG increased non-linearly with the seed FBG strength. Depending upon the reflectivity of seed FBG, for the remaining NICC value of $\eta \sim 0.1$, the predicted life time of the

FBGs at 1000 °C varied from $t \sim 0.75$ to 12.4 year. It was also observed that for same reflectivity FBGs, refractive index modulation (Δn_{ac}) decreases with increase in grating length for seed as well as regenerated FBG. The value of Δn_{ac} for regenerated FBG varied from 0.24×10^{-4} to 0.63×10^{-4} as the seed FBG Δn_{ac} varied from 1.71×10^{-4} to 6.48×10^{-4} . The optimization of these factors is used to regenerate the high reflectivity FBG (~88%) in hydrogen loaded telecommunication fiber. Studies on the residual reflectivity of the thermally regenerated grating at 1100 °C and its relation with change in dc refractive index are established. The decay of the FBG at 1000 °C is analyzed in terms of normalized integrated coupling coefficient. Based on these studies, FBG based single point high temperature sensors for temperature upto 1000 °C have been developed.

Chapter 5

Fiber Bragg grating based quasi distributed temperature sensors

5.0 Introduction

One and the foremost advantage of fiber Bragg grating (FBG) based temperature sensor is the multiplexing capabilities and reflection mode operation. In this scheme several FBGs of distinct wavelength are inscribed in a single fiber. The parameter used for making measurements is the shift in reflected Bragg wavelength. As an example, considering a measurement range of ± 50 °C, the wavelength shift would be typically ± 0.68 nm. If the broadband ASE source used in the sensing has a tunability of 100 nm, a maximum of $100/1.36 \sim 74$ distributed point sensors can be accommodated over a single fiber. The number of sensors can be further increased by the time division multiplexing. Multi-point FBG temperature sensors have been used to monitor the temperature upto 90 °C in the vicinity of nuclear reactor cores, or in environments with moderate gamma dose rates and neutron fluxes [252]. Multi-point sensing using FBG in the temperature range of 22 °C to 25 °C has also been utilized in leak detection of hazardous substances like petroleum hydrocarbons, which are very dangerous, may lead to a significant pollution of the environment and even to catastrophic results if not detected, localized and cured at the initial stage [253]. The high temperature distributed sensing was performed in tubular furnace upto 900 °C using thermally regenerated grating [254]. FBG based distributed temperature sensing is currently an active area of research for varied applications in temperature range 250 °C to 1000 °C.

This chapter presents results on the development, characterization and implementation of distributed temperature sensor based on fiber Bragg gratings for temperature monitoring in high EMI or radiation environment. Multi-point FBG sensor at different Bragg wavelengths are

inscribed in a single fiber by controlling the geometrical divergence of highly coherent UV (255 nm) beam incident on bi-prism or by tilting the phase mask with respect to the optical fiber. The thermal characterization equation is obtained by taking into account the non-linear sensitivity of the FBG at high temperature. Finally, the developed and characterized sensors are implemented for temperature measurement in high voltage and high EMI radiation such as CuBr laser tube and ultra-high vacuum test setup of Indus-2 beam line.

5.1 Inscription of multiple fiber Bragg gratings in single fiber

The Bragg wavelength of FBG is fixed for the normal incidence of UV beam on the phase mask or bi-prism. The FBGs at multiple wavelengths, in a single fiber, are made by tilting phase mask or fiber with respect to each other, by splicing the individual FBGs inscribed at different wavelength using phase mask of different period, by using phase mask and Lloyd mirror set up and by using single bi-prism with diverging/converging UV beam [69, 75, 161, 255-257]. In the present chapter, we have utilized following approaches for FBG writing at multiple wavelength on a single fiber.

5.1.1 By tilting the phase mask (Tilted FBG approach)

The grating normal is inclined with fiber axis in a Tilted FBG. The Tilted FBGs have been written by rotating the phase mask in the vertical plane. The schematic for TFBG inscription is discussed in section 2.4 of **Chapter 2**. The phase matching condition for the Bragg reflection wavelength λ_{Bragg} of a Tilted FBG (TFBG) can be expressed as follows

$$\lambda_{Bragg} = \frac{2 n_{co,eff} \Lambda}{\cos \theta} \quad (5.1)$$

where θ is the tilt angle and $n_{co,eff}$ is the effective refractive index of the core mode. Λ corresponds to the normal grating period and Λ_g corresponds to the grating period along the axis

of the fiber (figure 2.14). The relation between Λ and Λ_g can be described as $\Lambda = \Lambda_g \cos \theta$. The Bragg resonant wavelength with tilt angle for different fiber having different core refractive index is estimated using Eq. (5.1) and shown in figure 5.1 (a). It is observed that the Bragg peak shifted to longer wavelength with increase in phase mask tilt angle. For present calculation, the grating period is taken as $\Lambda \sim 530$ nm and the effective refractive index for the core mode is varied from $n_{co,eff} \sim 1.457$ to 1.445. The theoretically calculated Bragg wavelength is shifted $\Delta\lambda \sim 9$ nm for the change in phase mask tilt angle of $\Delta\theta \sim 6^\circ$. The tuning range depends upon three factors effective refractive index ($n_{co,eff}$), phase mask tilt angle (θ) and phase mask period (Λ). The tilt angle can be increased to only certain extent since the coupling coefficient decreases with increase in tilt angle. The effective refractive index of the fiber can be changed by splicing photosensitive fibers of different doping concentration and inscribing FBGs by tilting FBG method. It is clear from figure 5.1 (a) that by changing $n_{co,eff}$ from 1.445 to 1.457, the Bragg wavelength can be tuned from 1532 nm to 1554 nm. However in this method the splicing point of the fibers increases the losses at high temperature. Therefore, for low temperature operation (up to 200 °C), this method is suitable for multi-point FBG inscription. The phase mask of different period can also be used to inscribe FBGs at multiple wavelengths in a single fiber without any splicing. Figure 5.1 (b) shows the variation of Bragg wavelength with phase mask tilt angle for different periods of phase mask. It is clear that the Bragg wavelength tuning of 26 nm (from 1529 nm to 1555 nm) can be achieved by using the phase mask of periods 1054 nm, 1060 nm and 1066 nm. This method is expensive due to requirement of multiple phase masks, but the FBGs written in this method can work at high temperature (~ 500 °C). Figure 5.2 shows reflection spectra of 10 FBGs written by tilting the single phase mask and splicing two fibers namely PS-1250 (Ge-B co-doped) and SM-1500 (Ge doped).

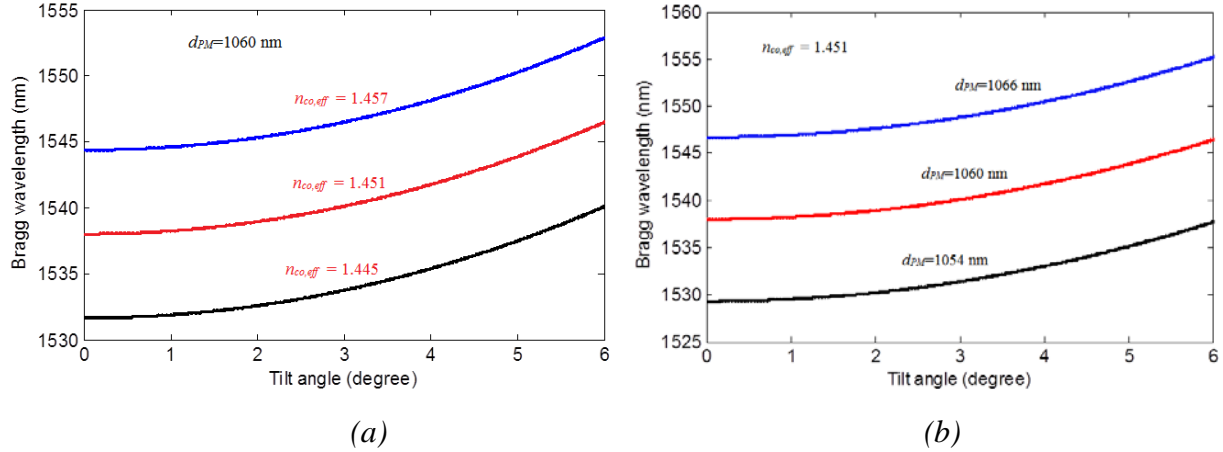


Fig. 5.1: Calculated Bragg wavelength shift with phase mask tilt angle for (a) different effective refractive index and (b) different phase mask periods

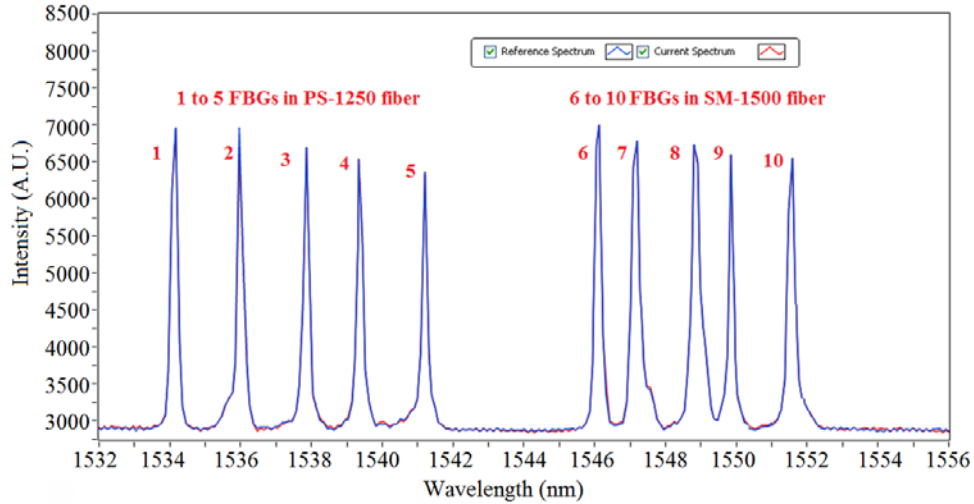


Fig. 5.2: Bragg wavelength tuning by splicing two fibers and writing Tilted FBGs

5.1.2 By changing the divergence of incident UV beam on bi-prism

The second method used for inscription of multiple FBGs in single fiber is based on single bi-prism and diverging/converging beam. The Bragg wavelength of each FBG can be changed by changing the divergence of the incident beam by shifting the position of L_6 lens as shown in figure 5.3. It is clear from figure 5.3 that the laser beam diverges for $u < f$ and converges for $u > f$. Here u is the position of the lens from the focal point and f is the focal length

of lens L₅. The half cone angle ($\theta/2$), calculated from the standard lens equation ($1/f = 1/u + 1/v$) and trigonometric relation, is given as,

$$\theta/2 \approx \tan(\theta/2) = \begin{cases} \frac{W}{2f} \frac{x}{f-x} & \text{for } u < f \\ \frac{-W}{2f} \frac{x}{f+x} & \text{for } u > f \end{cases} \quad (5.2)$$

where W is the selected width of the beam just after lens L₆ and $x = |(u - f)|$ is the translation of lens from the point of collimation.

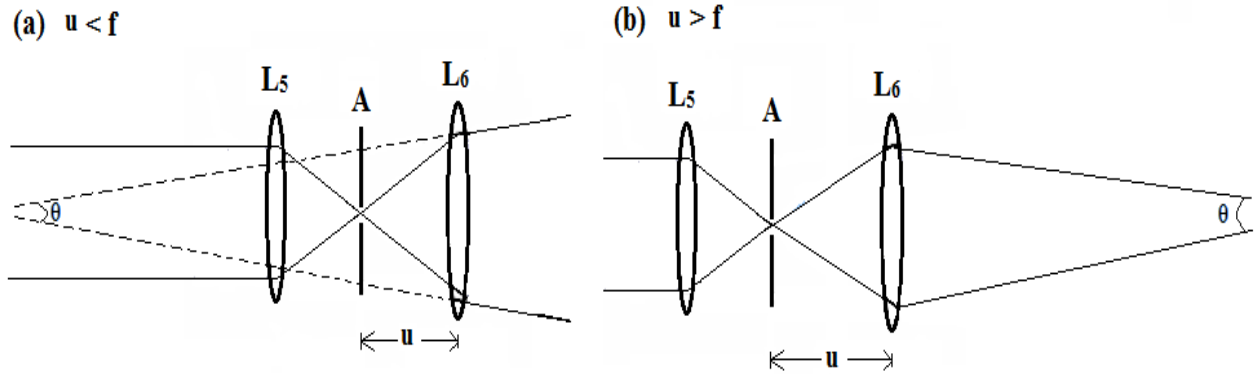


Fig. 5.3: Translation of lens position and its effect on divergence

For typical value of focal length of lens L₆ = 50 cm, the angle of incidence $\theta/2$ changes from 0.6019 degree to - 0.1505 degree as the distance x changes from -30 cm ($u < f$) to +30 cm ($u > f$). The collimated UV beam of wavelength (λ_{uv}) is incident normal to the hypotenuse of the bi-prism. For angle of incidence $\theta/2$, the angle of intersection is given as,

$$\alpha = \sin^{-1} \left[n_p \sin \left\{ A - \sin^{-1} \left(\frac{\sin(\theta/2)}{n_p} \right) \right\} \right] - A \quad (5.3)$$

The Bragg wavelength of the inscribed FBG is given as,

$$\lambda_B = 2 n_{eff} \Lambda = n_{eff} \frac{\lambda_{uv}}{\sin \alpha} \quad (5.4)$$

Where n_{eff} is the effective refractive index of the fiber and Λ is the period of grating. Using Eq. (5.3) and (5.4) the Bragg wavelength can be calculated for different angle of incidence.

Theoretical estimated results and experimentally observed Bragg wavelength, with change in the

position of lens, are shown in figure 5.4. The calculated Bragg wavelength changes from 1625.67 nm to 1526.89 nm as the distance x changes from -30 cm to +30 cm. Experimentally, the Bragg wavelength shifted from 1565.89 nm to 1530.49 nm as the distance x (translation of lens L_6) changes from -15 cm to +20 cm from the point of collimation.

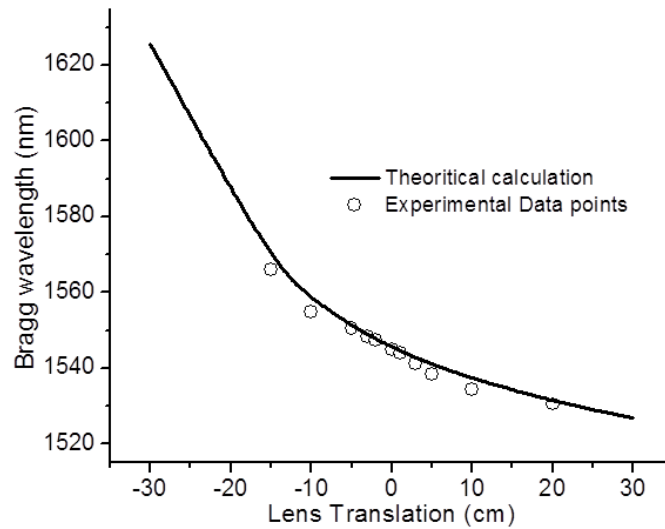


Fig. 5.4: Change in Bragg wavelength as a function of lens translation

5.2 Thermal characterization of the distributed temperature sensor

The thermal characterization of the developed multi-point FBGs in single fiber is carried out before its implementation in high EMI or radiation environment. Thermal characterization will be discussed in two parts. In the first part, the annealing of the FBG for thermal stabilization is discussed. In the second part, the characteristics equation for temperature estimation is carried out.

5.2.1 Annealing schedule for the thermal stabilization of FBG

A ramp annealing process to 600 °C is applied for thermal stabilization of the FBG. In this process the temperature of the FBG is increased to from 30 °C to 600 °C in 30 minutes and fixed for 240 minutes. At 600 °C, the decay in the reflectivity of all the gratings was recorded with time for the duration of 240 minutes. The observed thermal degradation of the FBG with time at

a fix temperature of 600 °C is analyzed by calculating normalized integrated coupling coefficient (NICC) using Eq. (3.1) and shown in figure 5.5 for one of the FBGs.

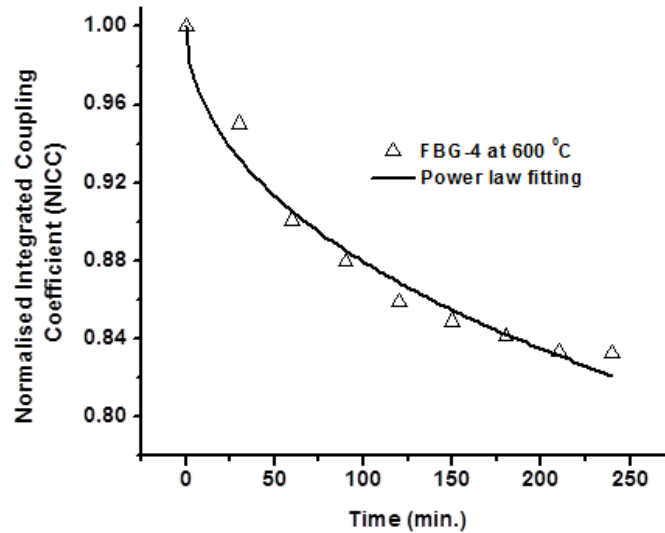


Fig. 5.5: Variation of normalized integrated coupling coefficient with time at 600 °C

The NICC is calculated from the ratio of the changes in refractive index modulation at temperature T and room temperature (as discussed in **Chapter 3**). From the experimental data, the thermal decay characteristics are simulated using the power-law model [231] as presented in **Chapter 3**. For the gratings with remnant NICC of 0.10, at 600 °C, the predicted life time of the FBGs is about ~10 years.

5.2.2 Estimation of temperature response of FBG

At higher operating temperature, the temperature sensitivity of FBG becomes non-linear due to non-linear temperature response of the thermo-optic coefficients [258-259]. Therefore for reliable operation of distributed temperature sensor, temperature response of FBGs needs to be characterized before its installation in high EMI or radiation environment. To obtain this characteristics curve, a single FBG was written by the same experimental set-up (255 nm UV beam and bi-prism) on a photosensitive fiber (SM-1500). The shift in the Bragg wavelength with temperature is studied upto 500 °C in a PID controller based oven. A thermocouple transducer

connected to a temperature controller is used to measure the temperature and the corresponding wavelength shift is recorded in OSA. Figure 5.6 (a and b) shows the variation in Bragg wavelength and average sensitivity with the temperature variation. The Bragg wavelength shifted from 1532.927 nm to 1539.525 nm as the temperature of the FBG increased from 30 °C to 500 °C. The observed average temperature sensitivity in the temperature range of 30 °C to 100 °C was 10.2 pm/°C and that between 30 °C to 500 °C was 13.2 pm/°C.

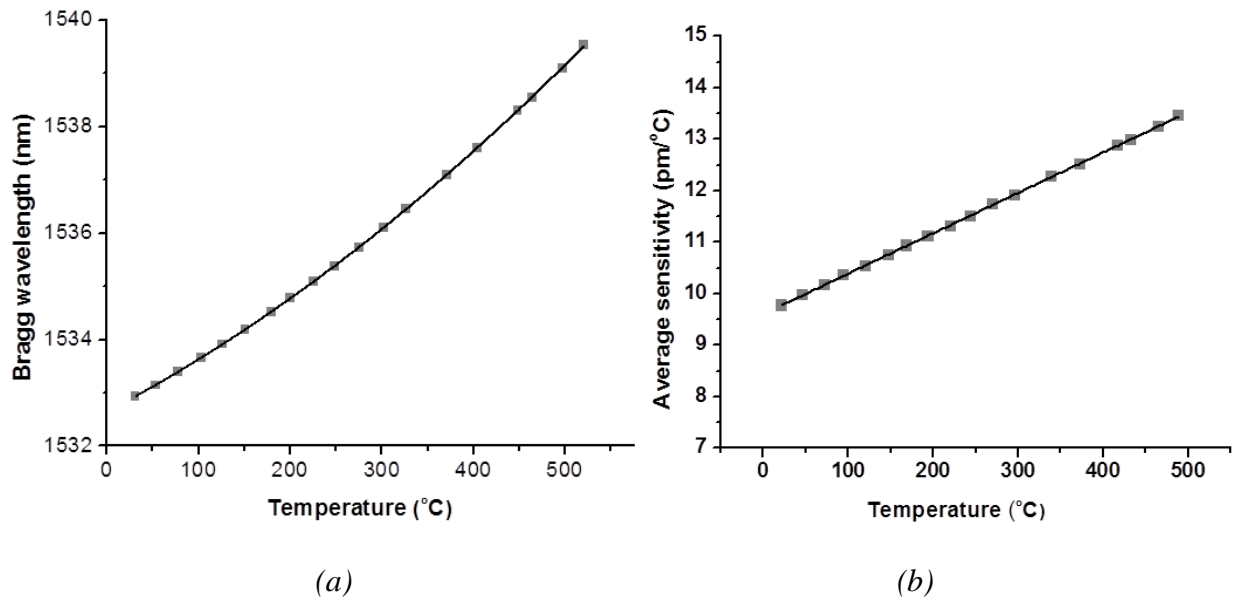


Fig. 5.6: (a) Bragg wavelength and (b) average temperature sensitivity with temperature

It is clear that the wavelength shift with temperature is not linear but the average sensitivity increases linearly with temperature. This gives indication that the Bragg wavelength response of the FBG to temperature change is quadratic and can be expressed as [161, 260],

$$\lambda(T) \approx \lambda(T_0) + a_1(T - T_0) + a_2(T - T_0)^2 \quad (5.5)$$

where $\lambda(T_0)$ is the Bragg wavelength at reference temperature (T_0) and a_1, a_2 are the coefficients which depend upon the fiber material and applied temperature. The temperature sensitivity of FBG at temperature T is given as,

$$\frac{d\lambda}{dT} = a_1 + 2a_2 (T - T_0) \quad (5.6)$$

The average temperature sensitivity is given as,

$$\langle \frac{d\lambda}{dT} \rangle = a_1 + a_2 (T - T_0) \quad (5.7)$$

The coefficients a_1 and a_2 are estimated from the linear fit of average temperature sensitivity. For SM-1500 fiber at $T_0 = 30^\circ\text{C}$, the values of a_1 and a_2 are $9.60741\text{pm}/^\circ\text{C}$ and $7.84 \times 10^{-3} \text{pm}/(^\circ\text{C})^2$ respectively. By solving Eq. (5.5), the temperature (T) calculated from Bragg wavelength shift ($\Delta\lambda$) can be expressed as,

$$T = T_0 + \frac{a_1}{2a_2} \left[\sqrt{\left(1 + \frac{4a_2}{a_1^2} \Delta\lambda\right)} - 1 \right] \quad (5.8)$$

Using Eq. (5.8), the temperature of FBG with the Bragg wavelength shift is simulated and shown in figure 5.7. From figure 5.7, the temperature of the FBG can be estimated by knowing the value of Bragg wavelength shift. This figure is used as characteristic curve for all FBGs used for distributed temperature sensing. Multiple cycles of thermal annealing (temperature upto 600°C) were applied to experimentally find out the temperature sustainability and accuracy of the measurement.

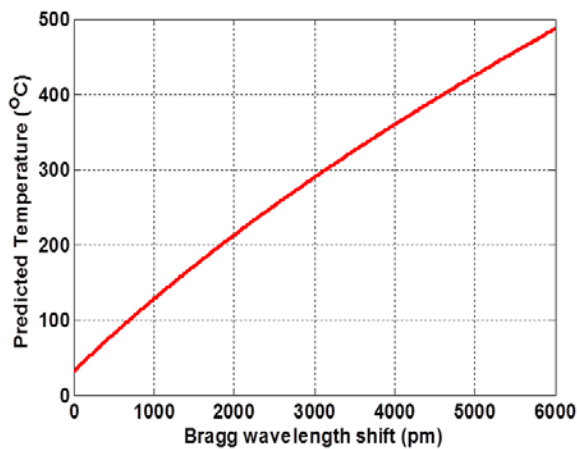


Fig. 5.7: Simulated Bragg wavelength shift vs temperature change

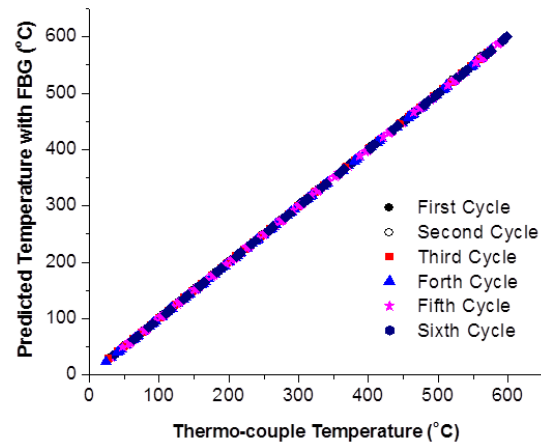


Fig. 5.8: Predicted temperature with FBG-4 vs Thermocouple temperature

Figure 5.8 shows the typical predicted temperature by one of the FBGs with applied temperature (measured with thermo-couple). The minimum resolution of FBG interrogator was about 5 pm (which corresponds to ~ 0.5 °C). In all six thermal cycles, the linearity of the curve was almost same with temperature accuracy of about ± 1 °C.

5.3 Utilization of distributed sensor in temperature measurement (up to 500 °C) of electrically pumped pulse gas discharge laser tube

(A) Requirement of distributed temperature monitoring of operating laser tube

The CuBr laser operating conditions such as high repetition rate and high specific power demand high electrical power loading. The laser is same as CVL (as shown in figure 1.8) however with low operating temperature of ~ 500 °C as compared to ~ 1500 °C of CVL. This, in turn affects the temperature distribution along the laser tube, the spatio-temporal evolution of laser beam characteristics, total laser average power and more importantly the green ($\lambda=510$ nm) to yellow ($\lambda=578$ nm) laser power ratio [261]. For many applications of CuBr laser, the ratio of green to yellow has very important implications. For example, in second harmonic conversion of green and yellow component of CuBr laser radiation, the laser power should be maximum corresponding to green or yellow component. While for sum frequency generation of CuBr laser, the ratio of green to yellow radiation is important. It has been shown that the ratios of green to yellow power is also important for efficient green to yellow conversion of CVL radiations using CVL pumped dye laser [262]. In this perspective, it is essential as well as interesting to carry out study on the temperature distribution in the active zone of the CuBr laser. Temperature measurements by contact sensing on the laser discharge tube of electrically pumped pulse gas discharge laser is almost an impossible task by other conventional sensor because of very high EMI background. In such high EMI and high voltage environment, the FBG based multi-point

temperature sensor will be an excellent option for online temperature monitoring along laser tube length.

(B) Deployment of FBG temperature sensor on the surface of operating laser tube

In the CuBr laser tube, high peak voltage of about 18.4 kV is switched with rise time of ~ 90 ns and peak current of ~ 217 A (figure 5.9). The peak power of about 4 MW was applied across the laser tube of diameter 5.5 cm and length 200 cm [263].

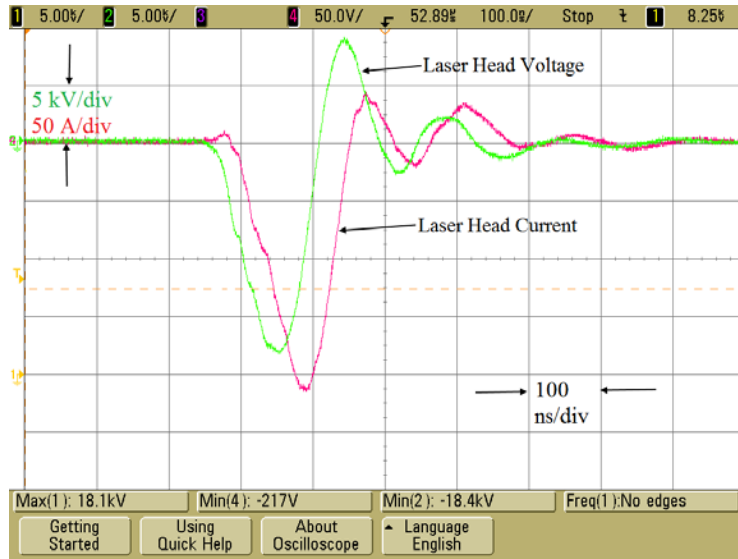


Fig. 5.9: Waveform of voltage and current pulses across the laser head for 40 W copper bromide (CuBr) laser

The maximum operating temperature of CuBr laser tube reached to about 500 °C. Considering a measurement range from room temperature (30 °C) to 500 °C and average sensitivity of the FBG ~ 13.2 pm/ °C, the maximum wavelength shift would be ~ 6.2 nm. Total wavelength span available for sensing in broad band ASE source is about 40 nm (from 1525 nm to 1565 nm). Then the number of distributed point sensors that can be accommodated over a single fiber will be [73],

$$N = \frac{\lambda_2 - \lambda_1}{\left(\frac{d\lambda}{dT}\right) (T_2 - T_1)} \approx \frac{40}{6.2} \approx 6 \quad (5.9)$$

Where $\lambda_2 - \lambda_1 =$ Total wavelength span available for sensing, maximum wavelength shift, $d\lambda/dT =$ average temperature sensitivity and $T_2 - T_1 =$ maximum temperature difference to be measured. To monitor the temperature profile along the length of the CuBr laser tube, the maximum six number of gratings are inscribed on the fiber which can clearly identify temperature upto 500 °C, since there will be no overlapping of the grating profile for these gratings. Six FBGs are written at central Bragg wavelength of 1530.211 nm (FBG-CB1), 1531.031 nm (FBG-CB2), 1536.954 nm (FBG-CB3), 1542.947 nm (FBG-CB4), 1549.464 nm (FBG-CB5) and 1555.811 nm (FBG-CB6) (shown in figure 5.12). Total length of the fiber is taken ~2 meter and six FBGs are inscribed at 30 cm apart from each other. The multiple FBGs are written in single fiber by changing the angular divergence envelope of the 255 nm UV beam incident on bi-prism.

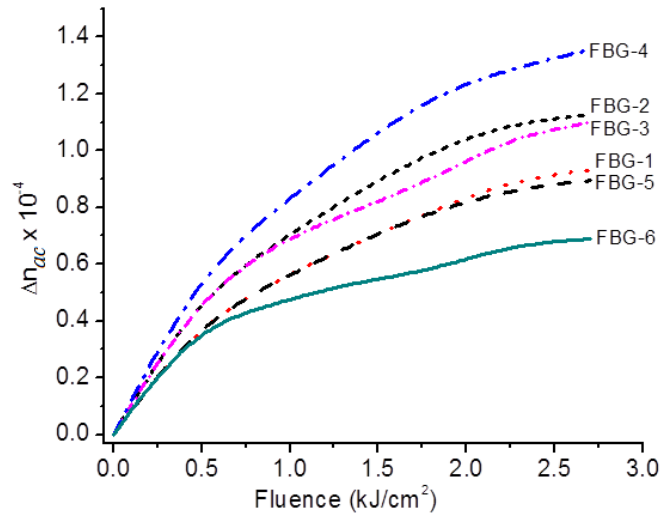


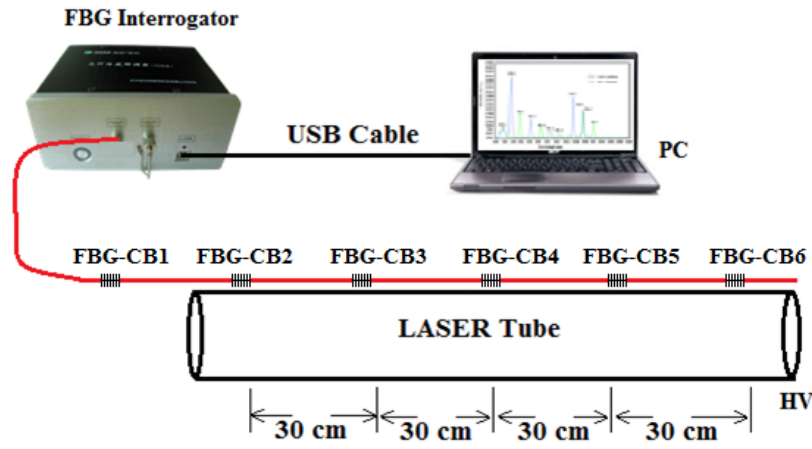
Fig. 5.10: Variation of refractive index modulation with cumulative fluence

The transmission spectra of the FBG evolution with cumulative UV fluence are recorded with OSA to estimate the reflectivity and refractive index modulation of these gratings. At the cumulative fluence of ~2.7 kJ/cm², the reflectivity of the inscribed FBGs are 70.8 %, 81.3 %, 80.1 %, 89.3 %, 68.4 % and 51.8 % for FBG-CB1, FBG-CB2, FBG-CB3, FBG-CB4, FBG-CB5

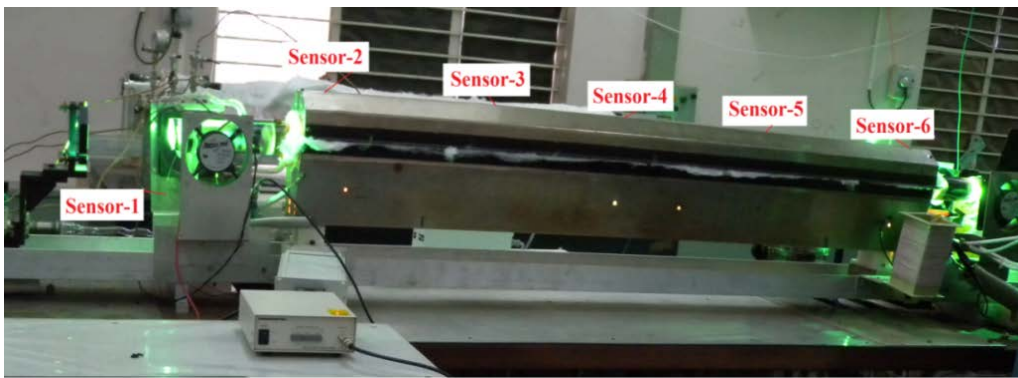
and FBG-CB6 respectively. The refractive index modulation is estimated from the evolution of transmission spectra of the FBG and shown in figure 5.10. From figure 5.10 it is noticed that the refractive index modulation (Δn_{ac}) increases with the fluence and reached to maximum value of at the cumulative fluence of 2.7 kJ/cm^2 . It is also clear from the figure that the refractive index modulation is highest (1.36×10^{-4}) for FBG-CB4 and lowest (0.69×10^{-4}) for FBG-CB6.

The typical scheme of six point FBG based distributed temperature sensor applied to CuBr laser tube is shown in figure 5.11 (a). Out of six FBGs, five FBGs (from FBG-CB2 to FBG-CB6) are placed along the CuBr laser tube. The FBGs were bare. These FBGs are placed on the upper side of the tube and held by loosely wrapped high temperature glass tape. This soft fiber holding arrangement did not produce any appreciable strain during the temperature measurement and would not affect the sensor performance. In present experimental set-up, the major sources of error are the spectral profile of the FBGs (FWHM bandwidth of the FBG $\sim 0.2 \text{ nm}$) and the applied strain or bending during wrapping of the FBGs on the laser tube. To minimize the inaccuracy in the temperature measurement, the bandwidth of the FBGs is tailored during the inscription process and all FBGs are placed on the upper side of the tube by wrapping loosely with high temperature glass tape, as already mentioned. FBG-CB1 (Bragg wavelength $\sim 1530.211 \text{ nm}$) is kept outside the tube for reference temperature (or ambient temperature) as shown in figure 5.11 (a). Figure 5.11 (b) shows the working of FBG based distributed temperature sensor with the CuBr laser tube. FBG-CB1 to FBG-CB6 is designated as sensor-1 to sensor-6, respectively. The temperature of the CuBr laser is increased as the input power of the laser tube is increased. The shift in reflected Bragg wavelength peak is measured using FBG interrogator (JPhotonics, wavelength range $\sim 1525\text{-}1565 \text{ nm}$) and is displayed on the computer.

The response time of FBGs based temperature sensor is controlled by the response time for data acquisition system. For the present case it is 1.0 second.



(a)



(b)

Fig. 5.11: (a) Schematic of temperature monitoring system and (b) actual implementation of multiple FBGs at different locations along the CuBr laser tube

As the electrical input power in laser tube increases, the temperature of the tube rises and hence the Bragg wavelength of the attached FBG changes. Figure 5.12 shows typical reflection spectrum of the FBG array at the maximum operating input electrical power of 4.3 kW. The Bragg peaks for FBG-CB2 to FBG-CB6 are shifted due to change in the temperature of laser tube. However no shift in peak of FBG-CB1 is observed because of constant ambient temperature. The Bragg wavelength shifted from 1531.031 nm to 1536.670 nm, 1536.954 nm to

1542.734 nm, 1542.947 nm to 1549.037 nm, 1549.464 nm to 1555.654 nm and 1555.811 nm to 1562.041 nm for FBG-CB2, FBG-CB3, FBG-CB4, FBG-CB5 and FBG-CB6 respectively.

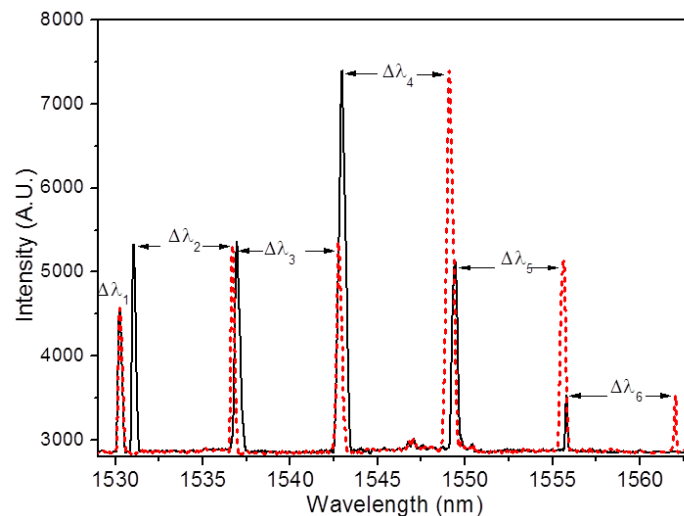


Fig. 5.12: Interrogator results showing Bragg wavelength shift with temperature for all the FBGs

The maximum Bragg wavelength shift corresponding to FBG-CB1, FBG-CB2, FBG-CB3, FBG-CB4, FBG-CB5 and FBG-CB6 is $\Delta\lambda_1=0$ nm, $\Delta\lambda_2=5.64$ nm, $\Delta\lambda_3=5.78$ nm, $\Delta\lambda_4=6.09$ nm, $\Delta\lambda_5=6.19$ nm and $\Delta\lambda_6=6.23$ nm respectively. Exact temperature at these points is calculated from value of wavelength shift using characterization curve (Figure 5.7 and 5.8) of these FBGs. The temperature at these six locations was 30 °C, 467 °C, 478 °C, 498.5 °C, 499 °C and 499.5 °C, respectively. The temperature of CuBr laser tube is measured at different spatial location along the axis by varying the electrical input power also. Figure 5.13 show the temperature profile of CuBr laser tube along axis from the high voltage end of the tube at various applied input electrical power. At input power of 2 kW, the temperature of the five locations on the laser tube was 201 °C, 205 °C, 204 °C, 206 °C, 203 °C for FBG-CB2 to FBG-CB6 respectively. The temperature increased to 383 °C, 392 °C, 405 °C, 407 °C and 410 °C on the same locations as the input electrical power increased to 3 kW. At the maximum input power of 4.3 kW, the

temperature increased to 467 °C, 478 °C, 498.5 °C, 499 °C and 499.5 °C. It is clear from the graph that the temperature variation along the tube is very small at input power of 2 kW. At maximum input power of 4.3 kW, the temperature of high voltage end was higher about 33 °C as compared to low voltage end. It is clear from the figure that the temperature at central portion of the laser tube increases from 204 °C to 498.5 °C as the electrical input power increases from 2 kW to 4.3 kW. It is to be noted that the on-line temperature measurement of gas discharge laser tube using multiple FBGs is reported for the first time.

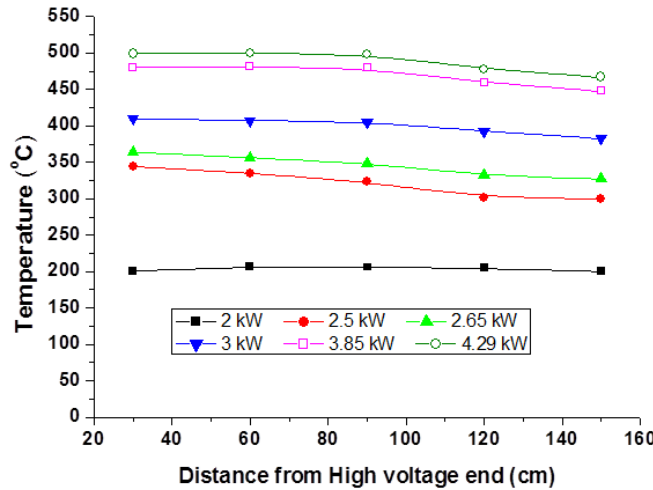


Fig. 5.13: Temperature profile along the laser tube with applied electrical power

5.4 Utilization of distributed temperature sensing in Indus-2

FBG based distributed temperature sensors are utilized in temperature monitoring of the walls of ultra-high vacuum (UHV) chambers being used as a part of synchrotron beam line of Indus-2. Here sensor can be implemented in following applications.

5.4.1 Distributed surface temperature monitoring of an UHV pump

(A) Requirement of precise distributed temperature monitoring

Non-Evaporable Getter (NEG) materials are capture pumps, which means materials able to remove molecules from the gas phase by fixing them into an internal surface. Capture pumps are

usually characterized by a sojourn time, defined as the time spent by a captured molecule on the surface of the pump

$$\tau = \tau_0 \exp(U/k_B T) \quad (5.10)$$

where τ_0 is a constant and U is the molecules binding energy on the material surface. It is needed that the sojourn time is long enough to guarantee that the molecules are stucked on the material surface for whole duration of the experiments. Getters are materials able to chemically react with the most of the gases present in a vacuum system; they form stable chemical compounds with them at room temperature. Because of the high binding energy, getters have a sojourn time suitable for vacuum application. In order to allow the reaction between the surface particles of the getters and the gases in the vacuum chamber, the surface must be free from contamination and free of the native oxide layer. This layer is due to the air exposition. For a NEG material, this layer is eliminated by heating in situ the surface; this procedure, called activation, allows the diffusion of the oxygen into the bulk of the material leaving a very reactive and clean surface. In large accelerator vacuum systems the length of NEG coated chambers are typical 2-5 meters. Now a day the heating of chambers are done with these heaters to 180-250 °C for 24 hours. The distributed temperature measurement is also required here to see the temperature profile of chambers accurately. For this purpose distributed FBGs are employed.

(B) Deployment of FBG based distributed temperature sensor

FBG based distributed temperature sensor is implemented for temperature measurement of ultra-high vacuum test set up required for synchrotron radiation source Indus-2 at RRCAT. The schematic and actual experimental set up is shown in figure 5.14. The UHV test set up consisted of two NEG coated chambers of length 90 cm. To monitor the temperature profile along the length of one chamber, an array of seven FBGs with different Bragg wavelengths 1525.259 nm

(FBG-UH1), 1527.549 nm (FBG-UH2), 1530.184 nm (FBG-UH3), 1534.141 nm (FBG-UH4), 1536.718 nm (FBG-UH5), 1539.737 nm (FBG-UH6) and 1543.781 nm (FBG-UH7) on the single photosensitive fiber is inscribed to monitor the temperature profile.

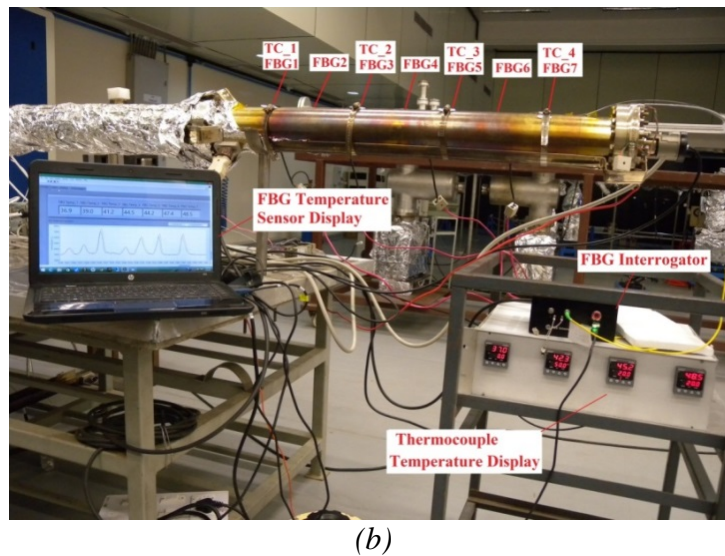
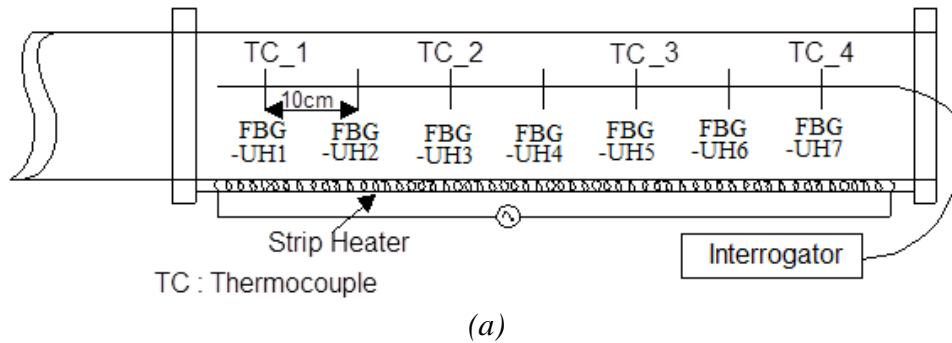


Fig. 5.14: (a) schematic and (b) actual implementation of distributed FBG temperature sensor to UHV set up

Exact temperature at different points is calculated from value of wavelength shift using characterization curve of these FBGs. A screen shot of the measurement of temperature is shown in figure 5.15. The measured temperature via FBG sensors were also simultaneously monitored by placing thermocouples at four locations. The temperature measured by the FBG was fast compared to thermocouple. Figure 5.16 shows the measured temperature by FBG-UH7 and thermocouple-4.



Fig. 5.15: Screen shot of the measured wavelength shift and corresponding temperature along the arm of the UHV pump

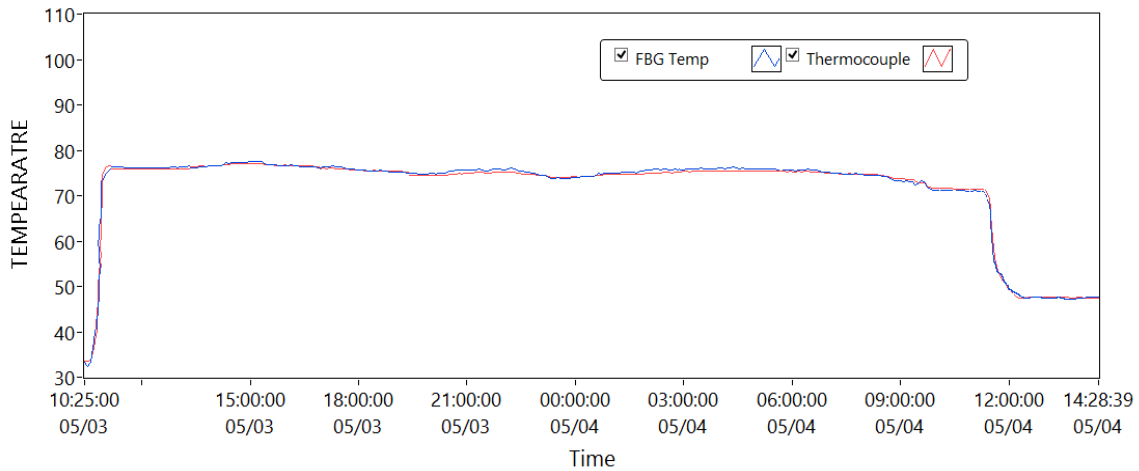


Fig. 5.16: Measured temperature of the UHV set up using FBG-UH7 and thermocouple-4 with respect to time (~28 hours)

The temperature is monitored on different input power and ambient conditions for 28 hours continuously. The temperature distribution along the length varied from 80 °C to 100 °C with the accuracy of ± 1 °C. Figure 5.17 shows the temperature profile along the length of the UHV pump with time. The temperature profile along the length is not uniform. The maximum difference between the higher and lower temperature is ~ 20 °C.

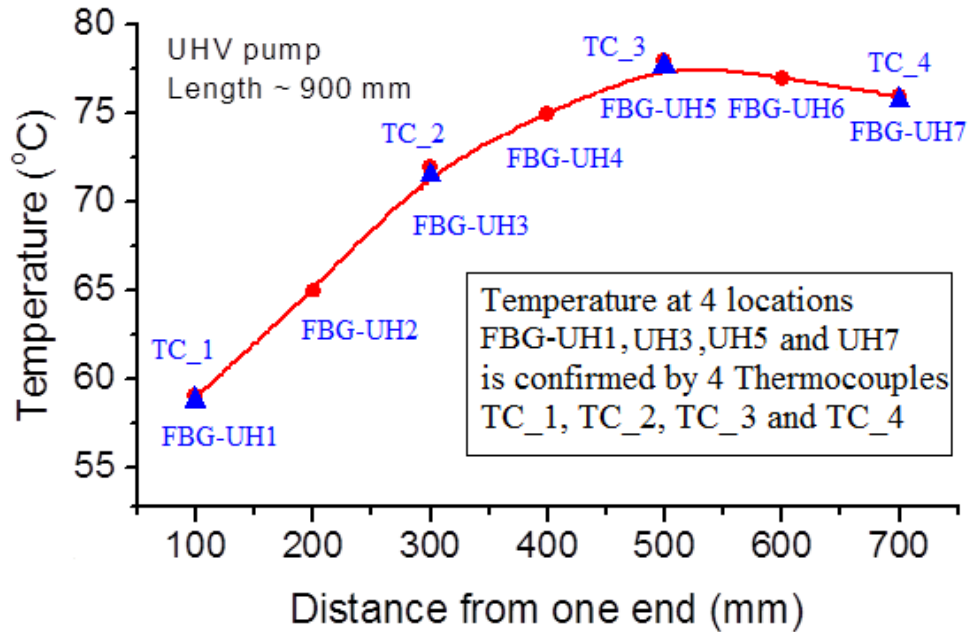


Fig. 5.17: Temperature profile along the length of the UHV pump

5.4.2 Distributed temperature monitoring of vacuum chamber of dipole magnet

(A) Requirement of distributed temperature monitoring

High energy electron accelerators have been designed upto an energy range from 2.5 GeV to 8 GeV with a beam current of 200 to 500 mA depending on requirement of scientific community. The Indus-2 ring at RRCAT is operating at 2.5 GeV and 200 mA. So the power deposition due to synchrotron radiation on the wall of vacuum chamber is very intense due to high energy. This in turn leads to instantaneous localized heating of chamber material and may lead to opening of welding joints of the vacuum components. Therefore, to monitor the localized temperature rise at the multiple locations, a distributed sensor of very fast response time is needed. Various types of electromagnets (total 328 Nos.) viz. dipole magnets, quadrupole magnets and sextupole magnets are used in Indus synchrotron radiation facility. 33 dipole magnets, 132 quadrupole magnets, 40 sextupole magnets are used in this facility. Each magnet assembly is accompanied by vacuum chambers.

(B) Deployment of FBG based distributed temperature sensor

A ten point FBG based distributed temperature sensor is designed fabricated and deployed for the measurement of temperature along the periphery of vacuum chamber of bending magnet (DP-12) in Indus-2. The schematic of the distributed temperature sensor is shown in figure 5.18.

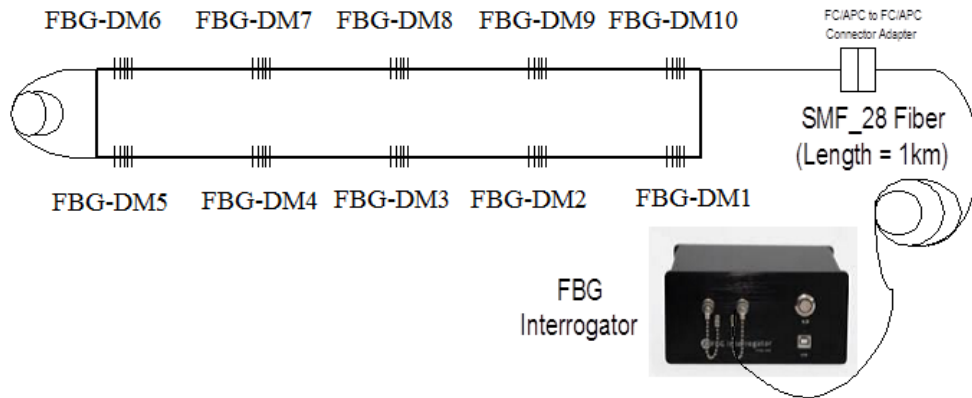


Fig. 5.18: Schematic of the distributed temperature monitoring

An array of ten FBGs with different Bragg wavelength in a single fiber is inscribed at the spatial separation of 7 cm, by tilting the phase mask with respect to the fiber. The Bragg wavelengths of the ten FBGs were 1535.181 nm (FBG-DM1), 1537.068 nm (FBG-DM2), 1539.498 nm (FBG-DM3), 1541.205 nm (FBG-DM4), 1542.673 nm (FBG-DM5), 1547.144 nm (FBG-DM6), 1549.101 nm (FBG-DM7), 1551.431 nm (FBG-DM8), 1553.210 nm (FBG-DM9) and 1555.305 nm (FBG-DM10), respectively. Five FBGs (FBG-DM1 to FBG-DM5) are installed at the lower half and five (FBG-DM6 to FBG-DM10) at the upper half of the chamber. The experimental set up is shown in figure 5.19. Figure 5.20 is the expanded view of the experimental arrangement of temperature measurement. The FBGs sensor array is connected to 1 km long single mode telecommunication fiber for remote monitoring the temperature. Exact temperature at different points is calculated from value of wavelength shift using characterization

curve of these FBGs. From the in-house developed computer software, the temperature data was collected at the interval of 1 sec and saved in the computer. The measured temperature via FBG sensors were also confirmed by monitoring the temperature using one thermocouple at location close to FBG-DM9.



Fig. 5.19: Experimental arrangement of the distributed temperature monitoring



Fig. 5.20: Expanded view of the experimental arrangement

From FBG based distributed temperature sensor, it is observed that the temperature of the chamber is not uniform along the periphery. It varied from 40 °C to 100 °C during operation of Indus-2. During shut down of Indus-2, the temperature of all locations was almost same within the measurement accuracy. Long term temperature recording for around ten days has been also carried out. Figure 5.22 shows the measured temperature at ten points of DP-12 vacuum chamber and its variation with time. The Indus-2 beam current information is also included in figure 5.21.

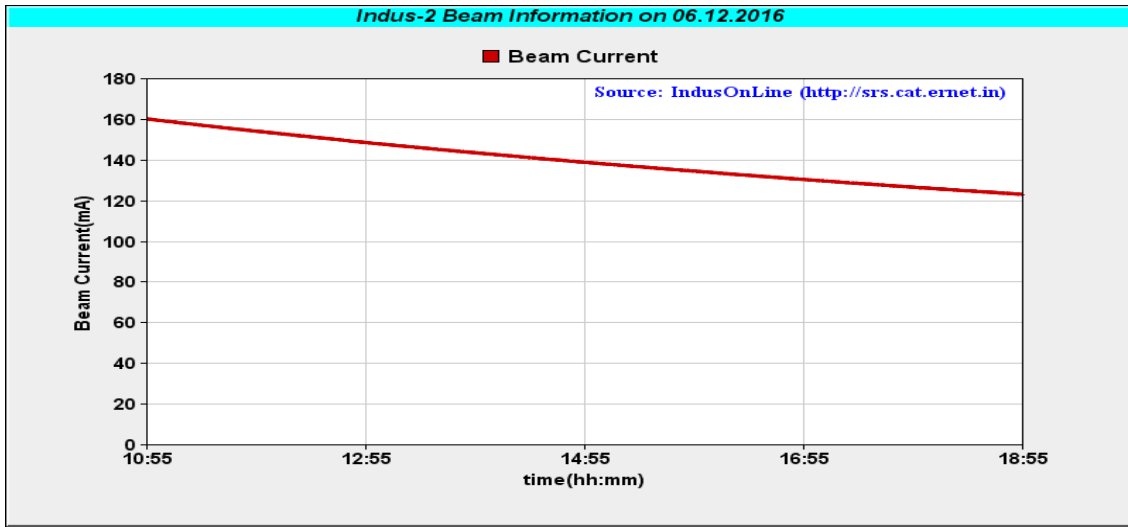


Fig. 5.21: Indus-2 beam current on 06/12/2016

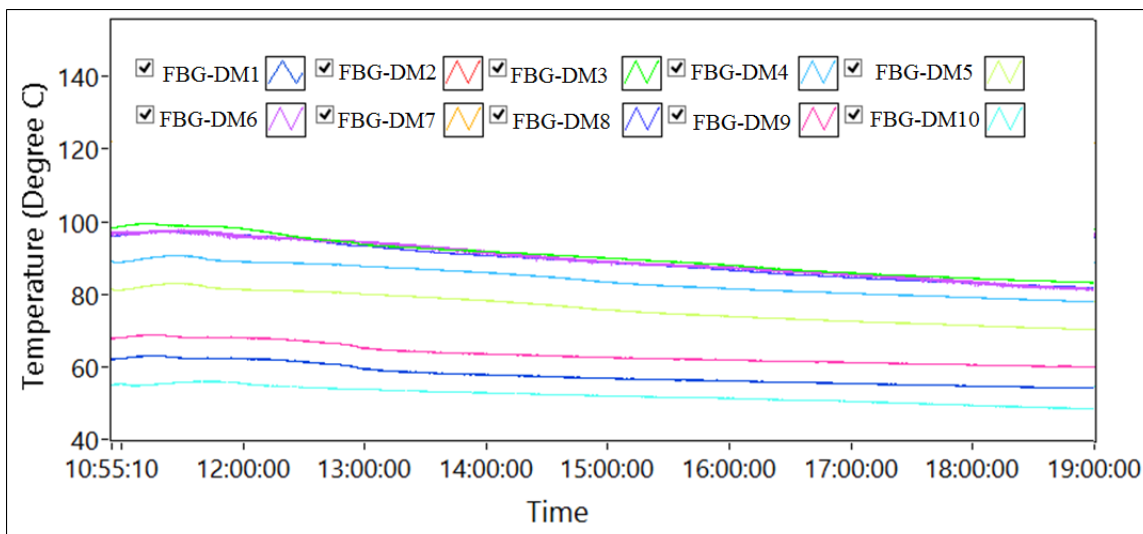


Fig. 5.22: Temperature of the exit port of DP-12 on 06/12/2016

The beam energy of Indus-2 was fixed at 2.5 GeV and the beam current decreased from 160 to 120 mA. It is observed that the temperature profile follows the variation of beam current. The FBGs based distributed temperature sensor has helped to detect the hot spot at vacuum chamber wall during Indus-2 operation.

5.5 Conclusion

In conclusion, FBGs based distributed temperature sensors are designed and implemented. Theoretical and experimental studies on the Bragg wavelength tuning in phase mask and bi-prism based inscription techniques are carried out. The maximum wavelength tuning of ~26 nm and ~40 nm was achieved using phase mask and bi-prism approach, respectively. The temperature of gas discharge laser tube in high voltage (HV) and high EMI environment is measured using FBG based distributed temperature. The operating temperature of gas discharge laser tube varied from 467 °C to 500 °C along the length at input electrical voltage of 4.3 kV. A ten point FBGs based distributed temperature sensor is also used for monitoring the temperature across the vacuum chamber of dipole magnet in a synchrotron radiation source. The temperature variation from 40 °C to 100 °C is noticed.

Chapter 6

Analytical and experimental studies of Etched FBGs

6.0 Introduction

The operating principle of FBG based refractive index sensor relies on the dependence of Bragg resonance peak shift on the effective refractive index and the grating pitch. For standard optical fiber, the effective refractive index is not influenced by external refractive and hence no sensitivity to external refractive index. However, if the cladding diameter is reduced along the grating region, the effective refractive index is affected by the external refractive index. This leads to shift in peak Bragg wavelength combined with a modulation of reflected amplitude. It has been shown that the clad diameter of etched FBGs controlled the refractive index sensitivity [141-144].

This chapter presents the numerical analysis and experimental results on the use of etched FBGs for refractive index sensing. A double clad approximation theory for cylindrical/rectangular waveguide geometry, for the thinned optical fiber, has been used to identify the dependence of the effective refractive index on the external medium refractive index. A graphical method is used to find the dependence of effective refractive index of the double clad fiber on cladding diameter and surrounding refractive index. The theoretical analysis explained the experimental results very well. The refractive index sensors are fabricated using FBGs written in single mode photosensitive fiber and etching by HF solution. The etching characteristics of different reflectivity and thermally regenerated FBG are also discussed in the present chapter and their sensing characteristic is paid due attention in **Chapter 7**.

6.1 Analysis and simulation on FBG based refractive index sensor (RIS)

The shift in Bragg wavelength with change in surrounding medium refractive index is to be estimated. The Bragg wavelength of the FBG is given by

$$\lambda_B = 2 n_{eff} \Lambda \quad (6.1)$$

where Λ is the grating period and n_{eff} is the effective refractive index of the propagating mode. Initially the Bragg wavelength shift is insensitive to the surrounding medium refractive index. As a FBG is inserted in HF solution its clad diameter started to decrease. At this time, the light in the fiber is guided by two clads i. e. first, by the partially etched clad and second by the surrounding medium. If Δn_{sur} is change in surrounding medium refractive index, then the change in Bragg wavelength can be written as

$$\Delta\lambda_B = 2 \Lambda \left(\frac{\partial n_{eff}}{\partial n_{sur}} \right) \Delta n_{sur} \quad (6.2)$$

To understand the propagation characteristics of the light in etched FBG it will be appropriate to use double clad approximation theory. Figure 6.1 shows the schematic of the refractive index profile for double clad fiber. Refractive index of the core (n_{core}) is higher than that of the partially etched clad (n_{clad}) and surrounding medium refractive index (n_{sur}). Surrounding medium works as a second clad for propagation of light inside the optical fiber. Hence

$$n_{core} > n_{clad} > n_{sur}$$

If a and b are the diameter of core and cladding then

$$n = \begin{cases} n_{core} ; (0 \leq |r| \leq a) \\ n_{clad} ; (a \leq |r| \leq b) \\ n_{sur} ; (|r| \geq b) \end{cases} \quad (6.3)$$

The double clad approximation theory can be applied either in slab waveguide geometry or cylindrical waveguide geometry.

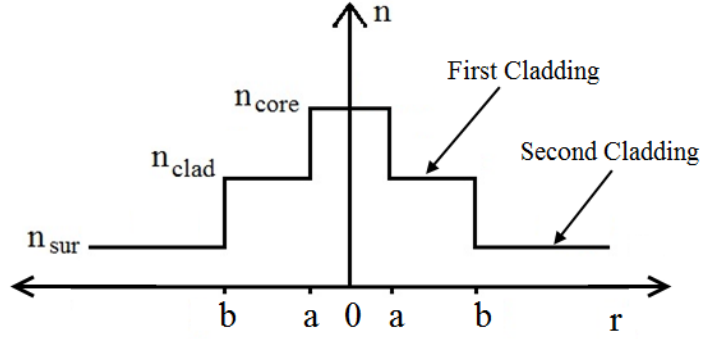


Fig. 6.1: Schematic of the refractive index profile for double clad fiber

6.1.1 Double clad slab waveguide geometry

In this approach, the fiber geometry can be approximated with a double clad slab waveguide. There are various methods used to study the light wave transmission mechanism in double clad slab waveguides or 3-layer slab waveguides [264-266]. The electric field distribution for a double clad slab waveguide can be written as [267],

$$E_y = \left\{ \begin{array}{l} A \cos \eta x ; (0 \leq |x| \leq a) \\ B \cos \gamma(x - a) + C \sin \gamma(x - a) ; (a \leq |x| \leq b) \\ D \exp \sigma(x - b) ; (|x| \geq b) \end{array} \right\} \quad (6.4)$$

where η , γ and σ are the transverse wave numbers which depends upon the refractive index of the core, inner clad, outer clad (surrounding medium in case of etched fiber) and propagation constant (β) of the fiber and given as,

$$\eta = k_0 \sqrt{n_c^2 - n_{eff}^2}, \gamma = k_0 \sqrt{n_{clad}^2 - n_{eff}^2} \text{ and } \sigma = k_0 \sqrt{n_{eff}^2 - n_{sur}^2} \quad (6.5)$$

Now applying the boundary conditions continuity of electric field (E_y) and its derivative (dE_y/dx) at the $x = \pm a$ and $x = \pm b$, the characteristic equation for even TE mode of double clad fiber is written as,

$$\eta \tan(\eta a) [\gamma + \sigma \tan\{\gamma(b - a)\}] = \gamma [\sigma - \gamma \tan\{\gamma(b - a)\}] \quad (6.6)$$

Eq. (6.6) can be solved numerically by several methods. We have used the simple graphical method as apart from providing estimates of the roots, graphical interpretations are important tools for understanding the properties of the functions. So Eq. (6.6) is solved using graphical method to find out the dependence of effective refractive index of the double clad fiber on cladding diameter and surrounding refractive index. Figure 6.2 show the curves plotted by left and right hand side of Eq. (6.6) as a function of effective refractive index. The intersections give the value of effective refractive index for particular cladding diameter and surrounding refractive index. Here n_1, n_2, n_3, n_4, n_5 and n_6 are the intersections of curves plotted for different surrounding medium refractive index 1, 1.1, 1.2, 1.3, 1.35 and 1.4 at 10 μm cladding diameter. The parameters chosen for the numerical analysis are, $n_{core} = 1.450, n_{clad} = 1.444, a = 6 \mu\text{m}, b = 6\text{-}125 \mu\text{m}, k_0 = 4.09 \times 10^6$ and $n_{sur} = 1.0$ to 1.44.

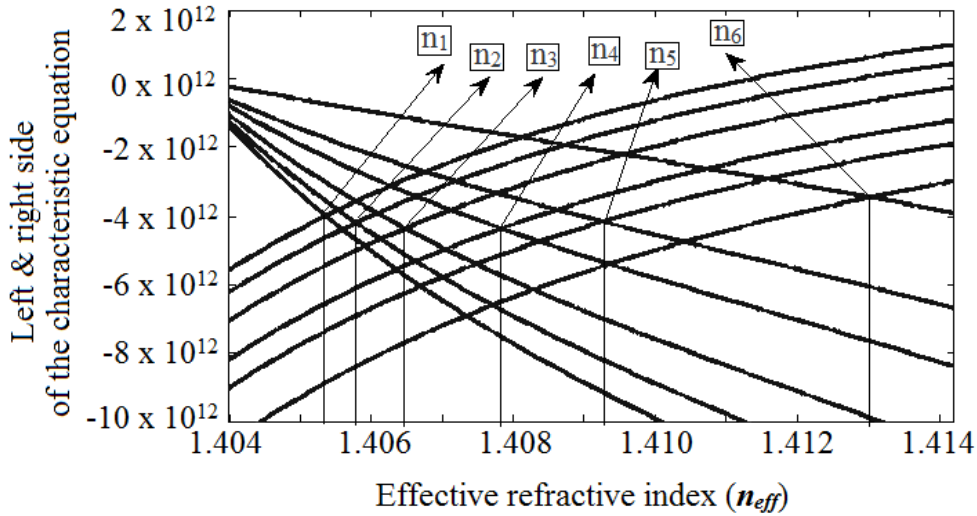


Fig. 6.2: Estimation of effective refractive index

6.1.2 Double clad cylindrical waveguide geometry

In this approach, the fiber geometry can be approximated with double clad cylindrical waveguide geometry. For a cylindrical geometry the axial field components for azimuthal order m can be written as [268]

$$\psi(r) = \left\{ \begin{array}{l} A_0 J_m \left(u \frac{r}{a} \right) ; (0 \leq |r| \leq a) \\ A_1 J_m \left(u' \frac{r}{a} \right) + A_2 Y_m \left(u' \frac{r}{b} \right) ; (a \leq |r| \leq b) \\ A_3 K_m \left(v \frac{r}{b} \right) ; (|r| \geq b) \end{array} \right\} \quad (6.7)$$

where J_m , Y_m and K_m are the usual and modified Bessel functions and A_0, A_1, A_2, A_3 are the field coefficients. The mode parameters u , u' and v are given as,

$$\begin{aligned} u &= ak_0 \sqrt{(n_{core}^2 - n_{eff}^2)} \\ u' &= bk_0 \sqrt{(n_{clad}^2 - n_{eff}^2)} \\ v &= bk_0 \sqrt{(n_{eff}^2 - n_{sur}^2)} \end{aligned} \quad (6.8)$$

The dispersion equation of the fiber with double cladding can be written by applying the boundary conditions i. e. continuity of the axial field and its derivative as [269],

$$\frac{[\hat{J}_m(u) - \hat{Y}_m(u'c)] [\hat{K}_m(v) - \hat{J}_m(u')]}{[\hat{J}_m(u) - \hat{J}_m(u'c)] [\hat{K}_m(v) - \hat{Y}_m(u')]} = \frac{J_{m+1}(u'c) Y_{m+1}(u')}{J_{m+1}(u') Y_{m+1}(u'c)} \quad (6.9)$$

where $c = a/b$ and

$$\hat{Z}_m(x) = \frac{Z_m(x)}{x Z_{m+1}(x)} \quad (6.10)$$

with $Z = J, Y$ and K

Eq. (6.9) can be simplified in following form as,

$$\frac{[u'c J_0(u) Y_1(u'c) - u J_1(u) Y_0(u'c)]}{[u'c J_0(u) J_1(u'c) - u J_1(u) J_0(u'c)]} = \frac{[u' K_0(v) Y_1(u') - v Y_0(u') K_1(v)]}{[u' K_0(v) J_1(u') - v J_0(u') K_1(v)]} \quad (6.11)$$

Eq. (6.11) can be solved using the same method as discussed in case of slab/rectangular geometry to find out the dependence of effective refractive index of the double clad fiber on cladding diameter and surrounding refractive index. If

$$\delta_1(n_{eff}) = [u'c J_0(u)Y_1(u'c) - u J_1(u)Y_0(u'c)] [u' K_0(v)J_1(u') - v J_0(u')K_1(v)] \quad (6.12)$$

$$\delta_2(n_{eff}) = [u' K_0(v)Y_1(u') - v Y_0(u')K_1(v)] [u'c J_0(u)J_1(u'c) - u J_1(u)J_0(u'c)] \quad (6.13)$$

Then

$$\delta_1(n_{eff}) = \delta_2(n_{eff}) \quad (6.14)$$

Using MATLAB software the Eq. (6.14) is solved numerically. Figure 6.3 show the curves plotted for $\delta_1(n_{eff})$ and $\delta_2(n_{eff})$ as a function of effective refractive index (n_{eff}). The intersection gives the value of effective refractive index for particular cladding diameter and surrounding refractive index. Figure 6.3 a, b, c and d show the intersection of the curves at 10 μm cladding diameter for surrounding medium refractive index of 1.0, 1.2, 1.3 and 1.42 respectively. The parameters chosen for the present numerical analysis are, $k_0 = 4.09 \times 10^6$, $a = 6 \mu\text{m}$, $b = 6 - 125 \mu\text{m}$, numerical aperture (NA) = 0.13, refractive index difference = 0.41%, refractive index of core (n_{core}) = 1.450, refractive index of cladding (n_{clad}) = 1.444, and surrounding medium refractive index (n_{sur}) = 1.0 to 1.44. The calculated variation in effective refractive index for different surrounding medium refractive index from 1.0 to 1.44 is shown in figure 6.4. In this figure, the change in Bragg wavelength with surrounding medium refractive index is also estimated from Eq. (6.11) and is plotted on the right side vertical axis. For a particular clad diameter, the effective refractive index increases with the increase in surrounding medium refractive index. From figure 6.3 (a, b, c and d) it is found that the refractive index sensitivity is higher for lower clad diameter fiber grating. The effective index (n_{eff}) of the guided TE modes can never be less than the cladding refractive index (n_{clad}). In our case also for un-etched FBG the n_{eff} is higher than the n_{clad} ($n_{clad} < n_{eff} < n_{core}$). But for the case of etched FBG the actual refractive index of the cladding ($n_{clad actual}$) is decided by n_{clad} and n_{sur} (in our case $n_{sur} < n_{clad}$). So for etched FBG the actual cladding index ($n_{clad actual}$) will be lower than the cladding index (n_{clad}) i.e. $n_{clad actual} < n_{clad}$.

In this case n_{eff} will be in between of n_{core} and $n_{clad actual}$ i.e. $n_{clad actual} < n_{eff} < n_{core}$. So the effective index of TE mode (n_{eff}) can be lower than the cladding index (n_{clad}).

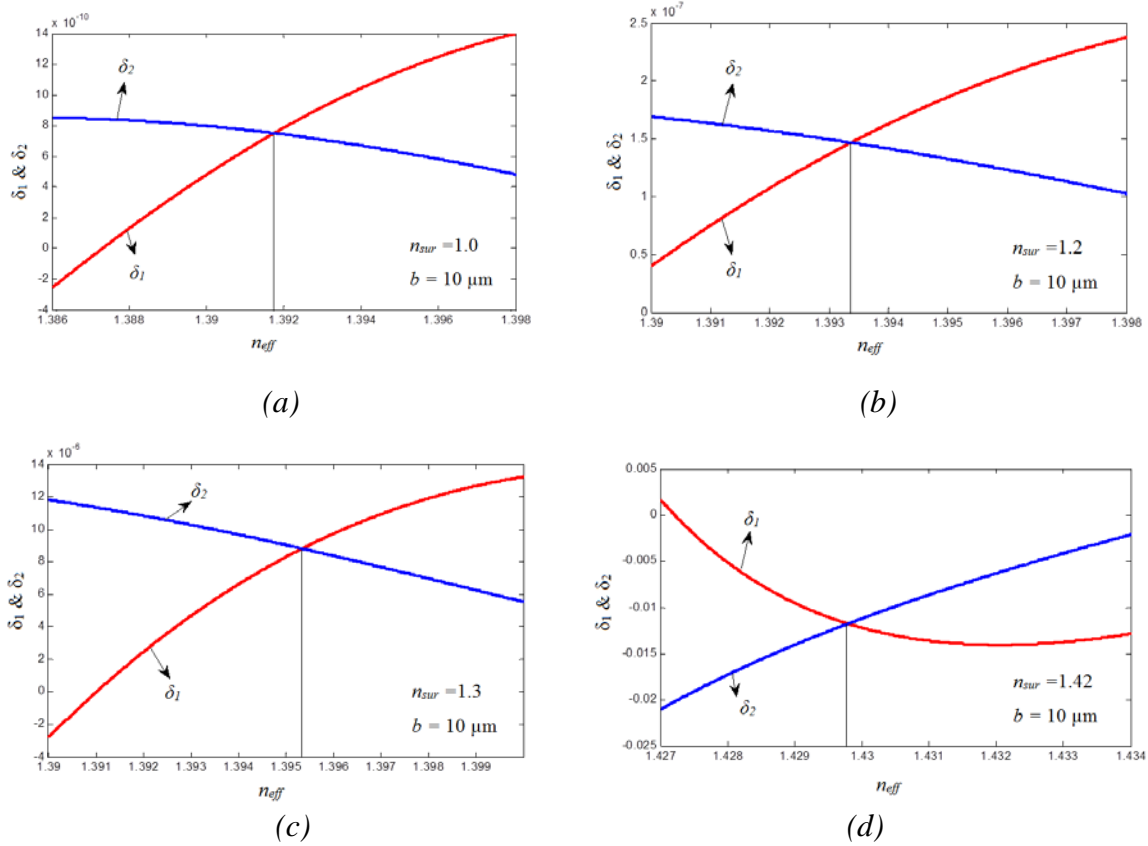


Fig. 6.3: Variation of δ_1 and δ_2 with n_{eff} for different surrounding refractive index ($n_{sur} = 1.0, 1.2, 1.3, 1.42$) at fixed clad diameter of $10 \mu\text{m}$

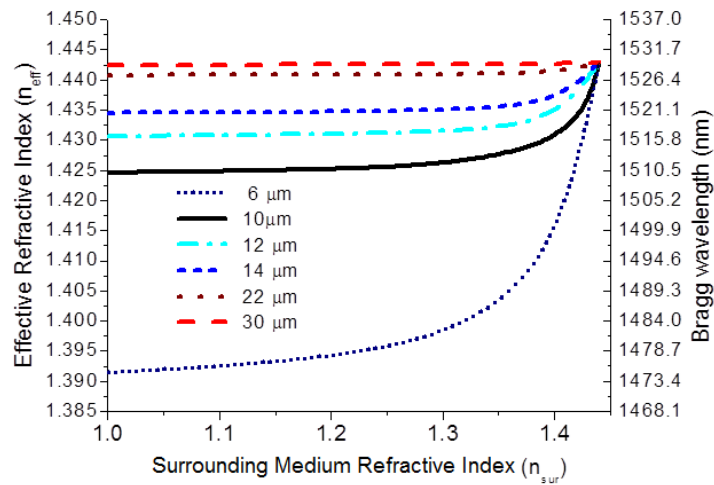


Fig. 6.4: Theoretical variation of effective refractive index (n_{eff}) of an EFBG with surrounding medium refractive index based on the algorithm defined in the text

6.2 Fabrication of etched FBG based refractive index sensors

The experimental set-up for HF based etching process and external medium sensing is shown in figure 6.5 (a and b). It comprises of a broad band ASE light source (1525 - 1600 nm), a directional 3 dB coupler to collect the reflected spectrum from the sensor head, and an optical spectrum analyzer (OSA) to monitor the changes in the Bragg grating reflection spectrum. HF is a highly corrosive acid, capable of dissolving many materials. Because of its high reactivity with glass and moderate reactivity with many metals, a Teflon container was used for the etching experiment. During the process of etching, the surrounding temperature was maintained at $25^{\circ}\text{C}\pm 1^{\circ}\text{C}$.

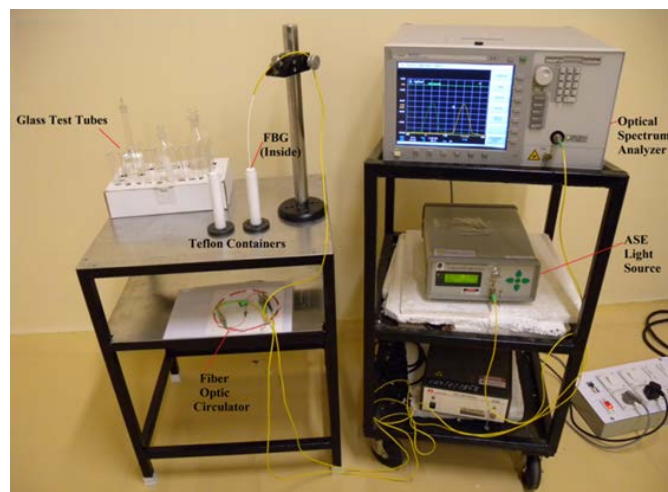
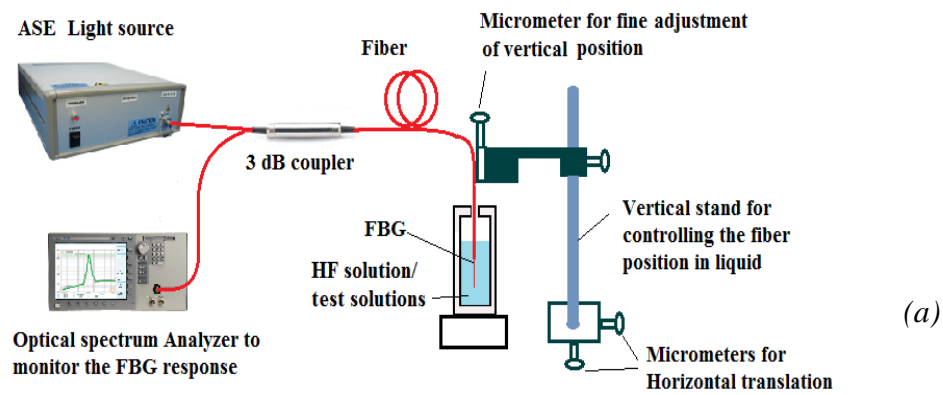


Fig. 6.5: (a) Schematic and (b) experimental set up for FBG clad etching/ refractive index sensing

The etching of the selected fiber region was carried out as follows. The fiber with FBG at one end is attached to a vertical mounting assembly fitted with precision micro-meter of travel range 25 mm (figure 6.5). The FBG is vertically immersed in this HF solution to a depth slightly larger than FBG length of 10 mm. The FBG (diameter ~ 125 μm) is dipped in the central portion of hollow cylindrical Teflon (I. D. ~ 10 mm, length ~ 100 mm) tube. The FBG remained vertical in the dipped solution due its much smaller diameter and length as compared to that of Teflon tube container. The FBG etching is uniform as confirmed by imaging with microscope. HF etching of the FBGs was carried out for two important applications (i) Dye concentration sensing useful in laser and textile industry and (ii) Methanol adulteration measurement useful in beverage industry. For this purpose two FBGs written in two different fibers were etched using HF solution. For the first FBG (FBG-DCS-Dye Concentration Sensing) the etching process is carried out in single step and for second FBG (FBG-MAS-Methanol Adulteration Sensing) the etching is carried out in two steps.

6.2.1 Single step HF-etching of FBG

Fiber Bragg grating (FBG-DCS) of length 10 mm was written in photosensitive fiber PS-1250. The exposed region where the gratings are formed is etched with 40% HF in single step. As the optical fiber without coating layer is immersed in an etching liquid, the cladding is etched gradually and the cladding radius decreases. Figure 6.6 shows the microscopic view (Stereoscopic Zoom Trinocular microscope make- Censico Model-STB-X-B) of the FBG cladding (a) before etching and (b) after etching. The intensity variation across the diameter is obtained using ImageJ software. The intensity variation is used to estimate the cladding diameter. Due to HF etching of about 32 minutes the FBG cladding diameter reduced from 125 μm to 62 μm . During etching the Bragg wavelength of the grating was monitored as a function of

time. Typical OSA traces of Bragg peak wavelength (traces) with etching time $t_1 \sim 0$ min, $t_2 \sim 20$ min, $t_3 \sim 24$ min, $t_4 \sim 28$ min and $t_5 \sim 32$ min are shown in figure 6.7. Figure 6.8 shows the change in Bragg wavelength and clad diameter with etching time.

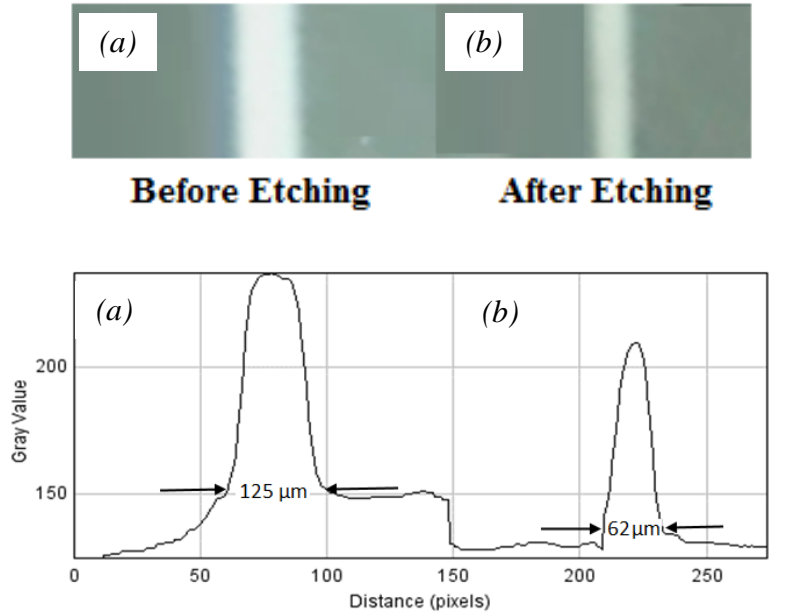


Fig. 6.6: Microscopic view of FBG cladding (a) before etching (b) after etching

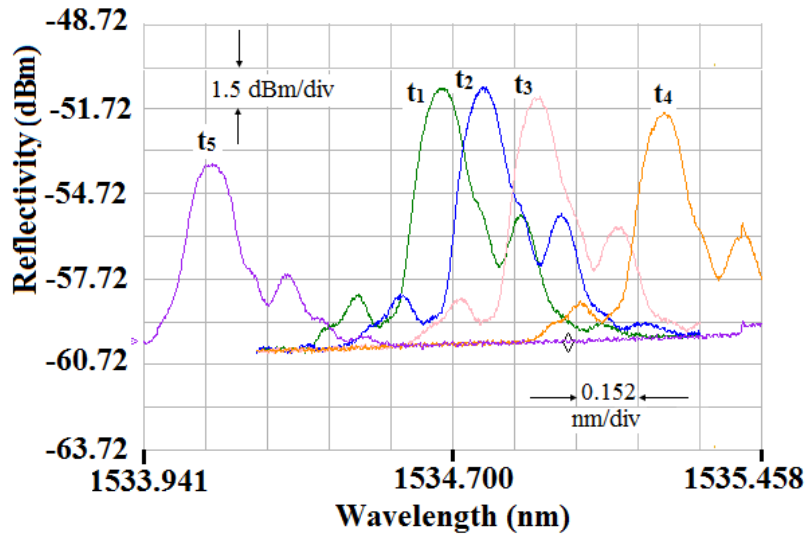


Fig. 6.7: OSA traces of Bragg wavelength shift with etching time ($t_1 < t_2 < t_3 < t_4 < t_5$)

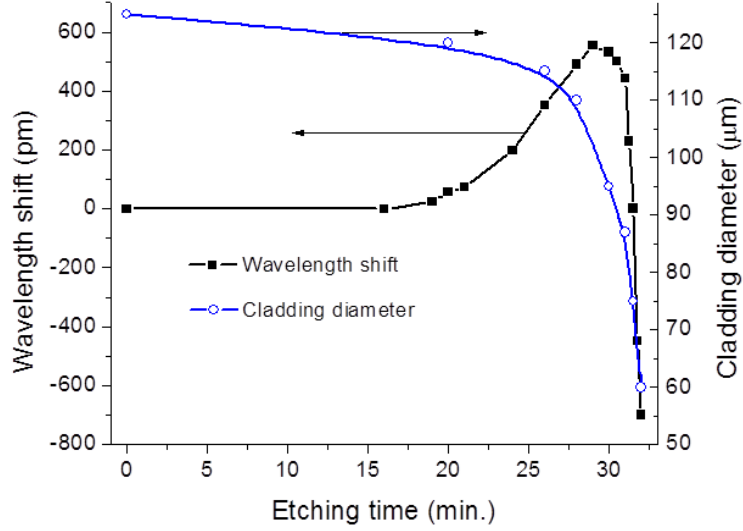


Fig. 6.8: Change in Bragg wavelength and clad diameter as a function of etching time

The Bragg wavelength shifted from 1534.670 nm to 1535.225 nm in 30 min and from this point to 1533.97 in next 2 min. The initial increase in Bragg peak is due to generation of heat caused by chemical reaction of HF with silica glass. After 30 minutes, the Bragg peak started to decrease as a consequence of decrease in effective refractive index caused by cladding diameter reduction. The average etching rate of cladding diameter is around 2.03 $\mu\text{m}/\text{min}$. The change in the Bragg wavelength associated with the chemical etching is given by [141-144],

$$\delta\lambda_B = 2 \Lambda \delta\eta (n_{sur} - n_{cl}) \quad (6.15)$$

where Λ is grating period, $\delta\eta$ is the change in the fraction of the total power of the unperturbed mode that flows in the etched region, n_{cl} is cladding refractive index and n_{sur} is surrounding medium refractive index. From above equation, it is clear that the difference in the surrounding medium refractive index and clad refractive index decides the Bragg peak wavelength shift. It is clear that Bragg wavelength increases slowly with etching time but after 30 min it decreases rapidly.

6.2.2 Double step HF-etching of FBG

The HF etching process is very fast with high concentration HF solution. Therefore for more controlled etching, two step etching process has been adopted. Fiber Bragg grating of ~10 mm length is written in CMS-1550-R1 photosensitive fiber. The exposed region, where the FBG is inscribed, is etched in two steps using HF solutions of concentration 40 % and 10 %. In the first step, the etching was carried out for 45 minutes using 40% HF solution. The optical fiber without protective coating is immersed in this HF solution and the clad is etched gradually and its diameter reduces. The Bragg wavelength shift of the grating is monitored with time as shown in figure 6.9 and 6.10. During the etching time the Bragg wavelength shifted from 1533.311 nm to 1532.906 nm. For this duration the maximum rate of wavelength shift is ~ 40 pm/min. After this point the etching is carried out using 10 % HF solution to avoid the drastic dissolution of the FBG. The Bragg wavelength shifted from 1532.906 nm to 1520.41 nm in 10 minutes with an initial rate of 43 pm/min and final rate of 8590 pm/min.

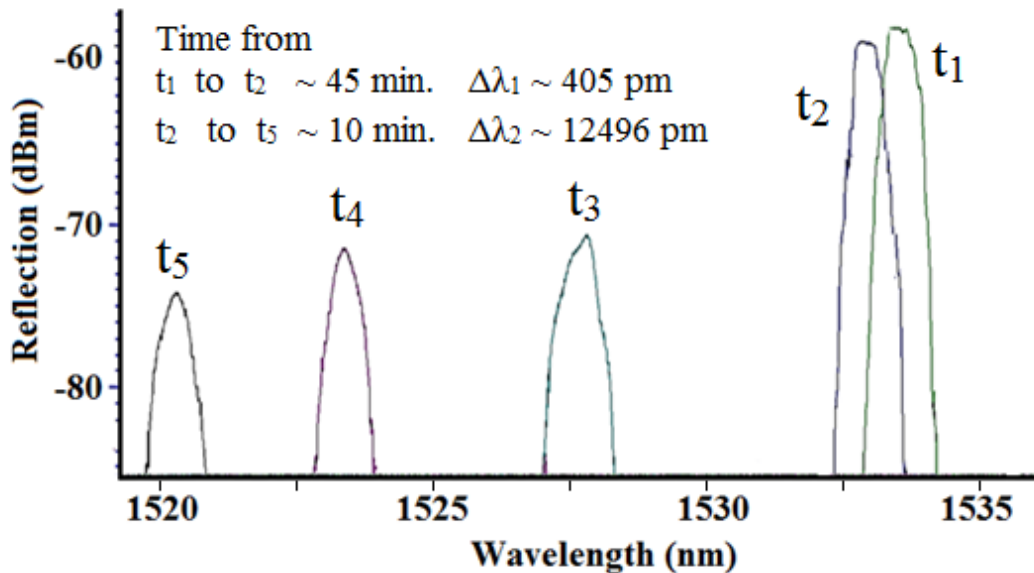


Fig. 6.9: OSA traces showing Bragg wavelength shift with etching time (t_1 to t_5)

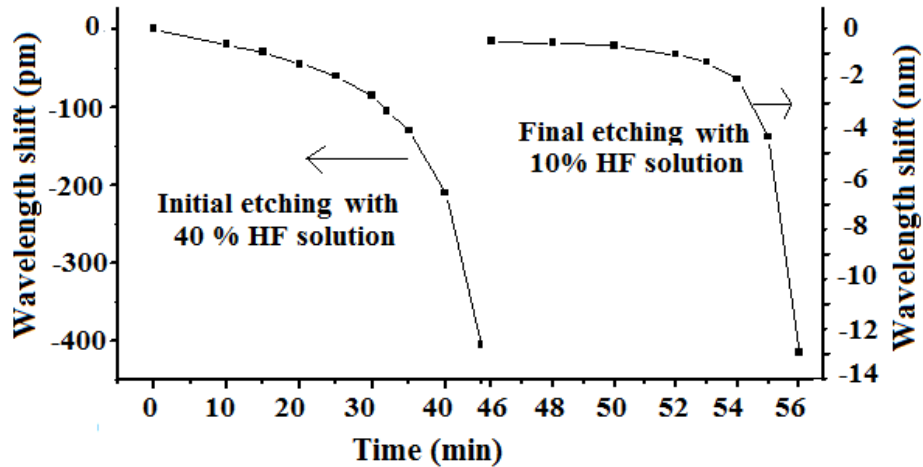


Fig. 6.10: Shift in Bragg wavelength with etching time observed during experiment

The diameter of the FBGs was measured by optical microscope (Leica DMC 2900). Microscopic images of optical fiber before and after the HF etching and their intensity variation (obtained using ImageJ software) across the diameter is shown in figure 6.11. The cladding diameter reduced from 125 μm to 15 μm due to HF etching.

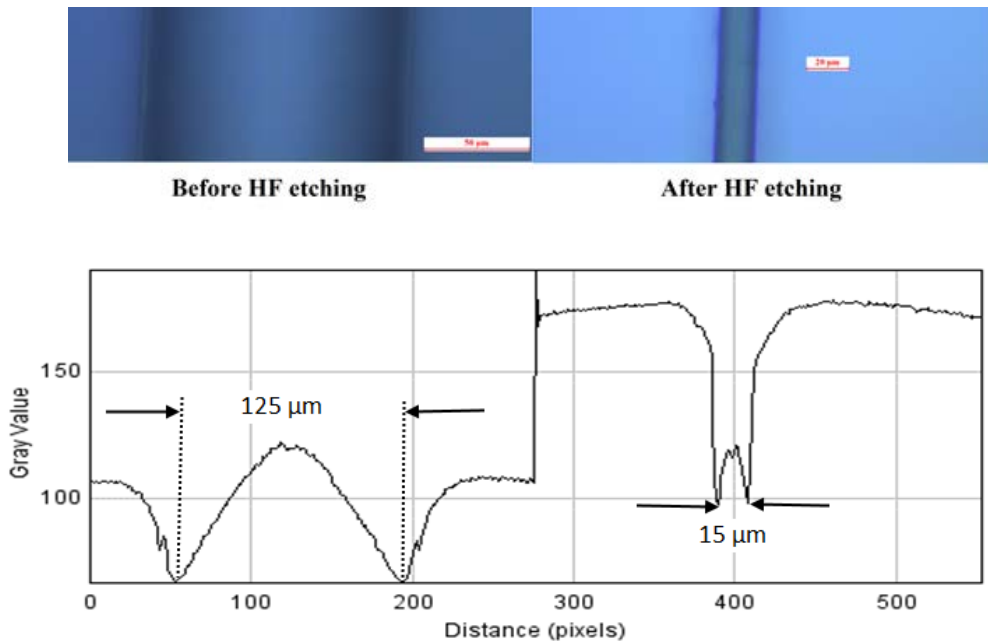


Fig. 6.11: Microscopic images of the optical fiber before and after HF etching

6.3 Experimental verification of the theoretically calculated effective refractive index at different cladding diameter

The variation in effective refractive index (Bragg wavelength on right side vertical axis) with cladding diameter using both the approaches i.e. cylindrical approximation and the rectangular piped approximation is plotted in figure 6.12. It is clear from the graph that as the cladding diameter reduces the effective refractive index of the fiber decreases. Hence the Bragg wavelength shifts to lower λ . In both the approaches, the trends of the curve are well matched except for the slight variation in the saturation level at large diameters. In cylindrical equivalent geometry approach of the fiber, the effective refractive index changes from 1.4464 to 1.4201 as the cladding diameter changes from 125 μm to 6 μm . From the slab waveguide approach the effective refractive index changes from 1.4439 to 1.4232 for the same change in the cladding diameter. So the refractive index estimated by the waveguide approach is lower by 2.5×10^{-3} at 125 μm cladding and higher by 3.2×10^{-3} at 6 μm cladding diameter from that estimated by cylindrical geometry or Bessel function approach. Experimentally observed Bragg wavelength shift during HF based clad etching of FBG is also shown in figure 6.12. It is evident from the figure that at higher cladding diameter ($> 25 \mu\text{m}$) the effective refractive index values obtained by Bessel function approach are quite close to those experimentally observed results. At lower cladding diameter ($< 25 \mu\text{m}$) the experimental data points are well explained by both the approaches i.e. Bessel function approach and planar waveguide approach. So for the case of rectangular piped geometry, the deviation in the effective refractive index from the experimental observed data increases as the cladding diameter increases. At 15 μm cladding diameter this deviation was 0.05% which increased to 0.18% at 100 μm .

Initially, we used a simpler geometry “rectangular piped” for explaining our experimentally observed results. To explain the difference between theoretical and experimental results the actual cylindrical geometry was used for calculation which provided very well matching with the experimental data. At lower cladding diameter ($< 25 \mu\text{m}$) the experimental data points are well explained by both the approaches i.e. Bessel function approach and planar waveguide approach. In case of rectangular piped geometry, the deviation in the effective refractive index from the experimental observed data increases as the cladding diameter increases. Here we have shown that both approaches can be used to explain the results for lower cladding diameter ($< 25 \mu\text{m}$). We have included both the results for the completeness of the analysis.

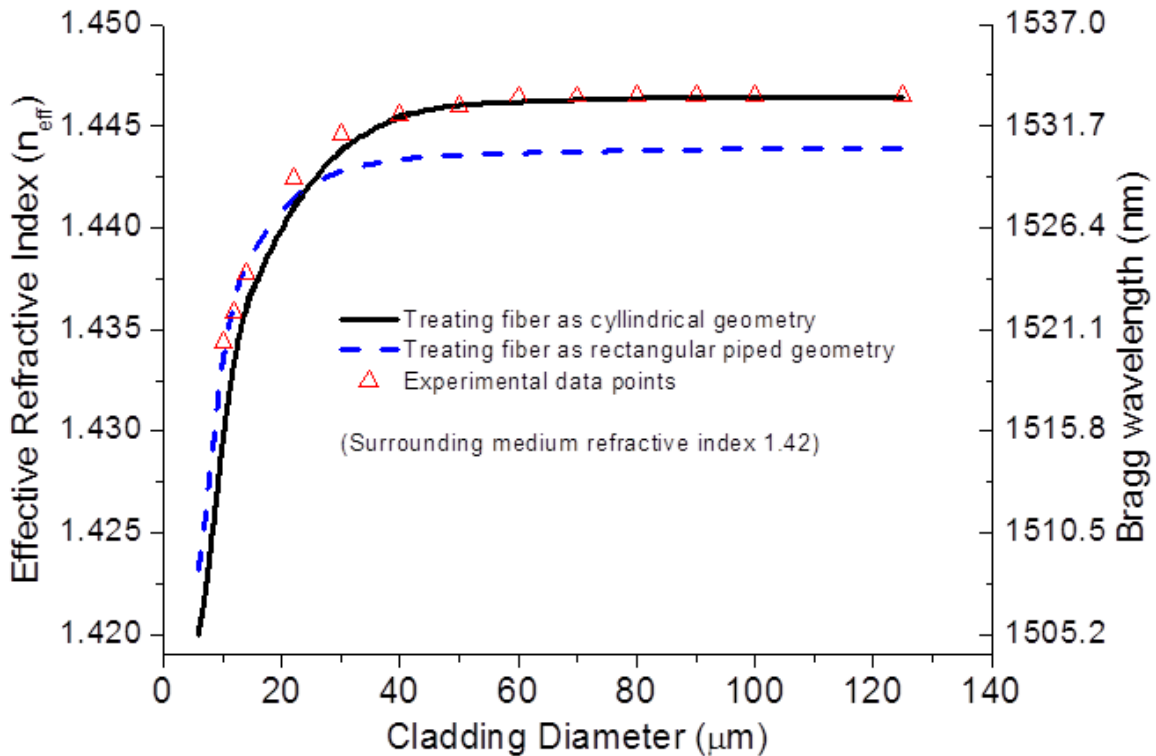


Fig. 6.12: Effective refractive index of an EFBG with different cladding diameter - calculated and experimental data

6.4 Etching characteristics of FBGs of different reflectivity

6.4.1 Experimental results

To study the role of FBGs reflectivity on the etching characteristics, two FBGs of same length (10 mm) but of different reflectivity are written by controlling the UV exposure time. These FBGs with Bragg wavelengths (i) 1533.948 nm at reflection 0.5 dB (11% reflectivity, FBG-F1) and (ii) 1534.714 nm at reflection 11.5 dB (93 % reflectivity, FBG-F2) are made at the ends of two single mode photosensitive fibers. The FBG reflectivity is directly related with the UV exposure time on the fiber. The exposure time for FBG-F1 was 15 sec and that for FBG-F2 was 10 min. The number of laser pulses used for writing the FBG-F1 and FBG-F2 were 82500 and 3300000, and corresponding total accumulated fluence were 0.15 kJ /cm^2 and 5.94 kJ /cm^2 respectively. For the further discussion, we refer FBG-F1 and FBG-F2 for FBG of reflectivity 11% and 93% respectively.

The UV exposed region of the gratings is etched with 40% HF solution. Etching of both the FBGs is carried out simultaneously in the same HF solution for the first 35 minutes. After 35 minutes, both the FBGs are etched separately in the same HF solution without changing the surrounding conditions. Thereafter, gratings are withdrawn each time to measure their cladding diameters. As the similar procedures are followed for both gratings, the etching conditions were same. The experimental set-up for HF based etching process and external medium sensing is shown in figure 6.5. The shift in the Bragg wavelength is recorded with respect to etching time. Figure 6.13 shows the Bragg wavelength shift with respect to etching time for FBG-F1 and FBG-F2. The initial increases in Bragg peak is due to generation of heat caused by chemical reaction of HF with silica glass. After 35-40 minutes Bragg peak started to decrease as a consequence of decrease in effective refractive index caused by cladding diameter reduction.

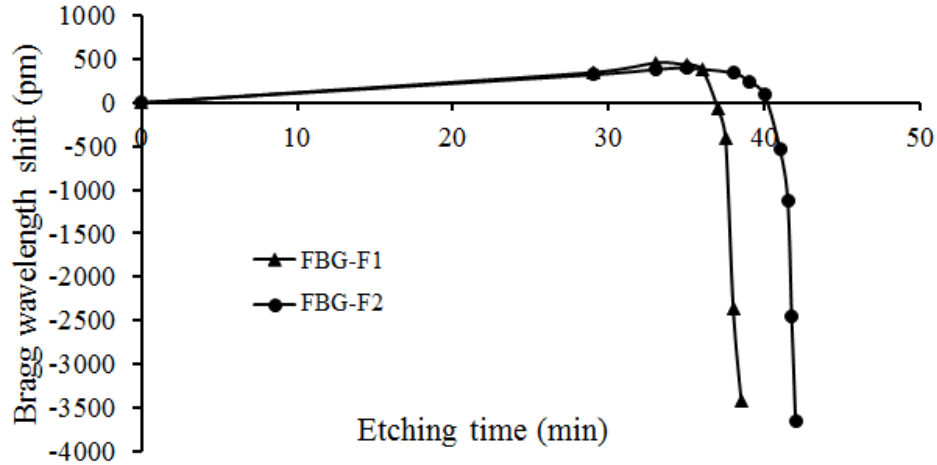


Fig. 6.13: Bragg wavelength shift with etching time

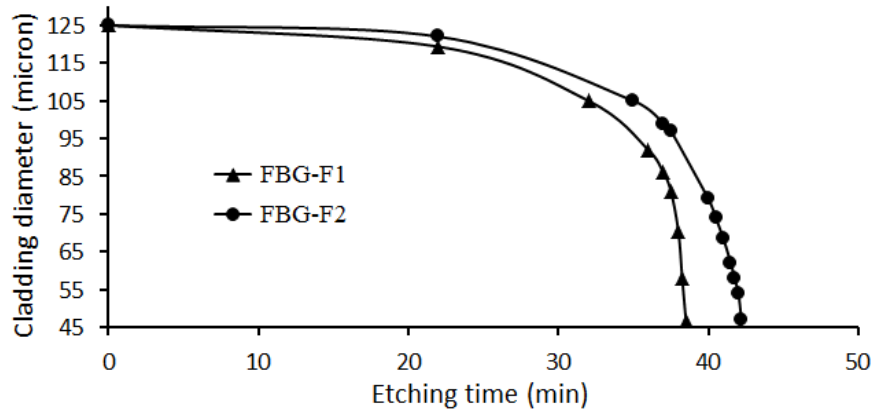


Fig. 6.14: Cladding diameter as a function of etching time

It is clear from the figure 6.13 that for FBG-F1, the Bragg wavelength shifted from 1533.948 nm to 1534.406 nm in 35 min and after this the Bragg peak shifted drastically to 1530.879 in the next 3 min. But in case of FBG-F2 the Bragg wavelength shifted from 1534.714 to 1534.990 nm in 39 min and from this point to 1532.267 nm in next 3 minutes. Figure 6.14 shows the variation of cladding diameter of the FBG vs etching time for both the gratings. For both FBGs, the etching was stopped after reaching the cladding diameter of around 47 μm from initial diameter 125 μm . It is clear from figure 6.14 that for FBG-F1, the decreasing in the cladding diameter was faster compared to FBG-F2. The average etching rate of cladding diameter for FBG-F1 and FBG-F2 were 2.03 $\mu\text{m}/\text{min}$ and 1.69 $\mu\text{m}/\text{min}$ respectively.

6.4.2 Discussion for the different behaviour

The observed difference in the etching behaviour of two FBGs may be explained on the basis of densification of fused silica upon UV exposure. In phase mask based FBG writing, the induced average refractive index and refractive index modulation profiles in the photosensitive fiber changes by the continuous exposure of UV fringes [270-271]. These exposure leads to change in the refractive index of clad as well as core. However the refractive index change in the core occurred mainly due to creation of defect centers formed by Ge/Bo co-doping [230]. Also, the two photon ionization process is believed to be the catalyst for UV induced densification in fused silica as the bandgap of fused silica is around 8.3 eV [272-273]. For a two photon ionization process, the absorbed two photon dose of UV is given by [274-275]

$$D_{\alpha} = \alpha \frac{NI^2}{\tau} \quad (6.16)$$

where α is the two photon absorption coefficient of UV beam in silica ($\sim 30 \text{ cm}^{-1}$ at 248 nm), N is the number of laser pulses in million, I is the pulse energy density (mJ/cm^2) and τ is effective pulse duration (ns) of the UV laser beam. The induced densification due to absorbed UV dose is given by [274-275]

$$\frac{\Delta\rho}{\rho} = a(D_{\alpha})^b \quad (6.17)$$

Pre-factor ' a ' and exponent ' b ' are decided by numerical fitting of the experimental data. In the reported literature these factor are not available for 255 nm. However, for 193 nm, these pre-factors are available for both un-doped and doped (photosensitive) fused silica [275]. Also, for 248 nm exposure, it is indicated that the fused silica densification will be about 10 times smaller than that of 193 nm [275-276]. Since 255 nm is very close to 248 nm, therefore it is expected value of ' a ' and ' b ' will be almost same as that for 248 nm. At 193 nm UV exposure, the typical reported values of ' a ' and ' b ' for fused silica (clad) are, $a=0.27$, $b=0.57$ and $a=45.5$, $b=0.57$ for

a highly photosensitive silica (core) [275]. For the assumed 193 nm exposure, in the case of present experiment with UV beam pulse energy density $I=1.8 \text{ mJ/cm}^2$, $N= 0.08$ million for FBG-1 and $N = 3.3$ million for FBG-2, and pulse width $\tau =10$ ns, the estimated clad densification ($\Delta\rho/\rho$) for FBG-1 and FBG-2 are 0.034 ppm and 0.2805 ppm respectively. Also, the estimated densification in the photosensitive core for FBG-1 and FBG-2 are 5.77 ppm and 47.27 ppm respectively. For the actual 255 nm beams, the densification values will be about ten times lower as that of estimated for 193 nm i.e. 0.577 ppm for FBG-1 and 4.727 ppm for FBG-2. Hence the clad or core densification for FBG-2 will be higher as compared to FBG-1. It has been shown that the etching rate of silica in HF acid drastically decreased with densification [277]. Hence the etching rate of FBG-2 will be slower as compared to FBG-1 as observed experimentally indeed.

A differential form of the Lorentz-Lorenz equation shows that the change in refractive index is associated with the change in densification by following relation [278]

$$\frac{\Delta n}{n} = \left(\frac{\Delta\rho}{\rho} \right) (1 + \Omega) \frac{(n^2-1)(n^2+2)}{6n} \quad (6.18)$$

where n is the refractive index of silica clad (~ 1.45) and Ω is the ratio of the relative change of the polarizability to the relative density change (~ -0.18 for fused silica) [279]. For the present case of 255 nm exposure, the estimated change in the refractive index ($\Delta n/n$) in the clad for FBG-1 and FBG-2 are 0.012×10^{-7} and 0.13×10^{-7} , respectively. While in the core, the change in refractive index ($\Delta n/n$) for FBG-1 and FBG-2 are 2.5×10^{-7} and 20.1×10^{-7} , respectively. However, these estimated ($\Delta n/n$) values are only approximate as the refractive index changes may differ from the actual values due to several factors such as residual cladding photosensitivity [280], percentage of OH in silica [279] and variation in doping of photosensitive core from fiber to fiber. It is expected that there will be change in the clad/core diameter due to UV laser induced densification. However, the main factor responsible for refractive index changes in the

core is creation of defect centres formed in the photosensitive core [270-271]. Due to this mechanism, the refractive index change in the core of FBG-1 and FBG-2 (estimated from the reflectivity of FBGs) are 1.7×10^{-5} and 9.8×10^{-5} respectively.

6.5 Etching characteristics of thermally regenerated FBGs

6.5.1 Inscription and thermal regeneration of the FBG

Three Type-I FBGs are inscribed in hydrogen loaded ($P = 100$ bar, $T = 100$ °C, duration ~5 days) germanosilicate fiber (SM-1500) as discussed in **Chapter 2**. These UV inscribed Type-I gratings are known as seed FBG. Figure 6.15 (a-b) shows the typical transmission spectra for one of the seed FBG and resulting regenerated FBG, respectively.

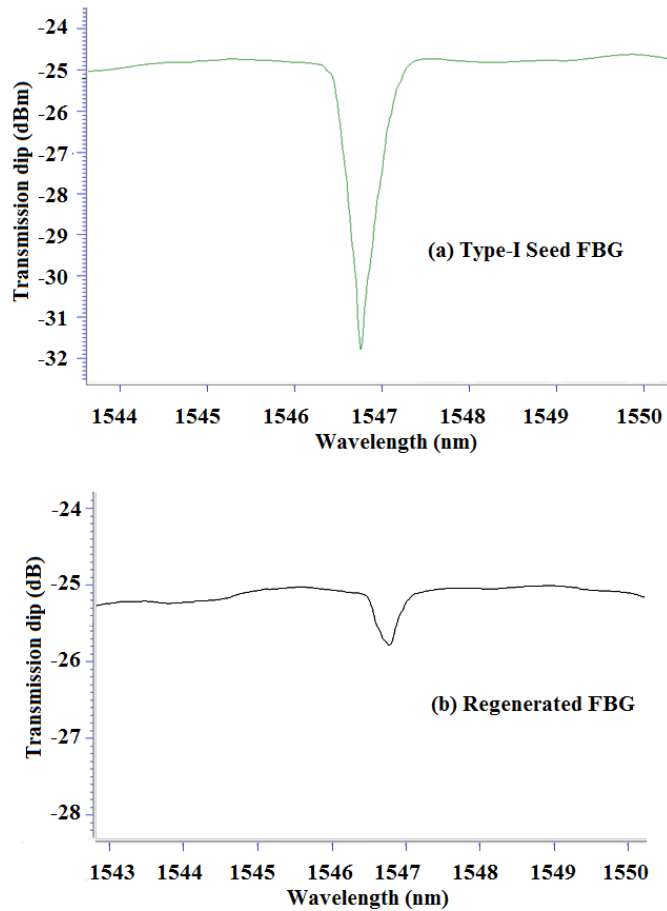


Fig. 6.15: Typical OSA transmission spectra of (a) Type-I seed FBG and (b) RFBG

From the transmission dip (~ 7.2 dB), the reflectivity (R) of the seed FBGs are estimated to be $R \sim 81\%$ and almost same for all three FBGs. For partially annealed or thermally regenerated FBGs, the step annealing schedule is applied as discussed in **Chapter 4** and shown in figure 6.16 (right y-axis). The three initial FBGs used in the study for etching and chemical sensing are marked as A, B and C as shown in figure 6.16.

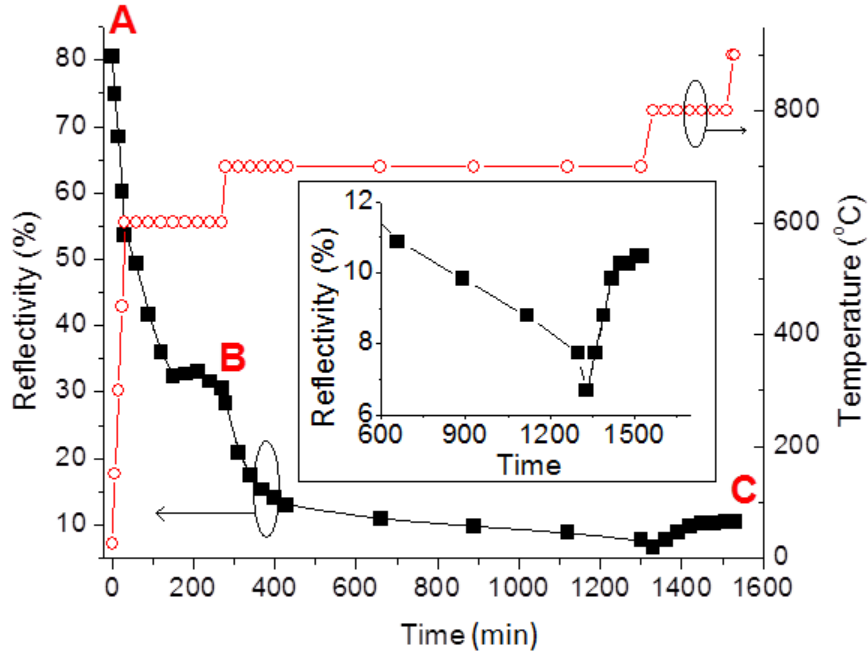


Fig. 6.16: Annealing schedule and regeneration of grating

Here, the temperature refers to the temperature (T) of surface of fused silica tube placed in oven as measured by thermocouple. The FBG is placed on the inside surface of the fused silica tube. For FBG temperature treatment, the dwell time (t_{dwell}) refers to the dwell (resident) period of FBG in oven with constant temperature. FBG-A is a non-annealed grating (without heating). The reflectivity of this non-annealed FBG-A was $R \sim 81\%$. FBG-B is maintained at $T = 600^\circ\text{C}$ for $t_{\text{dwell}} = 4$ hrs. The FBG-B reflectivity decreased from $R \sim 80.6\%$ (~ 7.1 dB) to $R \sim 53.7\%$ (3.3 dB) as the temperature increased from $T = 30^\circ\text{C}$ to 600°C in about 30 minutes. At $T = 600^\circ\text{C}$, the FBG B reflectivity dropped from $R \sim 53.7\%$ to 30.5% in $t_{\text{dwell}} = 240$ min. The FBG-B

was removed from the oven at this stage. This drop in FBG reflectivity on prolonged heating may be explained as follows. The FBG reflectivity depends directly on the modulation amplitude of the refractive index induced in the fiber core by the UV writing. A slow decay of this modulation amplitude is expected from relaxation of some unstable defects due to heating of FBGs as thermal deactivation of these defects is the most important source of grating degradation [231-239]. As the FBG temperature is elevated, the decay of refractive index modulation is higher leading to reduced FBG reflectivity [231]. FBG-C is regenerated FBG obtained via multi-step annealing process of Type-I seed FBG (similar to FBG-A) upto $T = 900$ °C in following four steps with different dwell times,

Step 1: $T = 600$ °C; $t_{\text{dwell}} = 240$ min (~ 4 hr).

Step 2: $T = 700$ °C; $t_{\text{dwell}} = 1020$ min (~ 17 hr).

Step 3: $T = 800$ °C; $t_{\text{dwell}} = 180$ min (~ 3 hr).

Step 4: $T = 900$ °C; $t_{\text{dwell}} = 30$ min (~ 1/2 hr).

At the end of step 1, the reflectivity of FBG-C was almost same as FBG-B. Further raising temperature to $T = 700$ °C, the reflectivity reduced from $R \sim 28.2\%$ to $R \sim 7.7\%$ in $t_{\text{dwell}} = 1020$ min. At $T = 800$ °C, reflectivity further decreased to $R \sim 6.67\%$ before starting to increase. This is indicative of the regenerated FBG (inset of figure 6.16). The regenerated FBG (FBG-C), reached, $R \sim 10.5\%$ in $t_{\text{dwell}} = 180$ min. The reflectivity of the regenerated FBG-C was almost constant with further temperature increase from $T = 800$ °C to $T = 900$ °C, dwelling for $t_{\text{dwell}} = 30$ min. The regeneration is likely due to the glass structural transformation arising from stress relaxation between fiber core and cladding at high temperatures [167, 250, 281-282]. Also, the three FBGs (A, B and C) will be having different stress between clad and core due to different annealing temperature and dwell times. These experiments on FBG-A, FBG-B and FBG-C were

repeated on three sets of same fiber. The results on FBG reflectivity were same within the measurement resolution.

A fourth non-annealed Type-I FBG-D of similar strength to the final regenerated grating (FBG-C) of $R \sim 11\%$ (~ 0.5 dB) was also fabricated by controlling the UV exposure time. This grating was etched and used in chemical sensing. The FBG-D is specifically fabricated to determine the role of FBG strength alone in affecting sensor response from all grating types after HF etching [283] and therefore whether there is an additional factor responsible for different performance observed with the regenerated FBG.

6.5.2 HF based clad etching of fiber gratings

All four gratings FBG-A, FBG-B, FBG-C and FBG-D were etched in hydrofluoric (HF) acid. The experimental set-up for monitoring HF etching process comprised of a broadband ASE source, a 3 dB directional coupler to collect the reflected spectrum from the sensor head and an optical spectrum analyzer (OSA) as shown in figure 6.5. The UV exposed region of the gratings is etched with 40% HF solution. The Bragg wavelength, λ_{Bragg} , and reflected power of the gratings are monitored with time as shown in figure 6.17 and 6.18 at constant room temperature of 25°C. After repeating experiment three times, the standard deviations in the wavelength shift for all FBGs are estimated to be within 10 pm. As the FBG wavelength shifts are much larger in comparison to standard deviation, it was not possible to indicate the uncertainty (standard deviation) in figure 6.17. However small portion on the graph is expanded (inset of figure 6.17) to show the uncertainty.

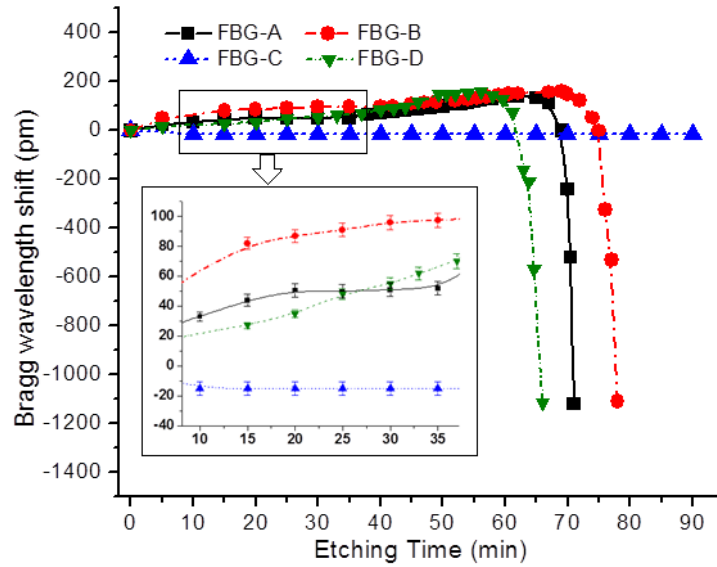


Fig. 6.17: Bragg wavelength shift during HF etching

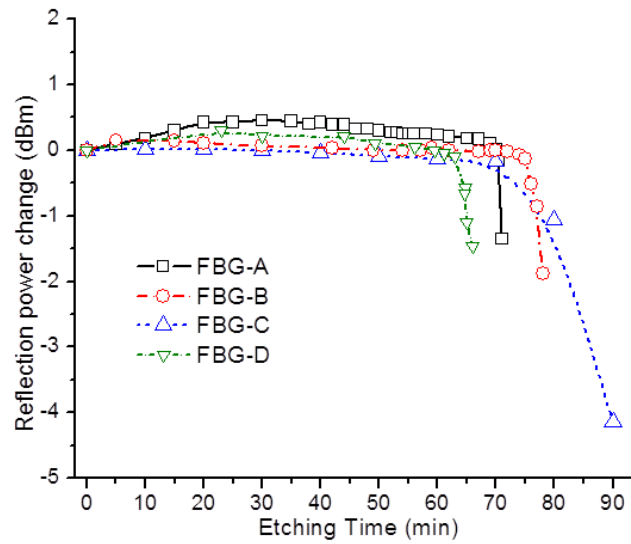


Fig. 6.18: FBG reflection power shift during HF etching

From this data, we can extract the following changes in wavelength and reflectivity:

FBG-A: $\Delta\lambda_{\text{Bragg}} \sim 1.12 \text{ nm}$; $\Delta R_p \sim -1.35 \text{ dBm}$

FBG-B: $\Delta\lambda_{\text{Bragg}} \sim 1.11 \text{ nm}$; $\Delta R_p \sim -1.88 \text{ dBm}$

FBG-C: $\Delta\lambda_{\text{Bragg}} < 0.005 \text{ nm}$; $\Delta R_p \sim -4.15 \text{ dBm}$

FBG-D: $\Delta\lambda_{\text{Bragg}} \sim 1.12 \text{ nm}$; $\Delta R_p \sim -1.45 \text{ dBm}$

The regenerated grating (FBG-C) shows unusual behavior to that of Type-I gratings with and without lower temperature annealing. FBG-D has the same reflectivity of the regenerated FBG-C and clearly highlights the difference with the regenerated FBG. It shows a similar wavelength shift of $\Delta\lambda_{\text{Bragg}} \sim 1.12 \text{ nm}$ as the non-annealed grating (FBG-A) of $\Delta\lambda_{\text{Bragg}} \sim 1.12 \text{ nm}$. By contrast, the regenerated grating (FBG-C) has a negligible $\Delta\lambda_{\text{Bragg}} < 5 \text{ pm}$. The diameter of the etched FBGs is measured by optical microscope (Leica DMC 2900) by placing these longitudinally. Figure 6.19 shows the images of the fibers at 50X magnification for the etched FBGs and their intensity variation (obtained using ImageJ software) across the diameter. The uniformity of the fiber etching is checked by comparing the images of etched fiber and that of same fiber rotated by about 90° . The measured diameters are within the accuracy of $\pm 1 \mu\text{m}$ confirming circularity of the etched fiber.

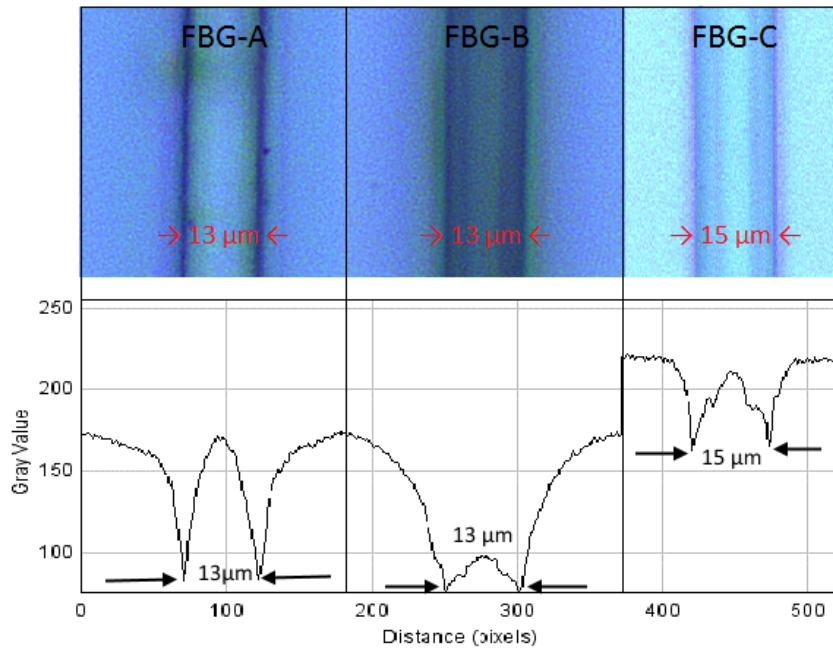


Fig. 6.19: Microscopic images of the etched FBGs and their intensity profile

The measured diameters of the etched FBGs are $(13 \pm 1) \mu\text{m}$, $(13 \pm 1) \mu\text{m}$ and $(15 \pm 1) \mu\text{m}$ for FBG-A, FBG-B and FBG-C, respectively. For all the cases, the etching depth does not

reach the core which has a diameter of $\phi \sim 4.0 \mu\text{m}$. This is evident from the clear discrimination of core and clad boundary for etched FBGs (B and C) after thermal heating (Figure 6.19). The contrast between core and cladding is clearly visible due to different values of refractive index.

6.5.3 Discussion about the different behavior of FBGs during etching

(A) Different etching time of the FBGs

Figure 6.17 indicates that the etching time and wavelength shift is different for different FBGs. Almost the same cladding diameter is achieved in FBG-A and FBG-B with different etching times. The cladding diameter reached due to HF etching was $d = 13 \mu\text{m}$ in $t = 70 \text{ min}$ for FBG-A, $d = 13 \mu\text{m}$ in $t = 80 \text{ min}$ for FBG-B and $d = 15 \mu\text{m}$ in $t = 90 \text{ min}$ for FBG-C. For FBG-B annealed at $600 \text{ }^\circ\text{C}$, and for the regenerated grating annealed at $800 \text{ }^\circ\text{C}$, the etching rate appears lower than the non-annealed FBG-A indicating the hardening of the fiber to chemical etching. The possible reason for hardening of fiber is the increased densification due thermal heating [284-286] as well as changes in surface stresses. It is expected that FBG-C will be more hardened as compared to FBG-B and FBG-A due to longer period of heating at higher temperatures. This is likely to be the cause of longer etching time for FBG-C as compared FBG-A, FBG-B and FBG-D despite being of same clad diameter.

(B) Different wavelength shift of the etched FBGs

The other related aspect is the different Bragg wavelength shift during HF etching. These values are $\Delta\lambda_{\text{Bragg}} \sim 1.12 \text{ nm}$, 1.11 nm , 1.12 nm and 5 pm for FBG-A, FBG-B, FBG-D and FBG-C respectively. In common optical fiber, the fundamental mode is practically not disturbed by the refractive index of medium surrounding the cladding. However, if the cladding diameter is reduced, the effective index of core shows the nonlinear dependence on the external refractive index, leading to shift in Bragg wavelength [287, 200]. Since the fiber clad diameter of all

etched FBGs (A-D) are almost similar, the almost negligible wavelength shift in FBG-C as compared to FBG-A, FBG-B and FBG-D needs to be explained. During inscription of type-I grating, a strong axial stress is developed in core of the fiber. This axial stress leads to change in the average refractive index of the optical fiber and hence the Bragg wavelength. After etching of an FBG, the remaining cladding is likely to feel the higher stress from the core which affects both the core and cladding indices. This leads to a stress-optic contribution to the effective cladding index [288]. So the Bragg wavelength of an FBG changes due to the change in this stress-optic contribution. The possible additional factor which influence the Bragg wavelength shift is the relaxation of stress between core and cladding. This stress relaxation is depended on whether the FBG is normal, partially annealed (before regeneration temperature) and regenerated FBG. For thermally regenerated FBG-C, the stress is relaxed at core-clad interface and also between UV fringe exposed and unexposed region of the core. Hence during the etching of thermally regenerated grating, the Bragg wavelength was not shifted as no any further stress relaxation occurred. However for non-annealed FBG-A or partially annealed FBG-B, the stress between core and cladding will change as the clad diameter reduces with HF etching.

6.6 Conclusion

The experimental results on the HF based clad etching of FBG are analyzed based on double clad approximation theory for cylindrical/rectangular waveguide geometry. A graphical method is used estimate the dependence of effective refractive index of the double clad fiber on cladding diameter and on surrounding refractive index. The effective refractive index is almost unaffected, by the surrounding medium refractive index, for cladding diameter reduction from 125 μm to 30 μm . Below 30 μm clad diameter, the effective refractive index increased with increase in surrounding medium refractive index. An experimental study on etching

characteristics of fiber Bragg gratings of different reflectivity fabricated under different UV exposure times is also carried out. The etching rates were $\sim 2.03 \mu\text{m}/\text{min}$ and $\sim 1.69 \mu\text{m}/\text{min}$ for low reflectivity FBG $R \sim 11\%$ and high reflectivity FBG $R \sim 93\%$, respectively. The differing behavior of FBGs is linked to the different degree of densification in fused silica fiber clad under different UV flux exposures. Studies on HF etching using a thermally regenerated FBG have been carried out. The regenerated grating shows almost no shift in $\lambda_{\text{Bragg}} < 5 \text{ pm}$ during HF etching.

Chapter 7

Studies on the chemical sensing characteristics of etched FBGs

7.0 Introduction

The etched FBGs with a single or a few propagating modes in the core, provide a simpler output signal for spectral peak detection compared to Tilted fiber Bragg gratings (TFBGs) and long period fiber gratings (LPFGs) which usually have several modes in the operating spectral band [193-194, 205-207]. The refractive index sensitivity of different chemicals is typically measured in terms of the shift in Bragg wavelength and sometimes also in change in reflected power of an etched FBG. In normal HF etched FBG, change in Bragg wavelength is monitored with the change in surrounding refractive index. However, in many situations such as metal nano-particle coated etched FBGs, the change in reflected power is measured for different surrounding medium refractive indices [290-291]. In such cases, the reflected power at λ_{Bragg} also changes [291]. This issue may affect the measurement accuracy as output power of an interrogation source such as a broad-band ASE source does not remain constant with wavelength. This inaccuracy can be minimized if λ_{Bragg} does not shift significantly with a change in the surrounding refractive index, greatly relaxing the demands and therefore cost on sensor technology.

In this chapter the studies on etched FBG based sensors for sensing the methanol content in ethanol and concentration sensing of laser dye in dye-ethanol solution are presented. Specific studies are carried out for the enhancement of refractive index sensitivity of the etched FBG. In the first study, the effect of FBG reflectivity on the chemical sensing characteristics is studied. The low reflectivity FBG provided better sensitivity. Secondly, the chemical sensing characteristics, of HF etched thermally regenerated fiber Bragg grating (FBG), are carried out. In

an etched thermally regenerated FBG based refractive index sensor, only a change in the reflected power, R_p , occurs with almost no change in λ_{Bragg} . In such a case, the sensor becomes wavelength independent. The wavelength independence from measurement greatly reduces sensor interrogation complexity allowing for simple amplitude based detection schemes. In the third study, the effect of nano-particle coating on etched FBG is studied. The refractive index sensitivity of nano-particle coated etched FBG was higher with larger physical strength i. e. larger clad diameter.

7.1 Application of HF etched Type-I FBGs for chemical sensing

7.1.1 Concentration sensing of laser dye in dye-ethanol solution

In the textile industry, colour matching assessment is required in textile dyeing processes. In this case, if the colour produced is different from the colour specified in the dyeing recipe, the manufactured goods have to be reworked or rejected. Conventional methods for colour determination employ colorimeters or spectrophotometers to estimate the colour from the dyed materials. It has been shown that FBG can also be used as chemical sensor by removing partially cladding region around the grating to make the FBG sensitive to changes in the surrounding refractive index. Figure 7.1 shows the typical reflection spectra of FBG-DCS for different concentrations of dye solution in ethanol. In this experiment, a HF etched FBG is used for detecting the concentration of Rhodamine 6G (Rh6G) dye in ethanol mixture. Solutions of different concentration of Rh 6G dye in ethanol are prepared in several glass tubes. The concentration of the dye solution varied from 0 to 1.5 mM. Figure 7.2 shows the change in the Bragg wavelength for different dye concentration. The Bragg wavelength changed from 1533.960 nm to 1534.056 nm as the surrounding media is changed from air to ethanol. The wavelength further changes from 1534.056 nm to 1534.162 nm as surrounding dye concentration

in ethanol changes from 0 to 1.5 mM. The sensitivity of the chemical sensor comes around 70 pm/mM. It is also clear from figure 7.2 that there is good linear relationship between the dye concentration in ethanol and the Bragg wavelength shift.

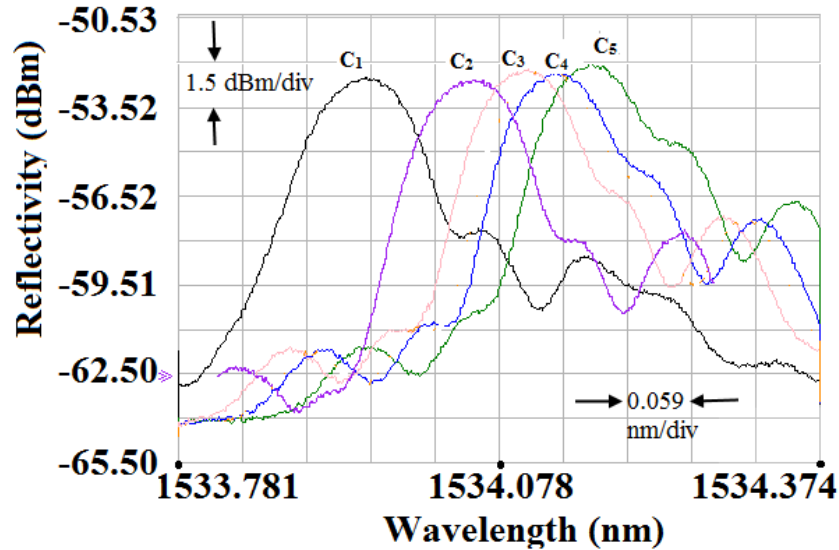


Fig. 7.1: OSA traces showing change in Bragg wavelength for different dye concentration (C_1 – Air, C_2 – 0.0 mM, C_3 – 0.5 mM, C_4 – 1.0 mM, C_5 – 1.5 mM)

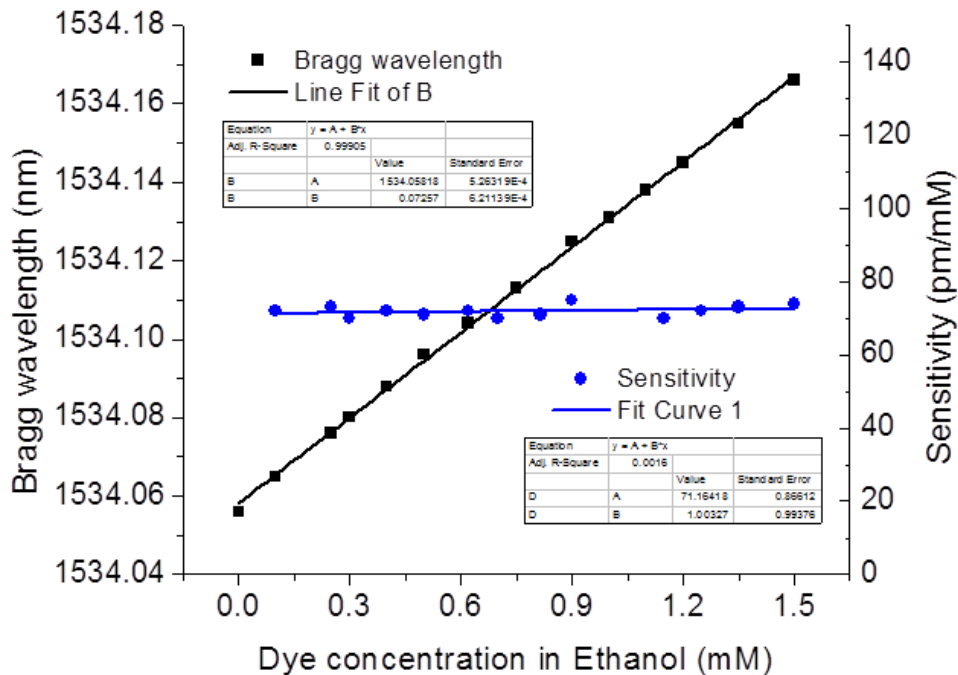


Fig. 7.2: Change in Bragg wavelength as a function of dye concentration

7.1.2 Determination of methanol content in ethanol

Methanol is very toxic for humans especially when inadvertently got mixed with ethanol liquor [292]. It even has a faint alcohol-like odour, which makes it impossible to detect methanol when mixed in alcoholic drinks. It has long been used in the production of imitated spirits and wine. The inhalation of methanol may cause headache, vertigo, fatigue, nausea, vomiting, blurred vision, blindness and even death. Many methods have been developed to detect methanol at various sensitivities in beverage products, such as colorimetric method [293], enzymatic method [294], near-infrared spectroscopy [295], gas chromatography [296] and several others. These methods have disadvantages as they cannot perform measurement in real-time. Therefore designing a sensor, which can perform measurement in-situ, is essential. In the present work, an optical fiber sensor based on an etched fiber Bragg grating (EFBG) for the measurement of methanol content in ethanol is studied. The fiber sensor is manufactured through the etching of the fiber cladding using hydrofluoric (HF) acid along the fiber portion containing the grating.

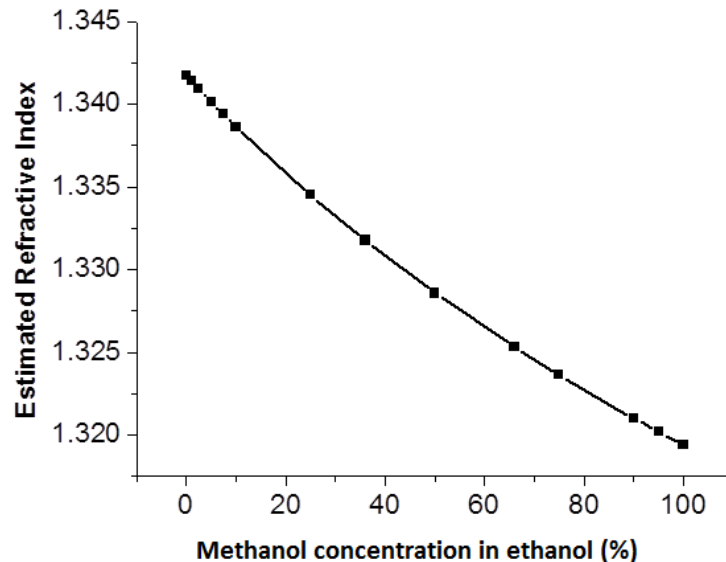


Fig. 7.3: Estimated refractive index of the ethanol-methanol solution at different percentage of methanol concentration in ethanol (Eq. 7.1)

To find out the chemical sensitivity of the etched FBG, 100 ml solution of different methanol concentration in ethanol is prepared in several glass test tubes. The methanol concentration in ethanol varied from 0.0% (pure ethanol) to 100% (pure methanol). Refractive index for different concentrations of methanol in ethanol can be estimated as [297]

$$n_{sur} = [k n_{methanol}^2 + (1 - k) n_{ethanol}^2]^{1/2} \quad (7.1)$$

Here k is the mole ratio of methanol in the solution, which can be estimated from the density, molar mass and volume of the solution. The value of density is 791.8 kg/m^3 and 789.0 kg/m^3 for methanol and ethanol respectively. The molar mass for methanol is 32.04 g/mol and that for ethanol is 46.07 g/mol . Refractive index of methanol ($n_{methanol}$) and ethanol ($n_{ethanol}$) at 1550 nm is 1.3194 and 1.3417 respectively [298]. Figure 7.3 and table 7.1 show the variation of estimated refractive index vs methanol concentration in ethanol.

Table 7.1: *Estimated refractive index of the solution and Bragg wavelength shift*

Methanol (%)	Ethanol (%)	Refractive index of solution	Bragg wavelength of EFBG (nm)
0	100	1.3417	1523.083
1	99	1.3414	1523.076
2.5	97.5	1.3411	1523.066
5	95	1.3406	1523.048
7.5	92.5	1.3400	1523.032
10	90	1.3395	1523.016
25	75	1.3361	1522.921
36	64	1.3337	1522.826
50	50	1.3306	1522.735
100	0	1.3194	1522.453

The estimated refractive index varied from 1.3417 to 1.3386 as the methanol concentration changed from 0 to 10 %. Typical OSA traces of the etched FBG for 100% methanol (trace A), 50% methanol (trace B), 33% methanol (trace C) and 0% methanol (trace D) content in ethanol are shown in figure 7.4.

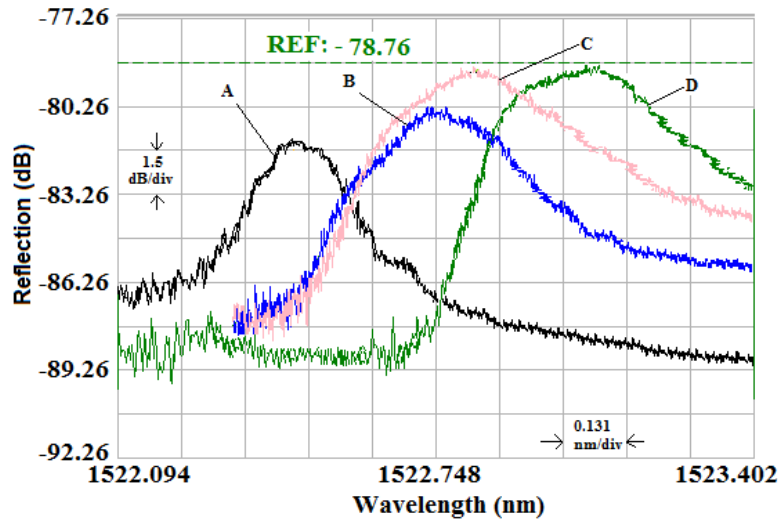
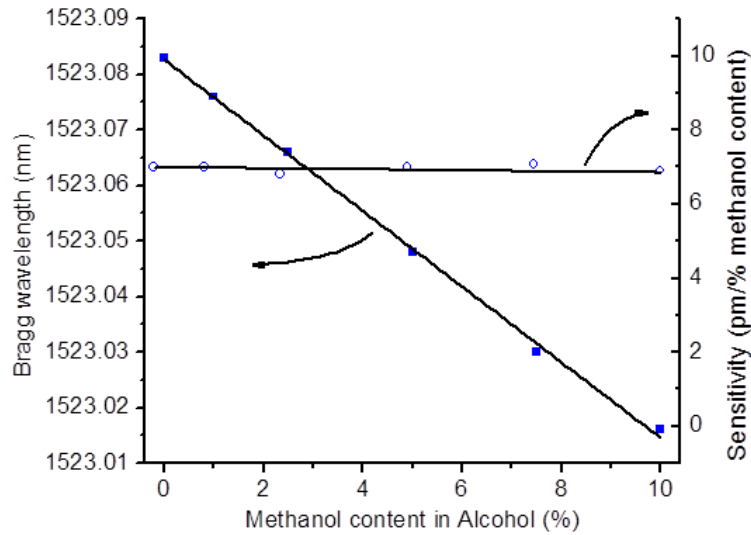


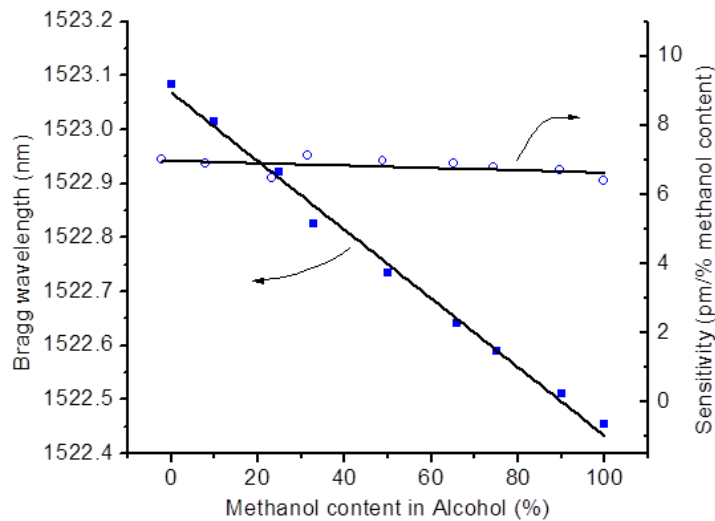
Fig. 7.4: OSA traces for different methanol content in ethanol for (A) 100%, (B) 50%, (C) 33% and (D) 0% methanol content in ethanol

Figure 7.5 (a) shows the Bragg wavelength shifted from 1523.086 nm to 1523.016 nm as the methanol concentration is changed from 0.0 % to 10 %. Figure 7.5 (b) shows that the Bragg wavelength shifted from 1523.086 nm to 1522.453 as the methanol concentration increases from 0.0% (pure ethanol) to 100% (pure methanol). The sensitivity of this EFBG is also shown in figure 7.5 (a and b). This shows the sensitivity of this chemical sensor is almost constant in the range 6.3 pm to 7 pm per % methanol content in alcohol. The sensitivity of the developed sensor in terms of refractive index unit (RIU) is about 30 nm/RIU. The minimum change in refractive index that can be measured is 2×10^{-4} . In case interrogation unit has wavelength resolution of 1 pm in C band [299], the refractive index resolution of the order of around 2×10^{-5} can possibly be measured. Better minimum concentration or better minimum refractive index change can be

detected by (a) increasing the resolution of OSA, this is practically and economically difficult due to increased cost of high resolution OSA (b) etching the FBG until the cladding is fully removed from the FBG, but at the cost of decreased physical strength of the FBG and (c) increasing the evanescent field strength of the fiber by applying nano-particle coating to the etched FBG as discussed in the last section of the present chapter.



(a)



(b)

Fig. 7.5: Bragg wavelength shift and sensitivity of EFBG for different methanol content in alcohol (a) For 0% to 10% (b) For 0% to 100%

7.2 Studies on the sensing characteristics of FBGs having different reflectivity

7.2.1 Effect on chemical sensitivity of etched FBGs

Two FBGs with different reflectivity FBG-F1 (~11%) and FBG-F2 (~93%) were etched in HF acid as discussed in **Chapter 6**. Figure 7.6 (a-d) show the typical OSA traces for both the etched FBGs indicating the wavelength shift for different chemical. Here figure 7.6 (a and b) show the reflection spectra for FBG-F1 and FBG -F2 for the non-etched FBG dipped in ethanol and ethylene glycol. No shift in the Bragg peak was noticed for the different liquids. It is clear that in this case the FBG is unable to distinguish between air, ethanol and ethylene glycol. Figure 7.6 (c) shows the shift in the Bragg peak for air, ethanol and ethylene glycol for FBG-F1 after the etching of about 38 min. The shifts in the Bragg peak for FBG-F2 are shown in figure 7.6 (d) after etching of about 42 min. For FBG-F2, no clear cut differences in the Bragg peak for different liquids were noticed after the etching of 38 minutes. Thus it is clear that Bragg peak shift for different liquids depend on the etching time of the FBGs. The peak wavelength for FBG-F2 was measured as the average value of left and right edge of the reflection spectrum.

In case of FBG-F1 the Bragg peak wavelength difference from air to ethanol was about 684 pm and from air to ethylene glycol was 1266 pm (figure 7.6 c). For FBG-F2 these values were 462 pm and 1008 pm (figure 7.6 d). Therefore the sensitivity of FBG-F1 is higher compared to FBG-F2. Figure 7.7 shows the shift in Bragg peak wavelength at different etching time for different surrounding medium. The Bragg wavelength scales up with the etching time and surrounding refractive index. In case of FBG-F1 same Bragg wavelength shift can be achieved at lower etching time as compared to FBG-F2.

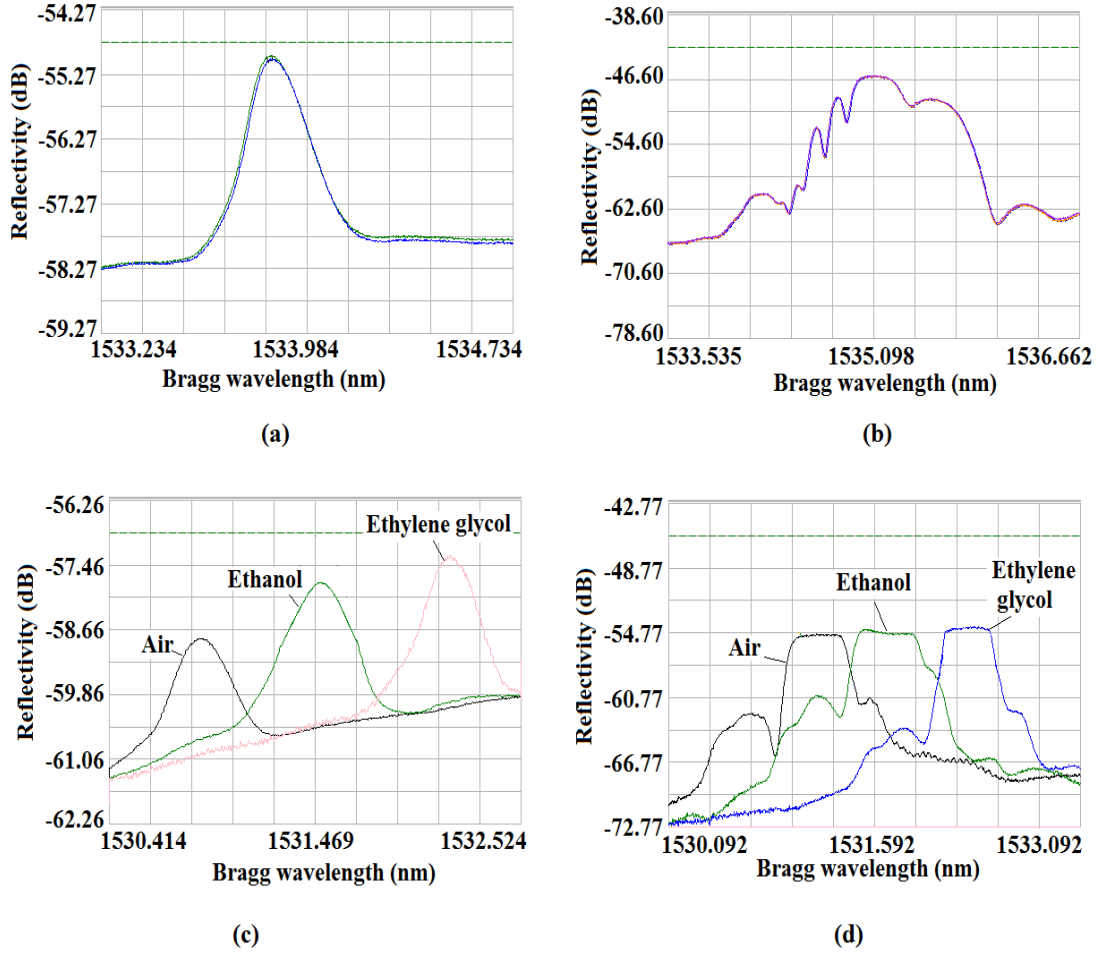


Fig. 7.6: OSA traces showing refractive index sensing with (a) non-etched FBG-F1 (b) non-etched FBG-F2 (c) 38 min etched FBG-F1 and (d) 42 min etched FBG-F2

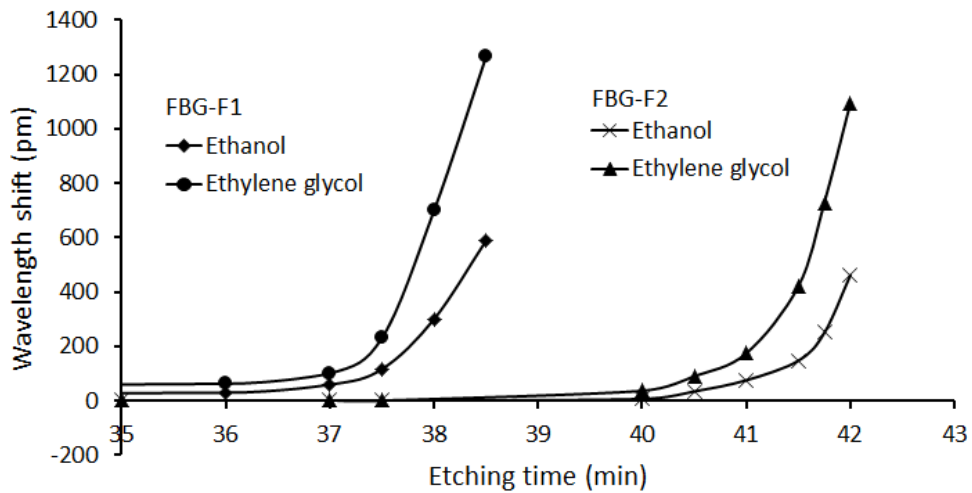


Fig. 7.7: Bragg wavelength shift as a function of etching time

Refractive index sensitivity (RIS) for ethanol and ethylene glycol for both the gratings are also calculated from figure 7.7 and plotted in figure 7.8 and 7.9. Figure 7.8 shows the refractive index sensitivity for different etching time and figure 7.9 for different cladding diameters.

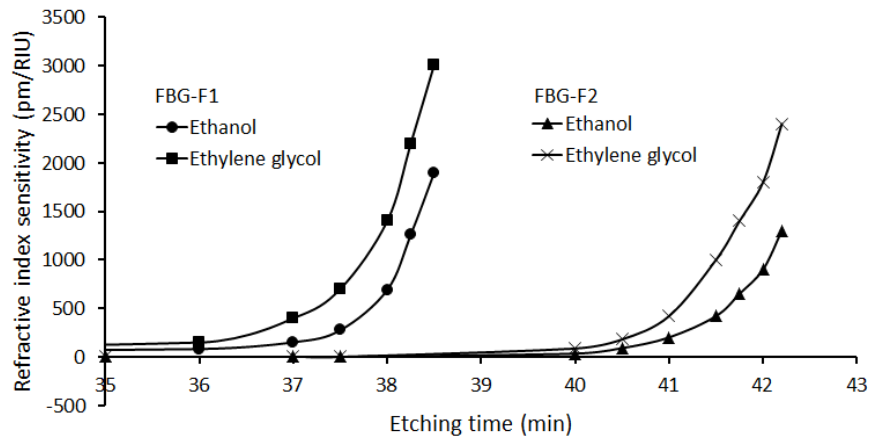


Fig. 7.8: Refractive index sensitivity as a function of etching time

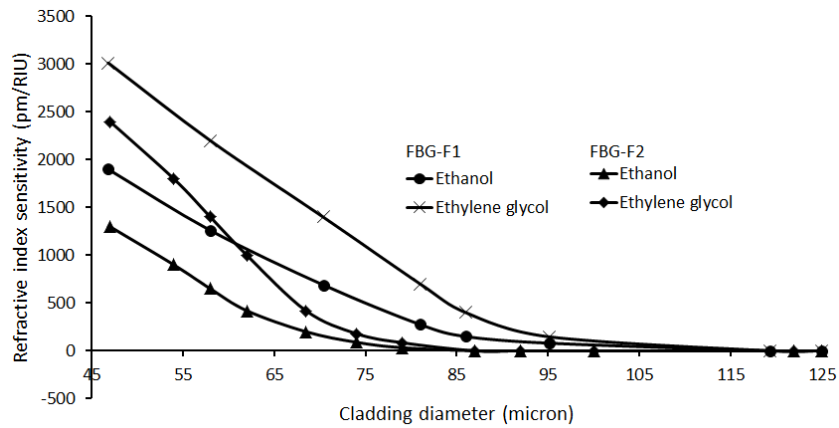


Fig. 7.9: Refractive index sensitivity as a function of cladding diameter of FBG

7.2.2 Results and discussion on FBG during chemical sensing

It is clear from the figure 7.8 and 7.9, that

- Refractive index sensitivity increases with etching time. For FBG-F1, the refractive index sensitivity in ethanol is 80 pm /RIU after 36 min etching, which increased to 1900 pm /RIU at

further etching of around 2 minutes. This is due to the lower cladding diameter of this FBG at higher etching time (figure 6.14). Since for lower cladding diameter the surrounding refractive index will affect the effective refractive index of FBG more prominently.

- Refractive index sensitivity is higher for FBG-F1 for the same etching time. Since the refractive index sensitivity is 0 pm/RIU for non-etched fiber and it increased to 1900 pm/RIU for ethanol and 3014 pm/RIU for ethylene glycol for FBG-F1. At the same etching time of 38 min the refractive index sensitivity is almost 0 pm/RIU for both liquids for FBG-F2.
- Refractive index sensitivity increases with surrounding medium refractive index. As for FBG-F1 the refractive index sensitivity at 38 minutes etching for ethanol was 1900 pm/RIU and for Ethylene glycol is around 3014 pm/RIU.
- For the same cladding diameter of FBG the refractive index sensitivity is higher for FBG-F1 as compared to FBG-F2. For the cladding diameter of 58 micron the refractive index sensitivity for FBG-F1 was 1260 pm/RIU and FBG-F2 was 650 pm/RIU for Ethanol.

As discussed in previous chapter, the Bragg wavelength shift associated with the chemical etching is given by [141-144, 300-301]

$$\delta\lambda_B = 2 \Lambda \delta\eta (n_{sur} - n_{cl}) \quad (7.2)$$

where Λ is grating period, $\delta\eta$ is the change in the fraction of the total power of the unperturbed mode that flows in the etched region, n_{cl} is cladding refractive index and n_{sur} is surrounding medium refractive index. From above equation, it is clear that the difference in the surrounding medium refractive index and clad refractive index decides the Bragg peak wavelength shift. The Refractive index sensitivity (change in the Bragg wavelength per unit refractive index change) associated with the change in surrounding medium refractive index can be estimated from Eq.(7.2) as

$$\frac{\delta\lambda_B}{\delta n} = 2 \Lambda \delta\eta \frac{(n_{sur} - n_{cl})}{(n_{sur} - n_{air})} \quad (7.3)$$

In above equation n_{air} is the refractive index of air, which is taken as reference medium for estimating the refractive index sensitivity. UV induced increase of refractive index occurred mainly due to the increase in the dipole density. The refractive index increases almost linearly with the density [302-304]. So the clad refractive index in case of FBG-F2 will be higher than FBG-F1, therefore from Eq. (7.3)

$$\left(\frac{\delta\lambda}{\delta n}\right)_{FBG-2} < \left(\frac{\delta\lambda}{\delta n}\right)_{FBG-1}$$

Hence the refractive index sensitivity for FBG-F1 (11% reflectivity) will be higher compared to FBG-F2 (93% reflectivity). The difference in the refractive index sensitivity for FBG-F1 and FBG-F2 for same cladding diameter (figure 7.9) may be linked to the different densification as well as different strength of coupling of evanescent wave from core to the clad for FBG of different reflectivity.

7.3 Sensing characteristics of thermally regenerated etched FBG

7.3.1 Chemical sensing using HF etched thermally regenerated FBG

Etching characteristics of three FBGs FBG-A, FBG-B and FBG-C where FBG-A is not heated, while other two FBGs were heated upto 600 °C (FBG-B) and 900 °C (FBG-C), respectively are discussed in **Chapter 6** (figure 6.16). All these HF-etched FBGs are used for detecting chemical species. These are: air ($n \sim 1$), methanol ($n \sim 1.3194$), ethanol ($n \sim 1.3417$) and ethylene glycol ($n \sim 1.4219$). Figure 7.10 shows the typical OSA traces for different surrounding media responses of FBG-A, B and C. The test solutions are kept in three glass test tubes. The fiber holding arrangement is similar as that was used during HF etching (Figure 6.5). The FBG is cleaned and dried every time before using in any solution. The position of the FBGs in the liquid

is precisely controlled with micrometer stages attached with the vertical mounting assembly.

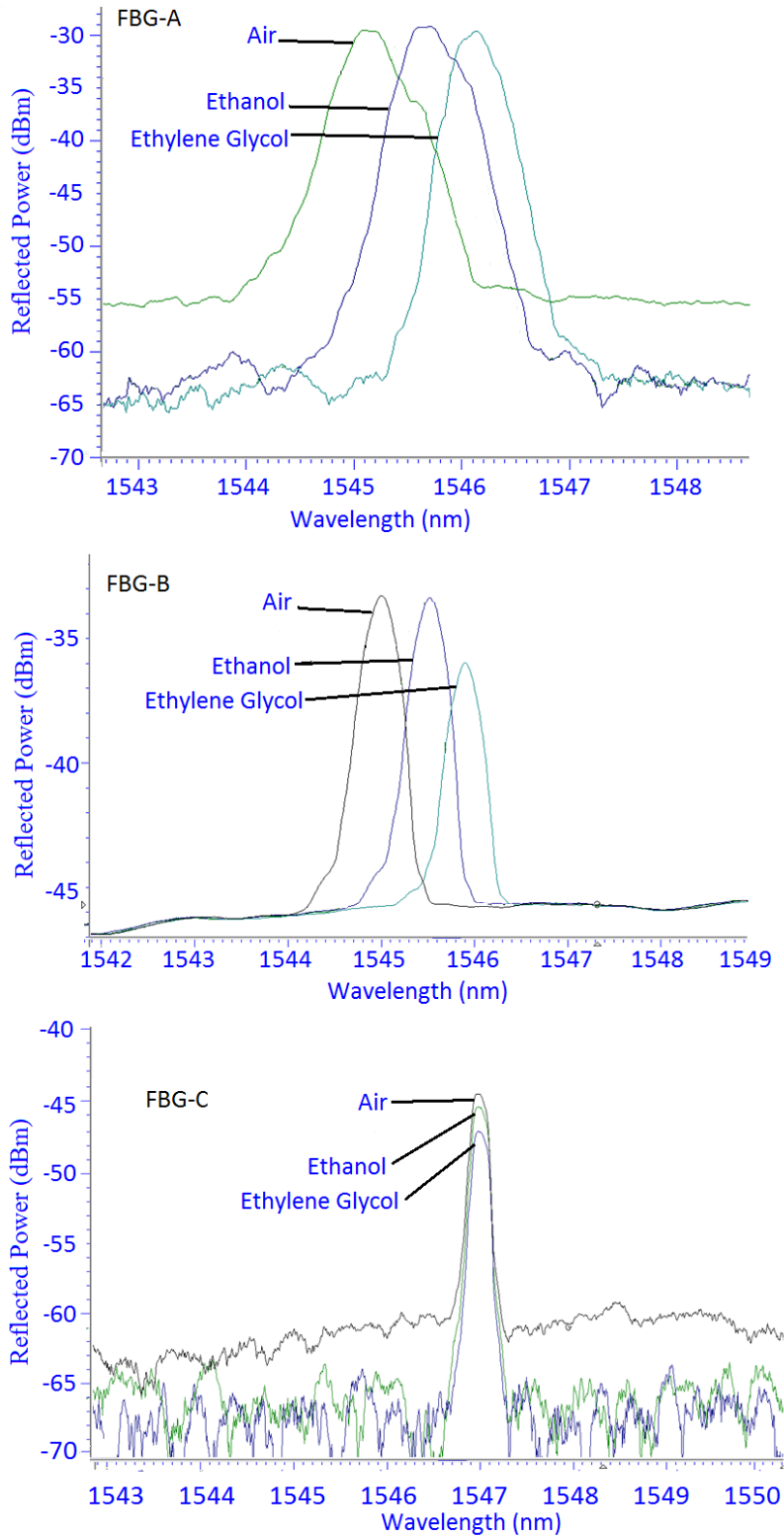


Fig. 7.10: Typical OSA traces for FBG-A, B and C for different surrounding media

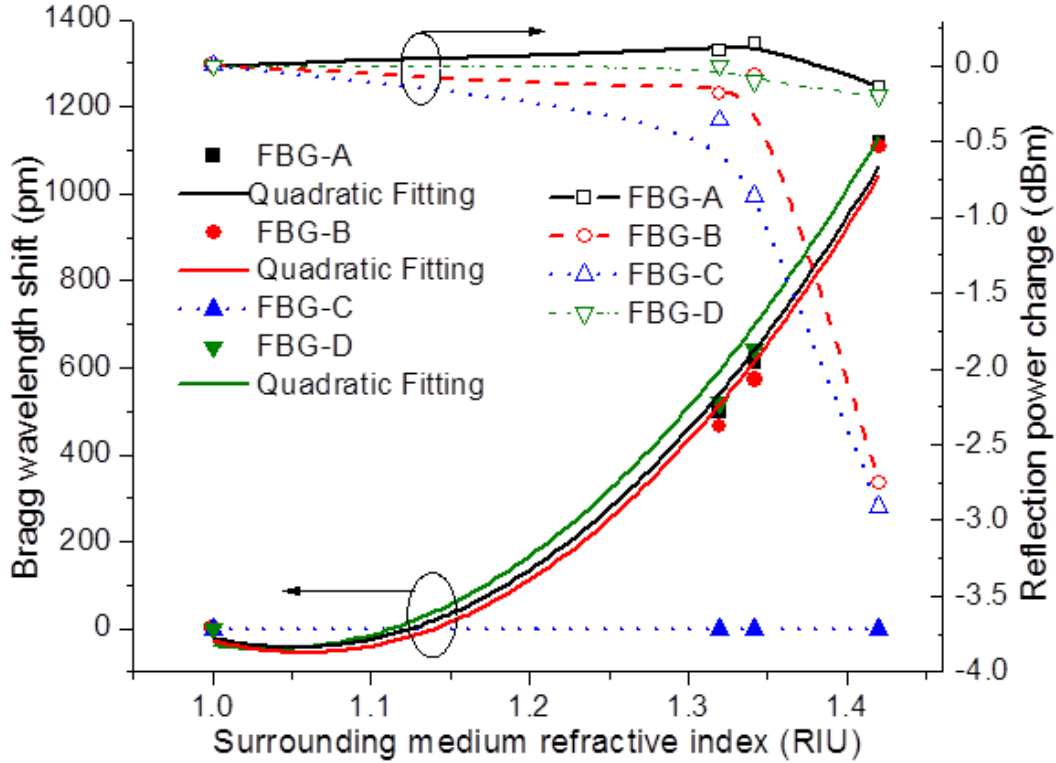


Fig. 7.11: Bragg wavelength shift and reflection power change for different surrounding media for FBG-A, B, C and D

The response of all the FBGs (A, B, C and D) is recorded in terms of λ and R_p shifts, shown in figure 7.11. For FBG-A, the Bragg wavelength is, $\lambda_{\text{Bragg}} = 1545.094$ nm, 1545.591 nm, 1545.707 nm and 1546.212 nm for air, methanol, ethanol and ethylene glycol respectively. For FBG-B, the Bragg wavelength is, $\lambda_{\text{Bragg}} = 1545.007$ nm, 1545.473 nm, 1545.580 nm and 1546.116 nm for air, methanol, ethanol and ethylene glycol respectively. By contrast, $\lambda_{\text{Bragg}} = 1546.972$ nm is almost insensitive to the surrounding medium refractive index for FBG-C. This wavelength independence of FBG peak is further tested in other solvents as well such as different proportion mixture of methanol in ethanol and separately in sodium hydroxide solution. The shift in FBG peak is again almost negligible in all the cases. However, these additional data are not included in figure 7.11 due to uncertainty in the exact values of refractive index as these

mixtures are home-made. For FBG-D, the Bragg wavelength is, $\lambda_{\text{Bragg}} = 1545.076 \text{ nm}$, 1545.596 nm , 1545.721 nm and 1546.293 nm for air, methanol, ethanol and ethylene glycol respectively. The experiment of chemical sensing with etched FBG is repeated for three times. The maximum value of standard deviation in wavelength shift is $< 10 \text{ pm}$. This small uncertainty has practically not affected the measurements.

Figure 7.11 also shows the trends in reflected power of etched FBGs (A, B, C, D) with respect to surrounding medium refractive index. For FBG-A $R_p = -29.42 \text{ dBm}$, -29.26 dBm , -29.38 dBm and -29.56 dBm for air, methanol, ethanol and ethylene glycol respectively. The variation in the power R_p is almost negligible. For FBG-B, the reflected power is $R_p = -33.21 \text{ dBm}$, -33.40 dBm , -33.48 dBm and -35.96 dBm for air, methanol, ethanol and ethylene glycol respectively. For FBG-C the reflected power is $R_p = -44.7 \text{ dBm}$, -45.06 dBm , -45.56 dBm and -47.61 dBm for air, methanol, ethanol and ethylene glycol respectively. In case of FBG-D, R_p is -55.31 dBm , -55.36 dBm and -55.56 dBm for air, ethanol and ethylene glycol respectively.

7.3.2 Discussion on the wavelength insensitivity of the etched FBG

The Bragg wavelength shift during HF etching are, $\Delta\lambda_{\text{Bragg}} \sim 1.12 \text{ nm}$, 1.11 nm , 1.12 nm and 5 pm for FBG-A, B, D and C respectively. Since the fiber clad diameter of all etched FBGs (A-D) are almost similar, the almost negligible wavelength shift in FBG-C as compared to FBG-A, B and D needs to be explained. The possible additional factor which influence the Bragg wavelength shift is the relaxation of stress between core and cladding, which is depended on whether the FBG is normal, partially annealed and regenerated FBG. This stress relaxation, between core and clad, affects the effective refractive index of the core and hence the Bragg wavelength shift [288-289]. The reduced wavelength sensitivity of regenerated FBG-C may be explained as follows.

The mode evanescent fields must reach the cladding-air interface for sensing to work. Hence changes in the cladding are critical to the effects observed. To reduce sensitivity to the outside material under test, the overlap integral in this region must be reduced for the regenerated grating. The fused silica fiber used in the present experiment is a step index fiber with [Ge] = 18 mol% in the core. The refractive index of the cladding is, $n = 1.445$ and the core refractive index is $n = 1.474$ (estimated from given data of numerical aperture $NA = 0.29$). The index difference between core and cladding is, $\Delta n = 0.029$. The core diameter is $\phi \sim 4.0 \mu\text{m}$ and the Mode Field Diameter is, $MFD = 4.46 \mu\text{m}$. MFD is estimated at $1/e^2$ point ($\sim 13.5\%$) of the peak intensity I_0 . For all intents and purposes the experimental data is consistent with little light reaching the cladding-air interface, although sufficient to affect grating properties. The difference of stress between core and clad need to be considered for non-annealed (FBG-A), partially annealed (FBG-B) and thermally regenerated (FBG-C) fibers cladding around the FBG region. After etching, the remaining cladding is likely to feel the higher stress from the core which affects both the core and cladding indices. This leads to a stress-optic contribution to the effective cladding index [288]. This in turn leads to the change in Bragg wavelength for FBG-A and FBG-B. The cladding is predominantly pure silica, so the required annealing temperature must be sufficiently high and of sufficient duration to relax these core cladding stress substantially and lead to higher indices particularly in the core [250, 281]. Only the regenerated grating provides high enough temperatures since the regeneration process itself relies on these high temperature relaxations in the presence of a gas such as hydrogen. The regeneration of gratings occurs due to the stress relaxation at high temperature ($\sim 800\text{-}900^\circ\text{C}$). Therefore for regenerated grating, the stress-dependent refractive index change of the core expected to be constant after the stress relaxation. Hence the effective refractive index will be constant and reflected in no shift of the Bragg

wavelength for FBG-C. After annealing, the refractive index of core goes up. This in-turn make the grating modal field much less sensitive to a sample on the outside. Also the NA must be increased so that the percentage field overlap in the cladding drops below $\eta \sim 14\%$ as estimated for the un-annealed fiber. However if we remove the clad diameter upto mode field diameter, the dependence of power loss to surrounding media increases. Hence the reflection intensity of etched regenerated FBG changes with surrounding medium refractive index. In contrast, the normal Type-I FBG (non-annealed) of similar reflectivity (FBG-D) has shown considerable shift in wavelength (figure 7.11). This ruled out the possibility of low reflectivity of thermally regenerated grating responsible for the wavelength independent refractive index sensing. The nonlinear response in index is easily explained as the detection is ultimately based on the evanescent field reaching the cladding-air interface and interacting with any medium placed there. Since the fiber geometry is a cylinder, there should be a quadratic dependence with index change, shown in figure 7.11. The quadratic fit for wavelength shift in FBG-A, B and D is carried out by suitable choice of coefficients. FBG-C shows the least change indicating that the FBG mode fields are much more strongly confined than that of the other gratings.

A similar trend is observed with chemical sensing of different liquids. There is no shift in Bragg wavelength as the medium surrounding the etched regenerated FBGs change from air to ethylene glycol ($n = 1$ to 1.42). However, the reflected power in λ_{Bragg} changed due to the surrounding medium refractive index change, which helps to draw some light out. The average refractive index sensitivity in terms of wavelength shift (from air to ethylene glycol) is, $\Delta\lambda/\Delta n = 2.65$ nm/RIU, 2.63 nm/RIU, 0.01 nm/RIU and 2.89 nm/RIU for FBG-A, B, C and D respectively. For FBG-A, B and D the wavelength sensitivity is almost equal but for FBG-C it is negligible. The average refractive index sensitivity in terms of reflection power change for the

same surrounding medium change is, $\Delta R_p/\Delta n = -0.33$ dBm/RIU, -6.51 dBm/RIU, -6.92 dBm/RIU and -0.46 dBm/RIU for FBG-A, B, C and D respectively. Annealing appears to have improved this coefficient suggesting the local index modulation has improved in the core. The decrease in reflected power R_p may be attributed to the etching induced multimodal change in propagation condition along the etched region [287]. This effect leads to reduction of the fundamental mode power and then the grating induced coupling. The reflected power of all the four gratings reflects the changes in modal overlap as the optical field is drawn out by higher refractive indices, R_p decreases with increasing index. The amount drawn out is generally small given the field overlap in this region is small.

7.4 Studies on the refractive index sensing using nano-particle coated etched FBG

Refractive index sensing using FBG can be done by etching the fiber cladding using HF solution, so that it becomes sensitive to surrounding medium refractive index. For further enhancement of refractive index sensitivity at higher physical strength the etched FBG is coated with silver nano-particle solution. The nanoparticle coating induces refractive index dependent waveguide losses, because of the variation of the evanescently guided part of the light. Hence the amplitude of the Bragg reflection is highly sensitive to refractive index changes of the surrounding medium. Studies on the refractive index sensitivities of the nanoparticle coated etched FBG and its subsequent utilization in chemical sensing has been carried out. Figure 7.12 shows the schematic of the HF etching and Ag nano particle coating on FBG. FBG in SM-1500 fiber is inscribed by phase mask technique as discussed in **Chapter 2**. The exposed region where the gratings are formed is etched using 40% HF solution. As the optical fiber without protective coating is immersed in this HF solution, the clad is etched gradually and its diameter reduces. The Bragg wavelength shift of the grating is monitored with time. During this time the Bragg

wavelength shifted from 1546.563 nm to 1546.404 nm. The cladding diameter of the etched FBG is also monitored during HF etching. In the present case the cladding diameter reduced from 125 μm to 60 μm . Figure 7.13 shows the OSA traces for FBG reflection before and after HF etching.

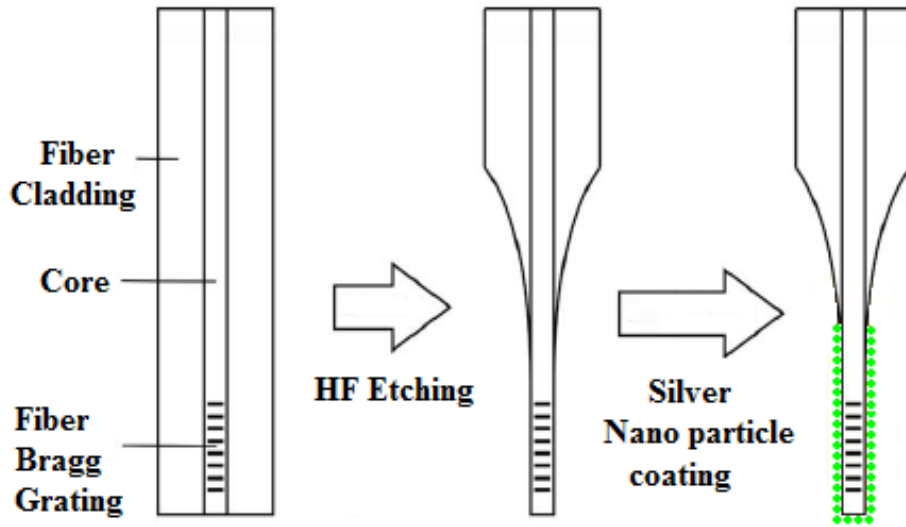


Fig. 7.12: Schematic of HF etching and Ag nano-particle coating on FBG

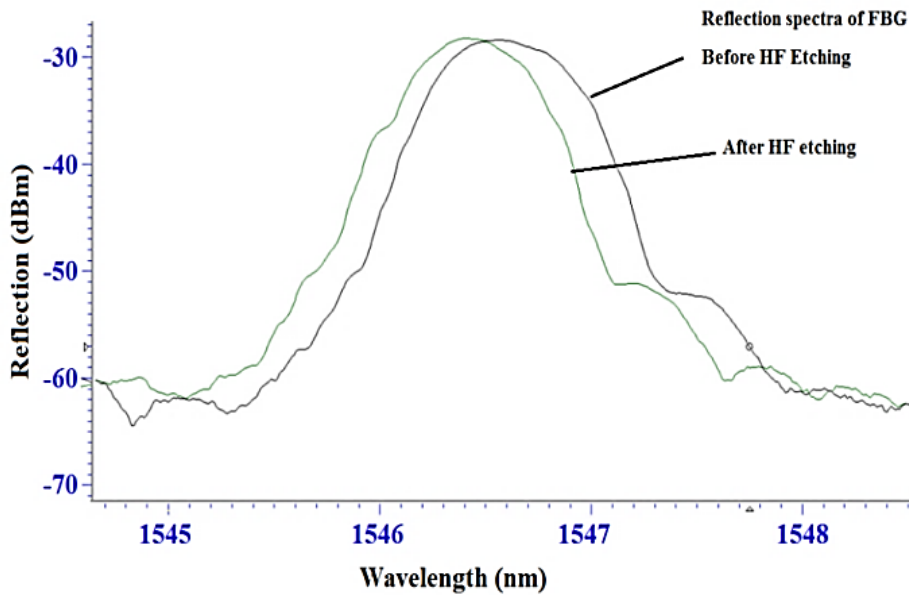


Fig. 7.13: Reflection spectra of FBG before and after HF etching

Silver nano-particles are coated by applying dip coating technique for 120 minutes. Change in Bragg wavelength and reflection power of the FBG is noticed during the coating process.

Initially the Bragg wavelength and peak reflection power of the FBG in Ag nano-particle solution is 1546.452 nm and -29.54 dBm respectively. The Bragg wavelength and reflection power changed to 1546.467 nm and -35.18 dBm within 120 minutes of the FBG dipping in solution. As the FBG is removed from solution to air the wavelength and reflection power were 1546.462 nm and -51.95 dBm.

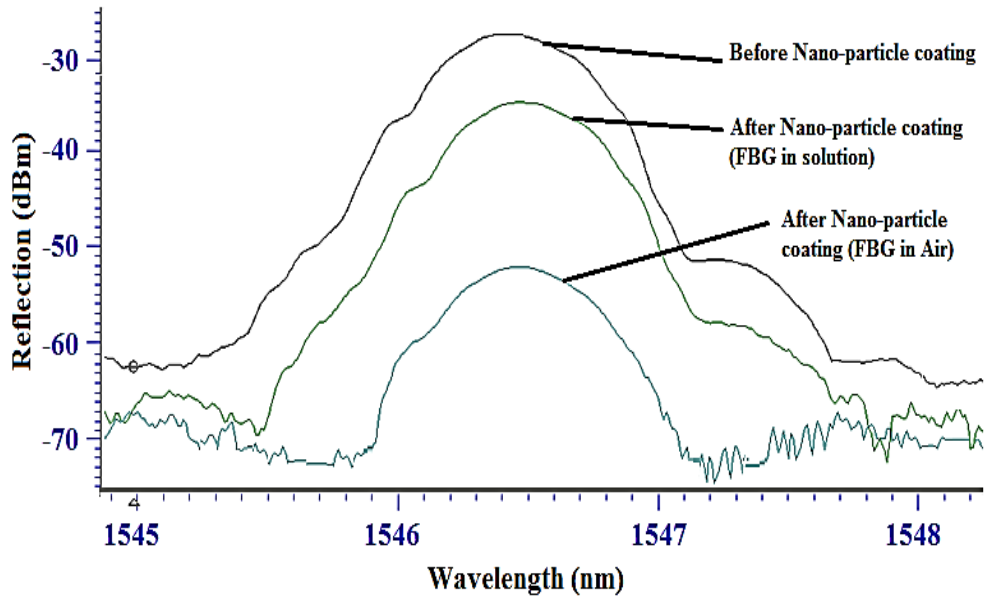


Fig. 7.14: Reflection spectra of FBG before and after Ag nano-particle coating

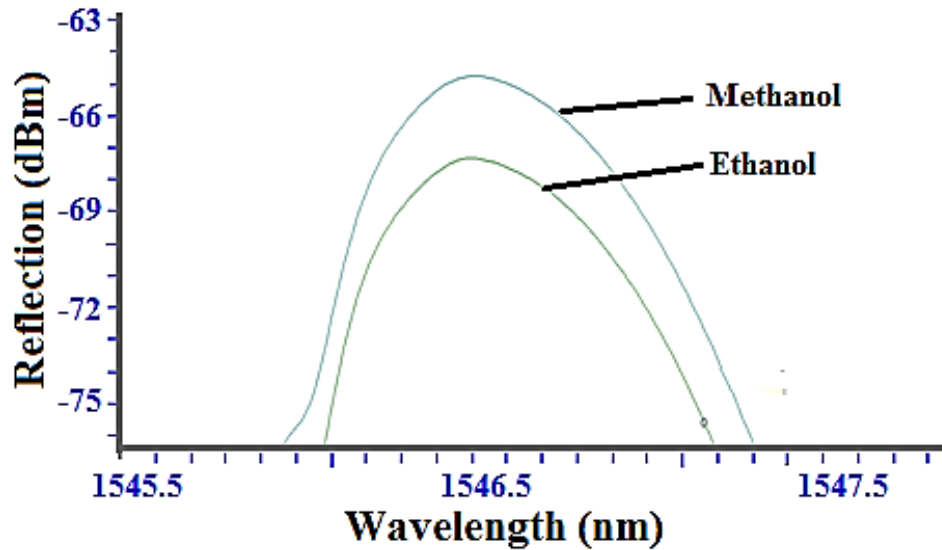


Fig. 7.15: Response of nano-particle coated etched FBG for different chemicals

Figure 7.14 shows the change in reflection spectra of the FBG with its dipping time in nano-particle solution. This nano-particle coated etched FBG is used for refractive index sensing of ethanol-methanol solution. As shown in figure 7.15, the Bragg wavelength changed from 1546.433 nm to 1546.445 nm and the reflection power changed from -64.46 dBm to -67.94 dBm for 100% methanol to 100% ethanol solution. So reflection power change is 3.5 dBm for the refractive index change of 0.0223. Refractive index sensitivity of the nano-coated EFBG sensor is 157 dBm/RIU. The minimum change in refractive index that can be measured with this sensor is 1×10^{-4} , which is equivalent to less than 1% methanol content in ethanol solution. It is worth mentioning here that the minimum refractive index measured using HF etched FBGs (without nano-particle coating) of cladding diameter 13 μm was $\sim 2 \times 10^{-4}$. So the nano-particle coated FBGs provided higher resolution even with the higher cladding diameter or in other words with higher physical strength. The drawback in refractive index sensor based on HF etched FBG was its lower physical strength. Using nano-particle coated etched FBG the higher refractive index sensitivity can be achieved with higher physical strength of the sensor. This differentiating behaviour of FBGs may be linked to the enhanced leakage of the light from clad to the surrounding medium due to nanoparticle coating.

7.5 Conclusion

In conclusion, the etched FBG have been applied for the refractive index sensing. The adulteration measurement of methanol content in ethanol and concentration sensing of dye in dye ethanol solution is carried out. The minimum refractive index change of 2×10^{-4} is measured using HF etched Type-I FBGs. The refractive index sensitivity of the developed sensor in terms of refractive index unit (RIU) was $\Delta\lambda/\Delta n \sim 30 \text{ nm/RIU}$. It has been demonstrated that same refractive index sensitivity could be achieved using lower reflectivity FBGs with larger clad

diameter as compared to high reflectivity FBGs with lower clad diameter. A novel concept of wavelength shift independent chemical sensing is demonstrated using etched thermally regenerated FBG. In this case, only amplitude of FBGs changes with surrounding refractive index medium. The average refractive index sensitivity in terms of reflection power change (from air to ethylene glycol) was, -0.33 dBm/RIU, -6.51 dBm/RIU and -6.92 dBm/RIU for non-annealed, partially annealed and thermally regenerated etched FBGs of almost same clad diameters. This has immediate applications in reducing both cost and complexity of FBG-based sensors exploiting detection at the cladding-air interface. It has been demonstrated that the high refractive index sensitivity can be achieved with a good mechanical strength by nano-particle coating of the etched fiber Bragg grating. The minimum change in refractive index measured with nano-particle coated etched FBG sensor was 1×10^{-4} .

Chapter 8

Summary and future scope

8.1 Summary of the thesis

The present thesis is a comprehensive study on the fabrication and utilization of different types of fiber Bragg gratings for temperature and refractive index sensor development. The FBGs have been inscribed by high repetition rate (~ 5.5 kHz), nano-second (~ 30 ns) pulses of high beam quality 255 nm UV wavelength. The whole thesis work consisted of closely interlinked extensive studies on fabrication and characterization of different types (Type-I, Type-IIa, and regenerated) of fiber Bragg gratings (FBGs), their annealing and temperature sensing characteristics, theoretical analysis and experimental results on refractive index sensing using etched gratings, studies on the enhancement of the refractive index sensitivity and selected applications of the developed FBGs as single point and distributed sensors.

For the development of FBGs as temperature or refractive index sensor, it is very important to thoroughly study the fiber grating's reflectivity and spectral characteristics for different fabrication techniques, UV exposure time, and fiber core doping concentration. Extensive experimental investigations are performed on FBGs fabrication by phase mask and bi-prism techniques with an indigenously developed fiber grating writing set up using the properly characterized 255 nm UV beam. Type-I, Type-IIa, Tilted and thermally regenerated FBGs have been fabricated and performance analyzed. Both the germanium and germanium–boron co-doped photosensitive fibers are employed in the FBG fabrication. Typically Type-I FBG of reflectivity 99 % (~ 20 dB) is fabricated in less than one minute while the maximum FBG reflectivity of 99.99 % (~ 42 dB) is achieved in hydrogen loaded fiber in less than 2 minutes time. Type-IIa FBG of reflectivity about 90 % (~ 10 dB) is achieved by the extended UV exposure of

about 30 minutes. For distributed temperature sensor, the multiple FBGs are written in a single fiber using either by tilted phase mask with incident collimated UV beam or by changing geometrical divergence of UV beam falling on the bi-prism. This Bragg wavelength tuning is also analyzed theoretically for matching with experimental results. Experimentally, the Bragg wavelength tuning of ~26 nm and ~40 nm was achieved using phase mask and bi-prism approach, respectively. Overall, the FBGs of different length, Bragg wavelength, reflectivity and bandwidth are written for further utilization as sensors.

For FBG based temperature sensor development, the next logical step was to study the thermal response of Type-I and Type-IIa FBGs in a thermal annealing schedule. This multi-step annealing process covered temperature from 30 °C to 900 °C with different dwell times in different temperature slots for the total span of about 28 hours. Studies on the role of fiber core doping on the thermal decay characteristic of both Type-I and Type-IIa FBG are carried out. It is demonstrated that Type-IIa FBGs can be inscribed at lower UV fluence in higher Ge-doped fibers. The refractive index rollover (transition from Type-I to Type-IIa) is observed at a lower cumulative UV fluence (~15.84 kJ/cm²) for the high Ge-doped fiber (~18 mol %) as compared to a higher fluence (~57.6 kJ/cm²) for the low Ge-doped fiber (~6 mol %). The thermal sustainability of Type-IIa FBGs is demonstrated to be higher in lower Ge-doped (~6 mol %) fibers.

The average temperature sensitivity (~13.9 pm/°C) was almost same for both the Type-I and Type-IIa FBGs. Type-I FBGs, written in germanium-boron co-doped fiber decayed substantially for temperature exceeding 300 °C. Type-I FBGs, written in only germanium doped fibers sustained upto 450 to 500 °C temperature with no significant decay in the reflectivity. In contrast, the Type-IIa FBG based temperature sensors operated reliability for long period and

repeated use for temperature upto 800 °C. The life time of different FBGs are also calculated based on theoretical analysis using power law. The predicted life time varied from twelve years to one year for Type-IIa FBG temperature operating range from 500 °C to 800 °C, respectively. Higher temperature stability of Type-IIa FBG is attributed to the combined effect of 1) Strong seed (Type-I) grating written by highly stabilized interference fringes made by highly coherent and low pointing stability 255 nm source, 2) Enhanced core-cladding stress release due to long UV exposure (~ 30 minutes) because of moderate UV pulse energy (~10s of μJ) and 3) Self-annealing effect due to heating of fiber via high repetition rate (5.5 kHz) pulse of separation $\sim 180 \mu\text{s}$ which is less than thermal diffusion time in the range of mili-seconds.

To further increase the FBGs temperature sustainability to higher temperature (~ 1000 °C), the thermal regeneration studies of FBGs in hydrogenated fibers are carried out. Dedicated investigation are made on the factors affecting the thermal regeneration process such as annealing schedules, seed FBG reflectivity, FBG length and fiber doping concentration. It is concluded that the reflectivity and the life time of regenerated FBG increased non-linearly with the seed FBG strength. For example, the regenerated FBG strength increased non linearly from 0.10 dB to 8.50 dB for the variation in seed FBG strength from 3.52 dB to 34.56 dB. Correspondingly, the value of Δn_{ac} for regenerated FBG varied from 0.24×10^{-4} to 0.63×10^{-4} as the seed FBG Δn_{ac} varied from 1.71×10^{-4} to 6.48×10^{-4} . It is also observed that for the same seed (Type-I) FBG reflectivity, the regenerated FBG reflectivity scales up with the grating length. The optimization of these factors is used to regenerate one of the highest reflectivity FBG ($R \sim 88\%$) in hydrogen loaded telecommunication (SMF-28, Corning) fiber. For FBG written in non-hydrogenated Ge-B doped fiber no thermal regeneration is observed, whereas for hydrogenated fiber, the regeneration occurred at 700 °C. It is also observed that the thermal

regeneration characteristics of the FBG depends on the Ge doping and hydrogen loading in the core of the optical fiber. FBG based single point high temperature sensors, for temperature upto 1000 °C with accuracy of ± 1 °C are developed and studied. The predicted life time of the FBG sensor at 1000 °C varied in the range of 0.75 year to ~12.4 year, depending on the reflectivity, length and doping concentration of the seed FBG. Studies on the residual reflectivity of the thermally regenerated grating at 1100 °C and its relation with change in dc refractive index are established. The FBG residual reflectivity of 40%, 43% and 10% is obtained for Ge doping of 3 mol%, 10 mol% and 18 mol% respectively, which was stable even after ~10 hours annealing at 1100 °C.

The temperature sensor part of thesis is concluded with the applications of FBG based single point and distributed sensors in the three real situations 1) Single point temperature monitoring of transformer oil in high voltage environment, 2) Multi-point distributed temperature sensing to study the spatial variation of temperature along the CuBr laser tube length in high EMI and high voltage environment and 3) Surface temperature monitoring of the exit port of a dipole magnet vacuum chamber of synchrotron radiation source Indus-2. In all these installations, the FBG based sensors have been successfully implemented in the different temperature ranges from 30 °C to 500 °C and their research results are presented.

The second part of the thesis is devoted to study and development of refractive index sensor using different types of the fiber Bragg gratings. Normal FBGs don't respond to the surrounding medium. Therefore, HF based clad etching technique is used to make the FBG sensitive to external medium. The Bragg wavelength and cladding diameter are monitored during etching of the FBG. It is observed that in double step (first step: 40% HF for time 30-35 minutes, second step: 10% HF for time 10 minutes) HF etching, the Bragg wavelength shifted from

1533.311 nm to 1520.41 nm in ~ 40 minutes. The etching rate is demonstrated to be depended both on HF concentration as expected and also on seed FBG reflectivity as a new result. The average etching rates are ~ 2.03 $\mu\text{m}/\text{min}$ and ~ 1.69 $\mu\text{m}/\text{min}$ for low reflectivity ($R \sim 11\%$) FBG and high reflectivity ($R \sim 93\%$) FBG, respectively. Dependence of etching rate on FBG reflectivity is explained based on different degree of fiber core densification under varying UV cumulative fluence. The cladding diameter reduced from 125 μm to 15 μm while the core diameter was ~ 6-8 μm . The experimental results on HF etching are analyzed based on double clad approximation theory for cylindrical/rectangular waveguide geometry. A graphical method is used to find the dependence of effective refractive index on the fiber cladding diameter and surrounding refractive index. The change in Bragg wavelength, with surrounding medium refractive index, is estimated. It is analytically shown that, for a particular clad diameter, the effective refractive index increased with increase in surrounding medium refractive index. The estimated results matched with the observed Bragg wavelength shift both for the reduced cladding diameter as well as for change in surrounding refractive index.

Applications of the etched Type-I FBG sensors are studied in three situations, 1) Adulteration measurement of methanol in ethanol and 2) Concentration sensing of laser dye in ethanol solution, 3) Refractive index sensing of different mediums such as air, ethanol, methanol and ethylene glycol. Minimum 1% concentration of methanol in ethanol could be reliably measured corresponding to change in refractive index of 2×10^{-4} . The sensitivity of the developed sensor, in terms of refractive index unit (RIU), is ~ 30 nm/RIU. For the second application, a minimum of 0.1 mM Rh6G dye concentration in dye-ethanol solution could be measured. For the third application, chemical sensing characteristics of FBGs of different reflectivity is studied for refractive index sensing from air ($n = 1$) to ethylene glycol ($n = 1.42$).

Typically, for the cladding diameter of 58 micron, the refractive index sensitivity for air to ethanol are 1260 pm/RIU for 11% reflectivity FBG and 650 pm/RIU for 93% reflectivity FBG. Same refractive index sensitivity could be achieved for FBG with lower reflectivity and larger residual (hence larger mechanical strength) clad diameter and FBG with higher reflectivity and lower residual clad diameter. In the direction towards good mechanical strength, study is also carried out on refractive index sensor of etched FBG with metal nanoparticle coating.

In the related study on FBG based chemical sensor, it is demonstrated the etching and sensing of thermally regenerated FBG is different from that of conventional Type-I FBG. The study is again carried out with air, ethanol, methanol and ethylene glycol as sensing media. The regenerated FBG shows almost no shift in Bragg wavelength during HF etching or in chemical sensing. The RFBG chemical sensor works on the basis of change in reflection power of grating with change in surrounding refractive index. This is a novel development which paves the way for wavelength independent FBG based chemical sensing.

In summary, the overall thesis starting from the review in the field and going through stages such as FBG fabrication, thermal characterization of Type-I and Type-IIa FBG, single as well as multipoint temperature sensing, high temperature sensing using thermally regenerated FBG, refractive index sensing characteristics of normal and thermally regenerated FBG and ending with future scope of work, is a comprehensive and meaningful document on the thesis “Development and studies on fiber grating sensors”.

8.2 Future scope of work

The present thesis work has an excellent future scope for research and development in the field of FBG. For example, very limited literature is available on the application of thermally regenerated gratings in temperature as well as chemical sensing. The research work related to

development of thermally regenerated FBGs from the seed FBGs, written in helium loaded fiber using different UV sources, can be further explored. Thermally regenerated FBGs offer very good potential application as mirrors for various high power fiber lasers laser. The studies on the development of high temperature sensor can be further augmented for temperature higher than 1000 °C using fs written FBGs in non-hydrogenated telecom fibers and sapphire fibers. The high temperature distributed sensor (~1000 °C) can be developed using thermally regenerated grating with proper packaging technique. Further studies on the enhancement of temperature sensitivity of FBG sensors can be done by metallic coating of the FBG. The temperature sensor for the purpose of use in the radiation environment such as nuclear reactor or synchrotron radiation environment needs further study to investigate the role of radiation on FBG performance.

The refractive index sensitivity can be enhanced further by etching the Tilted FBG. It is observed that the etched FBG based refractive index sensor requires a delicate and careful handling as a very thin FBG is used for sensing. Although it gives very high sensitivity, it can break very easily and is prone to micro-bending. The research work in the area of development of packaging system for etched FBGs also assumes great importance. Theoretical and experimental studies on the temperature and refractive index sensing characteristics of FBGs written in speciality fibers like glass photonic crystal fiber is likely to provide new directions in the field. The integration of specialty fiber sensor technology with bio-compatible polymer based micro-technology will open new opportunities for deployment of fiber sensors in the field of health care. The FBGs written in multimode fiber needs further exploration for the development of refractive index sensor with very high sensitivity.

REFERENCES

- [1]. B. Culshaw, J. Dakin, *Optical Fiber Sensors System and Applications*, Vol 2, Artech House (1989).
- [2]. Y. Yang, K. Chen, N. Gupta, *Fiber optic sensors*, Wiley Online Library (2017).
- [3]. K. T. V Grattan, B. T. Meggitt, *Optical Fiber Sensor Technology: Applications and Systems*, 3, Kluwer Academic Publishers (1999).
- [4]. L. Mescia, F. Prudenzano, "Advances on optical fiber sensors," *Fibers*, 2, 1-23(2014).
- [5]. G. Rajan, *Optical Fiber Sensors: Advanced Techniques and Applications*, CRC Press, Taylor and Francis Group (2015).
- [6]. M. Yasin, *Optical Fiber Sensors: An Overview*, Fiber Optic Sensors, InTech (2012).
- [7]. T. G. Giallorenzi, J. A. Bucaro, A. Dandridge, J. H. Cole, S. C. Rashley, R. G. Priest, "Optical fiber sensor technology," *IEEE Transactions on Microwave Theory and Techniques*, 30, 472-511 (1982).
- [8]. B. Culshaw, A. D. Kersey, "Fiber-optic sensing: a historical perspective," *Journal of Lightwave Technology*, 26, 1064-1078 (2008).
- [9]. J. L. Santos, F. Farahi, *Handbook of Optical Sensors*, CRC Press, Taylor and Francis Group (2015).
- [10]. D. A. Krohn, *Fiber Optic Sensors: Fundamentals and Applications*, 3rd edition, Instrumentation Systems (2000).
- [11]. X. Bao, L. Chen, "Recent progress in distributed fiber optic sensors," *Sensors*, 12, 8601-8639 (2012).
- [12]. A. Ukil, H. Braendle, P. Krippner, "Distributed Temperature Sensing: Review of Technology and Applications," *IEEE Sensors Journal*, 12 (5), 885 - 892 (2012).
- [13]. B. D. Gupta, A. M. Shrivastav, S. P. Usha, "Surface Plasmon resonance-based fiber optic sensors utilizing molecular imprinting," *Sensors*, 16(9), 1381 (1-33) (2016).
- [14]. I. Arghir, F. Delport, D. Spasic, J. Lammertyn, "Smart design of fiber optic surfaces for improved plasmonic biosensing," *New Biotechnology*, 32, 473-484 (2015).
- [15]. X. Li, Y. Shao, Y. Yu, Y. Zhang, S. Wei, "A highly sensitive fiber-optic Fabry-Perot interferometer based on internal reflection mirrors for refractive index measurement," *Sensors*, 16(6), 794 (1-12) (2016).

- [16]. A. Othonos, K. Kalli, *Fiber Bragg Gratings: Fundamentals and Applications in Telecommunications and Sensing*, Artech House (1999).
- [17]. C. C. Laborde, *Current Trends in Short- and Long-period Fiber Gratings*, InTech (2013).
- [18]. M. A. Soto, P. K. Sahu, S. Faralli, G. Bolognini, F. Di Pasquale, B. Nebendahl, C. Rueck, “Distributed temperature sensor system based on raman scattering using correlation-codes,” *Electronics Letters*, 43 (16), 862 – 864 (2007).
- [19]. C. S. Moreira, A. M. N. Lima, H. Neff, C. Thirstrup, “Temperature-dependent sensitivity of surface plasmon resonance sensors at the gold–water interface,” *Sensors and Actuators B: Chemical*, 134, 854–862 (2008).
- [20]. J. Kou, J. Feng, L. Ye, F. Xu, Y. Lu, “Miniaturized fiber taper reflective interferometer for high temperature measurement ,” *Optics Express*, 18, 14245–14250 (2010).
- [21]. Y. J. Rao, M. Deng, D. W. Duan, X. C. Yang, T. Zhu, G. H. Cheng, “Micro Fabry-Perot interferometers in silica fibers machined by femtosecond laser,” *Optics Express*, 15, 14123–14128 (2007).
- [22]. T. Wei, Y. Han, Y. Li, H. L. Tsai, H. Xiao, “Temperature-insensitive miniaturized fiber inline Fabry-Perot interferometer for highly sensitive refractive index measurement,” *Optics Express*, 16, 5764–5769 (2008).
- [23]. D. Sporea, A. Stancalie, D. Negut, G. Pilorget, S. Delepine-Lesoille, L. Lablonde, “Online Tests of an Optical Fiber Long-Period Grating Subjected to Gamma Irradiation,” *IEEE Photonics Journal*, 6 (6), 0600211 (2014).
- [24]. C. Menadier, C. Kissinger, H. Adkins, “The fotonic sensor,” *Instruments and Control Systems*, 40, 114–120 (1967).
- [25]. A. T. Moraleda, C. V. García, J. Z. Zaballa, J. Arrue, “A temperature sensor based on a polymer optical fiber macro-bend,” *Sensors*, 13(10), 13076–13089 (2013).
- [26]. W. R. Habel, V. G. Schukar, N. Kusche, “Fibre-optic strain sensors are making the leap from lab to industrial use—reliability and validation as a precondition for standards,” *Meas. Sci. Technol.* 24, 094006 (1-13) (2013).
- [27]. P. Roriz, O. Frazão, A. B. Lobo-Ribeiro, J. L. Santos, J.A. Simoes, “Review of fiber-optic pressure sensors for biomedical and biomechanical applications,” *J. of Biomedical Optics*, 18(5), 050903 (2013).

- [28]. S. Pevec, D. Donlagic, "Miniature fiber-optic sensor for simultaneous measurement of pressure and refractive index," *Optics Letters*, 39 (21), 6221-6224 (2014).
- [29]. H. C. Lefèvre, *The Fiber-Optic Gyroscope*, Second Edition, Artech House (2014).
- [30]. Y. Kitagawa, A. Hayashi, "Fiber-optic sensor for distance and velocity measurements using speckle dynamics," *Applied Optics*, 24(7), 955-959 (1985).
- [31]. A. Stefani, S. Andresen, W. Yuan, N. H. Rasmussen, O. Bang, "High sensitivity polymer optical fiber-Bragg-grating-based accelerometer," *IEEE Photonics Technology Letters*, 24 (9), 763-765 (2012).
- [32]. Y. Chen, Q. Han, T. Liu, X. Lan, H. Xiao, "Optical fiber magnetic field sensor based on single-mode-multimode-single-mode structure and magnetic fluid," *Optics Letters*, 38 (20), 3999-4001 (2013).
- [33]. D. Zhou, Z. Qin, W. Li, L. Chen, X. Bao, "Distributed vibration sensing with time-resolved optical frequency-domain reflectometry," *Optics Express*, 20, 13138-13145 (2012).
- [34]. L. H. Chen, T. Li, C. C. Chan, R. Menon, P. Balamurali, M. Shaillender, B. Neu, X. M. Ang, P. Zu, W. C. Wong, K. C. Leong, "Chitosan based fiber-optic Fabry-Perot humidity sensor," *Sensors and Actuators B: Chemical*, 169 (5), 167-172 (2012).
- [35]. F. B. Xiong, W. Z. Zhu, H. F. Lin, X. G. Merg, "Fiber-optic sensor based on evanescent wave absorbance around 2.7 μm for determining water content in polar organic solvents," *Applied Physics B*, 115, 129-135 (2014).
- [36]. H. Jiang, R. Yang, X. Tang, A. Burnett, X. Lan, H. Xiao, J. Dong, "Multilayer fiber optic sensors for in situ gas monitoring in harsh environments," *Sensors and Actuators B: Chemical*, 177, 205-212 (2013).
- [37]. X. Wang, O. S. Wolfbeis, "Fiber-optic chemical sensors and biosensors," *Anal. Chem.*, 85 (2), 487-508 (2013).
- [38]. A. Ricciardi, A. Crescitelli, P. Vaiano, G. Quero, M. Consales, M. Pisco, E. Esposito, A. Cusano, "Lab-on-fiber technology: a new vision for chemical and biological sensing," *Analyst*, 140, 8068-8079 (2015).
- [39]. J. A. Kim, T. Hwang, S. R. Dugasani, R. Amin, A. Kulkarni, S. H. Park, T. Kim, "Graphene based fiber optic surface plasmon resonance for bio-chemical sensor applications," *Sensors and Actuators B: Chemical*, 187, 426-433 (2013).

- [40]. T. H. Nguyen, T. Venugopala, S. Chen, T. Sun, K. T. V. Grattan, S. E. Taylor, P. A. M. Basheer, A. E. Long, "Fluorescence based fibre optic pH sensor for the pH 10–13 range suitable for corrosion monitoring in concrete structures," *Sensors and Actuators B: Chemical*, 191,498-507 (2014).
- [41]. C. S. Chu, "Optical fiber oxygen sensor based on Pd (II) complex embedded in sol–gel matrix," *Journal of Luminescence*, 135, 5-9 (2013).
- [42]. J. G. V. Teixeira, I. T. Leite, S. Silva, O. Frazao, "Advanced fiber-optic acoustic sensors," *Photonic Sensors*, 4 (3), 198-208 (2014).
- [43]. S. S. Chong, A. R. A. Aziz, S. W. Harun, "Fibre optic sensors for selected wastewater characteristics," *Sensors*, 13(7), 8640-8668 (2013).
- [44]. C. K. Y. Leung, K. T. Wan, D. Inaudi, X. Bao, W. Habel, Z. Zhou, J. Ou, M. Ghandehari, H. C. Wu, M. Imai, "Optical fiber sensors for civil engineering applications," *Materials and Structures*, 48 (4), 871–906 (2015).
- [45]. S. Villalba, J. R. Casas, "Application of optical fiber distributed sensing to health monitoring of concrete structures," *Mechanical Systems and Signal Processing*, 39, 441–451 (2013).
- [46]. X. W. Ye, Y. H. Su, J. P. Han, "Structural Health Monitoring of Civil Infrastructure Using Optical Fiber Sensing Technology: A Comprehensive Review," *The Scientific World Journal*, Article ID 652329, 11 pages (2014).
- [47]. Z. Ding, D. Yang, Y. Du, K. Liu , Y. Zhou, R. Zhang, Z. Xu, J. Jiang, T. Liu, "Distributed strain and temperature discrimination using two types of fiber in OFDR," *IEEE Photonics Journal*, 8(5), 6804608 (2016).
- [48]. J. Zhang, G. Liao, S. Jin, D. Cao, Q. Wei, H. Lu, J. Yu, X. Cai, S. Tan, Y. Xiao, J. Tang, Y. Luo, Z. Chen, "All-fiber-optic temperature sensor based on reduced graphene oxide," *Laser Phys. Lett.*, 11, 035901 (2014).
- [49]. G. Berkovic, E. Shafir, "Optical methods for distance and displacement measurements," *Advances in Optics and Photonics*, 4(4), 441-471 (2012).
- [50]. H. Z. Yang, X. G. Qiao, D. Luo, K. S. Lim, W. Y. Chong, S. W. Harun, "A review of recent developed and applications of plastic fiber optic displacement sensors," *Measurement*, 48, 333-345 (2014).

- [51]. M. Bravo, A. M. R. Pinto, M. Lopez-Amo, J. Kobelke, K. Schuster, "High precision micro-displacement fiber sensor through a suspended-core Sagnac interferometer," *Optics Letters*, 37 (2), 202-204 (2012).
- [52]. H. W. Qiu, S. C. Xu, S. Z. Jiang, Z. Li, P. X. Chen, S. S. Gao, C. Zhang, D. J. Feng, "A novel graphene-based tapered optical fiber sensor for glucose detection," *Applied Surface Science*, 329, 390-395 (2015).
- [53]. A. Barrias, J. R. Casas, S. Villalba, "A review of distributed optical fiber sensors for civil engineering applications," *Sensors*, 16(5), 748 (2016).
- [54]. W. Xiong, C. S. Cai, X. Kong, "Instrumentation design for bridge scour monitoring using fiber Bragg grating sensors," *Applied Optics*, 51 (5), 547-557 (2012).
- [55]. F. Gao, H. Liu, C. Sheng, C. Zhu, S. N. Zhu, "Refractive index sensor based on the leaky radiation of a microfiber," *Optics Express* 22, 12645 (2014).
- [56]. R. N. Mariammal, K. Ramachandran, B. Renganathan, D. Sastikumar, "On the enhancement of ethanol sensing by CuO modified SnO₂ nanoparticles using fiber-optic sensor," *Sensors and Actuators B: Chemical*, 169, 199-207 (2012).
- [57]. B. Renganathan, A. R. Ganesan, "Fiber optic gas sensor with nanocrystalline ZnO," *Optical Fiber Technology*, 20 (1), 48-52 (2014).
- [58]. Y. Huang, L. Wieck, S. Tao, "Development and evaluation of optical fiber NH₃ sensors for application in air quality monitoring," *Atmospheric Environment*, 66, 1-7 (2013).
- [59]. P. Roriz, A. Ramos, J. L. Santos, J. A. Simoes, "Fiber optic intensity-modulated sensors: A review in biomechanics," *Photonic Sensors*, 2 (4), 315–330 (2012).
- [60]. D. A. Krohn, "Intensity modulated fiber optic sensors overview," *Proceedings of SPIE 0718, Fiber Optic and Laser Sensors IV*, 2 (1987).
- [61]. C. Yang, S. O. Oyadiji, "Theoretical and experimental study of self-reference intensity-modulated plastic fibre optic linear array displacement sensor," *Sensors and Actuators A: Physical*, 222, 67-79 (2015).
- [62]. D. Lau, Z. Chen, J. T. Teo, S. H. Ng, H. Rumpel, Y. Lian, H. Yang, P. L. Kei, "Intensity-modulated microbend fiber optic sensor for respiratory monitoring and gating during MRI," *IEEE Transactions on Biomedical Engineering*, 60 (9), 2655 – 2662 (2013).
- [63]. N. Lagakos, J. Bucaro, "Phase-modulated fiber optic acoustic sensors," *ISA Transactions*, 28 (2), 1-6 (1989).

- [64]. S. Dante, D. Duval, B. Sepúlveda, A. B. González-Guerrero, J. R. Sendra, L. M. Lechuga, “All-optical phase modulation for integrated interferometric biosensors,” *Optics Express*, 20 (7), 7195-7205 (2012).
- [65]. K. Misiakos, I. Raptis, A. Salapatas, E. Makarona, A. Botsialas, M. Hoekman, R. Stoffer, G. Jobst “Broad-band Mach-Zehnder interferometers as high performance refractive index sensors: Theory and monolithic implementation,” *Optics Express*, 22 (8), 8856-8870 (2014).
- [66]. J. Zubia, L. Casado, G. Aldabaldetrekú, A. Montero, E. Zubia, G. Durana, “Design and development of a low-cost optical current sensor,” *Sensors*, 13, 13584-13595 (2013).
- [67]. X. Li, Q. Sun, D. Liu, R. Liang, J. Zhang, J. Wo, P. P. Shum, D. Liu, “Simultaneous wavelength and frequency encoded microstructure based quasi-distributed temperature sensor,” *Optics Express*, 20 (11), 12076-12084 (2012).
- [68]. X. Zou, A. Chao, Y. Tian, N. Wu, H. Zhang, T. Yu, X. Wang, “An experimental study on the concrete hydration process using Fabry–Perot fiber optic temperature sensors,” *Measurement*, 45 (5), 1077-1082 (2012).
- [69]. J. Albert, L. Shao, C. Caucheteur, “Tilted fiber Bragg grating sensors,” *Laser and Photonics Reviews*, 7 (1), 83-108 (2013).
- [70]. H. Guo, J. Tang, X. Li, Y. Zheng, H. Yu, H. Yu, “On-line writing identical and weak fiber Bragg grating arrays,” *Chinese Optics Letters*, 11 (3), 030602 (2013).
- [71]. Y. Wang, J. Gong, B. Dong, D. Y. Wang, T. J. Shillig, A. Wang, “A large serial time-division multiplexed fiber Bragg grating sensor network,” *Journal of Lightwave Technology*, 30 (17), 2751-2756 (2012).
- [72]. Z. Luo, H. Wen, H. Guo, M. Yang, “A time-and wavelength-division multiplexing sensor network with ultra-weak fiber Bragg gratings,” *Optics Express*, 21(19), 22799-22807 (2013).
- [73]. R. Kashyap, *Fiber Bragg Gratings*, 2nd Edition, Academic Press (2010).
- [74]. J. M. L. Higuera, *Handbook of Optical Fibre Sensing Technology*, John Wiley & Sons, 349-377 (2002).
- [75]. A. Othonos, “Fiber bragg gratings,” *Review of Scientific Instruments*, 68, 4309-4341 (1997).
- [76]. D. P. Hand, P. St. J. Russell, “Photoinduced refractive-index changes in germanosilicate fibers,” *Optics Letters*, 15, 102-104 (1990).
- [77]. M. Douay, W. X. Xie, T. Taunay, P. Bernage, P. Niay, P. Cordier, B. Poumellec, L. Dong, J. F. Bayon, H. Poignant, E. Delevaque, “Densification involved in the UV-based photosensitivity of

- silica glasses and optical fibers,” *IEEE Journal of Lightwave Technology*, 15(8), 1329–1342 (1997).
- [78]. Y. Hibino, H. Hanafusa, “Defect structure and formation mechanism of drawing-induced absorption at 630 nm in silica optical fibers,” *Journal of Applied Physics*, 60 (5), 1797-1801 (1986).
- [79]. D. L. Griscom, E. J. Friebele, “Fundamental defect centers in glass: ^{29}Si hyperfine structure of the nonbridging oxygen hole center and the peroxy radical in $\alpha\text{-SiO}_2$,” *Physical Review B*, 24 (8), 4896-4898 (1981).
- [80]. P. St. J. Russell, L. J. Poyntz-Wright, D. P. Hand, “Frequency doubling, absorption, and grating formation in glass fibers: effective defects or defective effects?,” *Proceedings of SPIE*, 1373, 126 (1990).
- [81]. R. M. Atkins, V. Mizrahi, T. Erdogan, “248 nm induced vacuum UV spectral changes in optical fibre preform cores: support for a colour centre model of photosensitivity,” *Electronics Letters*, 29, 385 (1993).
- [82]. C. Fiori, R. A. B. Devine, “Ultraviolet Irradiation Induced Compaction and Photoetching in Amorphous, Thermal SiO_2 ,” *Material Research Society Symposium Proceedings*, 61, 187 (1986).
- [83]. M. G. Sceats, S. B. Poole, “Stress-Relief—The mechanism of photorefractive index control in fiber cores,” *Australian Conference on Optical Fiber Technology*, 302 (1991).
- [84]. D. Wong, S. B. Poole, M. G. Sceats, “Stress-birefringence reduction in elliptical-core fibers under ultraviolet irradiation,” *Optics Letters*, 17, 1773-1775 (1992).
- [85]. D. L. Williams, B. J. Ainslie, J. R. Armitage, R. Kashyap, R. Campbell, “Enhanced UV photosensitivity in boron codoped germanosilicate fibres,” *Electronics Letters*, 29(1), 45–47 (1993).
- [86]. J. Albert, B. Malo, F. Bilodeau, D. C. Johnson, K. O. Hill, Y. Hibino, M. Kawachi, “Photosensitivity in Ge-doped silica optical waveguides and fibers with 193-nm light from an ArF excimer laser,” *Optics Letters*, 19 (6), 387-389 (1994).
- [87]. P. E. Dyer, R. J. Farley, R. Giedl, K. C. Byron, D. Reid, “High reflectivity fibre gratings produced by incubated damage using a 193 nm ArF laser,” *Electronics Letters*, 30, 860-862 (1994).

- [88]. P. J. Lemaire, R. M. Atkins, V. Mizrahi, W. A. Reed, "High pressure H₂/loading as a technique for achieving ultrahigh UV photosensitivity and thermal sensitivity in GeO₂/doped optical fibres," *Electronics Letters*, 29(13), 1191–1193 (1993).
- [89]. D. K. W. Lam, B. K. Garside, "Characterization of single-mode optical fiber filters," *Applied Optics*, 20(3), 440-445 (1981).
- [90]. K. O. Hill, G. Meltz, "Fiber Bragg grating technology fundamentals and overview," *IEEE Journal of Lightwave Technology*, 15, 1263-1276 (1997).
- [91]. H. Kogelnick, "Filter Response of Nonuniform Almost-Periodic Structures," *The Bell System Technical Journal*, 55, 109–126, 1976.
- [92]. L. A. Weller-Brophy, D. G. Hall, "Analysis of waveguide gratings: application of Rouard's method," *Journal of Optical Society of America A*, 2, 863–871 (1985).
- [93]. M. Yamada, K. Sakuda, "Analysis of almost-periodic distributed feedback slab waveguides via a fundamental matrix approach," *Applied Optics*, 26, 3474–3478 (1987).
- [94]. V. Mizrahi, J. E. Sipe, "Optical properties of photosensitive fiber phase gratings," *Journal of Lightwave Technology*, 11, 1513–1517 (1993).
- [95]. E. Peral, J. Capmany, J. Marti, "Iterative solution to the Gel'Fand-Levitan-Marchenko coupled equations and application to synthesis of fiber gratings," *IEEE Journal of Quantum Electronics*, 32, 2078–2084 (1996).
- [96]. L. Gruener-Nielsen, J. Hueber, "Photosensitive fiber for highly reflective Bragg gratings," WL16, Technical Digest, Optical Fiber Communication Conference (OFC97) 1997.
- [97]. G. Meltz, W. W. Morey, W. H. Glenn, "Formation of Bragg gratings in optical fibers by a transverse holographic method," *Optics Letters*, 14, 823-825 (1989).
- [98]. S. J. Mihailov, "Fiber Bragg grating sensors for harsh environments," *Sensors*, 12(2), 1898-1918 (2012).
- [99]. M. Becker, T. Elsmann, I. Latka, M. Rothhardt, H. Bartelt, "Chirped phase mask interferometer for fiber Bragg grating array inscription," *Journal of Lightwave Technology*, 33 (10), 2093-2098 (2015).
- [100]. R. Kashyap, J. R. Armitage, R. Wyatt, S. T. Davey, D. L. Williams, "All-fibre narrowband reflection gratings at 1500 nm," *Electronics Letters*, 26, 730-732 (1990).
- [101]. M. M. Broer, R. L. Cone, J. R. Simpson, "Ultraviolet-induced distributed-feedback gratings in Ce³⁺-doped silica optical fibers," *Optics Letters*, 16, 1391-1393 (1991).

- [102]. B. Malo, K. O. Hill, F. Bilodeau, D. C. Johnson, J. Albert, "Point-by-point fabrication of micro-Bragg gratings in photosensitive fibre using single excimer pulse refractive index modification techniques," *Electronics Letters*, 29, 1668- 1669 (1993).
- [103]. A.V. Dostovalov, A. A. Wolf, A. V. Parygin, V. E. Zyubin, S. A. Babin, "Femtosecond point-by-point inscription of Bragg gratings by drawing a coated fiber through ferrule," *Optics Express*, 24 (15), 16232-16237 (2016).
- [104]. M. Saad, L. R. Chen, X. Gu, "Highly reflective fiber Bragg gratings inscribed in Ce/Tm co-doped ZBLAN fibers," *IEEE Photonics Technology Letters*, 25(11), 1066-1068 (2013).
- [105]. K. P. Chen, P. R. Herman, R. Tam, "Strong fiber Bragg grating fabrication by hybrid 157-and 248-nm laser exposure," *IEEE Photonics Technology Letters*, 14, 170-172 (2002).
- [106]. L. Dong, W. F. Liu, L. Reekie, "Negative-index gratings formed by a 193-nm excimer laser," *Optics Letters*, 21, 2032- 2034 (1996).
- [107]. W. Yuan, A. Stefani, O. Bang, "Tunable polymer fiber Bragg grating (FBG) inscription: fabrication of dual-FBG temperature compensated polymer optical fiber strain sensors," *IEEE Photonics Technology Letters*, 24 (5), 401-403 (2012).
- [108]. C. J. Paddison, J. M. Dawes, D. J. W. Brown, M. J. Withford, R. I. Trickett, P. A. Krug, "Multiple fibre gratings fabricated using frequency-doubled copper vapour lasers," *Electronics Letters*, 34, 2407-2408 (1998).
- [109]. J. R. Armitage, "Fibre Bragg reflectors written at 262 nm using a frequency quadrupled diode-pumped Nd/sup 3+: YLF laser," *Electronics Letters*, 29, 1181-1183 (1993).
- [110]. Y. Ran, L. Jin, Y. Tan, L. Sun, J. Li, B. Guan, "High-efficiency ultraviolet inscription of Bragg gratings in microfibers," *IEEE Photonics Journal* , 4(1), 181-186 (2012).
- [111]. R. M. Atkins, R. P. Espindola, "Photosensitivity and grating writing in hydrogen loaded germanosilicate core optical fibers at 325 and 351 nm," *Applied Physics Letters*, 70, 1068-1069 (1997).
- [112]. G. Statkiewicz-Barabach, K. Tarnowski, D. Kowal, P. Mergo, W. Urbanczyk, "Fabrication of multiple Bragg gratings in microstructured polymer fibers using a phase mask with several diffraction orders," *Optics Express*, 21 (7), 8521-8534 (2013).
- [113]. G. Rajan, M. Y. M. Noor, E. Ambikairajah, G. Peng, "Inscription of multiple Bragg gratings in a single-mode polymer optical fiber using a single phase mask and its analysis," *IEEE Sensors Journal*, 14 (7), 2384-2388 (2014).

- [114]. T. Osuch, K. Jędrzejewski, L. Lewandowski, W. Jasiewicz, "Shaping the spectral characteristics of fiber Bragg gratings written in optical fiber taper using phase mask method," *Photonics Letters of Poland*, 4 (4), 128-130 (2012)
- [115]. X. Hu, C. J. Pun, H. Tam, P. Mégret, C. Caucheteur, "Highly reflective Bragg gratings in slightly etched step-index polymer optical fiber," *Optics Express*, 22 (15), 18807-18817 (2014).
- [116]. J. Thomas, C. Voigtländer, D. Schimpf, F. Stutzki, E. Wikszak, J. Limpert, S. Nolte, A. Tünnermann, "Continuously chirped fiber Bragg gratings by femtosecond laser structuring," *Optics Letters*, 33, 1560–1562 (2008).
- [117]. C. Voigtländer, J. Thomas, E. Wikszak, P. Dannberg, S. Nolte, A. Tünnermann, "Chirped fiber Bragg gratings written with ultrashort pulses and a tunable phase mask," *Optics Letters*, 34, 1888-1890 (2009).
- [118]. D. Z. Anderson, V. Mizrahi, T. Erdogan, A.E. White, "Production of in-fibre gratings using a diffractive optical element," *Electronics Letters*, 29, 566-568 (1993).
- [119]. J. Albert, S. Theriault, F. Bilodeau, D. Johnson, K. Hill, P. Sixt, M. Rooks, "Minimization of phase errors in long fiber Bragg grating phase masks made using electron beam lithography," *IEEE Photonics Technology Letters*, 8, 1334–1336 (1996).
- [120]. K. O. Hill, B. Malo, F. Bilodeau, D.C. Johnson, J. Albert, "Bragg gratings fabricated in monomode photosensitive optical fiber by UV exposure through a phase mask," *Applied Physics Letters*, 62, 1035-1037 (1993).
- [121]. D. Z. Anderson, V. Mizrahi, T. Erdogan, A.E. White, "Production of in-fibre gratings using a diffractive optical element," *Electronics Letters*, 29, 566-568 (1993).
- [122]. H. G. Bruckner, O. Leminger, R. Zengerle, M. Korn, "Performance of electron beam written dielectric waveguide grating filters considering fabrication tolerances," *Journal of Optical Communications*, 14, 18-24 (1993).
- [123]. F. Bilodeau, B. Malo, J. Albert, D. C. Johnson, K. O. Hill, Y. Hibino, M. Abe, M. Kawachi, "Photosensitization of optical fiber and silica-on-silicon/silica waveguides," *Optics Letters*, 18 (12), 953-956 (1993).
- [124]. P. E. Dyer, R. J. Farley, R. Giedl, C. Ragdale, D. Reid, "Study and analysis of submicron-period grating formation on polymers ablated using a KrF laser irradiated phase mask," *Applied Physics Letters*, 64 (25), 3389-3391 (1995).

- [125]. A. Dragomir, D. N. Nikogosyan, K. A. Zagorulko, P. G. Kryukov, E. M. Dianov, "Inscription of fiber Bragg gratings by ultraviolet femtosecond radiation," *Optics Letters*, 28 (22), 2171-2173 (2003).
- [126]. S. A. Slattery, D. N. Nikogosyan, G. Brambilla, "Fiber Bragg grating inscription by high-intensity femtosecond UV laser light: comparison with other existing methods of fabrication," *Journal of the Optical Society of America B*, 22 (2), 354-361 (2005).
- [127]. J. L. Archambault, L. Reekie, P. St. J. Russel, "100% reflectivity Bragg reflectors produced in optical fibres by single excimer laser pulses," *Electronics Letters*, 29, 453-455 (1993).
- [128]. H. Patrick, S. L. Gilbert, "Growth of Bragg gratings produced by continuous-wave ultraviolet light in optical fiber," *Optics Letters*, 18, 1484-1486 (1993).
- [129]. W. W. Morey, G. Meltz, W. H. Glen, "Photoinduced Bragg gratings in optical fibers," *Optics and Photonics News*, 1, 8-14 (1994).
- [130]. H. J. Booth, E. K. Illy, M. R. H. Knowles, G. T. Purves, A. J. Kearsley, "Manufacture of photonics components with a deep UV laser source at 255 nm," in *Proceedings of the ICALEO, Laser Institute, America*, paper M203 (2001).
- [131]. B. F. Johnston, A. J. Lee, M. J. Withford, J. A. Piper, "Laser assisted jacket removal and writing of fiber Bragg gratings using a single laser source," *Optics Express*, 10 (16), 818-823 (2002).
- [132]. O. Prakash, R. Mahakud, S.K. Dixit, U. Nundy, "Effect of the spatial coherence of ultraviolet radiation (255 nm) on the fabrication efficiency of phase mask based fiber Bragg gratings," *Optics Communications*, 263 (1), 65-70 (2006).
- [133]. S. A. Kukushkin, M. G. Shlyagin, P. L. Swart, A. A. Chtcherbakov, A. V. Osipov, "Type IIA photosensitivity and formation of pores in optical fibers under intense ultraviolet irradiation," *Journal of Applied Physics*, 102 (5), 053502 (2007).
- [134]. K. O. Hill, Y. Fujii, D. C. Johnson, B. S. Kawasaki, "Photosensitivity in optical fiber waveguides: Application to reflection filter fabrication," *Applied Physics Letters*, 32, 647-649 (1978).
- [135]. B. S. Kawasaki, K. O. Hill, D. C. Johnson, Y. Fujii, "Narrow-band Bragg reflectors in optical fibers," *Optics Letters*, 3, 66-68 (1978).

- [136]. D. Wiesmann, J. Hubner, R. Germann, I. Massarek, H.W.M. Salemink, G. L. Bona, M. Kristensen, H. Jackel, "Large uv-induced negative index changes in germanium-free nitrogen-doped planar SiO_2/Si waveguides," *Electronics Letters*, 34(4), 364-366 (1998).
- [137]. M. L. Blanc, S. Y. Huang, M. M. Ohn, R. M. Measures, "Tunable chirping of a fibre Bragg grating using a tapered cantilever beam," *Electronics Letters*, 30, 2163-2165 (1994).
- [138]. J. L. Cruz, L. Dong, L. Reekie, "Improved thermal sensitivity of fibre Bragg gratings using a polymer overlayer," *Electronics Letters*, 32, 385-387 (1996).
- [139]. M. A. Fokine, B. E. Sahlgren, R. Stubbe, Conference on Bragg gratings, photosensitivity and poling in glass fibres and waveguides, Williamsburg, Technical Digest, BSuD5 (1997).
- [140]. A. Asseh, S. Sandgren, H. Ahlfeldt, B. Sahlgren, R. Stubbe, G. Edwall, "Fiber optical Bragg grating refractometer," *Fiber and Integrated Optics*, 17, 51-62 (1998).
- [141]. A. Iadicicco, A. Cusano, S. Campopiano, A. Cutolo, M. Giordano, "Thinned fiber Bragg gratings as refractive index sensors," *IEEE Sensors Journal*, 5, 1288-1295 (2005).
- [142]. R. Liang, Q. Sun, J. Wo, D. Liu, "Investigation on micro/nanofiber Bragg grating for refractive index sensing," *Optics Communications*, 285(6), 1128-1133 (2012).
- [143]. B. Guan, J. Li, L. Jin, Y. Ran, "Fiber Bragg gratings in optical microfibers," *Optical Fiber Technology*, 19 (6), 793-801 (2013).
- [144]. A. P. Zhang, S. Gao, G. Yan, Y. Bai, "Advances in optical fiber Bragg grating sensor technologies," *Photonic Sensors*, 2 (1), 1-13 (2012).
- [145]. F. Baldini, M. Brenci, F. Chiavaioli, A. Giannetti, C. Trono, "Optical fibre gratings as tools for chemical and biochemical sensing," *Analytical and Bioanalytical Chemistry*, 402 (1), 109-116 (2012).
- [146]. G. Tsigaridas, D. Polyzos, A. Ioannou, M. Fakis, P. Persephonis, "Theoretical and experimental study of refractive index sensors based on etched fiber Bragg gratings," *Sensors and Actuators A: Physical*, 209, 9-15 (2014).
- [147]. A. Cusano, A. Iadicicco, S. Campopiano, M. Giordano, A. Cutolo, "Thinned and micro-structured fibre Bragg gratings: towards new all-fibre high-sensitivity chemical sensors," *Journal of Optics A: Pure and Applied Optics*, 7, 734-741 (2005).
- [148]. Sridevi S, K. S. Vasu, N. Jayaraman, S. Asokan, A. K. Sood, "Optical bio-sensing devices based on etched fiber Bragg gratings coated with carbon nanotubes and graphene oxide along with a specific dendrimer," *Sensors and Actuators B: Chemical*, 195, 150-155 (2014).

- [149]. K. Schroeder, W. Ecke, R. Mueller, R. Willsch, A. Andreev, "A fibre Bragg grating refractometer," *Measurement Science and Technology*, 12 (7), 757-764 (2001).
- [150]. *Laser focus world* 10 August 2016.
- [151]. K. Krebber, H. Henschel, U. Weinand, "Fibre Bragg gratings as high dose radiation sensors?," *Measurement Science and Technology*, 17 (5), 1095-1102 (2006).
- [152]. N. Jovanovic, "Narrow linewidth, 100 W cw Yb³⁺-doped silica fiber laser with a point-by-point Bragg grating inscribed directly into the active core," *Optics Letters*, 32, 2804-2806 (2007).
- [153]. W. Liang, Y. Huang, Y. Xu, R. K. Leeand, A. Yariv, "Highly sensitive fiber Bragg grating refractive index sensors," *Applied Physics Letters*, 86 (15), 151122 (2005)
- [154]. H. Zhou, J. Q. Wen, X. Z. Zhang, W. Wang, D. Q. Feng, Q. Wang, F. Jia, "Study on Fiber-optic Hydrogen Sulfide Gas Sensor," *Physics Procedia*, 56, 1102-1106 (2014).
- [155]. S. C. Tjin, Y. Wang, X. Sun, P. Moyo, J. M. W. Brownjohn, "Application of quasi-distributed fibre Bragg grating sensors in reinforced concrete structures," *Measurement Science and Technology*, 13 (4), 583-589 (2002).
- [156]. W. Du, X. M. Tao, H. Y. Tam, C. L. Choy, "Fundamentals and applications of optical fiber Bragg grating sensors to textile structural composites," *Composite Structures*, 42, 217-229 (1998).
- [157]. J. Canning, "Fibre gratings and devices for sensors and lasers," *Laser & Photonics Reviews*, 2, 275-289 (2008).
- [158]. R. Chen, A. Yan, Q. Wang, K. P. Chen, "Fiber-optic flow sensors for high-temperature environment operation up to 800 °C," *Optics Letters*, 39, 3966-3969 (2014).
- [159]. T. Chen, R. Chen, C. Jewart, B. Zhang, K. Cook, J. Canning, K. P. Chen, "Regenerated gratings in air-hole microstructured fibers for high-temperature pressure sensing," *Optics Letters*, 36, 3542-3544 (2011).
- [160]. S. D. Jackson, "Towards high-power mid-infrared emission from a fibre laser," *Nature Photonics*, 6 (7), 423-431 (2012).
- [161]. J. Kumar, O. Prakash, S. K. Agrawal, R. Mahakud, A. Mokhariwale, S. K. Dixit, S. V. Nakhe, "Distributed fiber Bragg grating sensor for multipoint temperature monitoring up to 500 °C in high-electromagnetic interference environment," *Optical Engineering Letters*, 55 (9), 0905021-4, (2016).

- [162]. N. Grothoff, J. Canning, "Enhanced type IIA gratings for high-temperature operation," *Optics Letters*, 29, 2360-2362 (2004).
- [163]. D. Grobnic, S. J. Mihailov, C. W. Smelser, H. Ding, "Sapphire fiber Bragg grating sensor made using femtosecond laser radiation for ultrahigh temperature applications," *IEEE Photonics Technology Letters*, 16 (11), 2505–2507 (2004).
- [164]. O. V. Butov, E. M. Dianov, K. M. Golant, "Nitrogen-doped silica-core fibres for Bragg grating sensors operating at elevated temperatures," *Measurement Science and Technology*, 17, 975-979 (2006).
- [165]. M. Fokine, "Formation of thermally stable chemical composition gratings in optical fiber," *Journal of the Optical Society of America B*, 19, 1759-1765 (2002).
- [166]. J. Canning, M. Stevenson, S. Bandyopadhyay, K. Cook, "Extreme silica optical fibre gratings," *Sensors*, 8, 6448-6452 (2008).
- [167]. S. Bandyopadhyay, J. Canning, M. Stevenson, K. Cook, "Ultrahigh-temperature regenerated gratings in boron-codoped germanosilicate optical fiber using 193 nm," *Optics Letters*, 33, 1917-1919 (2008).
- [168]. D. Grobnic, C. W. Smelser, S. J. Mihailov, R. B. Walker, "Long-term thermal stability tests at 1000 °C of silica fibre Bragg gratings made with ultrafast laser radiation," *Measurement Science and Technology*, 17, 1009-1013 (2006).
- [169]. S. Pal, "Characterization of thermal (in) stability and temperature-dependence of type-I and type-IIA Bragg gratings written in B-Ge co-doped fiber," *Optics Communications*, 262 (1), 68-76 (2006).
- [170]. O. Prakash, J. Kumar, R. Mahakud, S. K. Agrawal, S. K. Dixit, S. V. Nakhe, "Enhanced temperature (~800 °C) stability of type-IIa FBG written by 255 nm beam," *IEEE Photonics Technology Letters*, 26, 93–95 (2014).
- [171]. J. He, Y. Wang, C. Liao, C. Wang, S. Liu, K. Yang, Y. Wang, X. Yuan, G. P. Wang, W. Zhang, "Negative-index gratings formed by femtosecond laser overexposure and thermal regeneration," *Nature Scientific Reports*, 6, Article number: 23379 (1-9) (2016).
- [172]. M. Douay, W. X. Xie, T. Taunay, P. Bernage, P. Niay, P. Cordier, B. Poumellec, L. Dong, J. F. Bayon, H. Poignant, E. Delevaque, "Densification involved in the UV-based photosensitivity of silica glasses and optical fibers," *Journal of Lightwave Technology*, 15, 1329–1342 (1997).

- [173]. Y. Liu, J. A. R. Williams, L. Zhang, I. Bennion, "Abnormal spectral evolution of fiber Bragg gratings in hydrogenated fibers," *Optics Letters*, 27, 586–588 (2002).
- [174]. G. Violakis, M. Konstantaki, S. Pissadakis, "Accelerated recording of negative index gratings in Ge-doped optical fibers using 248-nm 500-fs laser radiation," *IEEE Photonics Technology Letters*, 18, 1182–1184 (2006).
- [175]. Y. Ran, L. Jin, S. Gao, L. Sun, Y. Huang, J. Li, B. Guan, "Type IIa Bragg gratings formed in microfibers," *Optics Letters*, 40 (16), 3802–3805 (2015).
- [176]. J. Kumar, R. Mahakud, A. Mokhariwale, O. Prakash, S. K Dixit, S. V. Nakhe, "Studies on thermal regeneration and temperature stability of type-I FBGs written in Ge–B codoped and Ge doped fibers by a kHz repetition rate nanosecond 255 nm beam," *Optics Communications*, 320, 109-113 (2014).
- [177]. E. Lindner, J. Canning, C. Chojetzki, S. Bruckner, M. Becker, M. Rothhardt, H. Bartelt, "Thermal regenerated type IIa fiber Bragg gratings for ultra-high temperature operation," *Optics Communications*, 284, 183–185 (2011).
- [178]. J. Canning, M. Stevenson, J. Fenton, M. Aslund, S. Bandyopadhyay, "Strong regenerated gratings," *Proceedings of SPIE*, 7503, 750326–750326 (2009).
- [179]. H. Z. Yang, X. G. Qiao, S. Das, M. C. Paul, "Thermal regenerated grating operation at temperatures up to 1400° C using new class of multimaterial glass-based photosensitive fiber," *Optics Letters*, 39 (22), 6438-6441 (2014).
- [180]. M. Busch, W. Ecke, I. Latka, D. Fischer, R. Willsch, H. Bartelt, "Inscription and characterization of Bragg gratings in single-crystal sapphire optical fibres for high-temperature sensor applications," *Measurement Science and Technology*, 20, 115301 (1-6) (2009).
- [181]. A. Kumar, T. V. B. Subrahmanyam, A. D. Sharma, K. Thyagarajan, B. P. Pal, I. C. Goyal, "Novel refractometer using a tapered optical fibre," *Electronics Letters*, 20, 534 -535, (1984).
- [182]. F. Xu, G. Brambilla, "Demonstration of a refractometric sensor based on optical microfiber coil resonator," *Applied Physics Letters*, 92 (10), 101126 (2008).
- [183]. A. T. Andreev, B. S. Zafirova, E. I. Karakoleva, "Single-mode fiber polished into the core as a sensor element," *Sensors and Actuators A: Physical*, 64 (3), 209-212 (1998).
- [184]. E. Kretschmann, "Decay of non-radiative surface plasmons into light on rough silver films. Comparison of experimental and theoretical results," *Optics Communications*, 6, 185-187 (1972).

- [185]. T. Takeo, H. Hattori, "Optical fiber sensor for measuring refractive index," *Japanese Journal of Applied Physics*, 21 (10), 1509-1512 (1982).
- [186]. P. Wang, Y. Semenova, Q. Wu, G. Farrell, Y. Ti, J. Zheng, "Macrobending single-mode fiber-based refractometer," *Applied Optics*, 48, 6044-6049 (2009).
- [187]. B. H. Lee, Y. Liu, S. B. Lee, S. S. Choi, J. N. Jang, "Displacements of the resonant peaks of a long-period fiber grating induced by a change of ambient refractive index," *Optics Letters*, 22, 1769-1771 (1997).
- [188]. D. W. Kim, F. Shen, X. Chen, A. Wang, "Simultaneous measurement of refractive index and temperature based on a reflection-mode long-period grating and an intrinsic Fabry-Perot interferometer sensor," *Optics Letters*, 30, 3000-3002 (2005).
- [189]. T. Zhu, Y. J. Rao, Q. J. Mo, "Simultaneous measurement of refractive index and temperature using a single ultralong-period fiber grating," *IEEE Photonics Technology Letters*, 17 (12), 2700-2702 (2005).
- [190]. O. Frazão, P. Caldas, J. L. Santos, P. V. S. Marques, C. Turck, D. J. Lougnot, O. Soppera, "Fabry-Perot refractometer based on an end-of-fiber polymer tip," *Optics Letters*, 34, 2474-2476 (2009).
- [191]. N. M. Hanumegowda, C. J. Stica, B. C. Patel, I. White, X. Fan, "Refractometric sensors based on microsphere resonators," *Applied Physics Letters*, 87 (20), 201107 (2005).
- [192]. H. Zhu, I. M. White, J. D. Suter, M. Zourob, X. Fan, "Integrated refractive index optical ring resonator detector for capillary electrophoresis," *Analytical Chemistry*, 79, 930-937 (2007).
- [193]. M. Kheiri, M. I. Zibaii, J. Sadeghi, H. Latifi, "Refractive index measurement by fat long period grating sensor on a single mode optical fiber," *Communications and Photonics Conference and Exhibition, ACP Asia*, ISSN: 2162-108X, 1-6, (2011).
- [194]. W. B. Ji, S. C. Tjin, B. Lin, C. L. Ng, "Highly sensitive refractive index sensor based on adiabatically tapered microfiber long period gratings," *Sensors*, 13, 14055-14063(2013).
- [195]. J. H. Chong, P. Shum, H. Haryono, A. Yohana, M. K.Rao, C. Lu, Y. N. Zhu, "Measurements of refractive index sensitivity using long-period grating refractometer," *Optics Communications*, 229, 65-69 (2004).
- [196]. L. Rindorf, O. Bang, "Highly sensitive refractometer with a photonic-crystal-fiber long-period grating," *Optics Letters*, 33, 563-565 (2008).

- [197]. D. K. C. Wu, B. T. Kuhlmeier, B. J. Eggleton, "Ultrasensitive photonic crystal fiber refractive index sensor," *Optics Letters*, 34, 322-324 (2009).
- [198]. A. Iadicicco, S. Campopiano, A. Cutolo, M. Giordano, A. Cusano, "Refractive index sensor based on microstructured fiber Bragg grating," *IEEE Photonics Technology Letters*, 17, 1250 - 1252 (2005).
- [199]. A. Cusano, A. Iadicicco, S. Campopiano, M. Giordano, A. Cutolo, "Thinned and microstructured fibre Bragg gratings: towards new all-fibre high-sensitivity chemical sensors," *Journal of Optics A: Pure and Applied Optics*, 7, 734-741 (2005).
- [200]. N. Chen, B. Yun, Y. Wang, Y. Cui, "Theoretical and experimental study on etched fiber Bragg grating cladding mode resonances for ambient refractive index sensing," *Journal of the Optical Society of America B*, 24, 439-445 (2007).
- [201]. X. F. Huang, Z. M. Chen, L. Y. Shao, K. F. Cen, D. R. Sheng, J. Chen, H. Zhou, "Design and characteristics of refractive index sensor based on thinned and microstructure fiber Bragg grating," *Applied Optics*, 47, 504-511 (2008).
- [202]. Z. Qian, N. Ti-gang, P. Li, L. Chao, "Spectral characterization of fiber Bragg grating with etched fiber cladding," *Optoelectronics Letters*, 8, 328-331 (2012).
- [203]. H. K. Bal, Z. Brodzeli, N. M. Dragomir, S. F. Collins, F. Sidirolou, "Uniformly thinned optical fibers produced via HF etching with spectral and microscopic verification," *Applied Optics*, 51 2282-2287 (2012).
- [204]. P. Pfeifer, U. Aldinger, G. Schwotzer, S. Diekmann, P. Steinrucke, "Real time sensing of specific molecular binding using surface plasmon resonance spectroscopy," *Sensors and Actuators B: Chemical*, 54, 166-175 (1999).
- [205]. G. Laffont, P. Ferdinand, "Tilted short-period fibre-Bragg-grating-induced coupling to cladding modes for accurate refractometry," *Measurement Science and Technology*, 12, 765-770 (2001).
- [206]. C. F. Chan, C. Chen, A. Jafari, A. Laronche, D. J. Thomson, J. Albert, "Optical fiber refractometer using narrowband cladding-mode resonance shifts," *Applied Optics*, 46, 1142-1149 (2007).
- [207]. A. Iadicicco, A. Cusano, G. V. Persiano, A. Cutolo, R. Bernini, M. Giordano, "Refractive index measurements by fiber Bragg grating sensor," *Proceedings of IEEE*, 1, 101-105 (2003).

- [208]. G. Ryu, M. Dagenais, M. T. Hurley, P. Deshong, "High specificity binding of lectins to carbohydrate-functionalized fiber Bragg gratings: A new model for biosensing applications," *IEEE Journal of Quantum Electronics*, 16 (3), 647–653 (2010).
- [209]. S. S. Saini, C. Stanford, S.M. Lee, J. Park, P. Deshong, W. E. Bentley, M. Dagenais, "Monolayer detection of biochemical agents using etched-core fiber Bragg grating sensors," *IEEE Photonics Technology Letters*, 19 (18), 1341–1343, (2007).
- [210]. A. N. Chryssis, S. S. Saini, S.M. Lee, H. Yi, W. E. Bentley, M. Dagenais, "Detecting hybridization of DNA by highly sensitive evanescent field etched core fiber Bragg grating sensors," *IEEE Journal of Quantum Electronics*, 11 (4), 864–872 (2005).
- [211]. S. M. Lee, S. S. Saini, M.Y. Jeong, "Simultaneous measurement of refractive index, temperature, and strain using etched-core fiber Bragg grating sensors," *IEEE Photonics Technology Letters*, 22 (19), 1431–1433 (2010).
- [212]. B. N. Shivannju, M. Renilkumar, G. R. Prashanth, S. Asokan, M. M. Varma, "Detection limit of etched fiber Bragg grating sensors," *Journal of Lightwave Technology*, 31 (14), 2441-2447 (2013).
- [213]. O. Prakash, R. Mahakud, R. Biswal, S. Gurram, H. S. Vora, S. K. Dixit, "Study on the quality of interference fringes from a pulsed UV source for application in a biprism based fiber Bragg grating writing," *Applied Optics*, 46 (24), 6210-6217 (2007).
- [214]. S. K. Dixit, J. K. Mittal, B. Singh, P. Saxena, R. Bhatnagar, "A generalized diffraction filtered resonator with a copper vapor laser," *Optics Communications*, 98, 91–94 (1993).
- [215]. D. W. Coutts, "Time resolved beam divergence from a copper vapor laser with unstable resonator," *IEEE Journal of Quantum Electronics*, 31 (2), 330-342 (1995).
- [216]. J. J. Chang, "Time-resolved beam-quality characterization of copper-vapor lasers with unstable resonators," *Applied Optics*, 33 (12), 2255-2265 (1994).
- [217]. O. Prakash, S. K. Dixit, R. Bhatnagar, "On the role of the coherence width and its evolution in a short-pulse fundamental beam in second harmonic generation from beta-barium borate," *IEEE Journal of Quantum Electronics*, 38 (6), 603-613 (2002).
- [218]. T. Omatsu, K. Kuroda, T. Shimura, M. Chihara, M. Itoh, I. Ogura, "Non-collinear interaction model of the second harmonic generation of a copper vapor laser," *Optics Communications*, 79 (1-2), 125-130 (1990).

- [219]. O. Prakash, R. Mahakud, S. K. Dixit, "Comparative study on second harmonic conversion and saturation characteristics of three copper vapor laser beams of same average power and different spatial coherence," *Optical Engineering*, 50 (11), 114201 (2011).
- [220]. D. N. Nikogosyan, "Multi-photon high-excitation-energy approach to fibre grating inscription," *Measurement Science and Technology*, 18, R1–29 (2007).
- [221]. P. Y. Fonjallaz, H. G. Limberger, R. P. Salathe, F. Cochet, B. Leuenberger, "Tension increase correlated to refractive-index change in fibers containing UV-written Bragg gratings," *Optics Letters*, 20(11) 1346-1348 (1995).
- [222]. P. Niay, P. Bernage, S. Legoubin, M. Douay, W. X. Xie, J. F. Bayon, T. Georges, M. Monerie, B. Poumellec, "Behaviour of spectral transmissions of Bragg gratings written in germania-doped fibres: writing and erasing experiments using pulsed or cw uv exposure," *Optics Communications*, 113, 176–192 (1994).
- [223]. N. H. Ky, H. G. Limberger, R. P. Salathe, F. Cochet, L. Dong, "UV-irradiation induced stress and index changes during the growth of type-I and type-IIA fiber gratings," *Optics Communications*, 225 (4-6), 313–318 (2003).
- [224]. L. Dong, J. Pinkstone, P. St. J. Russell, D. N. Payne, "Ultraviolet absorption in modified chemical vapor deposition preforms," *Journal of the Optical Society of America B*, 11, 2106–2111 (1994).
- [225]. N. Groothoff, J. Canning, E. Buckley, J. Zagari, "Bragg gratings in air–silica structured fibers," *Optics Letters*, 28 (4), 233-235 (2003).
- [226]. T. Erdogan, J. E. Sipe, "Tilted fiber phase gratings," *Journal of the Optical Society of America A*, 13 (2), 296-313 (1996).
- [227]. T. Erdogan, "Cladding-mode resonances in short-and long-period fiber grating filters," *Journal of the Optical Society of America A*, 14 (8), 1760-1773 (1997).
- [228]. W. W. Morey, G. Meltz, J. D. Love, S. J. Hewlett, "Mode-coupling characteristics of UV-written Bragg gratings in depressed-cladding fibre," *Electronics Letters*, 30 (9), 730-732 (1994).
- [229]. O. Prakash, J. Kumar, R. Mahakud, S. K. Dixit, "Development of tilted fibre Bragg gratings using highly coherent 255 nm radiation," *Pramana Journal of Physics*, 82 (2), 255-258 (2014).
- [230]. R. Mahakud, O. Prakash, S. V. Nakhe, S. K. Dixit, "Analysis on the saturation of refractive index modulation in fiber Bragg gratings (FBGs) written by partially coherent UV beams," *Applied Optics*, 51 (12), 1828-35 (2012).

- [231]. T. Erdogan, V. Mizrahi, P. J. Lemaire, D. Monroe, "Decay of ultraviolet-induced fiber Bragg gratings," *Journal of Applied Physics*, 76 (1), 73–80 (1994).
- [232]. Y. Lai, A. Martinez, I. Khrushchev, I. Bennion, "Distributed Bragg reflector fiber laser fabricated by femtosecond laser inscription," *Optics Letters*, 31 (11), 1672–1674 (2006).
- [233]. B. W. Zhang, M. Kahrizi, "High-temperature resistance fiber Bragg grating temperature sensor fabrication," *IEEE Sensors Journal*, 7 (4), 586–591 (2007).
- [234]. E. Lindner, C. Chojetzki, S. Brueckner, M. Becker, M. Rothhardt, J. Vlekken, H. Bartelt, "Arrays of regenerated fiber Bragg gratings in non-hydrogen-loaded photosensitive fibers for high-temperature sensor networks," *Sensors*, 9 (10), 8377–8381 (2009).
- [235]. K. Cook, L. Y. Shao, J. Canning, "Regeneration and helium: regenerating Bragg gratings in helium-loaded germanosilicate optical fibre," *Optical Materials Express*, 2 (12), 1733–1742 (2012).
- [236]. D. E. Swets, R. W. Lee, R. C. Frank, "Diffusion coefficients of helium in fused quartz," *The Journal of Chemical Physics*, 34 (1), 17–22 (1961).
- [237]. P. J. Lemaire, "Reliability of optical fibers exposed to hydrogen: prediction of long-term loss increases," *Optical Engineering*, 30 (6), 780–789 (1991).
- [238]. J. Stone, "Interactions of hydrogen and deuterium with silica optical fibers: A review," *IEEE Journal of Lightwave Technology*, 5(5), 712 – 733 (1987).
- [239]. S. Kannan, J. Z. Y. Guo, P. J. Lemaire, "Thermal stability analysis of UV-induced fiber Bragg gratings," *IEEE Journal of Lightwave Technology*, 15 (8), 1478-1483 (1997).
- [240]. S. Bandyopadhyay, J. Canning, P. Biswas, M. Stevenson, K. Dasgupta, "A study of regenerated gratings produced in germanosilicate fibers by high temperature annealing," *Optics Express*, 19 (2), 1198-1206 (2011).
- [241]. S. R. Baker, H. N. Rourke, V. Baker, D. Goodchild, "Thermal decay of fiber Bragg gratings written in boron and germanium codoped silica fiber," *IEEE Journal of Lightwave Technology*, 15 (8), 1470-1477 (1997).
- [242]. D.L. Williams, R.P. Smith, "Accelerated lifetime tests on UV written intra-core gratings in boron germania codoped silica fibre," *Electronics Letters*, 31 (24), 2120-2121 (1995).
- [243]. H. Choi, K. Park, S. Park, U. Paek, B. Lee, E. Choi, "Miniature fiber-optic high temperature sensor based on a hybrid structured Fabry–Perot interferometer," *Optics Letters*, 33 (21), 2455–2457 (2008).

- [244]. L. Nguyen, D. Hwang, S. Moon, D. Moon, and Y. Chung, "High temperature fiber sensor with high sensitivity based on core diameter mismatch," *Optics Express*, 16 (15), 11369–11375 (2008).
- [245]. G. Coviello, V. Finazzi, J. Villatoro, V. Pruneri, "Thermally stabilized PCF-based sensor for temperature measurements up to 1000° C," *Optics Express*, 17 (24), 21551–21559 (2009).
- [246]. Y. Rao, Z. Ran, X. Liao, H. Deng, "Hybrid LPFG/MEFPI sensor for simultaneous measurement of high-temperature and strain," *Optics Express*, 15 (22), 14936–14941 (2007).
- [247]. V. Churikov, V. Kopp, A. Genack, "Chiral diffraction gratings in twisted microstructured fibers," *Optics Letters*, 35 (3), 342–344 (2010).
- [248]. D. Grobnic, S. J. Mihailov, H. Ding, F. Bilodeau, C. W. Smelser, "Single and low order mode interrogation of a multimode sapphire fibre Bragg grating sensor with tapered fibres," *Measurement Science and Technology*, 17 (5), 980–984 (2006).
- [249]. Y. Li, M. Yang, D. Wang, J. Lu, T. Sun, K. Grattan, "Fiber Bragg gratings with enhanced thermal stability by residual stress relaxation," *Optics Express*, 17 (22), 19785–19790 (2009).
- [250]. J. Canning, S. Bandyopadhyay, M. Stevenson, P. Biswas, J. Fenton, M. Aslund, "Regenerated gratings," *Journal of the European Optical Society-Rapid Publications*, 4 (09052), 1-7 (2009).
- [251]. L. Polz, Q. Nguyen, H. Bartelt, J. Roths, "Fiber Bragg gratings in hydrogen-loaded photosensitive fiber with two regeneration regimes," *Optics Communications*, 313(1), 128-133 (2014).
- [252]. A. F. Fernandez, A. I. Gusarov, B. Brichard, S. Bodart, K. Lammens, F. Berghmans, M. Decreton, P. Megret, M. Blondel, A. Delchambre, "Temperature monitoring of nuclear reactor cores with multiplexed fiber Bragg grating sensors," *Optical Engineering*, 41 (6), 1246-1254 (2002).
- [253]. V. V. Spirin, M. G. Shlyagin, S. V. Miridonov, F. J. M. Jimenez, R. M. L. Gutierrez, "Fiber Bragg grating sensor for petroleum hydrocarbon leak detection," *Optics and Lasers in Engineering*, **32** (5), 497-503(2000).
- [254]. G. Laffont, R. Cotillard, P. Ferdinand, "Multiplexed regenerated fiber Bragg gratings for high-temperature measurement," *Measurement Science and Technology*, 24 (9), 094010 (2013)
- [255]. Q. Zhang, D. A. Brown, L. Reinhart, T. F. Morse, "Simple prism-based scheme for fabricating Bragg gratings in optical fibers," *Optics Letters*, 19 (23), 2030-2032 (1994).

- [256]. N. H. Rizvi, M. C. Gower, "Production of submicrometer period Bragg gratings in optical fibers using wavefront division with a biprism and an excimer laser source," *Applied Physics Letters*, 67 (6), 739-741 (1995).
- [257]. R. Mahakud, J. Kumar, O. Prakash, S. K. Dixit, S. V. Nakhe, "FBG inscription by a biprism interferometer: analysis and experiment," *Applied Physics B*, 121 (3), 283-295 (2015).
- [258]. G. Ghosh, "Model for the thermo-optic coefficients of some standard optical glasses," *Journal of Non-Crystalline Solids*, 189 (1-2), 191-196 (1995).
- [259]. S. Pal, T. Sun, K. T. V. Grattan, S. A. Wade, S. F. Collins, G. W. Baxter, B. Dussardier, G. Monnom, "Non-linear temperature dependence of Bragg gratings written in different fibres, optimised for sensor applications over a wide range of temperatures," *Sensors and Actuators A: Physical*, 112 (2-3), 211-219 (2004).
- [260]. R. Mahakud, J. Kumar, O. Prakash, S. K. Dixit, "Study of the nonuniform behavior of temperature sensitivity in bare and embedded fiber Bragg gratings: experimental results and analysis," *Applied Optics*, 52 (31), 7570-7579 (2013).
- [261]. D. W. Coutts, M. D. Ainsworth, J. A. Piper, "Efficient green/yellow conversion of copper vapour laser output," *Optics Communications*, 75 (3,4), 301-306 (1990).
- [262]. T. S. Petrov, N. V. Sabotinov, S. T. Trendafilov, "Dye jet amplifier of the yellow CuBr vapor laser output," *Optics Communications*, 84 (5-6), 295-298 (1991).
- [263]. G. N. Tiwari, R. K. Mishra, R. Khare, S. V. Nakhe, "Development of copper bromide laser master oscillator power amplifier system," *Pramana Journal of Physics*, 82 (2), 217-225 (2014).
- [264]. C. Y. H. Tsao, D. N. Payne, W. A. Gambling, "Modal characteristics of three-layered optical fiber waveguides: a modified approach," *Journal of the Optical Society of America A*, 6 (4), 555-563 (1989).
- [265]. S. Kumar, S. K. Raghuwanshi, "Derivation of eigenvalue equation for double clad/double core planar slab optical waveguides," *Proceeding of the national seminar on frontiers in Electronics & Communication and Instrumentation Technology (FECIT-2011)*, Indian School of Mines, Dhanbad, PTS-11, 38 (2011).
- [266]. A. S. Belanov, E. M. Dianov, G. I. Ezhov, A. M. Prokhorov, "Propagation of normal modes in multilayer optical waveguides I. Component fields and dispersion characteristics," *Soviet Journal of Quantum Electronics*, 6 (1), 43-50 (1976).
- [267]. J. M. Senior, *Optical fiber communications*, 3rd edition, Pearson Education limited (2009).

- [268]. H. G. Unger, *Planar Optical Waveguides and Fibers*, England, Clarendon Press, (1977).
- [269]. M. Monerie, "Propagation in doubly clad single-mode fibers," *IEEE Journal of Quantum Electronics*, 18 (4), 535-542 (1982).
- [270]. R. Mahakud, O. Prakash, J. Kumar, S.V. Nakhe, S. K. Dixit, "Analysis on the effect of UV beam intensity profile on the refractive index modulation in phase mask based fiber Bragg grating writing," *Optics Communications*, 285 (24), 5351–5358 (2012).
- [271]. R. Mahakud, O. Prakash, S. V. Nakhe, S. K. Dixit, "Analysis on the saturation of refractive index modulation in fiber Bragg gratings (FBGs) written by partially coherent UV beams," *Applied Optics*, 51 (12), 1828-1835 (2012).
- [272]. F. Piao, W. G. Oldham, E. E. Haller, "Ultraviolet-induced densification of fused silica," *Journal of Applied Physics*, 87 (7), 3287-3293 (2000).
- [273]. D. L. Griscom, "Nature of defects and defect generation in optical glasses," *Proceedings of SPIE*, 541, 38-59 (1985).
- [274]. N. F. Borrelli, C. Smith, D. C. Allan, T. P. Seward III, "Densification of fused silica under 193-nm excitation," *Journal of the Optical Society of America B*, 14 (7), 1606-1615 (1997).
- [275]. N. F. Borrelli, C. M. Smith, D. C. Allan, "Excimer-laser-induced densification in binary silica glasses," *Optics Letters*, 24 (20), 1401-1403 (1999).
- [276]. R. Schenker, P. Schermerhorn, W. G. Oldham, "Deep-ultraviolet damage to fused silica," *Journal of Vacuum Science & Technology B*, 12(6), 3275-3279 (1994).
- [277]. Y. Saito, S. Okamoto, H. Inomata, J. Kurachi, T. Hidaka, H. Kasai, "Micro-fabrication techniques applied to aluminosilicate glass surfaces: Micro-indentation and wet etching process," *Thin Solid Films*, 517 (9), 2900–2904 (2009).
- [278]. H. Mueller, "The theory of photoelasticity," *Journal of the American Ceramic Society*, 21(1), 27-33 (1938).
- [279]. R. E. Schenker, W. G. Oldham, "Ultraviolet-induced densification in fused silica," *Journal of Applied Physics*, 82 (3), 1065-1071 (1997).
- [280]. L. Dong, G. Qi, M. Marro, V. Bhatia, L. L. Hepburn, M. Swan, A. Collier, D. L. Weidman, "Suppression of cladding mode coupling loss in fiber Bragg gratings," *IEEE Journal of Lightwave Technology*, 18(11), 1583-1590 (2000).

- [281]. J. Canning, "Regeneration, regenerated gratings and composite glass properties: the implications for high temperature micro and nano milling and optical sensing," *Measurement*, 79, 236-249 (2016).
- [282]. A. Bueno, D. Kinet, P. Megret, C. Caucheteur, "Fast thermal regeneration of fiber Bragg gratings," *Optics Letters*, 38 (20), 4178-4181 (2013).
- [283]. J. Kumar, R. Mahakud, O. Prakash, S. K. Dixit, "Study on hydrofluoric acid-based clad etching and chemical sensing characteristics of fiber Bragg gratings of different reflectivity fabricated under different UV exposure times," *Optical Engineering*, 52 (5), 0544021-6 (2013).
- [284]. Y. Liang, C. R. Miranda, S. Scandolo, "Temperature-induced densification of compressed SiO₂ glass: A molecular dynamics study," *High Pressure Research - Taylor & Francis Online*, 28 (1), 35-44 (2008).
- [285]. C. R. Kurkjian, M. J. Matthewson, J. M. Rooney, "Effects of heat treatment and HF etching on the strength of silica lightguides," *Proceedings of SPIE*, 5465, 223-229 (2004).
- [286]. E. M. Dianov, V. M. Mashinsky, V. B. Neustruev, O. D. Sazhin, V. V. Brazhkin, V. A. Sidorov, "Optical absorption and luminescence of germanium oxygen-deficient centers in densified germanosilicate glass," *Optics Letters*, 22 (14), 1089-1091 (1997).
- [287]. A. Iadicicco, A. Cutolo, S. Campopiano, M. Giordano, A. Cusano, "Advanced fiber optical refractometers based on partially etched fiber Bragg gratings," *IEEE Sensors*, 3, 1218-1221 (2004).
- [288]. H. G. Limberger, P. Y. Fonjallaz, R. P. Salathe, F. Cochet, "Compaction-and photoelastic-induced index changes in fiber Bragg gratings," *Applied Physics Letters*, 68 (22), 3069-3071 (1996).
- [289]. G. Violakis, N. Aggarwal, H. G. Limberger, "Stress changes in H₂-loaded SMF optical fibers induced by cw-Ar⁺ 244 nm irradiation," *Optical Materials Express*, 2 (11), 1490-1495 (2012).
- [290]. J. Burgmeier, A. Feizpour, W. Schade, B. M. Reinhard, "Plasmonic nanoshell functionalized etched fiber Bragg gratings for highly sensitive refractive index measurements," *Optics Letters*, 40 (4), 546 -549 (2015).
- [291]. J. F. Akki, A. S. Lalasangi, K. G. Manohar, P. Raikar, T. Srinivas, U. S. Raikar, "Detection and determination of manganese concentration in water using a fiber Bragg grating coupled with nanotechnology," *Applied Optics*, 50 (32), 6033-6038 (2011).
- [292]. J. A. Kruse, "Methanol poisoning," *Intensive Care Medicine*, 18 (7), 391-397 (1992).

- [293]. R. N. Boos, N. Rahway, "Study of methanol catalyzed reaction between sodium 1, 2-naphthoquinone-4-sulfonate and hydroxyl ion and its application in the determination of methanol," *Journal of Analytical Chemistry*, 20 (10), 964-965 (1948).
- [294]. M. C. Wu, C. M. Jiang, Y. Y. Ho, S. C. Shen, H. M. Chang, "Convenient quantification of methanol in juices by methanol oxidase in combination with basic fuchsin," *Food Chemistry*, 100 (1), 412-418 (2007).
- [295]. B. R. Buchanan, D. E. Hongis, C. J. Lee, W. Roth, "Detection of ethanol in wines using optical-fiber measurements and near-infrared analysis," *Applied Spectroscopy*, 42 (6), 1106-1111 (1988).
- [296]. H. Pontes, P. G. Pinho, S. Casal, H. Carmo, A. Santos, T. Magalhaes, F. Remiao, F. Carvalho, M. L. Bastos, "GC determination of acetone, acetaldehyde, ethanol, and methanol in biological matrices and cell culture," *Journal of Chromatographic Science*, 47 (4), 272-278 (2009).
- [297]. C. Gaffney, C. K. Chau, "Using refractive index gradients to measure diffusivity between liquids," *American Journal of Physics*, 69 (7), 821-826 (2001).
- [298]. W. Xu, X. G. Huang, J. S. Pan, "Simple fiber-optic refractive index sensor based on fresnel reflection and optical switch," *IEEE Sensors Journal* 13 (5), 1571-1574 (2013).
- [299]. R. M. Measures, *Structural Monitoring with Fiber Optic Technology*, London, U. K., Academic press (2001).
- [300]. D. A. Pereira, O. Frazao, J. L. Santos, "Fiber Bragg grating sensing system for simultaneous measurement of salinity and temperature," *Optical Engineering*, 43 (2), 299-304 (2004).
- [301]. A. W. Snyder, J. D. Love, *Optical waveguide theory*, Chapman & Hall, London (1983).
- [302]. M. Rothschild, D. J. Ehrlich, D. C. Shaver, "Effects of excimer laser irradiation on the transmission, index of refraction, and density of ultraviolet grade fused silica," *Applied Physics Letters*, 55 (13), 1276-1278 (1989).
- [303]. C. M. Smith, N. F. Borrelli, "Behavior of 157 nm excimer-laser-induced refractive index changes in silica," *Journal of the Optical Society of America B*, 23 (9), 1815-1821 (2006).
- [304]. N. Kitamura, Y. Toguchi, S. Funo, H. Yamashita, M. Kinoshita, "Refractive index of densified silica glass," *Journal of Non-Crystalline Solids*, 159 (3), 241-245 (1993).